Low-crosstalk modular flip-chip architecture with superconducting kinetic-inductively coupled flux-qubit-resonator circuits

Zur Erlangung des akademischen Grades eines

DOKTORS DER NATURWISSENSCHAFTEN (Dr. rer. nat.)

von der KIT-Fakultät für Physik des

Karlsruher Instituts für Technologie (KIT)

genehmigte

DISSERTATION

von

M. Sc. Sören Alexander Ihssen

aus Hamburg

Tag der mündlichen Prüfung:	12.12.2025
Referent:	Prof. Dr. Ioan M. Pop
Korreferent:	Prof. Dr. Christopher Eichler

Abstract

In this thesis, we develop modular and extendable hardware for superconducting quantum processors. In the first part, we introduce a qubit-readout system in which the dispersive interaction is mediated by a kinetic inductance. This approach enables independent engineering of the dispersive shift without relying on large capacitances. We experimentally confirm the concept of kinetic-inductive coupling and realize generalized flux qubits in the plasmon and fluxon regimes. At the half-flux-quantum sweet spot, we measure dispersive shifts between 60 kHz and 2 MHz. The readout performance is comparable to conventional architectures, with preparation fidelities of 99.7 % (ground state) and 92.7 % (excited state), and leakage suppressed below 0.1 %. In the second part, we present a flip-chip architecture designed for arrays of coupled superconducting qubits, with the qubit and coupling chips each placed inside individual microwave enclosures. The qubit chips are electrically floating, allowing for a simple, fully modular assembly and significantly reduced microwave crosstalk. We validate the architecture using a chain of three qubits, in which the central qubit acts as a tunable coupler. We demonstrate a transverse coupling on/off ratio of approximately 70, zz-crosstalk below 1 kHz between resonant qubits, and isolation exceeding 60 dB between the outer qubit enclosures. Together, these results establish a modular flip-chip platform that combines kinetic-inductive dispersive readout with strong isolation and tunable coupling, outlining a route towards multi-qubit superconducting processors.

Zusammenfassung

In dieser Arbeit entwickeln wir modulare und erweiterbare Hardware für supraleitende Quantenprozessoren. Im ersten Teil stellen wir ein Qubit-Auslesesystem vor, bei dem die dispersive Wechselwirkung durch eine kinetische Induktivität erzeugt wird. Dieser Ansatz ermöglicht eine unabhängige Gestaltung der dispersiven Verschiebung, ohne auf große Kapazitäten angewiesen zu sein. Wir weisen das Konzept der kinetisch-induktiven Kopplung experimentell nach und realisieren Fluß-Qubits im Plasmon- und Fluxon-Regime. Am optimalen Arbeitspunkt des halben Fluxquants messen wir dispersive Verschiebungen zwischen 60 kHz und 2 MHz. Die Ausleseleistung ist mit herkömmlichen Architekturen vergleichbar, mit einer Wiedergabetreue von 99,7 % (Grundzustand) und 92,7 % (angeregter Zustand) und einer unter 0,1 % unterdrückten Leckage. Im zweiten Teil stellen wir eine Flip-Chip-Architektur vor, die für Arrays gekoppelter supraleitender Qubits entwickelt wurde, wobei die Qubit- und Kopplerchips jeweils in individuellen Mikro-Wellengehäusen untergebracht sind. Die Qubit-Chips sind elektrisch schwebend, was eine einfache, vollständig modulare Montage und eine deutlich reduzierte Mikrowellenübersprechung zur Folge hat. Wir validieren die Architektur anhand einer Kette aus drei Qubits, in der das mittlere Qubit als flussabhängiger Koppler agiert. Wir demonstrieren ein transversales Kopplungs-Ein-/Aus-Verhältnis von etwa 70, ein zz-Übersprechen unter 1 kHz zwischen resonanten Qubits und eine Isolation von über 60 dB zwischen den äußeren Qubit-Gehäusen. Zusammen ergibt sich eine modulare Flip-Chip-Plattform, die kinetisch-induktives dispersives Auslesen mit starker Isolation und einstellbarer Kopplung kombiniert und einen Weg zu supraleitenden Multi-Qubit-Prozessoren ermöglicht.

List of publications

Authors marked with † have contributed equally.

1. **S. Ihssen**†, S. Geisert†, G. Jauma, P. Winkel, M. Spiecker, N. Zapata, N. Gosling, P. Paluch, M. Pino, T. Reisinger, W. Wernsdorfer, J. J. García-Ripoll, and I. M. Pop, „Low crosstalk modular flip-chip architecture for coupled superconducting qubits“, *Applied Physics Letters* **126**, 13 (2025). doi: 10.1063/5.0245667.

2. S. Geisert†, **S. Ihssen**†, P. Winkel, M. Spiecker, M. Fechant, P. Paluch, N. Gosling, N. Zapata, S. Günzler, D. Rieger, D. Bénâtre, T. Reisinger, W. Wernsdorfer, and I. M. Pop, „Pure kinetic inductance coupling for cQED with flux qubits“, *Applied Physics Letters* **125**, 6 (2024). doi: 10.1063/5.0218361.

3. R. Hanna, **S. Ihssen**, S. Geisert, U. Kocak, M. Arfini, A. Hertel, T. J. Smart, M. Schleenvoigt, T. Schmitt, J. Domnick, K. Underwood, A. R. Jalil, J. H. Bae, B. Bennemann, M. Féchant, M. Field, M. Spiecker, N. Zapata, C. Dickel, E. Berenschot, N. Tas, G. A. Steele, D. Grützmacher, I. M. Pop, and P. Schüffelgen, „On-chip stencil lithography for superconducting qubits“, preprint at arXiv:2507.17005 (2025).

4. Z. Jiang, S. Geisert, **S. Ihssen**, I. M. Pop, and M. H. Ansari, „Enabling full localization of qubits and gates with a multi-mode coupler“, preprint at arXiv:2509.26211 (2025).

5. N. Zapata, I. Takmakov, S. Günzler, S. Geisert, **S. Ihssen**, M. Field, A. Nambisan, D. Rieger, T. Reisinger, W. Wernsdorfer, and I. M. Pop, „Granular Aluminum Parametric Amplifier for Low-Noise Measurements in Tesla Fields“, *Physical Review Letters* **133**, 260604 (2024). doi: 10.1103/PhysRevLett.133.260604.

6. D. Willsch†, D. Rieger†, P. Winkel, M. Willsch, C. Dickel, J. Krause, Y. Ando, R. Lescanne, Z. Leghtas, N. T. Bronn, P. Deb, O. Lanes, Z. K. Minev, B. Dennig, S. Geisert, S. Günzler, **S. Ihssen**, P. Paluch, T. Reisinger, R. Hanna, J. H. Bae, P. Schüffelgen, D. Grützmacher, L. Buimaga-Iarinca, C. Morari, W. Wernsdorfer, D. P. DiVincenzo, K. Michielsen, G. Catelani, and I. M. Pop, „Observation of Josephson harmonics in tunnel junctions“, *Nature Physics* **20**, 815–821 (2024). doi: 10.1038/s41567-024-02400-8.

Contents

1. Introduction

Many modern technologies operate on principles that rely on quantum mechanics, from solar cells, LEDs, and transistors to lasers and atomic clocks. More advanced applications harness quantum effects explicitly, including new generations of quantum sensors [1, 2], quantum computers [3, 4, 5, 6], quantum simulators [7, 8, 9], and quantum communication systems [10, 11, 12]. Examples range from quantization, band structure, and tunneling in conventional devices [13, 14] to superposition and entanglement in advanced technologies [15]. These concepts, which have no analogue in classical physics, form the foundation of modern quantum technology.

Among emerging quantum technologies, the universal quantum computer occupies a central position, as computing has become an essential component of modern society. Classical computers operate using binary logic implemented with transistors, an architecture fundamentally constrained by the discrete nature of classical bits. Replacing this logic with one grounded in quantum mechanics offers the potential to solve certain problems with far greater efficiency. A quantum computer uses qubits, which are two-level quantum systems that exist in superposition and can become entangled with each other [5, 15]. These properties allow us to perform certain calculations much more efficiently than with conventional bits. For example, Shor's algorithm [16] efficiently factors large numbers, Grover's algorithm [17] searches unsorted databases faster than classical methods, and quantum simulation techniques [18, 19] model complex quantum systems that are beyond the reach of classical computers. A practical quantum computer must fulfill the DiVincenzo criteria [3]: scalable and well-defined qubits, the ability to initialize them to known states, long coherence times, a universal set of quantum gates, and reliable qubit-specific measurements. Meeting all of these criteria simultaneously remains challenging, and no existing physical platform fully meets these requirements as of today.

To realize practical quantum computers, multiple physical platforms are being developed. Trapped ions achieve coherence times of several hours [20] and high single- and two-qubit gate fidelity [21, 22], but their operations are slow (typically tens of μs for high-fidelity gates) and scaling demands complex optical control systems [23]. Neutral atoms in optical lattices and tweezer arrays can form large-scale systems [24], yet despite recent progress in individual addressing [24], parallel entangling gates [25], and mid-circuit operations [26], scalable low-crosstalk readout and fully error-corrected operation remain challenging. Photonic qubits are good at transmitting quantum information over long distances, but unlike many matter-based qubits, they require additional nonlinear elements to implement entangling gates [27]. Semiconductor spin qubits are compatible with established complementary metal-oxide-

semiconductor (CMOS) fabrication methods. However, achieving the required device precision remains challenging, and the qubits are susceptible to substrate offset charges that are difficult to stabilize [28, 29].

Superconducting circuits stand out for their combination of macroscopic size with fully quantum behavior, as highlighted by the 2025 Nobel Prize in Physics, which recognized quantized energy levels and quantum tunneling in such circuits [30]. They conduct direct current without dissipation and can be lithographically patterned to realize arbitrary energy spectra and engineered couplings for precise control and readout in the microwave domain. Circuits with anharmonic spectra act as qubits, while propagating microwave photons can mediate entanglement between distant devices, enabling chip-to-chip links [31, 32] and even cryostat-to-cryostat links [33, 34]. Established processes are used for fabrication, which support large-scale integration. To suppress thermal excitations, they are operated at millikelvin temperatures in dilution refrigerators [35]. Their large dipole moments make them sensitive to environmental noise, cross-coupling to nearby circuits, and material defects. Overcoming these decoherence mechanisms remains a major research focus, but the platform's maturity and versatility have made superconducting qubits one of the most advanced contenders for large-scale quantum computing [36, 37].

Superconducting qubits are typically operated within the framework of circuit quantum electrodynamics (cQED) [38, 39], where they interact with on-chip microwave resonators and waveguides. The cQED framework adapts concepts from atomic cavity QED [40] for implementation in lithographically defined electrical circuits, enabling strong and controllable coupling between qubits and quantized electromagnetic fields. A particularly versatile mechanism in cQED is dispersive coupling between qubits and harmonic oscillators [39], which enables single-shot readout [41, 42, 43, 44], the creation of non-classical photonic states [45, 46, 47, 48, 49, 50], reservoir engineering for qubit state preparation [51, 52], and even the autonomous stabilisation of entangled states [53, 54]. Dispersive coupling is typically mediated by the electric field via a coupling capacitor, as is standard in transmon-based cQED architectures [6, 55, 56, 57, 58]. In complex devices, stray capacitances can cause crosstalk, alter the dispersive shift, and drive nonlinear elements when exposed to alternating magnetic fields or gradients [59]. To mitigate these effects, the community has developed approaches such as air-bridges [60], deep silicon vias [61, 62, 63], flip-chip devices [62, 64, 57], and chiplet-based architectures [65, 66].

Here, we propose an alternative approach that implements dispersive readout via kinetic-inductance coupling between a generalized flux qubit (GFQ) and a readout resonator. We choose the GFQ because its large anharmonicity enables fast gates with reduced leakage, and its small electric dipole moment makes it less sensitive to charge noise [67, 68]. In addition, the loop geometry provides a natural interface for inductive coupling, which we realize in a three-island circuit with two normal modes, a qubit and a resonator, coupled through a shared inductance. While such an inductance can be realized with Josephson junction (JJ) arrays, we demonstrate the concept using granular aluminum (grAl) [69, 70], a high kinetic inductance material that enables compact inductors and avoids the complexity of fabricating large junction arrays. The symmetry of our design effectively eliminates capacitive contributions to the qubit-readout interaction, rendering the coupling local and inherently less prone to spurious crosstalk.

However, coupling optimization alone does not address the broader challenge of building extendable and fault-tolerant superconducting quantum processors. Large monolithic two-dimensional (2D) processors with hundreds of qubits [6, 71] have demonstrated remarkable capabilities, including surface-code error correction [72, 73, 74, 55, 56], but as their size and complexity increase, new challenges emerge. As device density grows, phenomena such as correlated quasiparticle and phonon bursts [75, 76], charge offsets [77], and two-level-system reconfigurations due to ionizing radiation [78, 79] can simultaneously affect large portions of a processor, creating errors that cannot be corrected by surface-code error correction. In addition, the high device density in these processors results in non-negligible microwave crosstalk [56] and frequency crowding, while fabricating a chip with hundreds of qubits and no defective elements remains extremely challenging. A modular architecture would allow faulty elements to be isolated or replaced without compromising the entire system. These challenges highlight the need for scale-up strategies that mitigate microwave and phonon crosstalk while maximizing modularity.

Another approach places superconducting qubits inside three-dimensional (3D) microwave cavities [80], where the qubit is well isolated from its environment. This improved isolation has enabled coherence times exceeding hundreds of μs [68, 81, 82]. Scalable 3D integration schemes such as Refs. [83, 84, 85] have shown that high coherence can be retained in small multi-qubit prototypes. Realizing larger-scale systems will require solutions to accommodate the substantial physical footprint of cavities and increase their integration density. Hybrid technologies, such as flip-chip devices [62, 64, 57] and chiplet-based architectures [65, 66], can help increase integration density, but they often require complex multi-layer packaging with precise alignment. Additionally, advanced interconnect methods, including indium bump-bonding [86], deep silicon vias [61, 62, 63], and spring-loaded pogo pins [87], increase the engineering complexity of these architectures.

To address these challenges, we develop a modular flip-chip architecture that combines elements of both 2D and 3D approaches while avoiding the need for highly complex packaging techniques. The design consists of an array of coupled but crosstalk-resilient superconducting qubits, each placed on its own electrically floating chip inside an individual microwave enclosure. This arrangement provides strong isolation between neighboring devices and reduces sensitivity to correlated errors, such as those arising from phonon propagation.

This thesis is structured as follows: in Chapter 2, we introduce the theoretical background relevant to the work. We review fundamental concepts such as the quantum harmonic oscillator, the JJ, and the Bloch sphere representation of qubit states. We discuss decoherence mechanisms, present the charge and generalized flux qubit, and introduce the concept of a superinductance. We further describe dispersive readout and the magnetic flux hose, and conclude the chapter with the Schrieffer-Wolff transformation as a tool for deriving effective qubit-qubit couplings. In Chapter 3, we discuss our inductively coupled qubit readout circuit. It consists of a three-island GFQ dispersively coupled to a readout resonator through a shared kinetic inductance. We present the circuit design, analyze its symmetry properties, and provide

experimental evidence for the inductive coupling. We measure the readout fidelity and discuss quantum state preparation, and finally investigate the performance of our GFQs implemented with JJ arrays. In Chapter 4, we describe our modular flip-chip architecture, measure the isolation between neighboring GFQs and demonstrate tunable qubit-qubit coupling. Chapter 6 covers the experimental methods used in this work, including fabrication details and the cryogenic and room-temperature microwave measurement setup.

2. Theoretical background

Superconductivity is a macroscopic quantum phenomenon observed in many metals and alloys when cooled below their critical temperature T_c. At this transition, superconductors become perfect diamagnets, as first demonstrated by the Meissner effect [88], and their DC resistance vanishes [89]. The Meissner effect expels external magnetic fields from the superconductor up to a critical value by generating persistent surface currents, which screen the material's interior from magnetic fields [90]. This behavior is a direct signature of a macroscopic quantum state.

The microscopic mechanism underlying conventional superconductivity is described by the Bardeen-Cooper-Schrieffer (BCS) theory [91]. According to this theory, electrons near the Fermi surface experience a weak attractive interaction mediated by phonons [89]. This leads to the formation of Cooper pairs, which are bosonic bound states of two electrons with opposite spin and momentum. The pairs are bound by an energy Δ, which must be overcome to separate the electrons. The corresponding single-particle excitations at this energy are Bogoliubov quasiparticles. Below a material-specific critical temperature T_c, the thermal energy $k_B T$ is insufficient to break the pairs, and they condense into a collective macroscopic wavefunction

$$\Psi(\vec{x},t) = \sqrt{n_s}\, e^{i\varphi(\vec{x},t)}, \tag{2.1}$$

where n_s is the Cooper pair density and φ is the macroscopic superconducting phase. For conventional superconductors at temperatures $T \ll T_c$, the gap is given by

$$\Delta \approx 1.76 k_B T_c. \tag{2.2}$$

The macroscopic quantum properties of superconductors lead to flux quantization in superconducting loops [90]. From the London equation [92], the supercurrent density can be derived as

$$\vec{j}_s = \frac{e\, n_s}{m_e}\left[\frac{\hbar}{2}\vec{\nabla}\varphi - e\vec{A}\right], \tag{2.3}$$

where $\vec{A}$ is a vector potential satisfying $\vec{B} = \vec{\nabla}\times\vec{A}$. Integrating around a closed superconducting loop, we obtain the quantization condition

$$\oint \nabla\varphi \cdot d\ell = 2\pi k \quad \text{with} \quad k \in \mathbb{Z}. \tag{2.4}$$

This leads to the quantization of magnetic flux inside a superconducting loop in units of the magnetic flux quantum

$$\Phi_0 = \frac{h}{2e} \approx 2.067834 \cdot 10^{-15}\,\mathrm{Vs}. \tag{2.5}$$

Superconducting circuits provide an ideal platform for quantum applications due to their intrinsic macroscopic phase coherence, negligible dissipation, and well-defined quantized energy levels. Unlike classical circuits, where energy is continuously lost due to resistance, superconducting circuits allow quantum states to persist over long timescales up to the millisecond regime [93, 94]. These properties enable the implementation of quantum harmonic oscillators, superconducting qubits, and quantum gates, making them one of the leading architectures for quantum computing.

2.1. Quantum harmonic oscillator

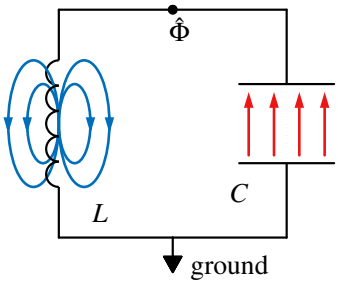

Figure 2.1.: **Circuit diagram of a quantum harmonic oscillator**, consisting of a parallel inductor L and capacitor C. The red arrows illustrate the electric field between the capacitor plates while the blue loops represent the magnetic field generated by the current through the inductor. Resonance is achieved when the energy stored in the electric and magnetic fields becomes equal, which occurs at the frequency $\omega_0 = 1/\sqrt{LC}$.

A fundamental superconducting circuit is the LC oscillator, which is formed by a parallel inductor and a capacitor as shown in Fig. 2.1. In the lumped-element approximation, the circuit size is much smaller than the electromagnetic wavelength, so that each capacitor and inductor can be treated as a single circuit node. As a result, the circuit is characterized by a single degree of freedom, which can be described either by the charge on the capacitor, $\hat{Q}$, or the flux through the inductor, $\hat{\Phi}$. The charge corresponds to the time integral of the current flowing through the inductor

$$\hat{Q} = \int_{-\infty}^{t} \hat{I}(\tau)\, d\tau, \tag{2.6}$$

while the flux is defined as the time integral of the voltage across the capacitance

$$\hat{\Phi} = \int_{-\infty}^{t} \hat{V}(\tau)\, d\tau. \tag{2.7}$$

By convention, the flux $\hat{\Phi}$ is treated as the position-like coordinate, while the charge $\hat{Q}$ acts as its conjugate momentum. As a result, they satisfy the fundamental commutation relation: $[\hat{\Phi}, \hat{Q}] = i\hbar$. Following the canonical quantization approach as outlined in [95], the Hamiltonian of a quantum LC oscillator is derived from its classical counterpart and given by

$$\hat{\mathcal{H}} = \frac{\hat{Q}^2}{2C} + \frac{\hat{\Phi}^2}{2L}, \tag{2.8}$$

where the kinetic energy is associated with the capacitive elements and the potential energy with the inductive elements. To diagonalize the Hamiltonian, the canonical coordinates $\hat{\Phi}$ and $\hat{Q}$ are expressed in terms of the creation and annihilation operators $\hat{a}^\dagger$ and $\hat{a}$, respectively:

$$\hat{\Phi} = \Phi_{\mathrm{ZPF}}\,(\hat{a}+\hat{a}^\dagger) \quad \text{and} \quad \hat{Q} = -iQ_{\mathrm{ZPF}}\,(\hat{a}-\hat{a}^\dagger), \tag{2.9}$$

where Φ_{ZPF} and Q_{ZPF} are the zero-point fluctuations of flux and charge

$$\Phi_{\mathrm{ZPF}} = \sqrt{\frac{\hbar Z}{2}} \quad \text{and} \quad Q_{\mathrm{ZPF}} = \sqrt{\frac{\hbar}{2Z}} \tag{2.10}$$

with the impedance $Z = \sqrt{L/C}$. This notation allows us to bring the Hamiltonian into its more compact form

$$\hat{\mathcal{H}} = \hbar\omega_0\,(\frac{1}{2}+\hat{a}^\dagger\hat{a}) \tag{2.11}$$

where $\omega_0 = \sqrt{1/LC}$ is the system's resonance frequency.

The LC oscillator is harmonic, with equally spaced energy levels. As a result, it cannot be used to selectively address only two states, since any drive that couples to the transition $|0\rangle \leftrightarrow |1\rangle$ will also excite higher transitions. To build qubits, a nonlinear element is required to break this degeneracy. The Josephson junction provides exactly such a nonlinearity while preserving superconductivity, and therefore forms the core element of superconducting qubits.

2.2. Josephson junction (JJ)

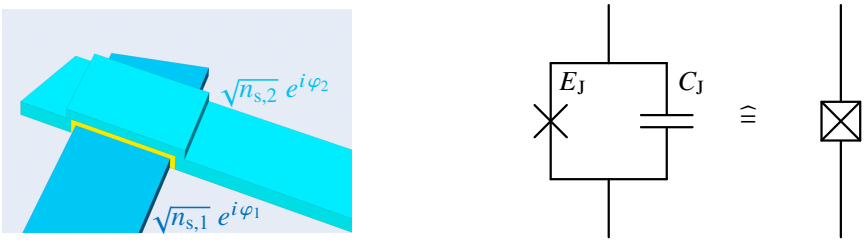

Figure 2.2.: **Josephson tunneling junctions** (JJs) in this thesis consist of two overlapping aluminum electrodes (dark and light blue), which are separated by a thin insulating aluminum-oxide barrier (yellow), as shown in the left panel (oxide barrier is not to scale). This structure forms a superconductor-insulator-superconductor (S-I-S) junction. The condensate in each electrode is described by its own complex wavefunction $\Psi_j = \sqrt{n_{s,j}}e^{i\varphi_j}$, coupled through the tunneling of Cooper pairs through the JJ. To account for the geometric capacitance across the tunnel barrier C_J, the junction is represented with a parallel capacitor in the equivalent circuit diagram as shown in the right panel.

In general, Josephson junctions (JJ) are areas of weak electrical coupling between two superconductors through which Cooper pairs can tunnel without losing their coherence [96]. In this thesis, superconductor-insulator-superconductor (S-I-S) JJ are used, where the superconducting electrodes are separated by a thin insulating barrier that is smaller than the coherence length ξ of the Cooper pairs. A difference in the phase between the two superconducting electrodes, $\varphi = \varphi_1 - \varphi_2$, gives rise to two Josephson equations. The first one describes the dissipationless current of Cooper pairs through the junction [97]

$$I(\varphi) = I_\mathrm{c} \sin(\varphi), \tag{2.12}$$

where I_c is the critical current. The second Josephson equation

$$V(t) = \frac{\hbar}{2e} \frac{\mathrm{d}\varphi}{\mathrm{d}t} = \frac{\Phi_0}{2\pi} \frac{\mathrm{d}\varphi}{\mathrm{d}t} \tag{2.13}$$

states that the time evolution of the phase difference leads to a voltage drop across the JJ. As a consequence, the inductance $L = V/\dot{I}$ of a JJ is given by

$$L_\mathrm{J}(\varphi) = L_\mathrm{J} \frac{1}{\cos(\varphi)} \quad \text{with} \quad L_\mathrm{J} = \frac{\Phi_0}{2\pi I_\mathrm{c}}. \tag{2.14}$$

The Josephson coupling energy

$$E_\mathrm{J}(\varphi) = \int I(\varphi) V(t)\, dt = E_\mathrm{J}(1 - \cos(\varphi)) \quad \text{with} \quad E_\mathrm{J} = \frac{\Phi_0 I_\mathrm{c}}{2\pi} \tag{2.15}$$

quantifies the strength of the superconducting coupling (i.e. coherent Cooper pair tunneling) across the junction.

In addition to these nonlinear relations, a JJ also exhibits a geometric shunt capacitance C_J across the tunnel barrier (see Fig. 2.2). Its characteristic capacitance per area is $C_\mathrm{J} \approx 50\text{-}100\,\mathrm{fF}/\mu\mathrm{m}^2$ [98, 99, 100, 101].

An important design tool is the Ambegaokar-Baratoff relation [102], which links the critical current I_c to the normal-state resistance R_n of the junction:

$$I_\mathrm{c} R_\mathrm{n} = \frac{\pi\Delta}{2e} \tanh\left(\frac{\Delta}{2k_\mathrm{B}T}\right), \tag{2.16}$$

where Δ is the energy gap of the superconductor at 0 K, i.e. $2\Delta(0)/k_\mathrm{B}T_\mathrm{c} = 3.53$ with $T_\mathrm{c} = 1.18$ K for bulk aluminum [103]. For thin film aluminum, values of $T_\mathrm{c} \approx 1.3 \pm 0.1$ K were measured [104]. This relation allows one to determine the Josephson energy E_J directly from resistance measurements[i], so that we can target qubit parameters during fabrication. With JJs as the nonlinear building blocks, superconducting circuits can be engineered to behave as qubits with discrete energy spectra. These devices realize quantum two-level systems (qubits) whose states can be described within the Bloch sphere representation.

[i] Tables with measured room-temperature resistances of JJs and inductors are shown in App. A.6

2.3. Bloch sphere representation of qubits

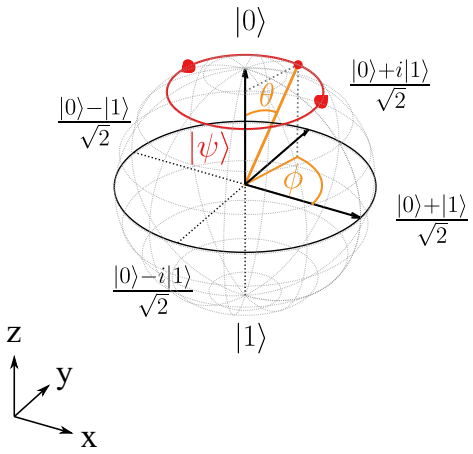

Figure 2.3.: **Bloch sphere.** Graphical representation of a qubit's Hilbert space spanned by $|0\rangle$ and $|1\rangle$. The six reference states along the coordinate axes correspond to specific superpositions. Any pure state $|\psi\rangle$ (red dot) on the sphere is defined by angles θ and ϕ. In the Schrödinger picture, $|\psi\rangle$ precesses around the z-axis at the qubit frequency ω_Q. Pure states lie on the surface; mixed states reside inside.

In general, qubits are quantum two-level systems whose states reside in a two-dimensional Hilbert $\mathscr{H}$ space spanned by a computational basis $\{|0\rangle, |1\rangle\}$. Any pure quantum state of a qubit can be written as a linear combination $|\psi\rangle = \alpha|0\rangle + \beta|1\rangle$, where $\alpha, \beta \in \mathbb{C}$ and $|\alpha|^2 + |\beta|^2 = 1$. A convenient way to visualize such a state is the Bloch sphere, where each pure state corresponds to a point on the surface of a unit sphere in three-dimensional space. A convenient parametrization for pure states is

$$|\psi\rangle = \cos\left(\frac{\theta}{2}\right)|0\rangle + \sin\left(\frac{\theta}{2}\right)e^{i\phi}|1\rangle, \tag{2.17}$$

where θ and ϕ define the orientation of the Bloch vector. Using these two angles each point on the Bloch sphere surface is uniquely defined as shown in Fig. 2.3. The poles represent by convention the basis states $|0\rangle$ (north-pole) and $|1\rangle$ (south-pole), while the equator contains equal superpositions with varying phase. In the laboratory frame, the qubit state $|\psi\rangle$ precesses around the z-axis at the qubit frequency ω_Q. In the frame rotating with ω_Q, the state is stationary for an undriven qubit. When a drive with frequency ω is applied, it is convenient to use a frame rotating at ω, where the state appears stationary only on resonance ($\omega = \omega_Q$). This simplifies the visualization of driven dynamics such as Rabi oscillations.
An ideal qubit in the laboratory frame, restricted to the Hilbert space $\mathscr{H} = \text{span}\{|0\rangle, |1\rangle\}$, is described by the Hamiltonian

$$\hat{\mathcal{H}} = \frac{\hbar\omega_Q}{2}\hat{\sigma}_z, \tag{2.18}$$

where $\hat{\sigma}_z$ is the Pauli operator and $\omega_Q = (E_1 - E_0)/\hbar$ is the qubit's transition frequency between the $|0\rangle$ and $|1\rangle$ states.

Rabi oscillations

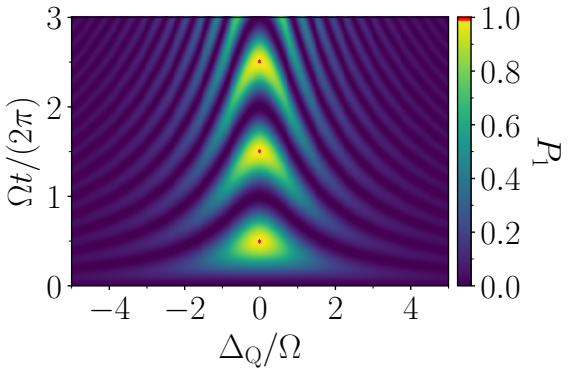

Figure 2.4.: **Rabi chevron pattern.** Probability P_1 to find the qubit in the excited state $|1\rangle$ vs. drive detuning Δ_Q. The drive is detuned by $\Delta_Q = \omega_Q - \omega$ from the qubit frequency. A continuous microwave drive with amplitude Ω is applied at time $t_0 = 0$.

To induce transitions between qubit states, a resonant microwave drive is applied. The dynamics are described by the Rabi Hamiltonian:

$$\hat{\mathcal{H}}_{\text{Rabi}} = \frac{\hbar\omega_Q}{2}\hat{\sigma}_z + \hbar\Omega\cos(\omega t)\hat{\sigma}_x, \tag{2.19}$$

where ω is the drive frequency, Ω the drive amplitude, and $\hat{\sigma}_x$ is the Pauli operator. This transverse coupling enables coherent transitions between $|0\rangle$ and $|1\rangle$. To simplify the dynamics, we move to a frame rotating at ω, defined by the unitary transformation $\hat{U}(t) = \exp(i\omega\hat{\sigma}_z t/2)$. In this frame, the qubit appears stationary when on resonance, and the Hamiltonian becomes time independent:

$$\hat{H}_{\text{Rabi}} = \frac{\hbar\Delta_Q}{2}\hat{\sigma}_z + \frac{\hbar\Omega}{2}\hat{\sigma}_x, \tag{2.20}$$

with detuning $\Delta_Q = \omega_Q - \omega$. The eigenstates of this Hamiltonian are superpositions of $|0\rangle$ and $|1\rangle$, and transitions occur at the generalized Rabi frequency

$$\Omega_R = \sqrt{\Omega^2 + \Delta_Q^2}. \tag{2.21}$$

On the Bloch sphere, the qubit state vector precesses around a fixed axis in the rotating frame, given by

$$\vec{n} = \frac{1}{\Omega_R}(\Omega, 0, \Delta_Q). \tag{2.22}$$

On resonance ($\Delta_Q = 0$) the axis becomes $\vec{n} = (1,0,0)$, resulting in full-amplitude Rabi oscillations between $|0\rangle$ and $|1\rangle$. For finite detuning, the axis tilts toward z, increasing the rotation speed while reducing the oscillation amplitude:

$$P_1 = \left(\frac{\Omega}{\Omega_R}\right)^2 \sin^2\left(\frac{\Omega_R t}{2}\right). \tag{2.23}$$

Fig. 2.4 shows the excited state probability P_1 as a function of time and detuning. The resulting interference pattern is known as the chevron pattern.

2.4. Decoherence

In the Bloch sphere picture, pure states evolve on the surface under unitary dynamics, assuming an isolated system. In practice, quantum systems interact with external degrees of freedom that are not

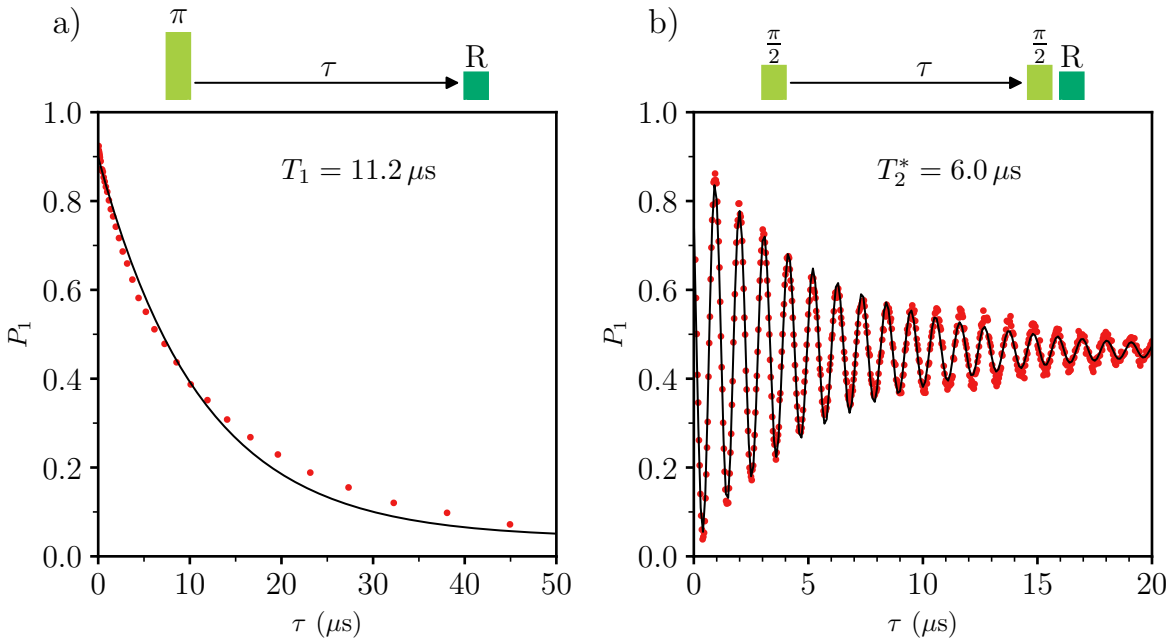

Figure 2.5.: **Energy relaxation and dephasing of qubit q7**, see App. A.2 and App. A.3. **a)** Energy relaxation measurement. The qubit is excited with a π-pulse (π) and measured with a readout pulse (R) after a delay τ. For each τ, the experiment is performed repeatedly, and the outcomes are averaged to determine the probability P_1 of finding the qubit in the $|1\rangle$ state. Fitting Eq. 2.27 to the measured data we extract $T_1 = 11.2\,\mu s$. **b)** Dephasing measurement using Ramsey interferometry. The qubit is prepared on the equator of the Bloch sphere with an $\frac{\pi}{2}$ pulse, detuned by $\Delta_Q = 936\,kHz$. After time τ, a second $\frac{\pi}{2}$ pulse maps the qubit back onto the z-axis. This is repeated multiple times for each τ to obtain P_1. Fitting Eq. 2.29 to the measured data, we extract $T_2^* = 6.0\,\mu s$. The data shown here serve as illustrative examples of how T_1 and T_2^* are extracted. Detailed descriptions of the devices and the sample box are given in section 3.1 and section 4.1, respectively.

directly accessible. This interaction leads to decoherence, i.e. the loss of information about the quantum state over time. The extent of the interaction with the environment is quantified by two characteristic time scales: the energy relaxation time T_1 and the decoherence time T_2. The examples in Fig. 2.5 illustrate how these quantities are extracted from experiment.

Energy relaxation

Energy relaxation describes the decay of qubit population toward thermal equilibrium due to coupling with the environment. It is characterized by the longitudinal relaxation time T_1, or the rate $\Gamma_1 = 1/T_1$. In the Bloch sphere picture, this corresponds to a contraction of the Bloch vector along the z-axis towards the thermal equilibrium state. Relaxation is driven by transverse noise coupling to $\hat{\sigma}_x$ or $\hat{\sigma}_y$, which mediates transitions between $|0\rangle$ and $|1\rangle$ via energy exchange. These transitions are described by upward and downward rates $\Gamma_1^{\uparrow}$ and $\Gamma_1^{\downarrow}$, with a total rate

$$1/T_1 = \Gamma_1 = \Gamma_1^{\downarrow} + \Gamma_1^{\uparrow}. \tag{2.24}$$

For typical experimental conditions ($T \approx 10\,\mathrm{mK}$, $f_\mathrm{Q} \in [2,5]\,\mathrm{GHz}$), the qubit transition energy satisfies $\hbar\omega_\mathrm{Q} \gg k_\mathrm{B}T$, such that

$$\Gamma_1^{\uparrow} = \Gamma_1^{\downarrow}\, e^{-\hbar\omega_\mathrm{Q}/k_\mathrm{B}T} \ll \Gamma_1^{\downarrow}. \tag{2.25}$$

The qubit relaxes predominantly from $|1\rangle$ to $|0\rangle$. The total relaxation rate can be decomposed into two contributions: a rate κ_Q due to coupling to the measurement port, and a rate γ due to uncontrolled loss channels:

$$\Gamma_1 = \kappa_\mathrm{Q} + \gamma. \tag{2.26}$$

In a direct measurement, κ_Q quantifies the rate at which information about the quantum state is extracted.

Experimentally, T_1 is extracted by preparing the qubit in $|1\rangle$ using a π-pulse, waiting for a time τ, and measuring the excited-state population P_1. Repeating the sequence yields an ensemble-averaged decay

$$P_1(\tau) = P_1(0)\, e^{-\tau/T_1}, \tag{2.27}$$

as shown in Fig. 2.5a.

Dephasing

Dephasing contributes to the overall decoherence characterized by the transverse relaxation (decoherence) time $T_2 = 1/\Gamma_2$, which includes both energy relaxation and dephasing:

$$\Gamma_2 = \frac{\Gamma_1}{2} + \Gamma_\phi, \tag{2.28}$$

where Γ_ϕ is the dephasing rate. In the limit $\Gamma_\phi \to 0$, decoherence is dominated by energy relaxation and $T_2 = 2T_1$. Dephasing describes loss of phase coherence in a superposition state without energy exchange. It is caused by longitudinal noise coupling to $\hat{\sigma}_z$, which leads to fluctuations in the qubit transition frequency.

Dephasing is typically measured using Ramsey interferometry. A $\pi/2$ pulse initializes the Bloch vector along the x-axis. In the rotating frame, the state precesses about the z-axis at a detuning Δ_Q. After a time τ, a second $\pi/2$ pulse maps the accumulated phase onto the z-axis for measurement. Repeating the experiment yields an average of P_1 as a function of τ. The resulting signal shows oscillations at a frequency Δ_Q that decay exponentially with characteristic time T_2^*:

$$P_1(\tau) = A\, e^{-\tau/T_2^*} \cos(\Delta_\mathrm{Q}\tau + \phi_0) + \text{offset}, \tag{2.29}$$

where ϕ_0, A, and the offset are fit parameters. This is illustrated in Fig. 2.5b. The symbol * indicates that the decoherence time T_2^* is obtained from a Ramsey experiment, which is sensitive to inhomogeneous broadening caused by low-frequency quasistatic noise (e.g., $1/f$). To mitigate sensitivity to quasistatic noise, a Hahn echo sequence can be used. In an echo sequence, a refocusing π pulse is inserted at $\tau/2$,

canceling low-frequency phase errors. The echo signal decays with a time constant $T_2^{\text{echo}} \geq T_2^*$, which reflects the high-frequency dephasing rate.

The impact of relaxation and dephasing depends strongly on the circuit implementation. In the following, we introduce the most relevant superconducting qubit types.

2.5. Charge qubit

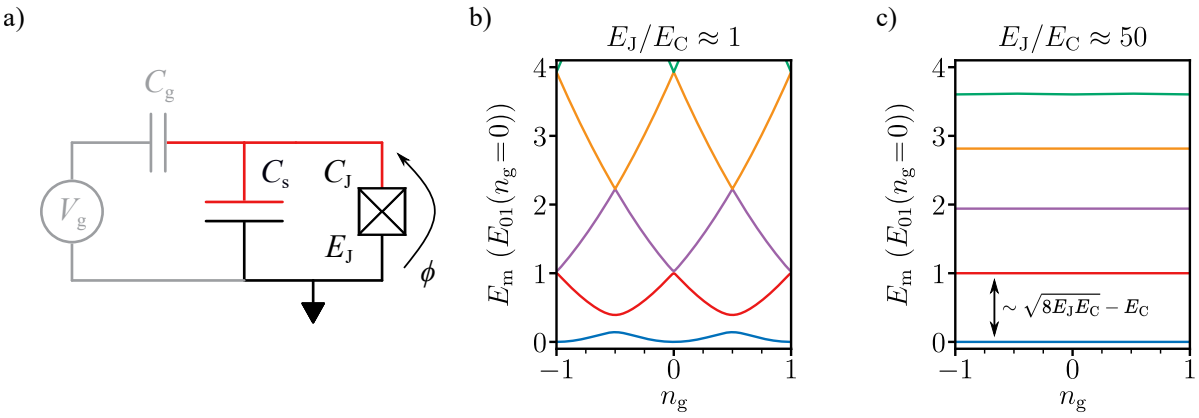

Figure 2.6.: **Charge qubit. a)** Circuit diagram of a charge qubit. Charge transfer between the environment and the small superconducting island (red) occurs through the JJ characterized by the Josephson energy E_J. The charging energy is given by $E_C = e^2/2C_\Sigma$, where C_Σ is the island's total capacitance. An external gate voltage V_g applied via a gate capacitance C_g induces an offset charge $n_g = V_g C_g/2e$ on the island. **b,c)** Energy spectra as functions of the offset charge n_g for $E_J/E_C \approx 1$ and $E_J/E_C \approx 50$, respectively. For better comparison, all energy levels are normalized to the $|0\rangle \rightarrow |1\rangle$ transition energy at $n_g = 0$, $E_{01}(n_g = 0)$. As E_J/E_C increases, the spectrum becomes increasingly flat, reflecting the exponential suppression of offset charge sensitivity with $e^{-\sqrt{8E_J/E_C}}$ in the transmon regime ($E_J/E_C \gg 1$).

One of the most fundamental superconducting qubits is the charge qubit, which is based on the Cooper pair box, introduced as the first superconducting qubit in 1999 [105]. It consists of a JJ that is shunted by a capacitance, so that at least one of the electrodes forms a superconducting island (see Fig. 2.6a). The island can exchange Cooper pairs with a reservoir through the JJ. A gate voltage V_g applied via C_g allows control of the offset charge $n_g = V_g C_g/2e$ of the island. The Hamiltonian of the charge qubit is

$$\hat{\mathcal{H}} = \frac{(\hat{q}-q_g)^2}{2C_\Sigma} + E_J\,(1-\cos(\hat{\varphi})) = 4E_C\,(\hat{n}-n_g)^2 + E_J\,(1-\cos(\hat{\varphi})), \tag{2.30}$$

where $E_C = e^2/2C_\Sigma$ and $C_\Sigma = C_s + C_g + C_J$. Here, $\hat{n} = \hat{q}/2e$ is the Cooper pair number operator on the island, and $\hat{\varphi} = 2\pi\hat{\phi}/\Phi_0$ is the superconducting phase difference across the junction. They obey the canonical commutation relation $[\hat{\varphi}, \hat{n}] = i$.

For small ratios $E_J/E_C \leq 1$ the qubit is typically described in the charge basis $|n\rangle$, representing the number of Cooper pairs on the island. The Josephson term couples neighboring charge states, hybridiz-

ing the parabolic charging-energy bands as a function of n_g and creating avoided crossings (Fig. 2.6b). While this coupling introduces the necessary anharmonicity for qubit operation, it also makes the energy levels highly sensitive to charge noise, leading to strong dephasing and coherence times of only a few nanoseconds.

To mitigate charge noise we can operate the qubit in the limit $E_J/E_C \gg 1$ (typically ≥ 50). In this regime, the wavefunctions extend over many charge states, making the spectrum nearly independent of n_g (Fig. 2.6c). The charge dispersion is suppressed by $e^{-\sqrt{8E_J/E_C}}$, and the dynamics are more naturally described in the phase basis $|\varphi\rangle$ [106]. The trade-off is a decreased anharmonicity, leading to an energy level spacing dominated by $\hbar\omega_{01} \approx \sqrt{8E_JE_C} - E_C$ which makes it more difficult to operate a transmon qubit as a two-level system.

An alternative strategy is the flux qubit, which trades charge sensitivity for flux tunability.

2.6. Generalized flux qubit

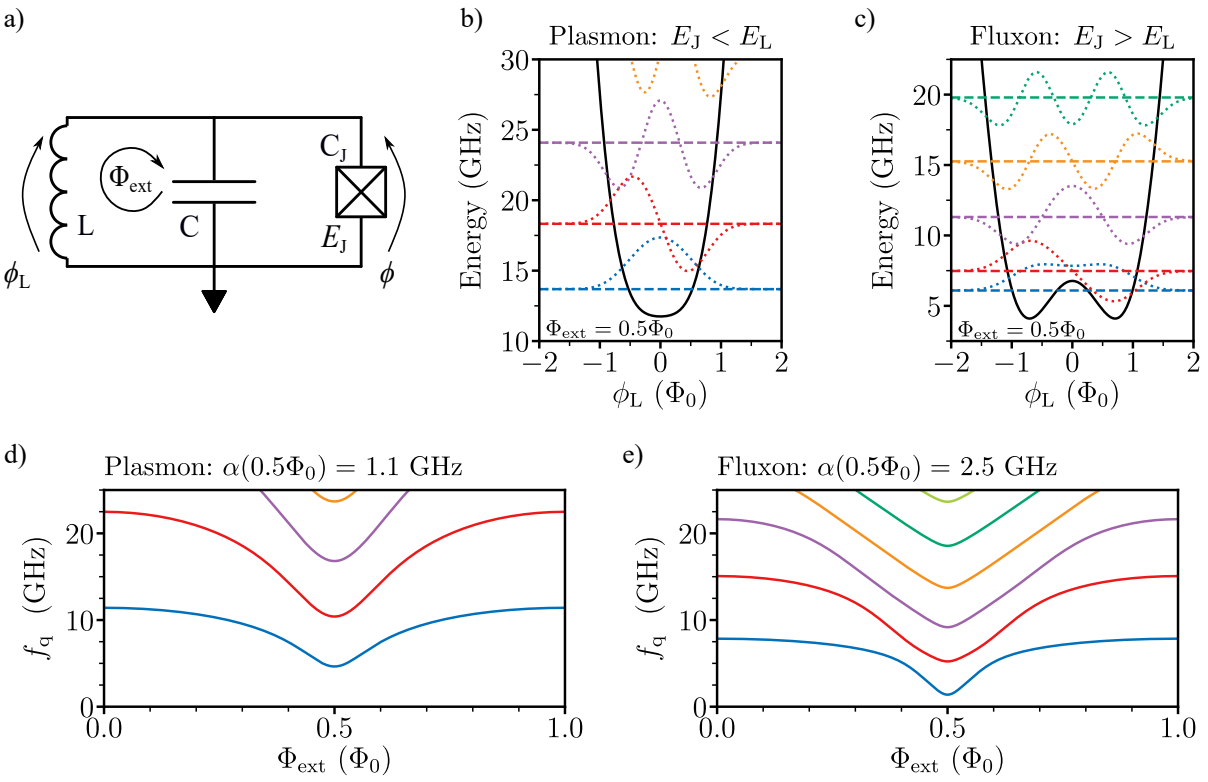

Figure 2.7.: **Generalized flux qubit. a)** Circuit diagram of a generalized flux qubit (GFQ), consisting of a JJ with Josephson energy E_J and capacitance C_J shunted by a capacitor C and an inductor L. The superconducting loop allows for external magnetic flux biasing Φ_{ext}. **b,c)** Potential energy landscape for $\Phi_{ext} = 0.5\Phi_0$ in the plasmon ($E_J < E_L$) and fluxon ($E_J > E_L$) regime, respectively. **d,e)** Energy spectra of the GFQ as a function of Φ_{ext} in both regimes. The flux periodicity of the spectrum and first-order insensitivity to flux noise at the extremal points are evident. Enhanced anharmonicity α in the fluxon regime enables fast qubit control while minimizing transitions to higher levels.

A generalized flux qubit (GFQ) is a superconducting circuit with a JJ and a parallel capacitor, additionally shunted by an inductor that screens charge offsets, as shown in Fig. 2.7a. The superconducting loop formed by the JJ and the inductance can be biased by an external magnetic flux Φ_{ext}. Using Kirchhoff's voltage law together with flux quantization around the loop [90], Eq. 2.7 and Eq. 2.13, the total generalized flux in the loop satisfies

$$\hat{\phi}_{\text{L}} - \hat{\phi} + \Phi_{\text{ext}} = k\Phi_0 \quad \text{with} \quad k \in \mathbb{Z}, \tag{2.31}$$

where $\hat{\phi}_{\text{L}}$ and $\hat{\phi}$ are the flux assigned to the inductance and junction respectively. We choose the junction flux variable $\hat{\phi}$ as the independent degree of freedom and express the inductor flux as $\hat{\phi}_{\text{L}} = \hat{\phi} - \Phi_{\text{ext}} + k\Phi_0$. Substituting this into the system, we obtain the Hamiltonian

$$\hat{\mathcal{H}} = \frac{\hat{q}^2}{2C_\Sigma} + \frac{1}{2L}(\hat{\phi} - \Phi_{\text{ext}} + k\Phi_0)^2 - E_{\text{J}}\cos(2\pi\hat{\phi}/\Phi_0), \tag{2.32}$$

where we neglect the constant term of the Josephson energy because it does not affect the transition energies. If no magnetic flux is trapped inside the loop ($k = 0$) and if Φ_{ext} remains static, we can perform a gauge transformation $\hat{\phi} \to \hat{\phi}' = \hat{\phi} + \Phi_{\text{ext}}$, which shifts Φ_{ext} into the argument of the Josephson cosine term [106]. Introducing the dimensionless phase variable $\hat{\varphi} = 2\pi\hat{\phi}/\Phi_0$, the Hamiltonian takes the more intuitive form

$$\hat{\mathcal{H}} = \frac{\hat{q}^2}{2C_\Sigma} + \frac{1}{2L}\hat{\phi}^2 - E_{\text{J}}\cos\left(\frac{2\pi}{\Phi_0}(\hat{\phi} + \Phi_{\text{ext}})\right) = 4E_{\text{C}}\hat{n}^2 + \frac{1}{2}E_{\text{L}}\hat{\varphi}^2 - E_{\text{J}}\cos(\hat{\varphi} + \varphi_{\text{ext}}), \tag{2.33}$$

where $\hat{n} = \hat{q}/2e$ is the number of Cooper pairs and $E_{\text{L}} = (\Phi_0/2\pi)^2/L$ the inductive energy. Eq. 2.33 is numerically solvable in the basis of the harmonic oscillator, where the non-linear Josephson potential is treated as a perturbation [107]. This yields the matrix elements

$$\hat{\mathcal{H}}_{m,n} = \langle h_m | \hat{\mathcal{H}} | h_n \rangle = \hbar\omega\left(\hat{a}^\dagger\hat{a} + \frac{1}{2}\right)\delta_{m,n} - E_{\text{J}}\langle h_m | \cos(\hat{\varphi} + \varphi_{\text{ext}}) | h_n \rangle . \tag{2.34}$$

The zero-point fluctuations of the harmonic mode are given by

$$\Phi_{\text{ZPF}} = \Phi_0\sqrt{\frac{Z}{4\pi R_{\text{Q}}}} \quad \text{and} \quad Q_{\text{ZPF}} = 2e\sqrt{\frac{R_{\text{Q}}}{4\pi Z}}, \tag{2.35}$$

where $R_{\text{Q}} = h/(2e)^2 \approx 6.45\,\text{k}\Omega$ is the resistance quantum.

Depending on the ratio $E_{\text{J}}/E_{\text{L}}$, different regimes of the universal double-well potential can be accessed [108]. These range from the fluxon-tunneling regime ($E_{\text{J}} > E_{\text{L}}$), where the barrier height exceeds the confining quadratic potential, to the single-well plasmon regime ($E_{\text{J}} < E_{\text{L}}$), where the system behaves as a single harmonic well as shown in Fig. 2.7b,c for $\Phi_{\text{ext}} = 0.5\Phi_0$. In Fig. 2.7d,e we show the frequency spectrum of a GFQ in the fluxon and plasmon regime as a function of Φ_{ext}. As can be seen, the energy levels of a GFQ are periodic in flux with a period of Φ_0 and are first-order insensitive to flux noise at their extremal points. The enhanced anharmonicity α, particularly in the fluxon regime of GFQs, is a major advantage, allowing for fast control of the $|0\rangle \to |1\rangle$ transition while minimizing unintended excitations to higher energy levels.

2.7. Superinductance

Superinductors are a main component in the GFQs used in this thesis. These elements are engineered to possess large inductances of tens to hundreds of nH, enabling the realization of circuits with high characteristic impedance $Z = \sqrt{L/C} \gg R_Q$. Entering this high impedance regime suppresses charge fluctuations which minimizes decoherence due to environmental charge noise. In this regime, the zero-point charge fluctuations Q_{ZPF} are smaller than the elementary charge e.

In addition to high impedance, a superinductor must fulfill several additional requirements: it should exhibit low microwave losses to preserve qubit coherence, maintain DC conductivity to short-circuit static offset charges, and avoid spurious resonances within the qubit's operational frequency range. Conventional geometric inductors based on aluminum thin films are limited in their achievable impedance due to low kinetic inductance and significant parasitic capacitance to ground. These constraints typically[ii] restrict the impedance to values below the vacuum impedance $Z_0 = 377\ \Omega$, rendering them unsuitable for the realization of superinductors with $Z \gg R_Q$ [110].

Kinetic inductance originates from the inertia of Cooper pairs in a superconductor, which causes a delayed response of the supercurrent to an alternating electric field. When a supercurrent flows, energy is stored in the motion of the charges. The total kinetic energy is given by

$$E = \int \frac{1}{2} n_s m v^2 \, \mathrm{d}V = \frac{1}{2} L_{kin} I^2, \tag{2.36}$$

where $m = 2m_e$ is the Cooper pair mass, v is the superfluid velocity, and I is the supercurrent. For a uniform wire of length ℓ and cross-sectional area S, the current is

$$I = 2e n_s v S, \tag{2.37}$$

which leads to the kinetic inductance

$$L_{kin} = \frac{2m_e \ell}{n_s (2e)^2 S}. \tag{2.38}$$

Josephson junction arrays as superinductors

One-dimensional chains of JJs were employed as superinductors in the original fluxonium qubit design [111]. They consist of N identical JJs connected in series, each characterized by a critical current I_c, junction capacitance C_J, and Josephson energy E_J. For drive frequencies $\omega \ll \omega_p$, where

$$\omega_p = 1/\sqrt{L_J C_J} = \sqrt{\frac{2eI_c}{\hbar C_J}} \tag{2.39}$$

is the junction plasma frequency, the chain behaves as a lumped-element linear inductor with effective inductance

$$L_{array} = N \cdot L_J = N \cdot \frac{\Phi_0}{2\pi I_c}, \tag{2.40}$$

[ii] Note that with specialized geometry and fabrication, even geometric coils can surpass the resistance quantum [109]

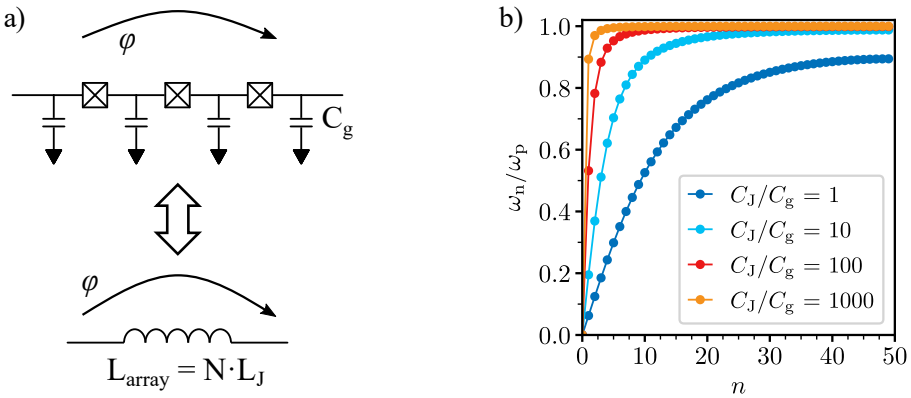

Figure 2.8.: **Implementation of a superinductance with a JJ array. a)** Schematic of a JJ array consisting of N identical junctions with Josephson energy $E_\mathrm{J} = (\Phi_0/2\pi)^2/L_\mathrm{J}$ and capacitance C_J. Each island is coupled to ground via a capacitance C_g. The collective phase difference across the chain is denoted by φ. In the lumped-element limit, the JJ array can be modeled as a linear inductor with total inductance $L_\mathrm{array} = NL_J$. **b)** Dispersion relation of the plasma modes for an array with $N = 50$ junctions, calculated for different ratios $C_\mathrm{J}/C_\mathrm{g}$. The mode frequencies ω_n are normalized by the single-junction plasma frequency $\omega_\mathrm{p} = 1/\sqrt{L_\mathrm{J}C_\mathrm{J}}$. Larger values of $C_\mathrm{J}/C_\mathrm{g}$ compress the mode spectrum and raise the lowest mode frequency.

as illustrated in Fig. 2.8a. Although each individual junction is nonlinear, the phase drop φ_n across each junction becomes small for large N, such that a Taylor expansion of the collective cosine potential becomes valid:

$$\mathcal{H} = -\sum_{n=0}^{N} E_\mathrm{J}\cos(\varphi_n) = -N\cdot\frac{(\Phi_0/2\pi)^2}{L_\mathrm{J}}\cos\left(\frac{\varphi}{N}\right) \approx -NE_\mathrm{J} + \frac{1}{2}\frac{\left(\frac{\Phi_0}{2\pi}\right)^2}{L_\mathrm{array}}\varphi^2 - \frac{1}{24}\frac{\left(\frac{\Phi_0}{2\pi}\right)^2}{L_\mathrm{array}}\frac{1}{N^2}\varphi^4. \tag{2.41}$$

The quartic term reflects the weak residual nonlinearity of the array, which scales as $1/N^2$ and gives rise to a photon-number-dependent frequency shift. This effect is captured by the self-Kerr coefficient K_{11} of the fundamental mode ω_1. For a JJ array in the weakly nonlinear regime ($K_{11}n = \delta\omega_K \ll \omega_1$ with n the average photon number in the mode) the Kerr coefficient is approximately [112]:

$$K_{11} \approx \left(\frac{1}{2} + \frac{1}{8}\right)\frac{\hbar^2\omega_1^2}{2NE_\mathrm{J}}. \tag{2.42}$$

While the Kerr effect is suppressed in arrays with large N, it remains observable for high drive powers or near resonance with multi-photon transitions.

To describe the electrodynamics of JJ arrays beyond the lumped-element approximation, their collective modes must be taken into account. The array forms a discrete transmission line with harmonic eigenmodes, where the dispersion relation is determined by the ratio $C_\mathrm{J}/C_\mathrm{g}$ between the junction capacitance and the capacitance to ground. The dispersion relation is given by [113]:

$$\omega_n = \omega_\mathrm{p}\sqrt{\frac{1-\cos(\pi n/N)}{C_\mathrm{g}/(2C_\mathrm{J}) + 1 - \cos(\pi n/N)}}, \tag{2.43}$$

where $n \in [0, N]$. A large C_J/C_g ratio pushes the self-resonant frequency of the array above the qubit's $|0\rangle \rightarrow |1\rangle$ transition frequency and avoids spurious mode hybridization, as shown in Fig. 2.8b. For a typical array junction with $A_{JJ} = 1\,\mu m^2$, $C = 50\,\frac{fF}{\mu m^2}$ and $j_c = 450\,\frac{nA}{\mu m^2}$ we calculate $f_p = \omega_p/2\pi \approx 26\,GHz$. Phase coherence across the array can be disrupted by quantum phase slips, i.e. tunneling events where the superconducting phase changes by 2π across a single junction. For junctions in the regime $E_J/E_C \gg 1$ the phase slip rate is exponentially suppressed [114]:

$$\Gamma_{ps} = N \cdot \frac{1}{h} \cdot \frac{4}{\sqrt{\pi}} \left(8E_J^3 E_C\right)^{1/4} e^{-\sqrt{8E_J/E_C}}. \tag{2.44}$$

In large-area junctions with $E_J/E_C \approx 100$ phase slips are negligible, with measured rates of less than 1 mHz [113].

Granular aluminum

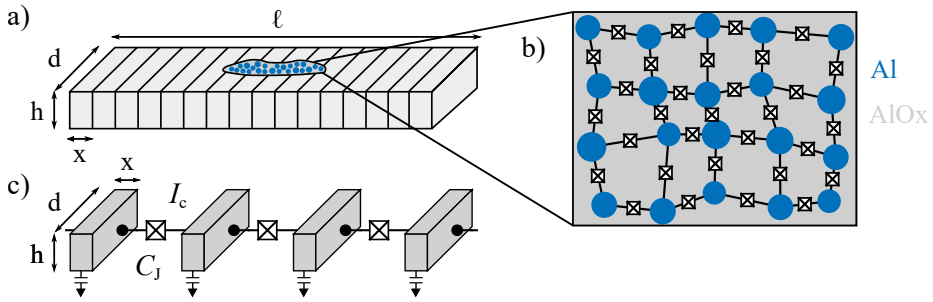

Figure 2.9.: **Modeling granular aluminum (grAl) as a Josephson junction (JJ) array. a)** Schematic of a grAl strip with length ℓ, height h, and depth d. For modeling purposes, the strip is divided into equally sized segments of length x. **b)** Sketch of the microstructure of grAl. The aluminum (Al) grains (blue) are embedded in an amorphous AlO_x matrix (grey). Cooper pair tunneling between grains leads to a nonlinear kinetic inductance, allowing the electrodynamics of grAl thin films to be modeled as networks of JJs. **c)** Circuit model of the grAl strip, where each segment is represented by an effective JJ with critical current I_c and capacitance C_J.

Granular aluminum (grAl) is obtained by evaporating pure aluminum (Al) in an oxygen atmosphere. By adjusting the partial oxygen pressure during deposition, its room-temperature resistivity can be tuned over several orders of magnitude, typically in the range of

$$\rho = R_n \cdot A/\ell \approx 10\text{–}10^4\,\mu\Omega cm\ [115, 116], \tag{2.45}$$

for a grAl film with normal-state resistance R_n, cross-section $A = h \cdot d$ and length ℓ. For grAl films fabricated at room-temperature with resistivities $\rho \geq 10\,\mu\Omega cm$, the granular structure consists of crystalline aluminum grains with a uniform diameter of $3 \pm 1\,nm$ [110]. These grains are separated by amorphous AlO_x barriers, as shown in Fig. 2.9. This microstructure allows grAl to be modeled as a disordered network of weakly coupled JJs, enabling its use as a superinductance in superconducting circuits. The

kinetic inductance dominates the electrodynamic response and can be estimated in the low-temperature limit $T \ll T_c$ with the Mattis-Bardeen relation [117]:

$$L_{\text{kin}} = \frac{\hbar R_n}{\pi \Delta}, \tag{2.46}$$

where $\Delta \approx 1.76\, k_B T_c$ ($T_{c,\text{grAl}} \approx 1.6{-}3\,\text{K}$ [118, 119]) is the superconducting gap. The nonlinear current-phase relation of the effective JJ network in grAl gives rise to a finite Kerr nonlinearity. For the fundamental mode, the self-Kerr coefficient K_{11} is [110]:

$$K_{11} = \frac{3}{16}\pi e a \cdot \frac{\omega_1^2}{j_c V_{\text{grAl}}}, \tag{2.47}$$

where a is the grain size, ω_1 is the mode's frequency, j_c is the critical current density, and V_{grAl} is the volume of the grAl inductor. This relation shows that the nonlinearity can be tuned via both material resistivity and circuit geometry. Kerr coefficients can range from sub-kHz to MHz, allowing the use of grAl in low-loss superinductors, parametric amplifiers, kinetic inductance detectors, and even qubit elements [120, 69, 121, 122]. Highly inductive grAl films with resistivity $\rho = 4000\,\mu\Omega\cdot\text{cm}$ (corresponding to a sheet resistance $R_{n,\square} \approx 2\,\text{k}\Omega$ and kinetic inductance $L_\square \approx 2\,\text{nH}/\square$) have been shown to exhibit plasma frequencies $f_p \approx 70\,\text{GHz}$ [110], consistent with the absence of spurious resonances up to 20 GHz [110, 120]. As evident from Eq. 2.16 and Eq. 2.39, a lower normal-state resistivity implies an increased plasma frequency. The amorphous grain structure also suppresses coherent quantum phase slips, as local phase fluctuations can relax without inducing global 2π slips.

Compared to JJ arrays, grAl offers a simpler and more scalable fabrication process, at the expense of in-situ tunability and increased sensitivity to quasiparticles [120]. GrAl superinductors exhibit internal quality factors $Q_i \geq 10^5$ and maintain high performance under magnetic fields up to 1 T [123], making them well suited for hybrid quantum circuits. A key limitation of high impedance grAl devices is their susceptibility to non-equilibrium quasiparticles, typically generated by cosmic rays and environmental radiation [120, 77]. These events cause sudden frequency shifts and can lead to correlated errors in multi-qubit architectures. Mitigation strategies include phonon trapping, substrate engineering, and radiation shielding [75, 124, 125].

2.8. Dispersive readout

The dispersive readout scheme originates from cavity quantum electrodynamics [126, 127], and it is based on the interaction between a quantized electromagnetic field and the two levels of an atom. In circuit quantum electrodynamics (cQED), this concept has been translated to solid-state platforms by replacing the atom with a superconducting qubit and the cavity with a microwave resonator [128, 38]. The qubit-resonator interaction is described by the Jaynes-Cummings Hamiltonian [129],

$$\hat{\mathcal{H}}_{\text{JC}} = \hbar\omega_R \hat{a}^\dagger \hat{a} + \frac{\hbar\omega_Q}{2}\hat{\sigma}_z + \hbar g(\hat{\sigma}_+ \hat{a} + \hat{\sigma}_- \hat{a}^\dagger), \tag{2.48}$$

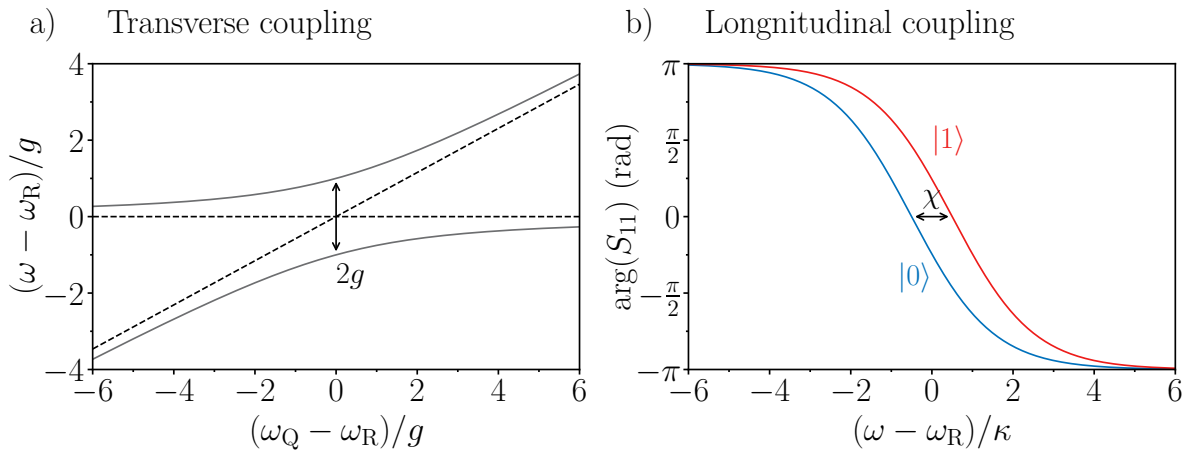

Figure 2.10.: **Comparison of transverse and longitudinal qubit-resonator coupling. a)** Normalized eigenfrequencies $(\omega-\omega_R)/g$ of a qubit-resonator system with transverse coupling, plotted against the normalized detuning $(\omega_Q-\omega_R)/g$. The dashed lines indicate the uncoupled modes, with ω_R corresponding to the resonator (horizontal) and ω_Q to the qubit (diagonal). Their hybridization results in an avoided crossing with a minimum gap of $2g$, which is an experimental signature of transverse coupling. **b)** Simulated resonator phase response $\arg(S_{11})$ as a function of normalized frequency detuning $(\omega-\omega_R)/\kappa$, with κ denoting the resonator linewidth. A longitudinal interaction produces a qubit-state-dependent frequency shift, yielding two distinct phase responses for the states $|0\rangle$ (blue) and $|1\rangle$ (red), separated by the dispersive shift χ (see Eq. 2.49).

where ω_R is the resonator frequency and g is the transverse coupling rate. Transverse coupling allows for the coherent exchange of excitations between the modes and gives rise to a characteristic avoided level crossing when ω_Q is tuned into resonance with ω_R as shown in Fig. 2.10a. The minimum splitting at resonance is $2g$ and provides a direct spectroscopic signature of the coupling strength.

In the dispersive regime, where the detuning $\Delta = |\omega_Q-\omega_R| \gg g$, no energy is exchanged between the two modes. Instead, the interaction leads to a qubit-state-dependent frequency shift of the resonator $\chi \approx 2g^2/\Delta$. This results in an effective Hamiltonian of the form [128]:

$$\hat{\mathcal{H}}_{\text{disp}} = \hbar(\omega_R+\frac{\chi}{2}\hat{\sigma}_z)\hat{a}^\dagger\hat{a}+\frac{\hbar}{2}(\omega_Q+\frac{\chi}{2})\hat{\sigma}_z. \tag{2.49}$$

This Hamiltonian is of longitudinal form, since the interaction term is proportional to $\hat{\sigma}_z\hat{a}^\dagger\hat{a}$ and therefore commutes with (and thus conserves) both the qubit state $\hat{\sigma}_z$ and the resonator photon number $\hat{a}^\dagger\hat{a}$. As a result, the resonator response splits into two distinct frequencies for $|0\rangle$ and $|1\rangle$, separated by the dispersive shift χ, as shown in Fig. 2.10b. Because the qubit state is conserved during the measurement, this scheme implements a quantum non-demolition (QND) readout of the qubit.

Typically the dispersive shift is chosen to be on the order of the resonator linewidth $\kappa \approx \omega_R/Q \approx \chi$, so that χ is small enough to minimize unwanted losses but large enough to remain detectable. The dispersive shift is calculated from the resonator and qubit spectrum using

$$\chi = \left(E_{|1,1\rangle}-E_{|0,1\rangle}\right)/h-\left(E_{|1,0\rangle}-E_{|0,0\rangle}\right)/h, \tag{2.50}$$

where $E_{|n_R,n_Q\rangle}$ is the energy level sorted by the readout (n_R) and qubit (n_Q) photon number.

Input-output theory

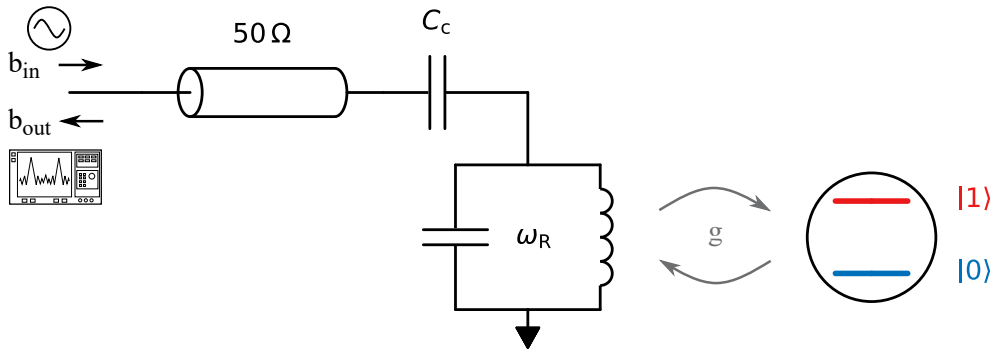

Figure 2.11.: **Circuit schematic for dispersive qubit measurement in reflection.** The readout resonator with frequency ω_R is coupled through the capacitor C_c to a 50 Ω transmission line with coupling rate κ. A probe signal b_{in} is sent through the line and reflects off the resonator. At the output the reflected signal b_{out} is measured. The qubit is modeled as a two-level system coupled to the resonator with strength g. In the dispersive regime, the resonator acquires a qubit-state-dependent frequency shift $\omega_R = \omega_{R,0} \pm \chi/2$.

The derivation of the dispersive Hamiltonian (Eq. 2.49) assumes an isolated qubit-resonator system. However, to perform a measurement, the resonator must be coupled to a classical measurement apparatus. Typically, this is achieved by coupling the resonator capacitively to a 50 Ω transmission line. In this work, we focus on the reflection setup, shown schematically in Fig. 2.11. The qubit is excluded from the dynamical treatment, reducing its effect to a dispersive shift χ of the resonator frequency. The resulting open-system dynamics are described by input-output theory [130], which is summarized below.

To analyze the signal response, we treat the resonator as a harmonic oscillator coupled to a semi-infinite transmission line. The total Hamiltonian includes three parts: the resonator, the transmission line, and their interaction,

$$\hat{\mathcal{H}}_{tot} = \hat{\mathcal{H}}_R + \hat{\mathcal{H}}_{tl} + \hat{\mathcal{H}}_{int}. \tag{2.51}$$

The transmission line is modeled as a continuum of harmonic modes, described by bosonic creation and annihilation operators $\hat{b}^\dagger_\omega$ and $\hat{b}_\omega$, which satisfy the commutation relation $[\hat{b}_\omega, \hat{b}^\dagger_{\omega'}] = \delta(\omega - \omega')$. The corresponding Hamiltonian is

$$\hat{\mathcal{H}}_{tl} = \int_0^\infty d\omega\, \hbar\omega\, \hat{b}^\dagger_\omega \hat{b}_\omega. \tag{2.52}$$

The resonator is coupled to the transmission line via a capacitive interaction, leading to the interaction Hamiltonian

$$\hat{\mathcal{H}}_{int} = \frac{1}{\sqrt{2\pi}} \int_0^\infty d\omega \sqrt{\kappa(\omega)}\, (\hat{b}^\dagger_\omega - \hat{b}_\omega)(\hat{a}^\dagger - \hat{a}), \tag{2.53}$$

where $\kappa(\omega)$ is the frequency-dependent coupling rate determined by the coupling capacitance C_c. We use two simplifications on $\hat{\mathcal{H}}_{tot}$: the rotating wave approximation (RWA) and the Markov approximation. The RWA allows us to neglect the fast oscillating terms in $\hat{\mathcal{H}}_{int}$. The Markov approximation allows

us to replace $\kappa(\omega)$ with a constant κ, if the drive is narrowband around the resonator frequency ($\kappa \ll \omega_R$).

In the Heisenberg picture, the evolution of the resonator field operator is given by

$$\dot{\hat{a}}(t) = \frac{i}{\hbar}[\hat{\mathcal{H}}_{tot}, \hat{a}(t)]. \tag{2.54}$$

Using the two approximations, the quantum Langevin equation in a frame rotating at the drive frequency ω is given by:

$$\dot{\hat{a}}(t) = -i(\omega_R - \omega)\hat{a}(t) - \frac{\kappa}{2}\hat{a}(t) - \sqrt{\kappa}\,\hat{b}_{in}(t), \tag{2.55}$$

where $\hat{b}_{in}(t)$ is the input field incident on the resonator. The field reflected from the resonator is described by the output operator $\hat{b}_{out}(t)$, related to the internal field via the input-output relation

$$\hat{b}_{out}(t) = \hat{b}_{in}(t) + \sqrt{\kappa}\,\hat{a}(t). \tag{2.56}$$

In steady state, when $\dot{\hat{a}}(t) = 0$, we solve Eq. 2.55 to obtain

$$\hat{a}(t) = \frac{-\sqrt{\kappa}}{-i(\omega_R - \omega) + \kappa/2}\,\hat{b}_{in}(t). \tag{2.57}$$

Substituting into Eq. 2.56 yields the reflected field,

$$\hat{b}_{out}(t) = \hat{b}_{in}(t)\left[1 - \frac{\kappa}{-i(\omega_R - \omega) + \kappa/2}\right]. \tag{2.58}$$

We define the complex reflection coefficient $S_{11}(\omega)$, as the ratio of the reflected to incident fields in frequency space:

$$S_{11}(\omega) = \frac{\hat{b}_{out}(\omega)}{\hat{b}_{in}(\omega)} = 1 - \frac{\kappa}{-i(\omega_R - \omega) + \kappa/2}. \tag{2.59}$$

This complex function describes the frequency-dependent reflection response of the resonator. The magnitude $|S_{11}(\omega)|$ gives the amplitude of the reflected signal, while $\arg[S_{11}(\omega)]$ determines the phase shift. At resonance ($\omega = \omega_R$), the reflection exhibits a phase flip and a minimum in amplitude, corresponding to maximum energy absorption by the resonator.

Signal-to-noise ratio

The dispersive Hamiltonian in Eq. 2.49 implies a qubit-state-dependent resonator frequency $\omega_R^{(0/1)} = \omega_R \mp \chi/2$. Probing the resonator at $\omega = \omega_R$ gives detunings of $\omega - \omega_R^{(0/1)} = \pm\chi/2$. Substituting into Eq. 2.59 yields:

$$S_{11}^{(0/1)} = \frac{\pm i\,\chi/2 - \kappa/2}{\pm i\,\chi/2 + \kappa/2}. \tag{2.60}$$

Identifying the measured quadratures with $I = \mathrm{Re}(S_{11})$ and $Q = \mathrm{Im}(S_{11})$ (scaled by $|\langle b_{in}\rangle|$) gives:

$$\langle I_{0,1}\rangle = \frac{\kappa^2 - \chi^2}{\kappa^2 + \chi^2}\,|\langle b_{in}\rangle| \quad \text{and} \quad \langle Q_{0,1}\rangle = \pm\frac{2\kappa\chi}{\kappa^2 + \chi^2}\,|\langle b_{in}\rangle|. \tag{2.61}$$

At $\omega = \omega_R$ and with our phase convention, the qubit information lies entirely in Q while I contains only noise. In general, the information appears along some axis in the (I, Q) plane. Measuring both quadratures with a heterodyne setup captures the full complex reflection (amplitude and phase) and allows a digital rotation of (I, Q) onto any axis [37, 131, 39].

The output signal is amplified to match the level of classical readout electronics. A quantum-limited phase-preserving amplifier adds half a photon of noise [132, 133]. Including vacuum fluctuations, the total variance is $\sigma_0^2 = 1/2$ for both quadratures. In a heterodyne detection scheme, the reflected signal is downconverted to an intermediate frequency ω_{IF} and digitally mixed with two reference signals at the same frequency, phase-shifted by 90° relative to each other. This process separates the signal into two orthogonal components I and Q. The resulting traces are integrated over the measurement time τ_{int}, yielding the measured components Q_m and (analogously) I_m:

$$Q_m = \int_{t_0}^{t_0+\tau_{int}} \left(\langle \hat{Q} \rangle + \delta Q \right) dt. \tag{2.62}$$

Here, $\langle \hat{Q} \rangle$ is given by Eq. 2.61, and δQ is normally distributed noise. Both the mean $\langle Q_m \rangle = \langle \hat{Q} \rangle \tau_{int}$ and variance $\sigma_m^2 \propto \tau_{int}$ grow linearly with τ_{int}.

The resonator photon number $\bar{n}$ in the dispersive regime can be calculated via the AC-Stark shift δf_{ac} (or more accurately by the procedure outlined in App. A.5). The AC-Stark shift is a shift in the qubit's frequency $f_Q \rightarrow f_Q + \delta f_{ac}$, caused by an increasing number of photons in the resonator. We derive from Hamiltonian Eq. 2.49:

$$\delta f_{ac} = \frac{\chi}{2\pi} \bar{n}, \tag{2.63}$$

and define the measurement photon number as:

$$n_m = \frac{\bar{n} \kappa \tau_{int}}{4}. \tag{2.64}$$

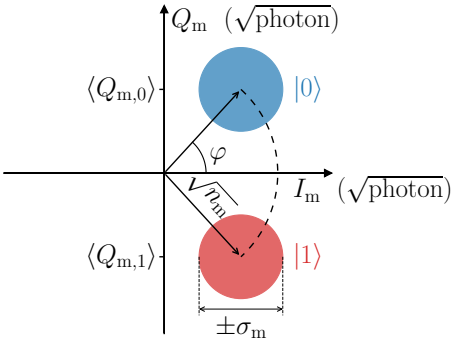

Figure 2.12.: **Qubit state separation in the *IQ* plane.** The two disks correspond to the $|0\rangle$ (blue) and $|1\rangle$ (red) pointer states of the resonator with equal variance $\langle (\Delta I_m)^2 \rangle = \langle (\Delta Q_m)^2 \rangle = \sigma_m^2$. The I and Q quadratures are rescaled to the square root of measurement photons, $\sqrt{n_m} = \sqrt{\bar{n} \kappa \tau_{int}/4}$ [134, 135].

In Fig. 2.12 we show a typical dispersive readout result. The IQ-plane shows two Gaussian pointer states corresponding to the qubit in ground (g, $|0\rangle$) and excited (e, $|1\rangle$) state. The quadratures are rescaled by

$\sqrt{n_\mathrm{m}}$, so that the variance σ_m becomes independent of τ_int. For quantum-limited readout, the variance is $\sigma_0^2 = 1/2$.

The separation of the $|0\rangle$ and $|1\rangle$ pointer states and their variances σ_m defines the signal-to-noise ratio (SNR):

$$\mathrm{SNR} = \frac{|\langle Q_\mathrm{m,g}\rangle - \langle Q_\mathrm{m,e}\rangle|}{\sigma_\mathrm{m,g} + \sigma_\mathrm{m,e}} = \frac{\sqrt{n_\mathrm{m}}}{\sigma_\mathrm{m}} \sin(\varphi). \tag{2.65}$$

The angle φ is defined as the angle between the ground-state pointer and the I-axis, $\varphi = \arctan(\langle Q_\mathrm{g}\rangle / \langle I_\mathrm{g}\rangle)$, and is given by

$$\sin(\varphi) = \frac{2\kappa\chi}{\kappa^2 + \chi^2}. \tag{2.66}$$

The optimal SNR is achieved for $\chi = \kappa$, corresponding to a 180° phase shift between the pointer states.

3. Kinetic inductance coupling for cQED with flux qubits

This chapter is based on results previously published in Ref. [136]. Adaptations and extensions have been made to better integrate the material into this thesis.

In this chapter, we present a coupling scheme between a readout resonator and a GFQ based on kinetic inductance, which enables dispersive interaction without direct capacitive coupling. First, we introduce the circuit design and highlight the role of geometric symmetry in suppressing unwanted capacitive interactions. We then develop a full quantitative model based on circuit quantization and derive the system Hamiltonian that we compare to an idealized inductively coupled qubit-readout system. The coupling mechanism is analyzed in detail and shown to result from a controlled inductive asymmetry, while the symmetric sample box is key to suppressing unwanted capacitive contributions. We validate the inductive coupling by comparing model predictions to measured data. In the final section, we characterize the readout fidelity and demonstrate high-fidelity active state preparation.

3.1. Circuit design and symmetry

The design of the qubit-resonator system (QR-system) shown in Fig. 3.1 follows three key principles. First, we employ the minimal configuration required to support two electromagnetic modes, a three-node circuit. Second, we assign distinct physical roles to the common and differential modes: the qubit mode corresponds to the differential excitation between two nodes connected by a Josephson junction (JJ), acquiring strong anharmonicity from the nonlinear Josephson potential, while the orthogonal common-mode excitation remains linear and defines the readout resonator. Third, to suppress undesired electric field coupling between the two modes, the capacitive environment of the qubits JJ is designed to be symmetric. This symmetry enforces a permutation invariance in the capacitance matrix for these nodes. A simplified lumped-element implementation of the circuit is shown in Fig. 3.1a. It consists of three superconducting islands: nodes **1**, **2**, and **3**, which are connected through grAl inductors. Nodes **1** and **2** form a closed superconducting loop interrupted by a JJ and threaded by an external magnetic flux Φ_{ext}, realizing a GFQ [108]. The total loop inductance L_{q} sets the inductive energy scale E_{L} of the qubit. When the circuit is symmetric with respect to the vertical axis through node **3**, so that nodes **1** and **2** exhibit identical capacitances C_{r} and inductances $L_{\text{q}}/2$, the differential and common electromagnetic modes become orthogonal. In this case, the current associated with the readout mode divides equally between the two branches of the qubit loop, resulting in zero net current shared with the qubit mode. To

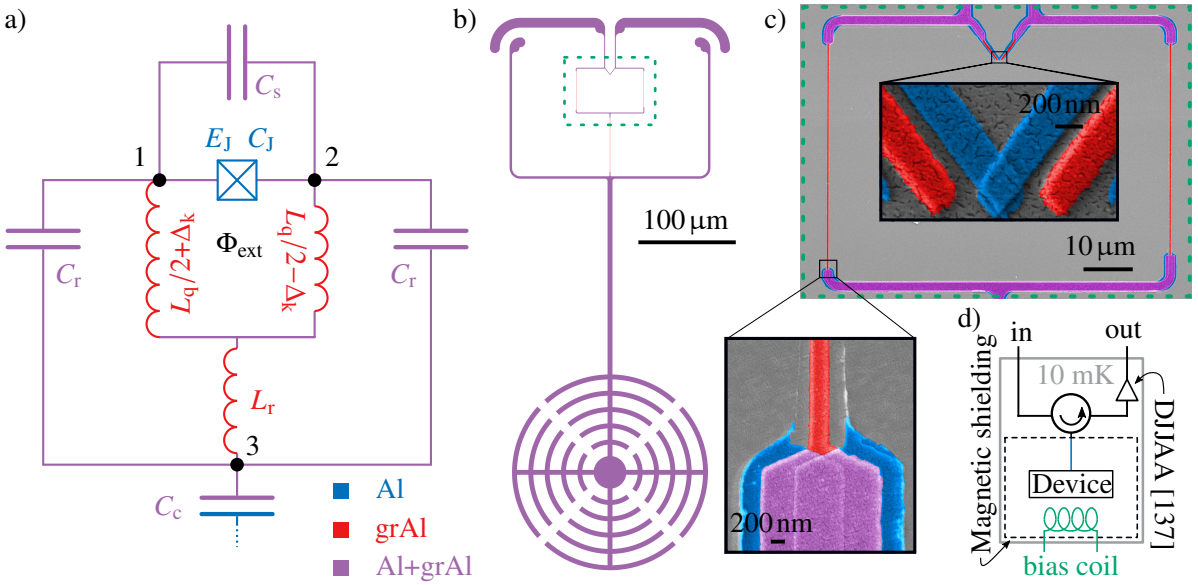

Figure 3.1.: **Qubit-readout circuit schematics and implementation**, figure and caption taken from [136]. **a)** The circuit consists of three islands labeled **1** to **3** (black dots). Islands **1** and **2** form the qubit loop, which consists of a JJ with energy E_J and capacitance C_J in parallel with a grAl inductance L_q and a capacitance C_s, together forming a GFQ. The third island defines the readout mode through its connection to the qubit loop via a grAl inductance L_r, resulting in an in-phase charge oscillation of islands **1** and **2**. The qubit-resonator coupling strength is set by an inductance asymmetry Δ_k between the two branches of the grAl loop. The readout mode is loaded by capacitances C_r and coupled to the feedline through C_c. The materials used are indicated by color: aluminum (blue), grAl (red), and structures of Al covered with grAl (purple), resulting from the three-angle evaporation process. **b)** Image of the device layout. The coupling capacitor C_c features a skeletal shape to suppress screening currents and vortex trapping. **c)** False-colored scanning electron micrograph of the qubit loop. The length and width of the grAl strips determine the resonator frequency, coupling strength, and qubit spectrum. Insets show the Al/AlO_x/Al JJ ($A_J \approx 0.06\,\mu m^2$) and a section of the grAl wire. The visible granularity is due to an evaporated gold film used for imaging. **d)** Simplified schematic of the microwave reflection measurement setup used for characterization at 10 mK. The full measurement setup is shown in section 6.4.

introduce a controlled interaction between the qubit and resonator, we deliberately break this symmetry by engineering a kinetic inductance imbalance $\Delta_k = \Delta_\square L_\square/2$, where $\Delta_\square$ is the difference in the number of squares of grAl wire in the two loop branches, and $L_\square$ denotes the sheet inductance of the grAl film. In the case of JJ arrays, this corresponds to a mismatch in either the number or size of the JJs in each branch. The resulting asymmetry leads to an uneven current distribution in the readout mode, establishing a finite coupling to the qubit. In this picture, the parameter Δ_k acts as an effective shared inductance, and the circuit becomes functionally equivalent to an inductively coupled qubit-resonator system [107].

Unlike conventional capacitive [111, 138] or geometric inductive [107, 69] coupling schemes for flux qubits, the approach presented here eliminates an additional circuit node by embedding the readout mode directly into the qubit loop. This integration offers several practical advantages. First, removing a circuit node increases the frequency of parasitic modes, thereby enhancing the spectral purity of the device.

Second, the resonator is coupled to the measurement line via the capacitor C_c at node **3**, while the qubit mode remains largely unaffected due to the circuit's axial symmetry. Third, the coupling between qubit and resonator arises purely from kinetic inductance, relaxing design constraints on capacitive elements and potentially enabling advanced schemes such as flux pumping [59].

Fig. 3.1b,c show the layout of the QR-system and a scanning electron micrograph of the qubit loop, respectively. The circuit parameters can be independently tuned by modifying purely geometrical features of the layout. Specifically, the inductance L_q is set by the length and width of the grAl wire, the Josephson energy E_J and JJ capacitance C_J are determined by the area of the JJ, and the shunt capacitance C_s is defined by the size of the capacitor electrodes. Importantly, these adjustments do not require changes to the overall circuit topology or to the fabrication parameters of the JJ or grAl film. The bottom inset in Fig. 3.1c shows a magnified view of a section of the grAl inductor. Through the large kinetic inductance of grAl, inductive asymmetries Δ_k of several nH can be introduced by adding just a few additional squares of grAl in one of the qubit loop branches. This enables fine control of the coupling strength with negligible impact on the total geometric inductance or the capacitance matrix. The central inset in Fig. 3.1c depicts the Al/AlO_x/Al JJ. Details of the QR-systems fabrication are provided in section 6.1. Different designs of the circuit, including the evolution of the JJ, are described in section 6.1. Experiments are performed at 10 mK in a dilution cryostat, as shown in Fig. 3.1d.

Circuit model

To accurately describe the QR-system introduced in section 3.1 we need a circuit model which takes into account all capacitive and inductive elements as they are shown in Fig. 3.2a. This includes: four superconducting islands, the inductances L_q, L_r and Δ_k, all capacitances between the island C_{ij} and the capacitances of the islands to ground C_{0i} with $i, j \in [1,2,3,4] \wedge i \neq j$. The flux variables for the islands are denoted by $\vec{\phi}^\top = (\phi_1, \phi_2, \phi_3, \phi_4)$. Using the canonical circuit quantization procedure as outlined in [95], the Lagrangian is given by

$$\mathcal{L} = \frac{1}{2}\dot{\vec{\phi}}^\top \mathbf{C}\,\dot{\vec{\phi}} - \frac{1}{2}\vec{\phi}^\top \mathbf{L}^{-1}\vec{\phi} + E_J \cos\left(\frac{2\pi}{\Phi_0}(\phi_2 - \phi_1 - \Phi_{ext})\right) \tag{3.1}$$

$$= \mathcal{L}_{lin} + E_J \cos\left(\frac{2\pi}{\Phi_0}(\phi_2 - \phi_1 - \Phi_{ext})\right), \tag{3.2}$$

where $\mathbf{C}$ is the capacitance matrix and $\mathbf{L}^{-1}$ the inverse inductance matrix[i]. Here, $\mathcal{L}_{lin}$ collects all linear contributions to the Lagrangian, encompassing both capacitive and inductive terms. The nonlinear dy-

[i] Note that inserting Φ_{ext} into the cosine potential assumes a quasi-static external flux bias [106]

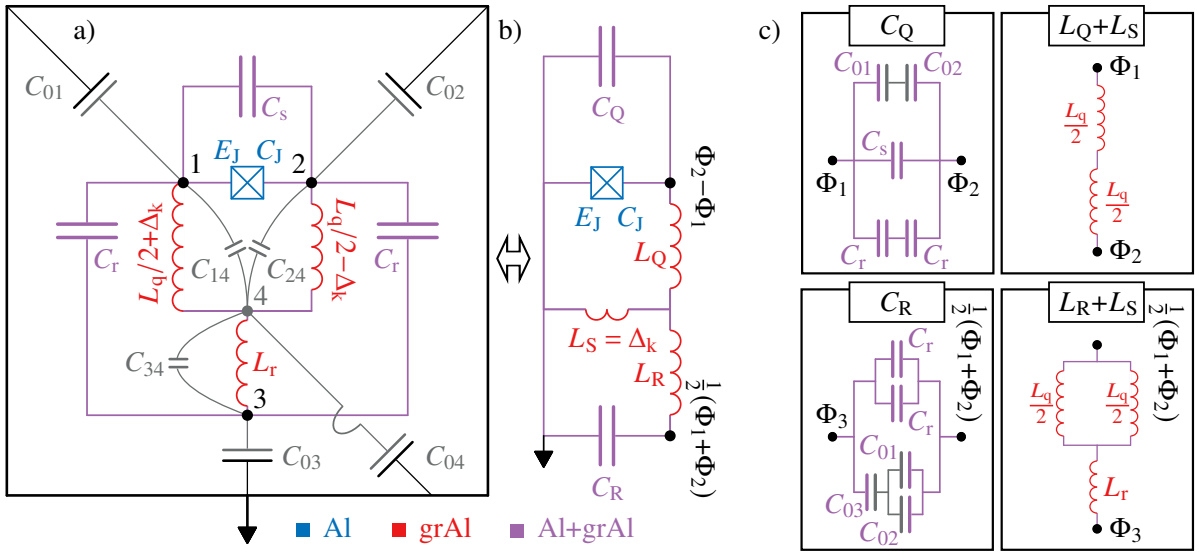

Figure 3.2.: **Extended and idealized circuit model**, figure and caption taken from [136]. **a)** Expansion of the three island configuration shown in Fig. 3.1. The island **1** to **3** are indicated as black dots, while island **4** is highlighted by a grey dot. Capacitances of the island to ground are labeled as C_{0i} with $i \in [1,2,3,4]$. Additional non-neglectable capacitances C_{ij} with $i,j \in [1,2,3,4] \wedge i \neq j$ between the island are shown in grey. The colors, blue, red and purple indicate the used materials and are consistent with Fig. 3.1. **b)** Assuming symmetric capacitances and neglecting the influence of island **4**, the circuit simplifies to an idealized inductively coupled model with an effective shared inductance $L_S = \Delta_k$. In this representation, the qubit and resonator modes are described by effective inductances L_Q, L_R and capacitances C_Q, C_R, respectively. **c)** The four panels illustrate the transformation steps used to extract the effective circuit parameters of the idealized model. The upper two diagrams show the decomposition of the qubit capacitance C_Q and inductance L_Q, while the lower two panels represent the corresponding quantities C_R and L_R for the readout resonator.

namics of the system arise solely from the JJ, which introduces a cosine potential between islands **1** and **2**. The capacitance matrix **C** is given by:

$$\mathbf{C} = \begin{pmatrix} C_{11}+C_J & -C_{12}-C_J & -C_{13} & -C_{14} \\ -C_{12}-C_J & C_{22}+C_J & -C_{23} & -C_{24} \\ -C_{13} & -C_{23} & C_{33} & -C_{34} \\ -C_{14} & -C_{24} & -C_{34} & C_{44} \end{pmatrix}. \tag{3.3}$$

The entries C_{ij} are calculated via electrostatic finite element simulations performed with Ansys Maxwell, which are discussed in section 3.1. The JJ capacitance C_J is not captured in the simulation and therefore added as an additional capacitive contribution between nodes **1** and **2**. The inverse inductance matrix $\mathbf{L}^{-1}$ is given by:

$$\mathbf{L}^{-1} = \begin{pmatrix} \frac{1}{L_q/2+\Delta_k} & 0 & 0 & -\frac{1}{L_q/2+\Delta_k} \\ 0 & \frac{1}{L_q/2-\Delta_k} & 0 & -\frac{1}{L_q/2-\Delta_k} \\ 0 & 0 & \frac{1}{L_r} & -\frac{1}{L_r} \\ -\frac{1}{L_q/2+\Delta_k} & -\frac{1}{L_q/2-\Delta_k} & -\frac{1}{L_r} & \frac{1}{L_q/2+\Delta_k}+\frac{1}{L_q/2-\Delta_k}+\frac{1}{L_r} \end{pmatrix}. \tag{3.4}$$

It captures the grAl inductances in the resonator branch and in the qubit loop with the inductive asymmetry Δ_k.

Circuit Hamiltonian

To derive the circuit Hamiltonian $\mathcal{H}$, we begin by transforming the flux coordinates $\vec{\phi}$ to $\vec{x} = \mathbf{C}^{1/2}\vec{\phi}$. This transformation brings the linearized Lagrangian into a form where the kinetic term is diagonal and the normal mode problem becomes a standard eigenvalue equation. The linearized Lagrangian takes the form

$$\mathcal{L}_{\text{lin}} = \underbrace{\frac{1}{2}\dot{\vec{x}}^{\top}\dot{\vec{x}}}_{\text{kinetic}} - \underbrace{\frac{1}{2}\vec{x}^{\top}\mathbf{C}^{-1/2}\mathbf{L}^{-1}\mathbf{C}^{-1/2}\vec{x}}_{\text{potential}}. \tag{3.5}$$

The eigenfrequencies ω_j are obtained by solving the eigenvalue problem

$$\mathbf{C}^{-1/2}\mathbf{L}^{-1}\mathbf{C}^{-1/2}\vec{\eta}_j = \omega_j^2\vec{\eta}_j, \tag{3.6}$$

with corresponding eigenvectors $\vec{\eta}_j$. The eigenvectors form the transformation matrix $\mathbf{S} = (\vec{\eta}_1, \vec{\eta}_2, \vec{\eta}_3, \vec{\eta}_4)$, so that the original coordinates are expressed in the eigenmode basis as

$$\vec{\eta} = \mathbf{S}^{\top}\vec{x}. \tag{3.7}$$

Introducing the canonical conjugate momenta $p_i = \partial\mathcal{L}_{\text{lin}}/\partial\dot{\eta}_i$, we perform a Legendre transformation [139] to obtain the diagonalized Hamiltonian of the linear system:

$$\mathcal{H}_{\text{lin}} = \sum_i p_i\dot{\eta}_i - \mathcal{L}_{\text{lin}} = \frac{1}{2}\sum_i \left(p_i^2 + \omega_i^2\eta_i^2\right). \tag{3.8}$$

This describes a set of uncoupled harmonic oscillators in the normal mode basis.

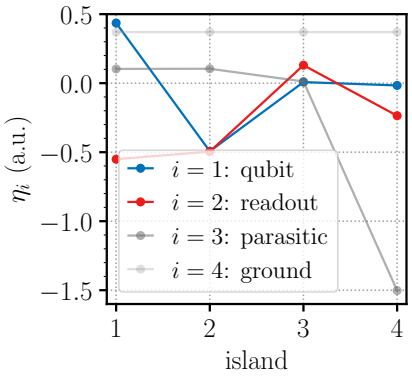

Figure 3.3.: **Mode structure of the circuit obtained from the eigenvectors $\vec{\eta}_i$ of the linearized Lagrangian**, for the example qubit q_{ex} [ii]. Each curve represents the components $\eta_{i,j}$ of the i-th eigenvector across the four superconducting islands j of the extended circuit model, see Fig. 3.2. Based on the spatial profiles, we identify mode $i = 1$ (blue) as the qubit mode, characterized by a strong differential signal between islands **1** and **2**; mode $i = 2$ (red) as the readout mode, which primarily modulates islands **1** and **2** in phase with respect to island **3**; mode $i = 3$ (dark grey) as a parasitic mode; and mode $i = 4$ (light grey) as a common mode with respect to ground mode.

The eigenmodes are identified based on the spatial profiles of the eigenvector components $\eta_{i,j}$, where i labels the mode number and j indexes the superconducting islands. These components indicate the

[ii] For the example qubit q_{ex}, we assume $L_r = 11.73$ nH, $L_q = 39.06$ nH, $\Delta_k = 0.28$ nH, $E_J = 4.83$ GHz and $C_J = 1.85$ fF. The capacitance matrix elements are listed in App. A.1.

relative participation of each island's flux coordinate in the corresponding normal mode, as shown in Fig. 3.3. The qubit mode is defined as $\eta_Q = \eta_1$, characterized by the strongest differential signal across nodes **1** and **2**, i.e. $|\mathbf{S}_{21}-\mathbf{S}_{11}| > |\mathbf{S}_{2j}-\mathbf{S}_{1j}| \forall j \neq 1$. The readout mode is defined as $\eta_R = \eta_2$, corresponding to the dominant common-mode contribution, $|\mathbf{S}_{22}+\mathbf{S}_{12}| > |\mathbf{S}_{2j}+\mathbf{S}_{1j}| \forall j \neq 2$.

To evaluate the nonlinear interactions of the JJ in the eigenmode basis, we re-express the original node flux variables $\vec{\phi}$ in terms of the normal mode coordinates $\vec{\eta}$. This is done using the inverse transformation

$$\vec{\phi} = \underbrace{\mathbf{C}^{-\frac{1}{2}}\mathbf{S}}_{\mathbf{S}'}\vec{\eta}. \tag{3.9}$$

Using this transformation, the differential and common-mode fluxes across the JJ can be expressed in terms of the qubit η_Q and readout η_R mode coordinates as

$$\begin{aligned} \phi_2-\phi_1 &\approx \left(\mathbf{S}'_{2Q}-\mathbf{S}'_{1Q}\right)\eta_Q+\left(\mathbf{S}'_{2R}-\mathbf{S}'_{1R}\right)\eta_R, \\ \phi_2+\phi_1 &\approx \left(\mathbf{S}'_{2Q}+\mathbf{S}'_{1Q}\right)\eta_Q+\left(\mathbf{S}'_{2R}+\mathbf{S}'_{1R}\right)\eta_R. \end{aligned} \tag{3.10}$$

In this approximation, we neglect both the zero-frequency common-mode and the high-frequency mode associated with island **4** [140]. This is justified because the zero mode carries no dynamics, and the high-frequency mode lies around 30 GHz and is sufficiently detuned to have negligible impact on the low energy spectrum.

If we neglect the nonlinearity of the grAl wire, the JJ remains the sole source of nonlinearity in the circuit. In the harmonic oscillator basis, it enters as a cosine potential that is driven by the differential flux mode across nodes **1** and **2**. Substituting Eq. 3.10 into the cosine argument in Eq. 3.2, we obtain

$$U_{JJ} = E_J \cos\left(\frac{2\pi}{\Phi_0}\left(\phi_2-\phi_1-\Phi_{ext}\right)\right) = E_J \cos\left(\frac{2\pi}{\Phi_0}\left[\left(S'_{2Q}-S'_{1Q}\right)\eta_Q+\left(S'_{2R}-S'_{1R}\right)\eta_R-\Phi_{ext}\right]\right). \tag{3.11}$$

Applying canonical quantization, the mode coordinates become

$$\eta_{R,Q} = \sqrt{\frac{\hbar}{2\omega_{R,Q}}}\left(\hat{a}_{R,Q}+\hat{a}^\dagger_{R,Q}\right) \qquad \text{and} \qquad p_{R,Q} = i\sqrt{\frac{\hbar\omega_{R,Q}}{2}}\left(\hat{a}^\dagger_{R,Q}-\hat{a}_{R,Q}\right), \tag{3.12}$$

so that the Josephson potential enters the Hamiltonian as

$$U_{JJ} = -E_J \cos\left(\lambda_Q(\hat{a}_Q+\hat{a}^\dagger_Q)+\lambda_R(\hat{a}_R+\hat{a}^\dagger_R)-\frac{2\pi}{\Phi_0}\Phi_{ext}\right), \tag{3.13}$$

with the dimensionless coupling strengths defined as

$$\lambda_R = \frac{2\pi}{\Phi_0}\sqrt{\frac{\hbar}{2\omega_R}}\left(\mathbf{S}'_{2R}-\mathbf{S}'_{1R}\right) \qquad \text{and} \qquad \lambda_Q = \frac{2\pi}{\Phi_0}\sqrt{\frac{\hbar}{2\omega_Q}}\left(\mathbf{S}'_{2Q}-\mathbf{S}'_{1Q}\right). \tag{3.14}$$

The full system Hamiltonian then becomes:

$$\begin{aligned} \mathcal{H} = &\hbar\omega_Q\left(\hat{a}^\dagger_Q\hat{a}_Q+\frac{1}{2}\right)+\hbar\omega_R\left(\hat{a}^\dagger_R\hat{a}_R+\frac{1}{2}\right) \\ &-E_J\cos\left(\lambda_Q(\hat{a}_Q+\hat{a}^\dagger_Q)+\lambda_R(\hat{a}_R+\hat{a}^\dagger_R)-\frac{2\pi}{\Phi_0}\Phi_{ext}\right). \end{aligned} \tag{3.15}$$

The intuitive picture of a nonlinear qubit mode coupled to a linear readout mode remains valid in the regime where $\lambda_R \ll \lambda_Q$. In the limit of perfect symmetry, i.e. for $\Delta_k \to 0$, the coupling between the qubit and readout mode vanishes, as $\lambda_R \to 0$.

In this thesis we numerically diagonalize the Hamiltonians from Eq. 3.15 in the photon number basis with $N_R = 15$ photons in the readout resonator and $N_Q = 30$ photons in the qubit.

Idealized circuit model

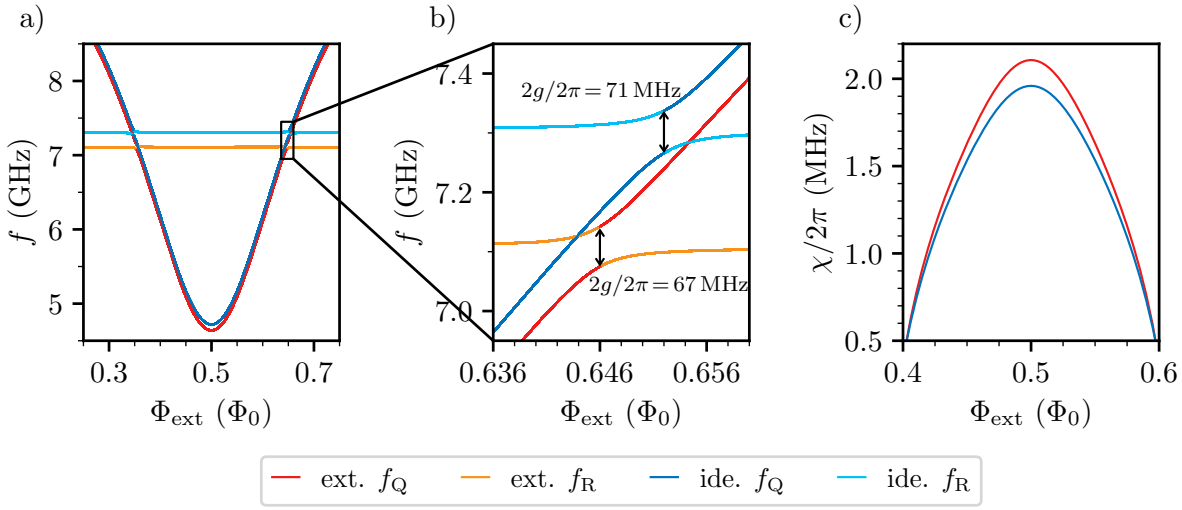

Figure 3.4.: **Comparison between the extended and idealized circuit models,** for the example qubit q_{ex}^{ii}. **a)** Qubit and resonator frequencies are calculated for both the extended (red and orange) and idealized (dark and light-blue) models as a function of external magnetic flux Φ_{ext}. **b)** Zooms into the avoided crossing, indicating the qubit-resonator coupling strength $g/2\pi$. **c)** Dispersive shift $\chi/2\pi$ as a function of Φ_{ext} for both models. The idealized model captures the essential qualitative features of the qubit-resonator coupling and spectrum. Quantitative deviations arise due to the non-negligible capacitances associated with island **4**, which are not included in the idealized model.

While the extended circuit model introduced above enables accurate numerical calculation of the qubit-resonator spectrum, a simplified version can be more insightful. It provides a clearer analytical understanding of the underlying circuit behavior. We reduce the full linearized model to its two most relevant degrees of freedom: the flux coordinates $\vec{\phi}^T = (\phi_1, \phi_2)$ associated with islands **1** and **2**.

Neglecting the capacitances associated with node **4**, we eliminate this inactive node using Kirchhoff's current conservation law

$$\frac{\phi_4 - \phi_3}{L_r} = \frac{\phi_2 - \phi_4}{\frac{L_q}{2} - \Delta_k} + \frac{\phi_1 - \phi_4}{\frac{L_q}{2} + \Delta_k}. \tag{3.16}$$

We fix the reference potential by choosing $\phi_3 = 0$ and solve for ϕ_4:

$$\phi_4 = \frac{1}{\Sigma_\mathrm{L}}\left(L_\mathrm{r}\left(\frac{L_\mathrm{q}}{2}+\Delta_\mathrm{k}\right)\phi_2+L_\mathrm{r}\left(\frac{L_\mathrm{q}}{2}-\Delta_\mathrm{k}\right)\phi_1\right), \tag{3.17}$$

where

$$\Sigma_\mathrm{L} = L_\mathrm{r}L_\mathrm{q}+\frac{L_\mathrm{q}^2}{4}-\Delta_\mathrm{k}^2. \tag{3.18}$$

Substituting Eq. 3.17 into the inductive energy terms associated with node **4** yields the effective potential:

$$U = \sum_{j\in\{1,2,3\}}\frac{1}{2L_{4j}}(\phi_4-\phi_j)^2 = \frac{1}{2L_\mathrm{r}}\phi_4^2+\frac{1}{2\left(\frac{L_\mathrm{q}}{2}+\Delta_\mathrm{k}\right)}(\phi_1-\phi_4)^2+\frac{1}{2\left(\frac{L_\mathrm{q}}{2}-\Delta_\mathrm{k}\right)}(\phi_2-\phi_4)^2, \tag{3.19}$$

where L_{4j} are the inductive elements between node **4** and the nodes **1**, **2** and **3**. Using Eq. 3.18, we rewrite Eq. 3.19 as:

$$U = \frac{1}{2\Sigma_\mathrm{L}}\left[\left(L_\mathrm{r}+\frac{L_\mathrm{q}}{2}-\Delta_\mathrm{k}\right)\phi_1^2+\left(L_\mathrm{r}+\frac{L_\mathrm{q}}{2}+\Delta_\mathrm{k}\right)\phi_2^2-2L_\mathrm{r}\phi_1\phi_2\right]. \tag{3.20}$$

In matrix form, the inductive energy is written as $U = \frac{1}{2}\vec{\phi}^\intercal\mathbf{L}^{-1}\vec{\phi}$ with the inverse inductance matrix

$$\mathbf{L}^{-1} = \frac{1}{\Sigma_\mathrm{L}}\begin{pmatrix} L_\mathrm{r}+\frac{L_\mathrm{q}}{2}-\Delta_\mathrm{k} & -L_\mathrm{r} \\ -L_\mathrm{r} & L_\mathrm{r}+\frac{L_\mathrm{q}}{2}+\Delta_\mathrm{k}\end{pmatrix}. \tag{3.21}$$

To account for stray capacitances to ground, we eliminate the ground node by enforcing charge conservation. This yields

$$C_{10}(\dot{\phi}_0-\dot{\phi}_1)+C_{20}(\dot{\phi}_0-\dot{\phi}_2)+C_{30}(\dot{\phi}_0-\dot{\phi}_3) = 0 \underset{\phi_3=0}{\Rightarrow} \dot{\phi}_0 = \frac{C_\mathrm{J0}}{C_{30}+2C_\mathrm{J0}}(\dot{\phi}_1+\dot{\phi}_2), \tag{3.22}$$

with $C_\mathrm{J0} = C_{10} = C_{20}$. The capacitive energy becomes

$$T = \frac{1}{2}\sum_{i,j\in\{1,2\}}\mathbf{C}_{ij}\dot{\phi}_i\dot{\phi}_j = \frac{1}{2}\left(C_\mathrm{r}+C_\mathrm{s}+C_\mathrm{J0}-\frac{C_\mathrm{J0}^2}{C_{30}+2C_\mathrm{J0}}\right)\left(\dot{\phi}_1^2+\dot{\phi}_2^2\right)-\left(C_\mathrm{s}+\frac{C_\mathrm{J0}^2}{C_{30}+2C_\mathrm{J0}}\right)\dot{\phi}_1\dot{\phi}_2, \tag{3.23}$$

or in matrix form $T = \frac{1}{2}\dot{\vec{\phi}}^\intercal\mathbf{C}\dot{\vec{\phi}}$, with

$$\mathbf{C} = \begin{pmatrix} C_\mathrm{r}+C_\mathrm{s}+C_\mathrm{J0}-\frac{C_\mathrm{J0}^2}{C_{30}+2C_\mathrm{J0}} & -C_\mathrm{s}-\frac{C_\mathrm{J0}^2}{C_{30}+2C_\mathrm{J0}} \\ -C_\mathrm{s}-\frac{C_\mathrm{J0}^2}{C_{30}+2C_\mathrm{J0}} & C_\mathrm{r}+C_\mathrm{s}+C_\mathrm{J0}-\frac{C_\mathrm{J0}^2}{C_{30}+2C_\mathrm{J0}}\end{pmatrix}. \tag{3.24}$$

For $\Delta_\mathrm{k} = 0$, the differential and common-mode basis

$$\phi_\mathrm{Q} = \phi_2-\phi_1, \tag{3.25}$$

$$\phi_\mathrm{R} = \frac{1}{2}(\phi_1+\phi_2), \tag{3.26}$$

diagonalizes both $\mathbf{C}$ and $\mathbf{L}^{-1}$, with transformed coordinates

$$\vec{\phi}^* = \begin{pmatrix}\phi_\mathrm{R}\\ \phi_\mathrm{Q}\end{pmatrix}. \tag{3.27}$$

For finite Δ_k, the matrices in this basis read

$$\mathbf{L}^{*-1} = \frac{1}{\Sigma_L}\begin{pmatrix} L_q & -\Delta_k \\ -\Delta_k & L_r+\frac{L_q}{4} \end{pmatrix} \tag{3.28}$$

and

$$\mathbf{C}^* = \begin{pmatrix} 2C_r+\left(\frac{1}{2C_{J0}}+\frac{1}{C_{30}}\right)^{-1} & 0 \\ 0 & \frac{C_r}{2}+C_s+\frac{C_{J0}}{2} \end{pmatrix}. \tag{3.29}$$

To provide a more intuitive description of the circuit in terms of its normal modes, we introduce effective parameters for the qubit and resonator branches. These are defined as

$$\begin{aligned} L_Q &= L_q-\Delta_k, \\ L_R &= L_r+\frac{L_q}{4}-\Delta_k, \\ L_S &= \Delta_k, \\ C_R &= 2C_r+\left(\frac{1}{2C_{J0}}+\frac{1}{C_{30}}\right)^{-1}, \\ C_Q &= \frac{C_r}{2}+C_s+\frac{C_{J0}}{2}, \end{aligned} \tag{3.30}$$

and represent their lumped inductance and capacitance values. A schematic overview of this parameterization is shown in Fig. 3.2c for clarity. Using these definitions, the transformed inductance and capacitance matrices in the qubit-resonator basis take the form

$$\mathbf{L}^{*-1} = \frac{1}{L_R L_Q+L_R L_S+L_Q L_S}\begin{pmatrix} L_Q+L_S & -L_S \\ -L_S & L_R+L_S \end{pmatrix}, \tag{3.31}$$

and

$$\mathbf{C}^* = \begin{pmatrix} C_R & 0 \\ 0 & C_Q \end{pmatrix}, \tag{3.32}$$

respectively. This formulation corresponds to the simplified lumped-element circuit shown in Fig. 3.2b, and highlight the role of $L_S = \Delta_k$ as the effective coupling element. We can now write down the Hamiltonian of the idealized circuit in the qubit-resonator basis as [141]

$$\mathcal{H} = \frac{1}{2}C_Q\dot{\phi}_Q^2+\frac{1}{2}C_R\dot{\phi}_R^2+\frac{1}{2}\frac{\phi_Q^2}{L_Q}+\frac{1}{2}\frac{\phi_R^2}{L_R}+\frac{1}{2}\frac{(\phi_Q-\phi_R)^2}{L_S}-E_J\cos\left(\frac{2\pi}{\Phi_0}(\phi_Q-\Phi_{ext})\right). \tag{3.33}$$

A numerical comparison with the full extended model is presented in Fig. 3.4. While the idealized model captures the qualitative features of the qubit-resonator spectrum, quantitative differences arise due to the neglected capacitances associated with island **4**. For example, in the case where $C_{14} \wedge C_{24} \approx C_{13}$, a non-neglectable portion of the resonator-mode charge resonates between the JJs electrodes and island **4**. As

a result, much less current flows through L_r, effectively increasing the resonator frequency compared to the prediction of the idealized model. This redistribution of current also reduces the mutual participation of the shared inductance $L_S = \Delta_k$, leading to a weaker effective coupling g between qubit and resonator than estimated from the idealized circuit.

Symmetric environment

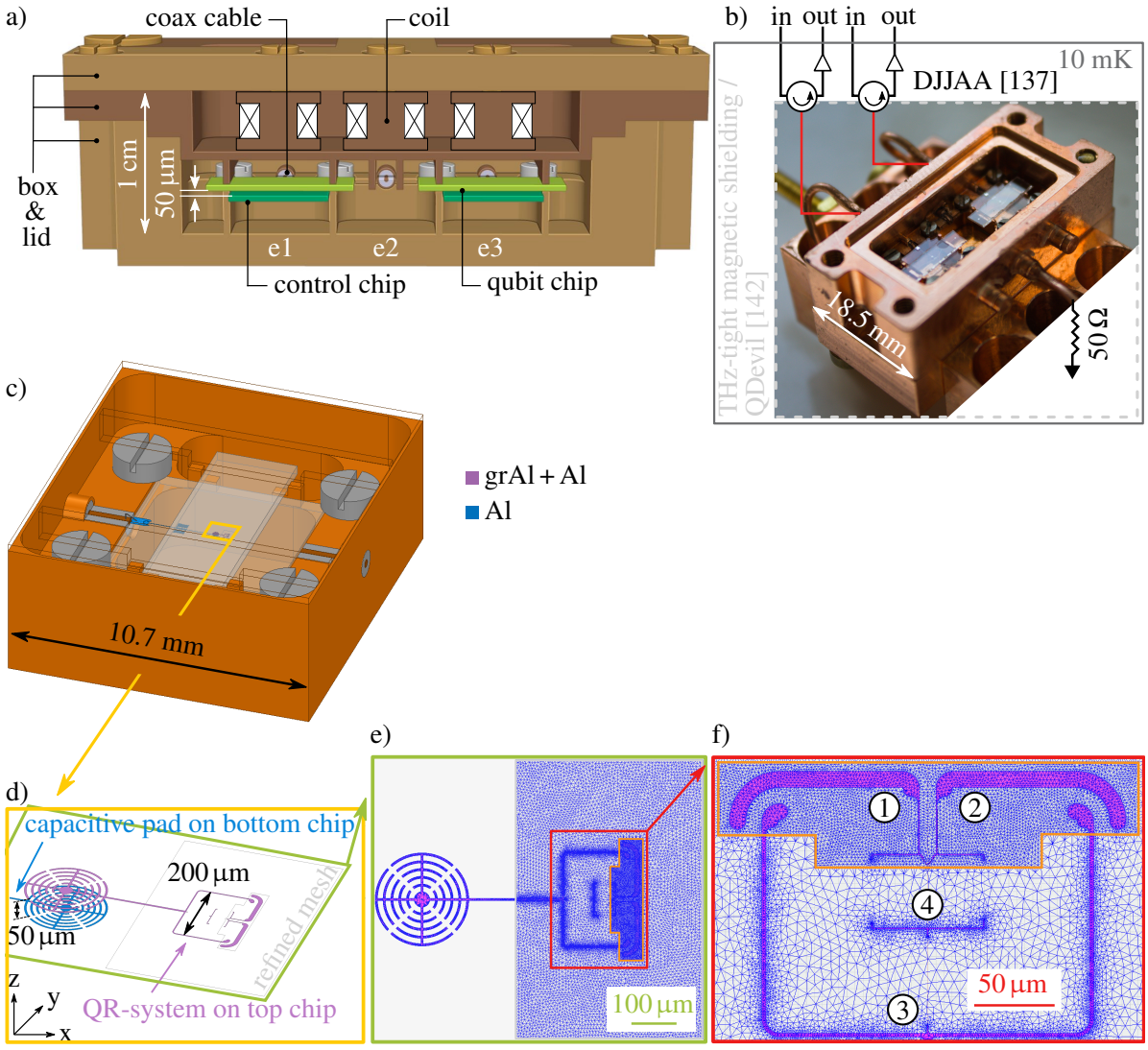

Figure 3.5.: **Symmetric environment for experiments and simulation,** figure and caption adapted from [136]. **a)** Cross-section of the copper sample box showing the three enclosures (e1-e3). The outer enclosures (e1 & e3) each house a control chip (dark green) and an upside-down qubit chip (light green) on which the QR-system is located. Both chips are made out of sapphire. The control chips are attached to the sample box using titanium or copper screws and wire bonded to the coaxial ports. The qubit chips are glued with a tiny amount of vacuum grease to pedestals which are part of the sample box. The pedestals define the $50\pm10\,\mu$m gap between the chips. The central enclosure (e2) is left empty. Empty pockets are added to the left of e1 and to the right of e3. As a result, the QR-systems in the outer enclosures experience a symmetric capacitive environment. Static flux biasing for each enclosure is achieved via a coil integrated into the lid (black X). **b)** Optical image of the sample box equipped with qubit and control chips. Experiments are performed in reflection with THz-tight magnetic shielding in a dilution refrigerator that has a base temperature of 10 mK. A complete schematic of the cryogenic measurement setup is provided in section 6.4 **c)** Simplified 3D model used to simulate the capacitance matrix **C** with the electrostatic finite element solver Ansys Maxwell. To allow visual access to the interior of the model, the lid is rendered transparent. The control chip inhibits a band-pass filter whose center frequency is tuned to the readout resonator's frequency. The model captures all essential features of the experimental setup, including the exact design of the QR-system, the exact design of the control chip and the correct material properties of the substrate and the sample box. Al structures are colored in blue, Al covered by grAl is colored in purple. **d)** Zoom-in on the central region to highlight the QR-system. The inductive elements (pure grAl wires) are omitted, as they do not contribute to the electrostatic simulation. The coupling capacitor C_c is formed with the capacitive pad on the bottom chip. To ensure accurate simulation of fine features, the mesh is locally refined within the light grey-marked region. **e)** Mesh (in blue) used during the electrostatic simulations, shown within the refined region. Inside the orange-marked area, the mesh is further refined to accurately capture the geometry of sensitive circuit structures. **f)** Zoom in on the red region to highlight the tetrahedral mesh around the qubit loop, with precision of more than 1 μm. The superconducting islands are labeled **1** through **4**. Slight derivations of the meshes' symmetry along the vertical axis between islands **1** and **2** are due to automatic mesh generation.

The qubit-resonator devices are operated in a copper sample box, shown in Fig. 3.5a,b. The box contains an array of three enclosures (e1,e2,e3). The outer enclosures house qubit-control chip pairs mounted in a flip-chip configuration, separated by a $50\pm10\,\mu$m vacuum gap. The QR-systems are located on the top qubit chip. The bottom control chip houses the circuitry required to read out the QR-system. The central enclosure e2 is left empty. This ensures that the electromagnetic environment of the qubits is symmetric with respect to the vertical midplane through the qubit loop. In the ideal case, this symmetry cancels all parasitic capacitances of the qubit islands. As a result, the qubit couples to the resonator only through the designed inductive asymmetry Δ_k in the grAl loop.

To model the capacitive environment, we perform electrostatic simulations using the finite-element solver Ansys Maxwell. The simplified 3D model used for the simulation is shown in Fig. 3.5c. The kinetic inductors and the JJ are omitted to isolate the capacitive contributions of the four islands in the QR-system, see Fig. 3.5d. To ensure a homogeneous mesh around the QR-system, we define multiple mesh

refinement regions with varying precision, as shown in Fig. 3.5e. This is particularly important for islands **1** and **2**, as meshing inaccuracies here directly affect the dispersive shift χ that we calculate from the simulations. Both islands are therefore placed inside the same high precision mesh refinement zone (resolution better than 1 µm) to ensure identical mesh quality, see Fig. 3.5e. Despite this, minor meshing asymmetries remain, resulting in convergence errors up to 10 aF. Simulations are run overnight until the available system memory (32 GB RAM) is fully used to achieve the highest possible precision. The extracted capacitance values are listed in App. A.1.

Capacitive asymmetry from chip misalignment

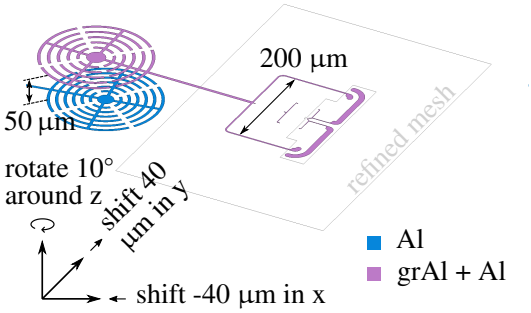

Figure 3.6.: **Simulation to estimate the capacitive asymmetry Δ_C.** Compared to Fig. 3.5d the qubit chip is displaced by ±40 µm along the x- and y-axis and rotated by 10° around the z-axis. From the finite-elements simulations we estimated a maximum of $\Delta_C = \pm 25$ aF due to chip misalignment.

A possible misalignment of the floating chip with respect to the symmetric sample holder breaks the capacitive symmetry between islands **1** and **2** resulting in an unequal coupling of the islands to ground. This is illustrated in Fig. 3.6, where the qubit chip is rotated by 10° around the z-axis and shifted by ±40 µm along the x- and y-axis. As a result, the effective capacitances between islands **1** and **3** and between islands **2** and **3** change. Neglecting any contribution from island 4, as $C_{i3} \gg C_{j4}$ with $i, j \in [1,2]$, we model this effect by introducing a capacitive asymmetry

$$\Delta_C = \frac{C_{13} - C_{23}}{2} \tag{3.34}$$

in the capacitance matrix

$$\mathbf{C}' = \begin{pmatrix} C_{11}+C_J+\Delta_C & -C_{12}-C_J & -C_{13}+\Delta_C & -C_{14} \\ -C_{12}-C_J & C_{22}+C_J-\Delta_C & -C_{23}-\Delta_C & -C_{24} \\ -C_{13}+\Delta_C & -C_{23}-\Delta_C & C_{33} & -C_{34} \\ -C_{14} & -C_{24} & -C_{34} & C_{44} \end{pmatrix}. \tag{3.35}$$

By comparing the capacitance matrices $\mathbf{C}$ (Eq. 3.3) and $\mathbf{C}'$ (Eq. 3.35) of the simulations with/without displaced qubit chip we estimate a maximum $\Delta_C \leq \pm 25$ aF.

For $\Delta_C \neq 0$, a residual electric dipole interaction adds to the designed inductive coupling between the qubit and resonator modes. The combined influence of both effects is illustrated for an example qubit q_{ex} in Fig. 3.7. As can be seen, technologically relevant dispersive shifts of $\chi/2\pi \approx 1$ MHz can be

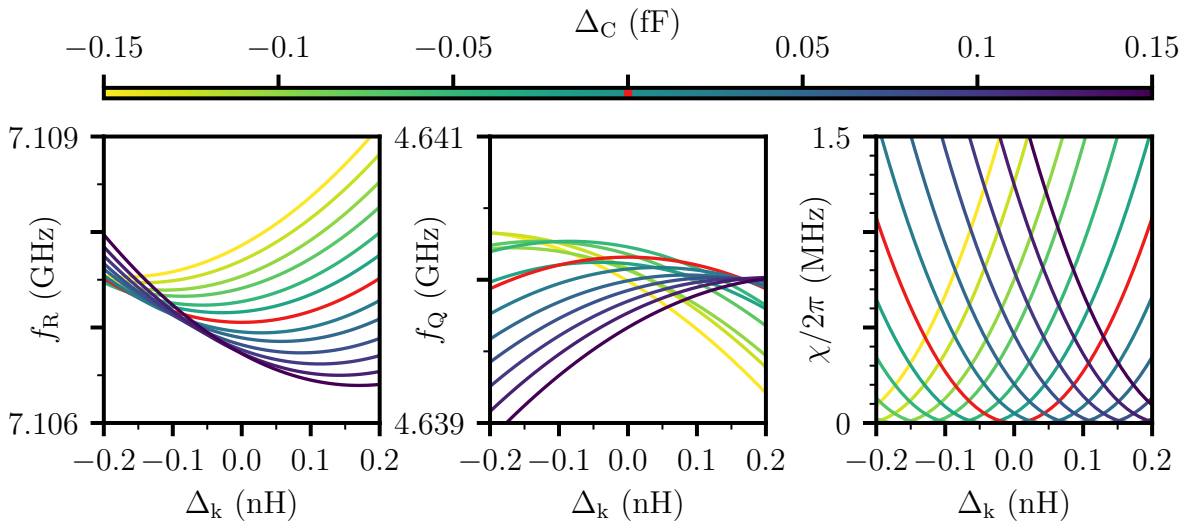

Figure 3.7.: **Effects of capacitive asymmetry Δ_C and inductive asymmetry Δ_k,** for the example qubit $q_{ex}{}^{ii}$. Numerical simulation of the resonator's frequency f_R (left), the qubit's frequency f_Q (center) and the dispersive shift χ (right) as a function of Δ_k for various values of Δ_C at $\Phi_{ext} = \Phi_0/2$. The red line visualizes the case $\Delta_C = 0$. To highlight the effect of capacitive and inductive contributions, we eliminated all asymmetric contributions from the capacitance matrix: $C_{11} = C_{22} \wedge C_{13} = C_{23} \wedge C_{14} = C_{24}$. Therefore, in a symmetric setting with $\Delta_k = \Delta_C = 0$ the qubit-resonator coupling vanishes ($\chi = 0$). Deviations from symmetry (inductive $\Delta_k \neq 0$ or capacitive $\Delta_C \neq 0$) introduce qubit-resonator coupling, as indicated by non-zero χ.

implemented either with a capacitive asymmetry of $\Delta_C \approx 100\,\text{aF}$ or an inductive asymmetry of $\Delta_k \approx 200\,\text{pH}$. This emphasizes the importance of precise chip alignment and a symmetric sample holder design to suppress unwanted capacitive contributions.

3.2. Experimental proof for kinetic inductance coupling

To validate the concept of kinetic coupling, we measure the spectra of 14 GFQs as a function of external flux Φ_{ext} (see App. A.2) using two-tone spectroscopy. An example spectrum for q6 is shown in Fig. 3.8a. We fit the qubit and resonator spectra simultaneously using the circuit Hamiltonian from Eq. 3.15. This yields the parameters L_r, L_q, Δ_k, C_J, and E_J, which are listed in App. A.2 for all measured qubits. The capacitances C_r and C_s are fixed from finite-element simulations and can be found in App. A.1. The coupling asymmetry Δ_k is extracted from the width of the avoided crossing. The parameters L_q, C_J, and E_J are determined by the qubit level structure.

The qubit spectra are explained by universal double-well physics [108] that was introduced in section 2.6. As shown in Fig. 3.8b, the GFQs range from the fluxon-tunneling regime ($E_J > E_L$) to the single-well plasmon regime ($E_J < E_L$). Towards the plasmon regime, frequencies increase and anharmonicities decrease. Towards the fluxon regime, frequencies decrease and anharmonicities increase, consistent

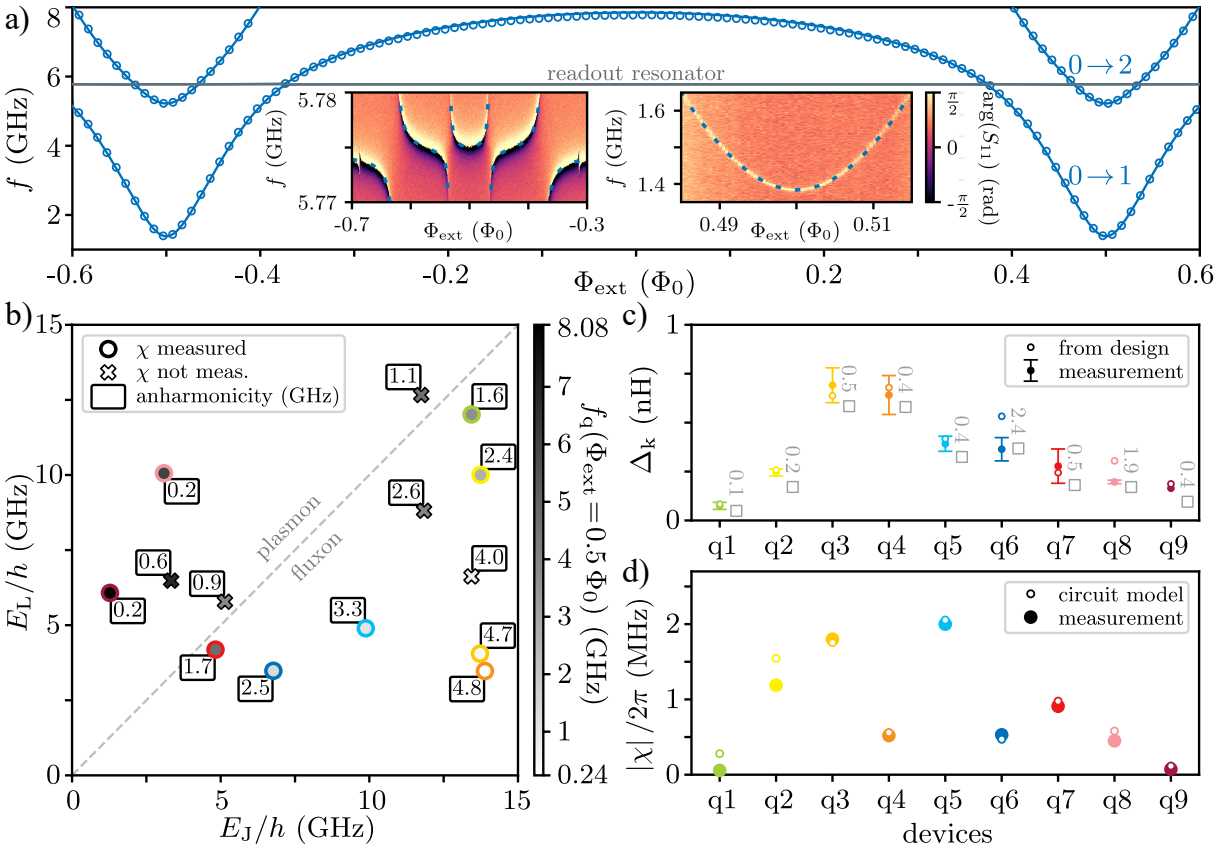

Figure 3.8.: **From plasmon to fluxon: summary of measured qubit parameters**, figure and caption taken from [136]. **a)** Combined plot of typical single and two tone spectroscopy of $0 \rightarrow 1$ and $0 \rightarrow 2$ qubit transitions (blue circles) vs. flux bias Φ_{ext} of device q6 as well as the 5.77 GHz resonance of the readout resonator (grey horizontal line). The inset on the left shows the measured phase response $\arg(S_{11})$ of the readout mode in the vicinity of the qubit-readout avoided level crossings when probing the system with a single tone. The inset on the right shows the phase response of the resonator on resonance when probing the qubit with a second tone near the qubit frequency in the vicinity of the half-flux sweet spot $\Phi_{\text{ext}} = \Phi_0/2$. The blue lines (dashed and continuous) correspond to the fitted circuit model with fit parameters E_{J}, L_{q}, L_{r}, C_{J} and Δ_{k}. **b)** Phase diagram E_{L} vs. E_{J} for the measured GFQs. The grey-scale intensity of the marker filler indicates the $0 \rightarrow 1$ transition frequency f_{q} at the half-flux point, with corresponding labels indicating the anharmonicity. The diagonal grey line separates the plasmon regime on the left from the fluxon regime on the right. Devices for which the dispersive shift χ was measured (was not measured) have a circular (cross-shaped) marker. **c)** Qubit loop asymmetry Δ_{k} for selected devices. The filled circles indicate the values of Δ_{k} extracted from the joint fit of the qubit and resonator spectroscopy (cf. left inset of panel **a** and App. A.2). The errorbars correspond to possible capacitive coupling arising from asymmetries $\Delta_{\text{C}} = \pm 25\,\text{aF} < 0.01 \times C_{\text{r}}$ in the capacitance matrix. The design values, shown as empty circles, are given by the product of the sheet inductance and the length difference between the qubit branches. The sheet inductance is extracted from the fitted L_{q} and the designed number of squares in the loop. The discrepancy between the measured and design values is shown in grey labels in units of squares. The marker color assigned to each sample is consistent in all panels. **d)** Qubit state dependent dispersive shift $\chi/2\pi$ at $\Phi_{\text{ext}} = \Phi_0/2$ for selected devices. Filled circles show χ values extracted from complex plane distributions of single shot measurements (cf. App. A.2). Empty circles indicate the calculated χ assuming pure kinetic inductance coupling.

with exponential scaling of the qubit frequency with barrier height [143]. At half-flux bias, we measure coherence times between 1 µs and 10 µs. Coherence times for all qubits are listed in App. A.3.
In Fig. 3.8c we compare the fitted and designed values of the inductive coupling asymmetry Δ_k. The total qubit-readout coupling includes both the designed inductive part Δ_k and spurious capacitive asymmetries Δ_C, as introduced in section 3.1. We estimate a maximum $\Delta_C = \pm 25\,\mathrm{aF}$, arising from potential misalignment of the qubit chip. These uncertainties in the fitted Δ_k are shown as error bars in Fig. 3.8c.
To calculate the designed value of Δ_k, we first determine the sheet inductance $L_\square$ of the grAl films used:

$$L_\square = \frac{L_q\, w_{q,grAl}}{l_{q,grAl}}, \tag{3.36}$$

where L_q is the fitted qubit loop inductance, $w_{q,grAl}$ the designed film width, and $l_{q,grAl}$ the designed loop length. All calculated $L_\square$ values are listed in App. A.2. Using these, the designed inductive asymmetry is obtained as

$$\Delta_k = \frac{L_\square\, l_{\Delta_k,grAl}}{w_{q,grAl}}, \tag{3.37}$$

where $l_{\Delta_k,grAl}$ is the designed length of the asymmetry segment in the grAl loop.
As can be seen in Fig. 3.8c, most of the measured and fitted data points agree within $0.5\,\square$ of grAl, indicating that the observed qubit-resonator coupling is primarily due to the intentional inductive asymmetry Δ_k.

In Fig. 3.8d we compare for nine qubits the measured dispersive shifts χ to the model predictions. To measure χ, we sweep the readout probe frequency while applying a $\pi/2$ qubit pulse and record single-shot IQ distributions at each probe frequency. The data are fitted with a two-state Gaussian mixture model. The state-dependent resonator response, given by $\arg(S_{11})$ (see App. A.2), yields χ. We use Eq. 2.50 to calculate the modeled χ. The data matches the model assuming $\Delta_C = 0$, confirming the validity of the kinetic inductive coupling design. The small deviations in χ observed for q1 and q2 arise from an old qubit design that lacked vertical mirror symmetry across the loop. More details on the initial device layout can be found in section 6.1.

3.3. Readout fidelity and quantum state-preparation

To quantify readout performance, we performed the following characterizations on qubit q7 at its half flux point ($\Phi_{ext} = 0.5\Phi_0$): contiguous measurement correlations and active state reset.
All readout powers in this section are given in units of average circulating photons in the readout resonator $\bar{n}$. We use the AC Stark shift of the qubit's frequency δf_{ac} to calculate $\bar{n}$ as explained in section 2.8[iii]. We extract δf_{ac} from Ramsey interferometry by fitting the qubit inversion to a damped oscillation (see Eq. 2.29), as shown in Fig. 3.9a for example drive powers. The extracted frequency shifts δf_{ac}

[iii] Although the photon-number calibration based on measurement-induced dephasing (see App. A.5) provides higher accuracy, we decided to use the AC-Stark-shift method as it is faster and sufficiently precise for our measurements

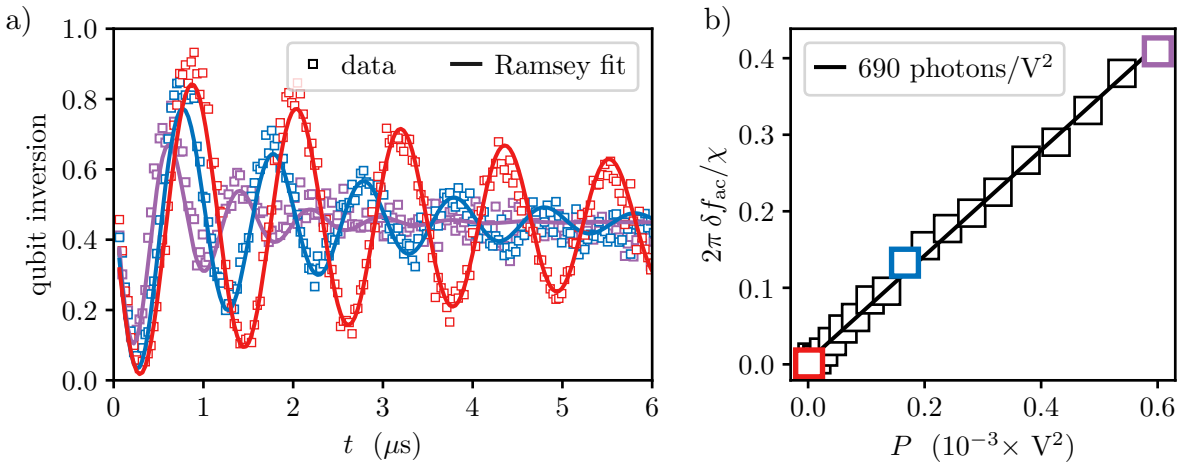

Figure 3.9.: **Photon number calibration**, figure and caption taken from [136]. **a)** Ramsey fringes are recorded while simultaneously populating the readout resonator with three different drive powers P: 0 (red), $0.17 \cdot 10^{(-3)}$ V^2 (blue) and $0.6 \cdot 10^{(-3)}$ V^2 (purple). The fringes are fitted to Eq. 2.29 (continuous lines) to obtain the AC Stark shift of the qubit frequency δf_{ac} with respect to P. **b)** The linear fit of δf_{ac} vs. P (continuous line) gives the photon number calibration. The three colored markers correspond to the Ramsey fringes shown in panel a. For q7 we measured $\chi/2\pi \approx 0.9$ MHz.

are plotted against readout power and fitted linearly to determine the photon number per drive power, see Fig. 3.9b. We determine a photon number calibration of 690 photons/V^2.

Contiguous measurement correlation

In this subsection, we discuss contiguous measurement correlation. The pulse sequence is shown in Fig. 3.10a. We use a SNR of ≈ 3.7, as defined in section 2.8. The SNR is obtained by adjusting the integration times $\tau_{int} \in (1600, 208)$ ns depending on $n \in (10, 150)$. Fig. 3.10b shows a section of a contiguously measured quantum jump trace for q7. We apply a Gaussian mixture model to traces with 10^6 points at fixed $\bar{n}$ to extract qubit populations in $|0\rangle$, $|1\rangle$, and $|2^+\rangle$ (see Fig. 3.10c), where $|2^+\rangle$ denotes all qubit states $\geq |2\rangle$. From the same data, we compute the correlations P_{00} and P_{11} between successive measurements. The conditional probability P_{xx} for remaining in the same qubit state $|c_j\rangle$ across two successive data points is given by

$$P_{xx} = \frac{\sum_{j=1}^{N-1} \delta_{c_j,x} \cdot \delta_{c_{j+1},x}}{\sum_{j=1}^{N-1} \delta_{c_j,x}}, \tag{3.38}$$

where $x \in \{0, 1\}$, $\delta_{a,b}$ is the Kronecker delta, $c_j \in \{0, 1, 2^+\}$ is the assigned state at index j, and N is the total number of samples. The correlations are shown in Fig. 3.10d.

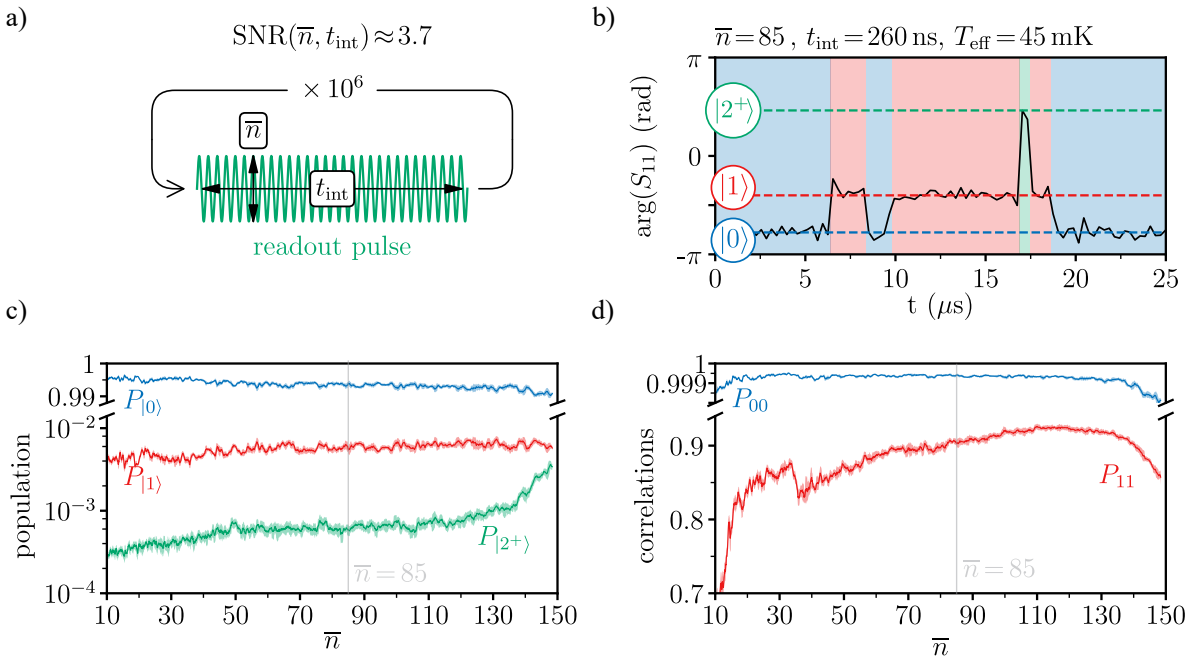

Figure 3.10.: **Readout fidelity**, figure and caption taken from [136]. **a)** Pulse sequence for the continuous-wave measurement protocol: 10^6 contiguous readout pulses are sent and integrated for different photon numbers $\overline{n}$. For each $\overline{n}$, the integration time t_{int} is adapted to keep the SNR = 3.7±0.2. **b)** Typical quantum jump trajectory visible in the measured phase of the reflection coefficient S_{11} shown in a window of 25 µs for device q7. The qubit states are assigned using a Gaussian mixture model and indicated by the color of the background: blue ($|0\rangle$ = ground), red ($|1\rangle$ = excited) and green ($|2^+\rangle$ = other). **c)** Measured states population vs. $\overline{n}$. Note that leakage to the $|2^+\rangle$-states accelerates for $\overline{n} \gtrsim 130$. **d)** Correlation P_{xx} for consecutive measurements in the ground ($x = 0$) or excited ($x = 1$) state vs. $\overline{n}$. The minimal integration time, 200 ns, is approximately three times larger than the resonator response time.

Similarly to Ref. [144], the resilience of the grAl GFQ to readout-induced leakage [145, 146, 147] is illustrated by the fact that up to $\bar{n} \approx 100$, the qubit populations remain approximately constant. For $\bar{n} = 85$ this corresponds to an effective temperature of

$$T_{\text{eff}} = \frac{h f_q}{k_B \ln(P_0/P_1)} = 42.5 \pm 2.5\,\text{mK}, \tag{3.39}$$

with $f_q = 4.640$ GHz. Leakage outside the computational subspace stays below 0.1 %.

Within the qubit subspace, we observe a clear difference in readout correlations between the ground and excited state. Ground-state measurements are highly correlated, with $P_{00} > 99.9\,\%$ across a broad range of readout powers. In contrast, P_{11} depends on the readout strength and reaches $P_{11} \geq 90\,\%$ for $\bar{n} \in (75, 140)$. The deviation of P_{11} from unity can be attributed to three effects. First, energy relaxation during the measurement reduces P_{11}. Using $\tau_{int} = 352$ ns for $\bar{n} = 85$ and $T_1 = 8.0 \pm 2.4$ µs, we calculate a reduction of

$$P_{\text{decay}} = 1 - \exp(-\tau_{int}/T_1) \leq 6\,\%. \tag{3.40}$$

Second, the readout tone modifies the qubit's spectral position and linewidth, which can increase its overlap with environmental noise and thus enhance relaxation [148]. Third, increasing $\bar{n}$ activates demolition effects [149], including leakage outside the qubit subspace [145]. The latter two contributions account for at least 4 % of the P_{11} infidelity. They reflect the limits of the qubit-readout coupling scheme and motivate further optimization.

Active state reset

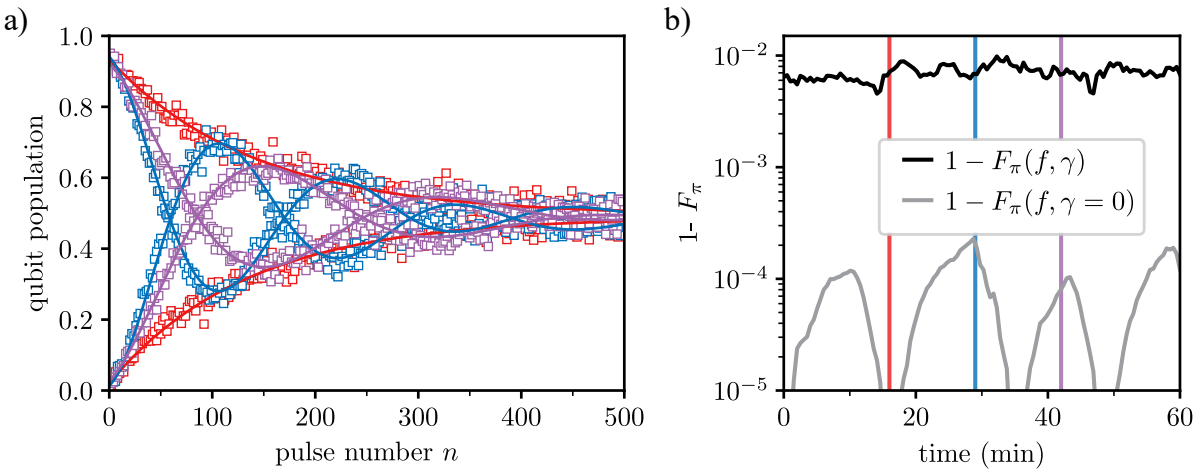

Figure 3.11.: **π-pulse fidelity**, figure and caption taken from [136]. **a)** The qubit population is plotted versus a subsequently played number of π-pulses for three individual experiments conducted 13 min apart. Oscillations in this measurement indicate the imperfection of the π-pulse over- or undershooting a perfect bit-flip that sum up to an inversion of the qubit population after half a period of the oscillation. The oscillations are dampened by energy relaxation. **b)** The experiment in a) is conducted contiguously over the course of one hour and we plot $F_\pi(f,\gamma)$ and $F_\pi(f,\gamma=0)$ as black and grey lines, respectively. $F_\pi(f,\gamma=0)$ drifts continuously with a period of tens of minutes.

In this subsection, we discuss active state reset. This requires calibrated π-pulses. We fine-tune the π-pulse amplitude by minimizing the beating in the qubit population after a sequence of n pulses. Three representative measurements are shown in Fig. 3.11a. The qubit population as a function of pulse number is modeled by

$$P(n) = a\left(\frac{1}{2} - \frac{1}{2}\cos(\pi n + 2\pi f n)\right)\exp(-\gamma n) + o, \tag{3.41}$$

where f is the detuning-induced beating frequency and γ accounts for energy decay. The parameters a and o account for readout errors. From the fit parameters, we define the π-pulse fidelity as

$$F_\pi(f,\gamma) = \frac{P(1) - P(0)}{a} = \left(\frac{1}{2} - \frac{1}{2}\cos(\pi + 2\pi f)\right)\exp(-\gamma).$$

Fig. 3.11b shows $F_\pi(f,\gamma)$ and the calibration-only fidelity $F_\pi(f,\gamma=0)$ over the course of one hour. While $F_\pi(f,\gamma=0)$ varies due to calibration drift, the dominant fidelity loss is due to energy decay. The

π-pulse has a length of 40 ns and its fidelity exceeds 99 %.

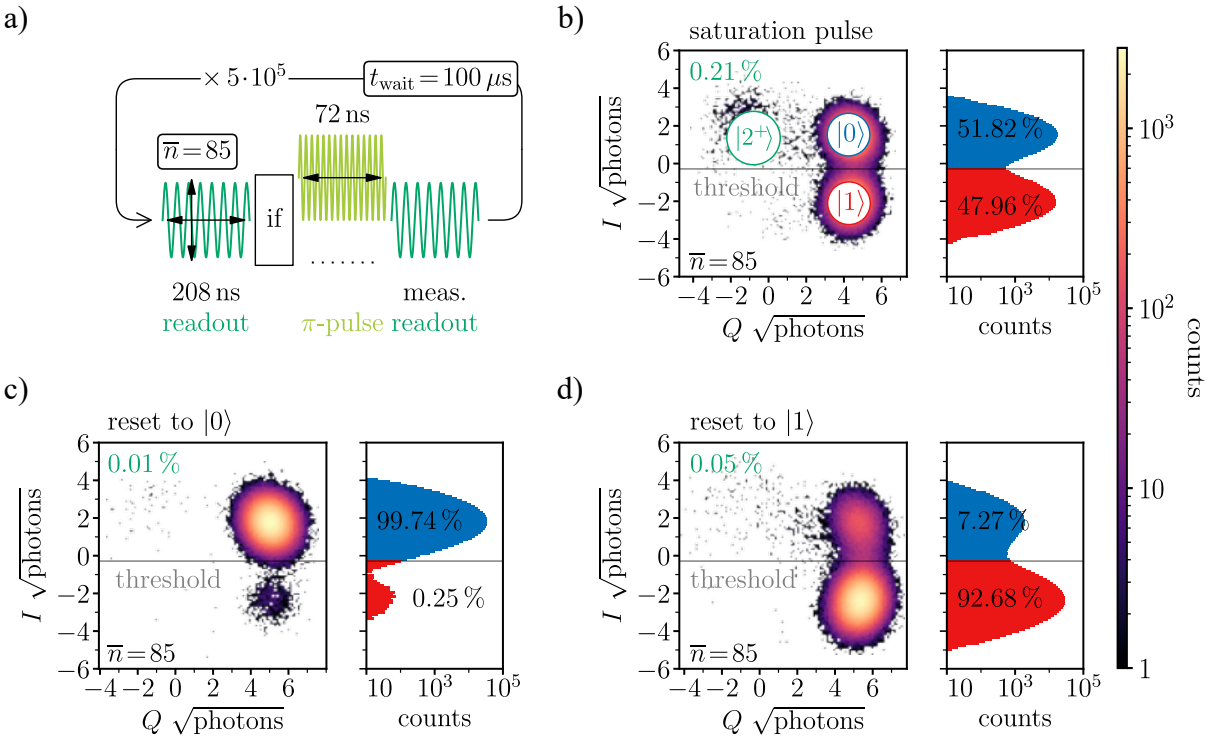

Figure 3.12.: **Quantum state preparation**, figure and caption taken from [136]. **a)** Pulse sequence used for active state reset. The measurement outcome of the first readout pulse is used to condition a π-pulse on the qubit. The result of the second readout is used to assess the fidelity of the reset protocol. We use $\overline{n} = 85$ and $t_{\text{int}} = 208\,\text{ns}$ resulting in a state separation of $\approx 6\sigma$. We repeat the sequence 5×10^5 times with a waiting time of $t_{\text{wait}} = 100\,\mu\text{s}$ in between. The measured pointer state distributions for 50 % polarization, active reset to $|0\rangle$ and $|1\rangle$ are shown in panels **b**, **c** and **d**, respectively. The grey line is the threshold used for state assignment in the active reset protocol. The green label indicates leakage into higher states. The measurement outcomes are depicted as histograms in logarithmic scale.

With the calibrated π-pulses, we perform active state reset experiments. We initialize the qubit from its thermal state and apply a conditional π-pulse for state preparation. The pulse sequence is shown in Fig. 3.12a. The discrimination threshold between $|0\rangle$ and $|1\rangle$ is determined from the measured IQ cloud distributions after a saturation pulse, see Fig. 3.12b. At $\bar{n} = 85$, this results in a state separation of

$$\frac{d}{\sqrt{\sigma^2_{\text{max}}}} \approx 6\sigma, \tag{3.42}$$

where $d = \sqrt{(I_0 - I_1)^2 + (Q_0 - Q_1)^2}$ is the distance between the two Gaussian means and σ^2_{max} is the maximum variance of the two fitted Gaussian. Using this setting, we achieve reset fidelities of $P_0^{\text{active}} = 99.7\,\%$ for the ground state and $P_1^{\text{active}} = 92.7\,\%$ for the excited state, see Fig. 3.12c,d. The dominant error sources are energy decay during readout and quantum demolition effects. Contributions of the π pulses used are negligible. The measured performance matches previous results for fluxoniums and trans-

mons [144, 150, 151], but remains below state-of-the-art fidelities reaching 99 % [152]. The primary limitation is the qubit relaxation time T_1, which may be improved through materials and design optimization [153].

3.4. GFQs with junction arrays

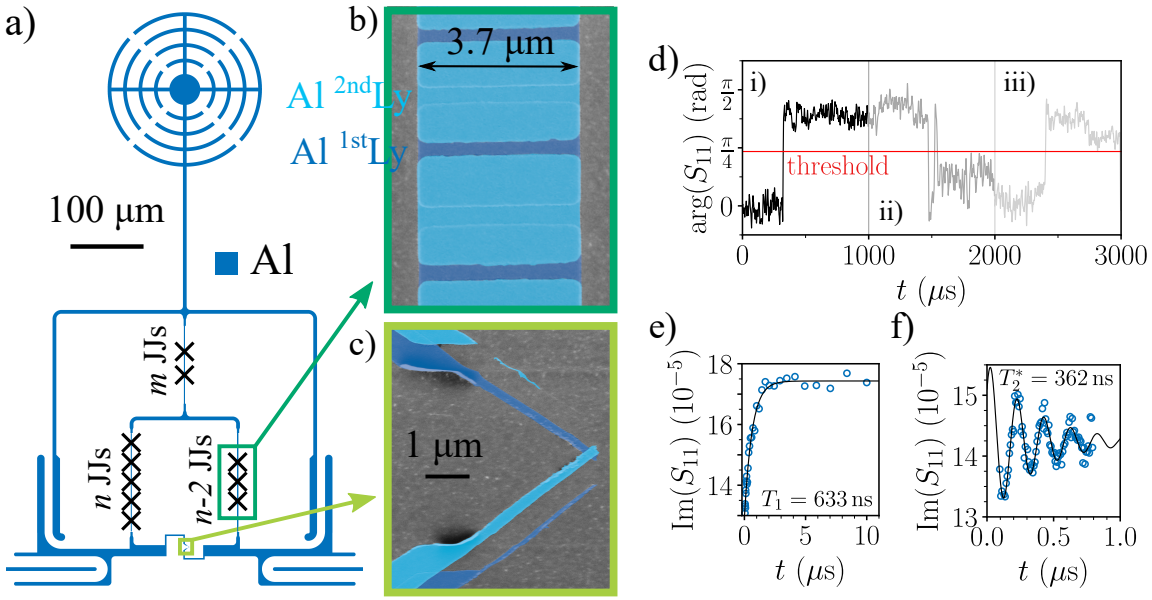

Figure 3.13.: **GFQ with JJ arrays. a)** Image of a GFQ that uses Al (blue) JJ arrays as inductances instead of grAl. The circuit diagram is identical to Fig. 3.2. The JJ array in the left branch has n, in the right branch $n-2$ and at the top m JJs. For this device: $n = 32$, $m = 0$. **b)** False-colored SEM image of a JJ array. The array is fabricated using Dolan bridges as described in section 6.1. The bottom Al layer is colored dark blue, the top layer light blue. **c)** False-colored SEM image of the Al/AlO_x/Al α JJ ($A_J \approx 0.06\,\mu m^2$). **d)** Three consecutive VNA traces (i: black, ii: darkgrey, iii: lightgrey) with increasing readout power ($P_{VNA} = -47, -46, -45$ dBm) of the phase response $\arg(S_{11})$ of the harmonic mode at $f_r = 6.250$ GHz vs. time. We apply a 1D Gaussian filter ($\sigma = 2$) to the traces for better visibility. The red line indicates the threshold used to distinguish between the two phase states. **e,f)** T_1 / T_2^* measurement of q15 at the half flux point showing the imaginary part of the reflected signal $\mathrm{Im}(S_{11})$ with 250,000 averages per data point, yielding $T_1 = 633$ ns / $T_2^* = 362$ ns. T_2^* was measured using Ramsey interferometry.

In an effort to improve the coherence times of our GFQs, we replaced the granular aluminum (grAl) inductances with arrays of JJs, as shown in Fig. 3.13a,b,c. We distinguish between the large JJs forming the inductive arrays, denoted as β JJs, and the small JJ at the bottom of the loop, referred to as the α JJ. Substituting grAl with JJ arrays eliminates inductive losses inherent to disordered superconductors, which can be estimated using Fermi's Golden Rule [154]:

$$\frac{1}{T_1} = \frac{8\pi^3 E_L}{hQ_{ind}} |\langle 0|\hat{\varphi}|1\rangle|^2 \left(1+\coth\left(\frac{hf_q}{2k_B T}\right)\right), \tag{3.43}$$

with the inductive energy E_L, the flux operator $\hat{\varphi}$ in units of Φ_0, and the qubit frequency f_q. The matrix elements $|\langle 0|\hat{\varphi}|1\rangle|^2$ are listed in App. A.4. The energy relaxation times observed in GFQs correspond to inductive quality factors in the range $10^5 < Q_{\text{ind}} \lessapprox 10^6$, consistent with loss estimates for grAl [120]. Measured relaxation times and the corresponding Q_{ind} values are provided in App. A.3. Fabrication details for the JJ arrays using Dolan bridges are discussed in section 6.1.

As in the case of the grAl-based GFQs, these devices have two modes: an anharmonic differential mode and a harmonic readout mode as described in section 3.1. The resonator phase fluctuates between two discrete values at a rate of $\Gamma_{\text{jp}} \approx 2\,\text{mHz}$, as shown in Fig. 3.13d for an example qubit q15. We distinguish the two states using a threshold and extract rates of $\Gamma_\uparrow \approx 3.2\,\text{mHz}$ and $\Gamma_\downarrow \approx 1.7\,\text{mHz}$, which yields $T_{1,\text{jp}} \approx 200\,\mu\text{s}$ (see Eq. 2.24). These random phase jumps hinder qubit spectroscopy, and we were only able to resolve the spectrum near the half-flux point for two out of four JJ array GFQs.

In App. A.2, we fit the spectrum of q15 and extract the following parameters: $L_q = 31.1\,\text{nH}$, $C_q = 33.9\,\text{fF}$ ($\Rightarrow E_c \approx 0.6\,\text{GHz}$), and $E_{J,\alpha} = 7.6\,\text{GHz}$. Using Eq. 2.14 and Eq. 2.15 and having 62 JJs in the qubit loop, we estimate $E_{J,\beta} = 326\,\text{GHz}$. Assuming a JJ capacitance density $C_J \approx 50\,\text{fF}/\mu\text{m}^2$ (see section 2.2) and JJ area $A_{J,\beta} \approx 4\,\mu\text{m}^2$, we obtain $E_{c,\beta} \approx 0.1\,\text{GHz}$. Finally, from Eq. 2.44, we calculate a phase-slip rate $\Gamma_{\text{ps},\beta} \lll 1/\text{day}$, indicating that the observed jumps are not caused by quantum phase slips in the β JJs.

A possible explanation for the phase jumps observed in Fig. 3.13d are quantum jumps of the qubit, which we investigated through time-domain measurements at the half-flux point. These measurements proved even more challenging than spectroscopy, and we were only able to extract coherence times for q15. As shown in Fig. 3.13e,f, we measure $T_1 = 633\,\text{ns}$ and $T_2^* = 362\,\text{ns}$, both over two orders of magnitude shorter than the jump-limited lifetime $T_{1,\text{jp}}$. We therefore conclude that the observed phase jumps of the resonator are not caused by quantum jumps of the qubit.

Compared to the relaxation times in the grAl-based GFQs (see App. A.3), these coherence times are approximately an order of magnitude lower. As all other parameters (sapphire chips, box environment, cryogenic setup, fabrication process) remained unchanged, we attribute this additional loss to the replacement of grAl inductances with JJ arrays in the qubit loop. This result is surprising, since transmon qubits fabricated in the same evaporator, using identical oxidation parameters, and measured in the same sample box show T_1 times above $25\,\mu\text{s}$. While the exact mechanism behind the reduced coherence remains to be identified, our results show that JJ arrays cannot be straightforwardly used as replacements for grAl inductances in our QR-system and require further work to reach acceptable performance.

In inductively coupled circuits based on JJ-array superinductors, long coherence times and stable resonator operation have been demonstrated. For example, Ref. [113] reports JJ arrays with $E_J/E_C \approx 180$ exhibiting phase-slip-induced resonator jumps only at sub-mHz rates (≤ 1 per hour), while the QR-

system in Ref. [135] achieves coherence times exceeding 100 µs[iv]. The significantly shorter coherence times and resonator instabilities observed in our devices therefore point to additional loss mechanisms not intrinsic to JJ-array-based inductors. One possible source of loss are fabrication-related imperfections in our JJ arrays (e.g., variations in I_c or C_J, or defects and residues within the JJs), to which our JJs may be more susceptible due to their larger area (4 µm^2) compared to those in Refs. [113, 135]. However, optical microscopy of all four devices revealed no visible defects and only slight asymmetries in the array JJs, which we confirmed for q15 using SEM imaging.

[iv] In fluxonium circuits capacitively coupled to readout resonators, such as Refs. [111, 155, 156], no readout current flows through the superinductor. A direct comparison to our architecture therefore does not apply. These circuits reach coherence times well above 100 µs without resonator instabilities.

4. Modular flip-chip architecture

This chapter is based on results previously published in Ref. [157]. Adaptations and extensions have been made to better integrate the material into this thesis.

In this chapter, we present our modular flip-chip architecture for superconducting qubits, where each qubit resides on a dedicated chip in its own microwave enclosure, enabling high isolation between the GFQs. We describe the mechanical and microwave properties of the architecture and evaluate them through finite-element simulations. We measure an isolation of over 60 dB between the outer enclosures and extract residual $\sigma_z\sigma_z$ crosstalk below 700 Hz between the outer qubits. Finally, we demonstrate tunable coupling of $g_{13}^{\max}/2\pi \approx 1.6$ MHz between these qubits and observe population swapping.

4.1. Architecture

The sample box contains three electromagnetic enclosures (e1,e2,e3), each measuring $a{\times}b{\times}d = 6.0{\times}6.1{\times}6.1\,\mathrm{mm}^3$, see Fig. 4.1a. These dimensions push the lowest cavity mode for each enclosure [131] above

$$f_{mnl} = f_{011} = \frac{c}{2\sqrt{\mu_r \epsilon_r}}\sqrt{\left(\frac{m}{a}\right)^2+\left(\frac{n}{b}\right)^2+\left(\frac{l}{d}\right)^2} > 30\,\mathrm{GHz}, \tag{4.1}$$

with $\mu_r = 1$ and $\epsilon_r = 1$ for vacuum. This matches with finite-element simulations. Enclosures are spaced by 6.5 mm to ease assembly. In e1 and e3, we mount an upside-down qubit-chip above a control-chip, see Fig. 4.1b. In e2 we place a single coupler-chip. The qubit-chips measure $2.85{\times}10.0\,\mathrm{mm}^2$ and extend into neighboring enclosures for inter-chip coupling. The qubit-chips are fixed with vacuum grease to metal pedestals, while bottom chips are screwed to the box and wire-bonded to coaxial lines. The spacing between bottom and top chips is $d = 50{\pm}10\,\mu\mathrm{m}$, defined by the pedestal height. We omit ground planes on all chips to keep the microwave environment clean (to avoid parasitic modes in the ground planes).
Each qubit-chip hosts a qubit-resonator (QR) system as described in section 3.1 to which we added capacitive extenders that reach into adjacent enclosures, see Fig. 4.1c,d. Capacitive extenders need to be added on both sides of the QR-system to preserve symmetry, so that the concept of purely inductive coupling between qubit and readout modes remains valid, as described in detail in App. A.9. Several types of capacitive extenders were tested, and a $\lambda/2$-resonator-like design made of a single Al strip was chosen, as detailed in App. A.9. To ensure a high resonance frequency, the extenders should be made as short as possible [131]:

$$f_{\mathrm{r,extenders}} = \frac{c}{2L\sqrt{\varepsilon_{\mathrm{r}}}} > 30\,\mathrm{GHz}, \tag{4.2}$$

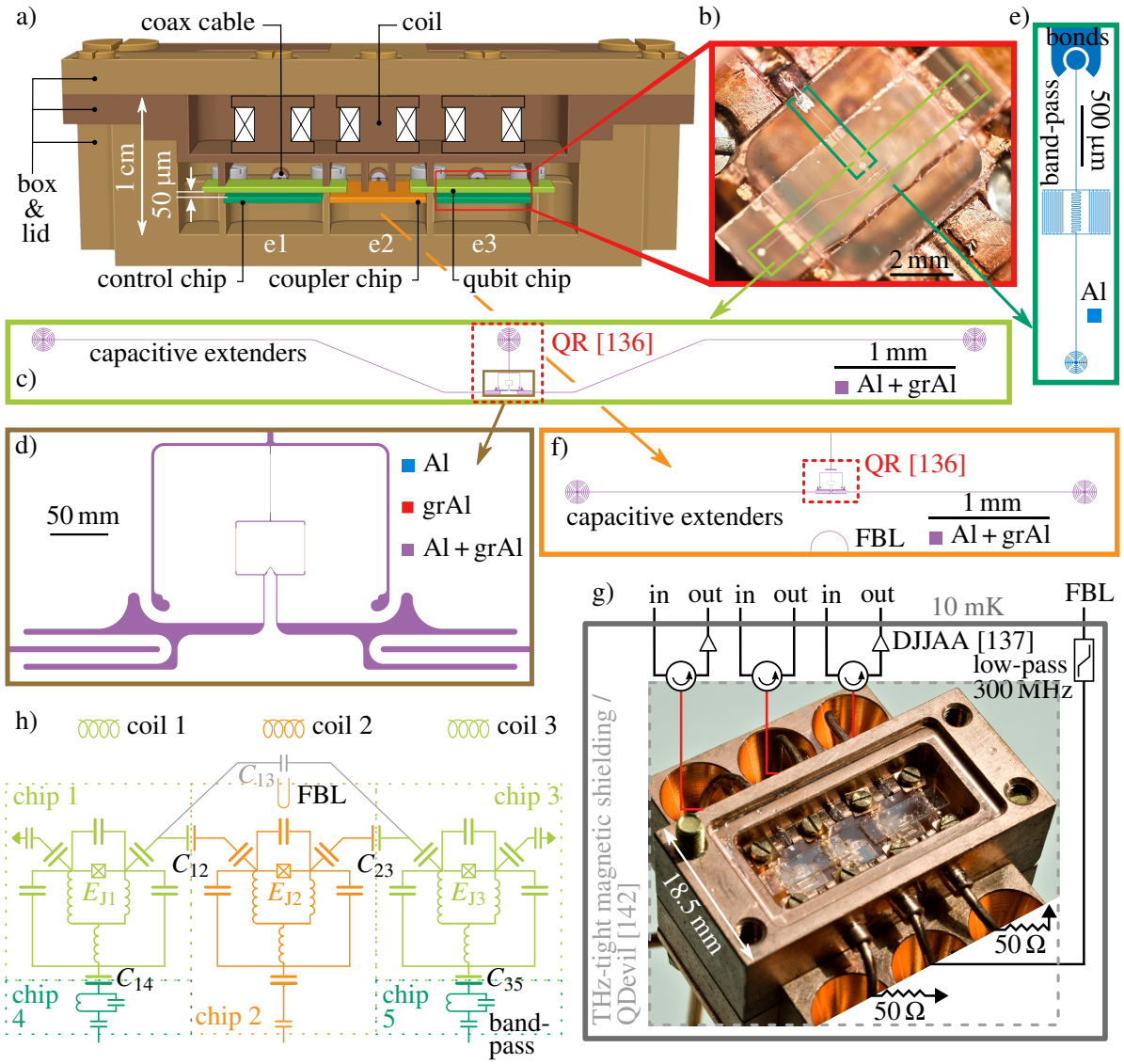
a)
coax cable
coil
box & lid
1 cm
50 µm
e1
e2
e3
control chip
coupler chip
qubit chip
b)
2 mm
e)
bonds
band-pass
500 µm
Al
c)
capacitive extenders
QR [136]
1 mm
Al + grAl
d)
50 mm
Al
grAl
Al + grAl
f)
QR [136]
capacitive extenders
FBL
1 mm
Al + grAl
g)
in
out
in
out
in
out
10 mK
FBL
DJJAA [137]
low-pass
300 MHz
THz-tight magnetic shielding / QDevil [142]
18.5 mm
50 Ω
50 Ω
h)
coil 1
coil 2
coil 3
chip 1
chip 3
C_{13}
FBL
C_{12}
C_{23}
E_{J1}
E_{J2}
E_{J3}
C_{14}
C_{35}
chip 4
chip 2
chip 5
band-pass

Figure 4.1.: **Modular flip-chip architecture based on individual qubit and coupler enclosures**, figure and caption adapted from [157]. **a)** Cross-section of the sample box: two of the three enclosures (e1 & e3) contain control (dark green) and qubit (light green) chips, while the middle enclosure (e2) houses a qubit-chip used as a coupler (orange). Each enclosure can be accessed by two coaxial cables perpendicular to the cross-section plane, one cable on each side. The static magnetic field in each enclosure is controlled by coils integrated into the top lid, which are highlighted via the black X symbols. **b)** Optical image of the qubit-chip above the control-chip in e1, without a coupler-chip present. **c-f)** Layouts of the qubit-chip, zoomed-in qubit region, control chip, and coupler-chip, respectively. The qubit(Q)-resonator(R) system consists of a generalized flux qubit inductively coupled to a readout resonator, as described in section 3.1 and in [136]. The QR-system is indicated by the red frames in panels c and f. Two capacitive extenders are capacitively coupled to the qubit JJ electrodes to enable capacitive coupling to the adjacent chips via the skeletal-shaped pads. The middle pad in panel c is used to couple the QR-system to the input-output line on the control-chip shown in panel e. The band-pass filter implemented by the meandered inductor and finger capacitor visible in the center of the chip in panel e is used to reduce Purcell decay [158, 159]. Through pulses on the flux bias line (FBL) visible in panel f, the frequency of the coupler qubit is tunable. The color legend indicates the material used for each circuit element: blue for aluminum (Al), red for granular aluminum (grAl) and purple for Al covered with grAl. **g)** Optical image of the fully equipped sample box and schematics of the reflection measurement setup in a magnetically shielded environment at 10 mK. A complete schematic of the cryogenic measurement setup is provided in section 6.4. The FBL is connected to a commercial low-pass filter with a cutoff frequency of 300 MHz. **h)** Circuit diagram of the coupled qubit array. Each qubit-chip (chip 1 & 3) contains a QR-system [136] with a corresponding band-pass filter (cf. panel e) on its control-chip (chip 4 & 5, respectively). The QR-system used as coupler is located on chip 2. The coupling capacitances C_{12}, C_{23}, C_{14} and C_{35} bridge the gaps between individual chips, enabling a modular flip-chip architecture. The capacitance C_{13} is not implemented on the chips and represents the direct capacitive coupling between the outer qubits.

with $c \approx 3{\cdot}10^8$ m/s, $L \leq 4.5$ mm the length of the extender and $\varepsilon_r \approx 1$[i]. Coupling pads at the chip center and extender tips enable capacitive inter-chip connections. The skeletal pad design prevents flux trapping. The coupler-chip in e2 also holds a QR-system, with extenders aligned to the neighboring qubit pads, see Fig. 4.1f.

Control-chips in e1 and e3 include a band-pass filter that is capacitively coupled to the qubit-chip via the central coupling pad, as shown in Fig. 4.1e. These filters reduce Purcell loss [158, 159] and define the readout-feedline interface. We chose a lumped-element design rather than a $\lambda/2$-resonator for the band-pass filter, as it minimizes crosstalk. Supporting simulations are shown in App. A.9. Control structures on the coupler-chip include a readout line and fast flux bias line (FBL). The FBL is wire-bonded to a coaxial port equipped with a commercial 300 MHz low-pass filter. Simulations (see App. A.9) show that the FBL on this coupler-chip has a mutual inductance of $1/M \approx 7\,\mathrm{mA}/\Phi_0$. Following Ref. [160], we

[i] $\varepsilon_r \approx 1$ is justified as the thickness of the sapphire chips is much smaller than the dimensions of the enclosure: $330\,\mu\mathrm{m} \ll a/2 = 6\mathrm{mm}/2$.

estimate the critical current I_c of the FBL using the Ginzburg-Landau depairing current density J_d. This approach yields:

$$I_{c,FBL} \approx J_d A \approx 2.8\,\mathrm{mA} \qquad \text{with} \qquad J_d = \frac{2\sqrt{2}}{3\sqrt{3}} \frac{H_c}{\lambda} = 27.9\,\mathrm{mA}/\mu\mathrm{m}^2, \tag{4.3}$$

where $A \geq 20\,\mathrm{nm} \times 5\,\mu\mathrm{m} = 0.1\,\mu\mathrm{m}^2$ is the minimal cross section of the Al-film[ii]. We use a critical field for thin film Al of $B_c(0\,\mathrm{K}) = 10.5\,\mathrm{mT} \Rightarrow H_c = B_c/\mu_0 = 8.38\,\mathrm{nA}/\mu\mathrm{m}$ [161] and a thin film penetration depth of $\lambda(0\,\mathrm{K}) \approx 163\,\mathrm{nm}$ [162]. In this configuration, a full Φ_0 cannot be induced in the qubit loop. However, the FBL must still respond on short timescales, which requires a small self-inductance. The chosen parameters therefore represent a compromise between minimizing self-inductance and achieving sufficient mutual inductance to switch the coupler on and off.

In early versions of the sample box we considered adding FBLs to the outer enclosures and explored on-chip low-pass filters to suppress their associated losses, as discussed in App. A.10. However, given the excellent qubit-qubit isolation of our architecture even with qubits being on resonance (see section 4.3), FBLs are not needed and were omitted in the final design to avoid additional complexity. While the architecture works reliably without FBLs, it would still be advantageous to have the possibility of tuning the qubit frequencies on fast timescales. An alternative solution are magnetic flux hoses, which we became aware of only later in the project. Their integration into the sample box is discussed in App. A.12.

Fig. 4.1g shows the full five-chip assembly mounted in the copper sample box and anchored to the 10 mK base plate of a dilution refrigerator. The electromagnetic enclosures are defined by the metallic lid, not shown in the picture. Fig. 4.1f provides the corresponding circuit diagram. Fig. 4.1g shows a simplified schematic of the microwave readout and control lines. Qubit readout is performed in reflection via the on-chip resonators. We use dimer JJ array parametric amplifiers (DJJAAs) [137] for amplifying the readout signals from e1 and e3. Qubit control pulses are sent through the same lines.

For the QR-systems it is paramount to shunt the two capacitive extenders among themselves and with islands 1 and 2 during fabrication. This is done to avoid static discharges that break the JJ. The shunt must only be removed immediately before the sample is mounted inside the box. For more detail about the fabrication and the static discharge see section 6.1.

Simulations

To assess the impact of chip misalignment, band-pass filter mismatch, and losses through the copper box, we perform eigenmode simulations using Ansys HFSS. The 3D model used for the simulations is shown in Fig. 4.2. To save computational resources our model consists of a single enclosure, with a QR-system that has no capacitive extenders. We can omit the capacitive extenders in the simulations, since

[ii] The effective $I_{c,FBL}$ may be further reduced, for example due to non-ideal interfaces between the Al film and the Al wire bonds.

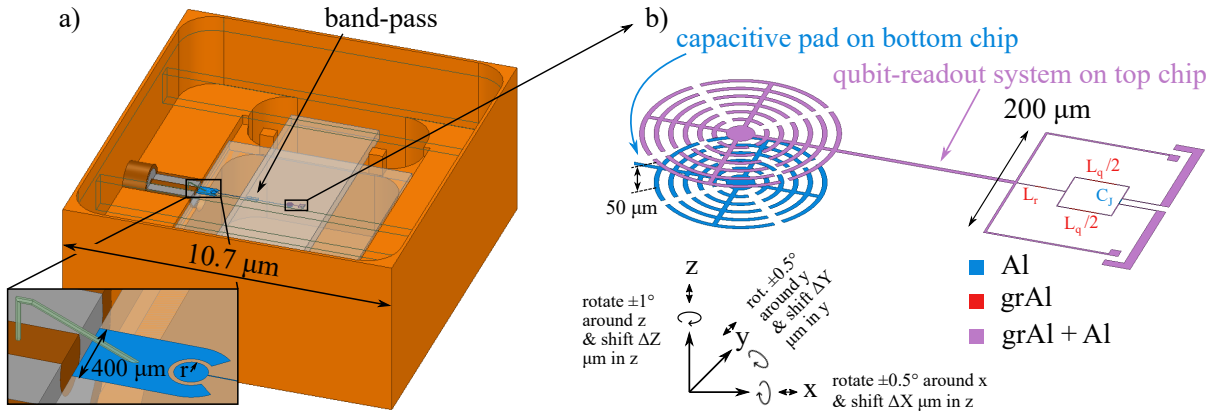

Figure 4.2.: **Samplebox for Ansys eigenmode simulations**, figure and caption taken from [157]. **a)** Simplified copper sample box in which we perform the Ansys finite-element eigenmode simulations with transparent lid for better visibility. The band-pass filter is capacitively coupled to the bond pad through a circular capacitor with variable radius r. To save computational resources, we omit the capacitive extenders and replace the finger capacitance of the band-pass filter with a variable lumped capacitance. Boundary conditions consist of perfect conductors (PerfE) on the outside of the sample box and a $R = 50\,\Omega$ resistor at the coaxial port. **b)** Zoom-in towards the overlapping capacitive pad on the control-chip and the QR-system on the top chip, which is based on QR-system 1 (see Tab. 4.2). Readout inductance L_r and qubit inductance L_q are replaced by lumped inductors, while the JJ is replaced by a lumped capacitor C_J. Both chips are spaced by 50 µm. As indicated by the coordinate system in the bottom left corner, the qubit-chip is shifted up to ±40 µm in X, Y & Z direction and rotated by ±0.5° in X&Y / by ±1.0° in Z direction. The color legend indicates the material used for each circuit element: blue for Al, red for grAl and purple for Al covered with grAl.

the qubit coherence times remain unchanged with or without extenders (see App. A.3), indicating that they are not the dominant loss mechanism. Simulations are based on the parameters of Q1 (see Tab. 4.2) and terminated at a convergence error below 1%. We model the grAl inductors as lumped elements with $L_\mathrm{r} = 15\,\mathrm{nH}$, $L_\mathrm{q} = 25\,\mathrm{nH}$, and $\Delta_\mathrm{k} = 0.5\,\mathrm{nH}$. Since ANSYS cannot simulate the nonlinearity of the JJs directly, we replace the JJ by a lumped capacitor $C_\mathrm{J} = 4\,\mathrm{fF}$, such that the resulting mode is purely harmonic and has a simulated resonance frequency of $f_\mathrm{sim} \approx 7.7\,\mathrm{GHz}$.

To analyze the architecture's susceptibility to misalignment, we simulate the bandwidth $\kappa/2\pi = f_\mathrm{R}/Q$ of the readout mode for a qubit-chip that is shifted and rotated in X, Y & Z directions. The results are shown in Fig. 4.3. As can be seen, shifts in X and Y direction of up to ±40 µm and rotations of the qubit-chip of ±0.5° around the X and Y axis and ±1.0° around the Z axis have no impact on κ, i.e. the coupling strength of the resonator to port 1. Only deviations in Z direction (i.e. pedestal height) impact κ. However, this effect can be compensated by coupling the resonator stronger to the readout port by increasing the radius r of the coupling pads, see Fig. 4.4a.

In Fig. 4.4a, we show the dependence of $\kappa/2\pi = f_\mathrm{R}/Q$ on the band-pass frequency f_b and the capacitive coupling strength to the rf-port (expressed by the radius r of the circular capacitance). We observe a reduction of κ with r. When the band-pass and resonator have the same frequency, $f_\mathrm{b} \approx f_\mathrm{R}$, both modes

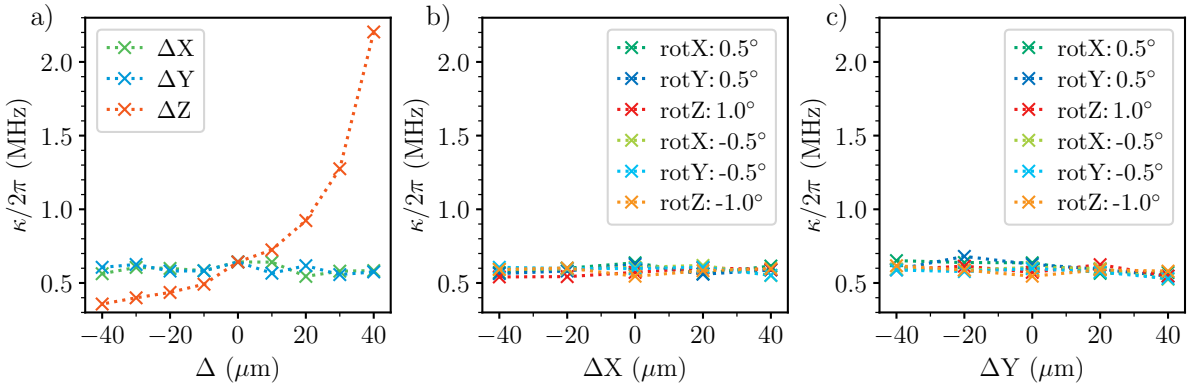

Figure 4.3.: **Simulations for chip misalignment**, figure and caption taken from [157]. Bandwidth of the readout resonator $\kappa/2\pi$ vs. **a)** shift in X, Y & Z direction and **(b/c)** shift in X/Y direction for rotations of ±0.5° around the X&Y axis and ±1.0° around the Z axis of the qubit-chip.

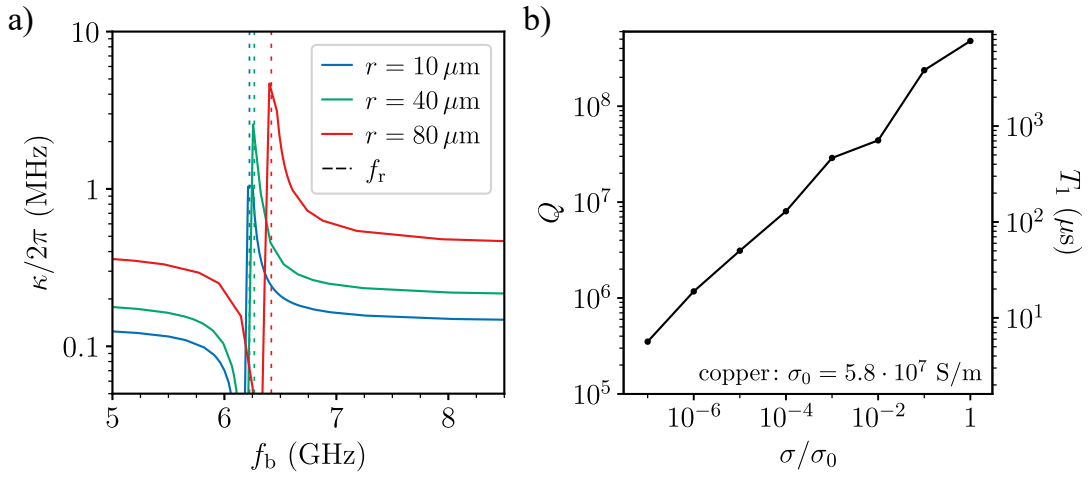

Figure 4.4.: **Simulations for band-pass filter and material losses**, figure and caption taken from [157]. **a)** Bandwidth $\kappa/2\pi$ for different radii r of the circular capacitor vs. the frequency of the band-pass filter f_b. The frequencies of the readout resonators are indicated by the dashed lines. **b)** Simulated quality factor Q of a harmonic mode including the JJ, oscillating at a frequency of $f_{sim} \approx 7.7\,\text{GHz}$ versus the conductivity of the bulk sample holder material. The predicted qubit energy relaxation time T_1 for inductive loss is calculated via Eq. 3.43.

hybridize, increasing κ significantly. For $f_R \lesssim f_b$ we observe destructive interference between the two modes resulting in $\kappa/2\pi < 0.05\,\text{MHz}$.

To assess the contribution of the copper box to qubit energy relaxation, we simulate the quality factor Q of the mode that includes the JJ while reducing the conductivity of the box. At 300 K the conductivity of copper is $\sigma_0 = 5.8{\cdot}10^7\,\text{S/m}$. To calculate the qubit relaxation time T_1 from the simulated Q, we use Fermi's Golden Rule (see Eq. 3.43 and App. A.4). The simulated Q factors and resulting T_1 values

for $E_L \approx 5.3\,\text{GHz}$, $f_q \approx 3.9\,\text{GHz}$, $\hat{\varphi} = 0.5$ and $T = 45\,\text{mK}$, are shown in Fig. 4.4. For copper, we find $T_1(\sigma_0) > 10^3\,\mu\text{s}$, indicating that box losses are currently not a limiting facto[iii].

Flux calibration

We use the superconducting coils on top of each enclosure to statically control the magnetic flux Φ_{ext} inside the enclosure. Due to their large self-inductance, these coils cannot be used for fast flux biasing. For a coil with radius r, height h, number of turns n, and current I, the magnetic flux Φ_{ext} through a qubit loop of area A, placed a distance z along the coil axis, can be approximated for $h \ll z$ and $r \ll z$ by [163]:

$$\Phi_{\text{ext}}(r, n, z, A, I) = B \cdot A = \frac{\mu_0 n I r^2}{2(r^2+z^2)^{3/2}} \cdot A. \tag{4.4}$$

Using the formula with typical parameters $r = 1.2\,\text{mm}$, $h = 2\,\text{mm}$, $n = 10$, $z = 3.9\,\text{mm}$, and $A = 60{\times}45\,\mu\text{m}^2$ ($h/z \approx 0.51$, $r/z \approx 0.31$), we estimate the induced flux and find $\Phi_{\text{ext}} = \Phi_0$ for a current of $I \approx 5.7\,\text{mA}$. A value of $5.7\,\text{mA}/\Phi_0$ can be easily controlled using our Yokogawa GS200 [164] DC voltage/current source.

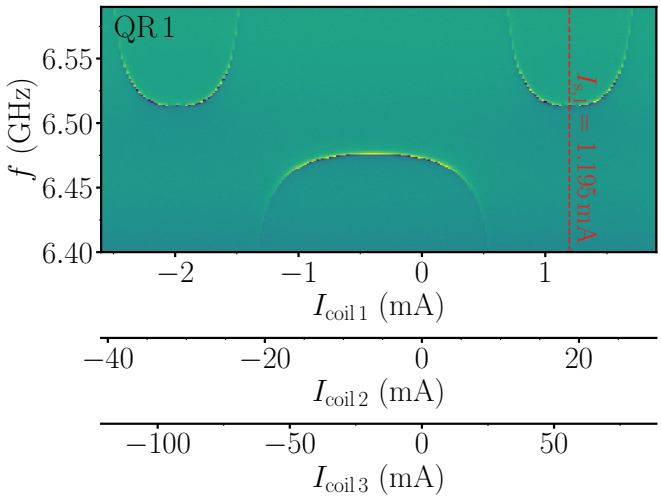

Figure 4.5.: **Calibrating magnetic crosstalk.** Flux sweep of QR-system 1 with coil 1, 2 and 3 to determine the mutual inductances M_{11}, M_{12}, M_{13} between coils 1, 2 and 3 and the device. The half flux point of coil 1 is highlighted by the red line at $I_{s,1} = 1.195\,\text{mA}$.

The three coils on top of the enclosures create magnetic crosstalk to neighboring and next neighboring enclosures as shown in Fig. 4.5 for QR-system 1. To compensate the crosstalk the following equation system must be solved:

$$\begin{pmatrix} M_{11} & -M_{12} & -M_{13} \\ -M_{21} & M_{22} & -M_{23} \\ -M_{31} & -M_{32} & M_{33} \end{pmatrix} \begin{pmatrix} I_{\text{coil 1}} \\ I_{\text{coil 2}} \\ I_{\text{coil 3}} \end{pmatrix} = \begin{pmatrix} \Phi_{\text{ext,Q1}} \\ \Phi_{\text{ext,Q2}} \\ \Phi_{\text{ext,Q3}} \end{pmatrix} - \begin{pmatrix} \frac{1}{2} - M_{11}\ I_{\text{s,1}} \\ \frac{1}{2} - M_{22}\ I_{\text{s,2}} \\ \frac{1}{2} - M_{33}\ I_{\text{s,3}} \end{pmatrix}, \tag{4.5}$$

[iii] Note that the conductivity σ_0 of copper is further reduced at millikelvin temperatures, which would make box losses even less relevant.

where M_{ij} with $i, j \in [1,2,3]$ are the mutual inductances between each QR-system (index i) and each coil (index j), $I_{\text{coil}\,j}$ is the current through each coil and $I_{\text{s},i}$ the current at the half flux point ($\Phi_{\text{ext}} = \frac{\Phi_0}{2}$) from coil i in QR-system i. All mutual inductances M_{ij} and the current $I_{\text{s},i}$ must be determined in calibration measurements (similar to Fig. 4.5) and are listed in Tab. 4.1. In addition it must be ensured that the current is flowing in the correct direction through the coils, which may make a change of sign for some of the off-diagonal matrix elements in Eq. 4.5 necessary (signs of the off-diagonal terms are mirror-symmetric with respect to the diagonal).

$1/M_{ij}$	j=1 (mA/Φ_0)	j=2 (mA/Φ_0)	j=3 (mA/Φ_0)	$I_{s,i=j}$ (mA)
i=1	3.17	49.8	148.0	1.195
i=2	52.7	4.68	58.7	1.95
i=3	106.5	33.4	2.40	-0.825

Table 4.1.: **Calibration values needed to compensate flux crosstalk.** Mutual inductances $1/M_{ij}$ in mA/Φ_0 and current at half-flux point $I_{\text{s},i}$ ($\Phi_{\text{ext}} = \frac{\Phi_0}{2}$) needed to compensate flux crosstalk. Index i denotes QR-systems and index j the coils.

In total, nine calibration measurements are required for a three-qubit setup. While manageable at this scale, the procedure becomes a bottleneck for larger systems. This motivates the integration of magnetic flux hoses for magnetic biasing, which are expected to simplify calibration and reduce magnetic crosstalk as detailed in App. A.12. In principle, magnetic crosstalk could also be suppressed by encasing the coils inside superconducting individual enclosures. To explore this approach, we replaced the copper sample box and lid with Al, making the enclosures superconducting. In this configuration, the coils must be mounted on the inside of the Al walls, since magnetic fields in a superconductor are exponentially suppressed on the length scale of the London penetration depth ($\lambda_{\text{L}} \approx 45\,\text{nm}$ for Al [103]). The corresponding design is shown in App. A.11. However, implementing this configuration is technically challenging, and the first design iteration did not show a significant reduction of magnetic crosstalk between neighboring enclosures compared to the copper box.

4.2. Qubit spectra

Fig. 4.6 shows two-tone spectroscopy of the used qubits and coupler near their half-flux sweet spots. The measurements are fitted with the flux qubit Hamiltonian (see Eq. 2.33 and App. A.2). Fit results and coherence times are listed in Tab. 4.2, while Tab. 4.3 shows the resonator parameters. Qubit frequencies are tuned independently via the three calibrated magnetic field coils (see section 4.1). The idle configuration sets qubit 1 (Q1) and the coupler (Q2) to their sweet spots at $f_{\text{Q1}}(\frac{\Phi_0}{2}) = 3.465\,\text{GHz}$ and $f_{\text{Q2}}(\frac{\Phi_0}{2}) = 3.147\,\text{GHz}$ and qubit 3 (Q3) to its bias point at $\Phi_{\text{ext},3} = 0.539\,\Phi_0$ ($f_{\text{Q3}}(0.539\,\Phi_0) = 3.465\,\text{GHz}$). Qubits 1 and 3 are always operated on resonance. Coupling is activated by fast flux pulses on the FBL,

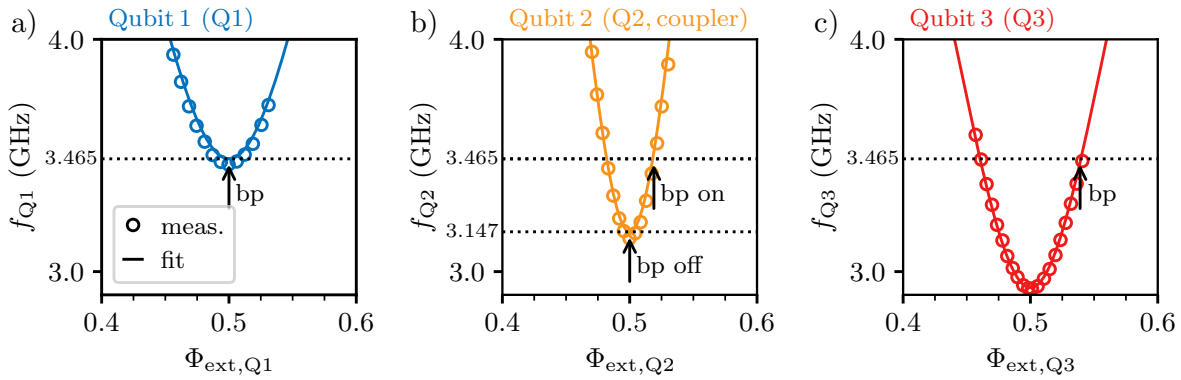

Figure 4.6.: **Overview of qubit and coupler spectra with bias points (bp).** The measured (circles) and fitted (lines) spectra of **a)** qubit 1 (Q1, blue) in e1, **b)** the coupler (qubit 2 (Q2), orange) in e2 and **c)** qubit 3 (Q3, red) in e3 vs. the external flux Φ_{ext} through the respective qubit/coupler loops are shown. During all experiments both qubits (Q1 & Q3) are operated at a frequency of $f_{Q1} \approx f_{Q3} \approx 3.465\,\text{GHz}$ (see the corresponding bp in panel a and c), corresponding to the half-flux point of Q1 ($\Phi_{ext,\,Q1} = \Phi_0/2$). To switch the coupler off, coil 2 is used to park the coupler at its half flux point ($\Phi_{ext,\,Q2} = \Phi_0/2$), corresponding to bp off at a frequency of 3.147 GHz. To switch the coupler on, a DC pulse is played on the FBL, aligning f_{Q2} at bp on, resonant with f_{Q1} and f_{Q3}.

tuning the coupler into resonance with the qubits.

device	E_J/h [GHz]	L_Q [nH]	C_Q+C_J [fF]	f_q @ $\frac{\Phi_0}{2}$ [GHz]	T_1 @ $\frac{\Phi_0}{2}$	T_2^* @ $\frac{\Phi_0}{2}$	T_1 @ bp	T_2^* @ bp
Q1	6.14	25.32	27.93	3.465	2.1 µs	1.9 µs	–	–
coupler (Q2)	10.14	20.53	22.19	3.147	–	–	–	–
Q3	6.59	26.71	29.52	2.927	1.7 µs	1.1 µs	800 ns	160ns

Table 4.2.: **Qubit parameters.** The fitted lumped element parameters, frequencies f_q and measured coherence times[iv] for the qubits at the sweet spot or the bias point, respectively.

device	f_R @ $\Phi_0/2$ [GHz]	$\kappa/2\pi$ [MHz]	Q_L
R1 (readout 1)	6.508	2.2	3000
R2 (rout-coupler)	6.274	4.2	1500
R3 (readout 3)	5.226	1.3	3900

Table 4.3.: **Readout parameters**[iv]**.** The frequencies f_R, bandwidth $\kappa/2\pi$ and total quality factors Q_L of the devices readout resonators.

[iv] Coherence times, readout parameters and population swaps were measured in a previous cooldown using the same setup.

4.3. Isolation

Since the qubits operate on resonance ($f_{Q1} = f_{Q3} = 3.465\,\text{GHz}$), it is crucial to know the isolation and crosstalk between enclosures with the coupling turned off. In this section, we measure the port-to-port isolation, and the transverse and longitudinal crosstalk between qubit Q1 and Q3 with switched off coupler. Switched off coupler means that for all experiments in this section the coupler is tuned to its half flux point at $f_{Q2} = 3.147\,\text{GHz}$[v].

Isolation between enclosures

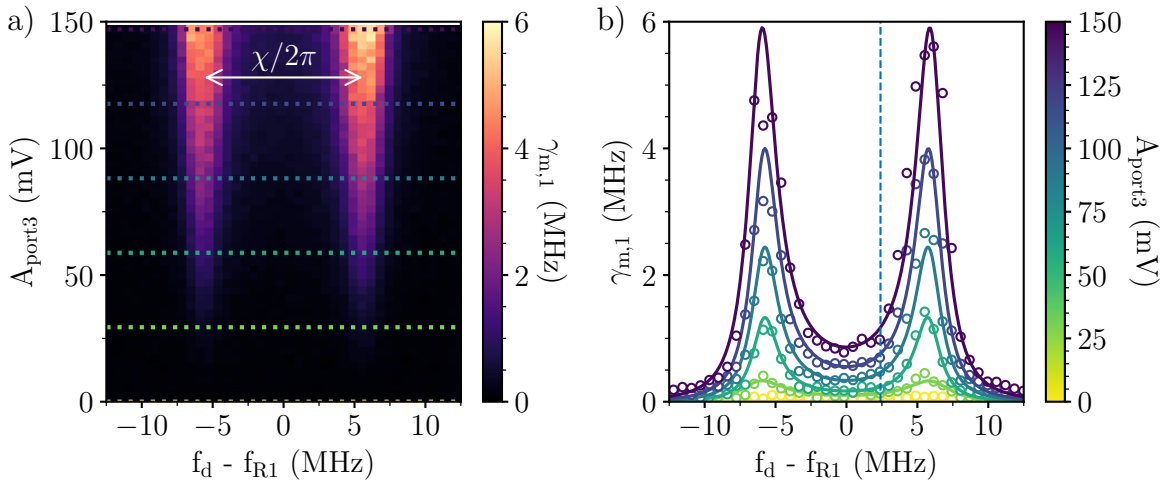

Figure 4.7.: **Power calibration via measurement-induced dephasing**, figure and caption taken from [157]. **a)** Additional dephasing $\gamma_{\text{m,1}}$ of Q1 due to resonator photons measured from Ramsey fringes for different drive frequencies f_d and drive amplitudes A_{port3} when driven through port 3. The features correspond to driving at $f_d = f_{R1} \pm \frac{\chi/2\pi}{2}$. The horizontal dotted lines indicate the cross sections which are shown in panel b. **b)** The plot shows the data points and individual fits for different drive amplitudes, yielding a set of possible transfer coefficients η_{ij} for different drive amplitudes. The vertical blue line at $f_d - f_{R,1} = 2.4\,\text{MHz}$ indicates where we extracted $\gamma_{\text{m,1}}$ for the data points (squares) in Fig. 4.9.

To identify the port-to-port isolation, we drive resonators 1 ($f_{R1} = 6.508\,\text{GHz}$) and 3 ($f_{R3} = 5.226\,\text{GHz}$) through the port of e3 and measure the resulting readout-induced dephasing $\gamma_{\text{m},i}$ of Q1 and Q3 as a

[v] The isolation experiments were performed at a coupler detuning of $\Delta f_{Q2} \approx -300\,\text{MHz}$. Only later did we calibrate an even weaker coupling between the resonant qubits at $\Delta f_{Q2} \approx -100\,\text{MHz}$ (see section 4.4).

function of drive power and frequency. This dephasing, arising from photon number fluctuations in the dispersively coupled resonator, is modeled by Ref. [165] as:

$$\gamma_{\mathrm{m},i} = \epsilon_i^2\, 2\pi \left(\underbrace{\frac{1}{\kappa_i^2/4+(2\pi f_\mathrm{d}-2\pi f_{\mathrm{R},i}+\chi_i/2)^2}}_{\text{photon number for qubit in } |0\rangle} + \underbrace{\frac{1}{\kappa_i^2/4+(2\pi f_\mathrm{d}-2\pi f_{\mathrm{R},i}-\chi_i/2)^2}}_{\text{photon number for qubit in } |1\rangle} \right) \frac{\kappa_i \chi_i^2/4}{\kappa_i^2/4+\chi_i^2/4+(2\pi f_\mathrm{d}-2\pi f_{\mathrm{R},i})^2}, \tag{4.6}$$

where $f_{\mathrm{R},i}$, κ_i and χ_i are the resonator's frequency, linewidth and dispersive shift. The two terms in parentheses represent the circulating photon number for the qubit in each of these states[vi]. The drive amplitude ϵ_i at resonator i relates to the input amplitude as $\epsilon_i^2 = \eta_{ij} A_{\mathrm{port},j}^2$, where η_{ij} is the power transfer coefficient. We define the port-to-resonator isolation as

$$d = 10 \log_{10}(\eta_{13}/\eta_{33}). \tag{4.7}$$

In Fig. 4.7a we plot for Q1 the dephasing rate $\gamma_{\mathrm{m},1}$ vs. drive power at port 3 (A_{port3}) and drive frequency f_d. Each $\gamma_{\mathrm{m},1} \approx 1/T_2$ value in the colormap is extracted from an individual Ramsey experiment. We observe two maxima of $\gamma_{\mathrm{m},1}$ in f_d which are spaced by $\chi/2\pi$ and correspond to the qubit in the $|0\rangle$ and $|1\rangle$ states. In panel b we shows $\gamma_{\mathrm{m},1}$ vs. f_d for selected drive amplitudes along with fits to Eq. 4.6. To determine the dephasing rate for Q3, analog measurements are performed (see App. A.7).

	Q1	Q3
η_{ij}	$(1.5\pm0.3)\cdot10^4$	$(3.5\pm0.3)\cdot10^{10}$
$f_{\mathrm{R},i}$	6508±0.1 MHz	5226±0.1 MHz
$\chi_i/2\pi$	11.8±0.2 MHz	11.3±0.3 MHz
$\kappa_i/2\pi$	2.3±0.3 MHz	5.6±0.6 MHz

Table 4.4.: **Average fit parameters for dephasing rates** when fitting Eq. 4.6 to measured dataset for each amplitude. The errors given are the errors of the mean.

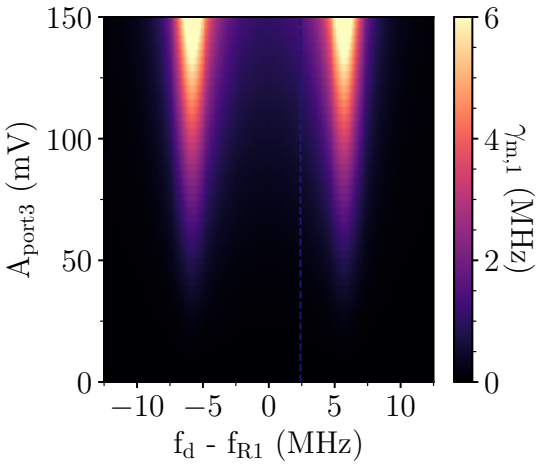

Figure 4.8.: **Calculated dephasing rate $\gamma_{\mathrm{m},1}$ for Q1** (figure and caption taken from [157]), using the average fit parameters from Tab. 4.4 and Eq. 4.6. The blue line at $f_\mathrm{d} - f_{\mathrm{R},1} = 2.4$ MHz indicates where we extract the calculated $\gamma_{\mathrm{m},1}$ values for Fig. 4.9.

[vi] A comparison of this approach for photon number calibration with the AC Stark shift method introduced in section 2.8, is provided in App. A.5.

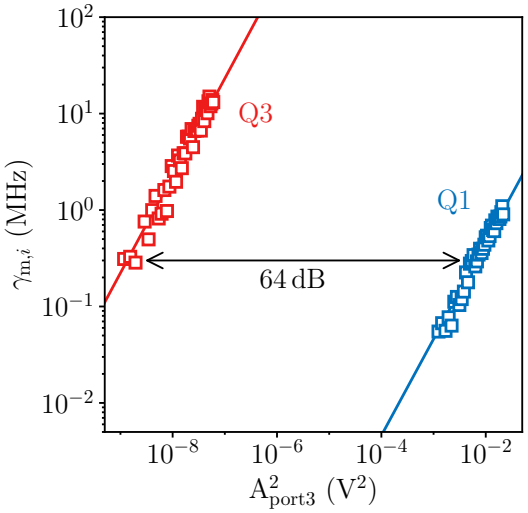

Figure 4.9.: **Isolation between enclosures**, figure and caption taken from [157]. Measurement-induced dephasing rate $\gamma_{m,i}$ of Q1 (blue) and Q3 (red) as a function of drive power at port 3. The squares correspond to the rates extracted from the fits to Eq. 4.6 at $f_d - f_{R,i} = 2.4\,\text{MHz}$. The lines are calculated using the average fit parameters listed in Tab. 4.4. Using Eq. 4.7 we extract an isolation between enclosures 1 and 3 of 64±0.5 dB. The black double-arrow serves as a guide to the eye.

For Q1 and Q3 we fit each trace using η_{ij}, $f_{R,i}$, χ_i, and κ_i as free parameters. The average fit parameters are listed in Tab. 4.4. Using these average fit parameters we calculate with Eq. 4.6 predictions for $\gamma_{m,i}$. This is shown for Q1 in Fig. 4.8. We extract the fitted dephasing rates $\gamma_{m,i}$ for $f_d - f_{R,i} = 2.4\,\text{MHz}$ (see the blue line in Fig. 4.8 for Q1 and the red line in App. A.7 for Q3) and plot them vs. the drive power A_{port3} in Fig. 4.9. The red and blue lines in Fig. 4.9 are calculated using Eq. 4.6 and the average fit parameters from Tab. 4.4. Using the spread of the fitted η_{ij} and Eq. 4.7, we extract an isolation of $d = 64\pm0.5\,\text{dB}$ from the comparison of Q1 and Q3.

Isolation between qubits

To evaluate control crosstalk, we drive through port 3 and measure power Rabi oscillations on both qubits using a $t_{pulse} = 640\,\text{ns}$ pulse. To calculate the Rabi frequency Ω_3 for Q3 we use:

$$\Omega_3 = \frac{0.5+n}{t_{pulse}}, \tag{4.8}$$

where $n \in \mathbb{N}_0$ is the number of full oscillation cycles observed in the Rabi oscillation curve (excluding the initial rise) for Q3 within the pulse duration t_{pulse}, as shown in the top panel in Fig. 4.10a. The calculation of the Rabi frequency Ω_1 for Q1 when driven through port 3 (Q1(P3)) is more challenging, as even at full generator power we observe less than 1 % of a full oscillation period (see Fig. 4.10a, bottom). To extract Ω_1, we normalize the Q1(P3) signal to the Q1(P1) reference, yielding the qubit inversion P_{inv} for Q1(P3). Using the Bloch sphere relation $P_{inv} = \sin^2\left(\frac{\theta}{2}\right)$ (see section 2.3) and the trigonometric identity $\sin^2(\theta) = (1-\cos(\theta))/2$ we obtain the Rabi frequency in Hz as:

$$\Omega_1 = \frac{\arccos(1-2P_{inv})}{2\pi t_{pulse}}. \tag{4.9}$$

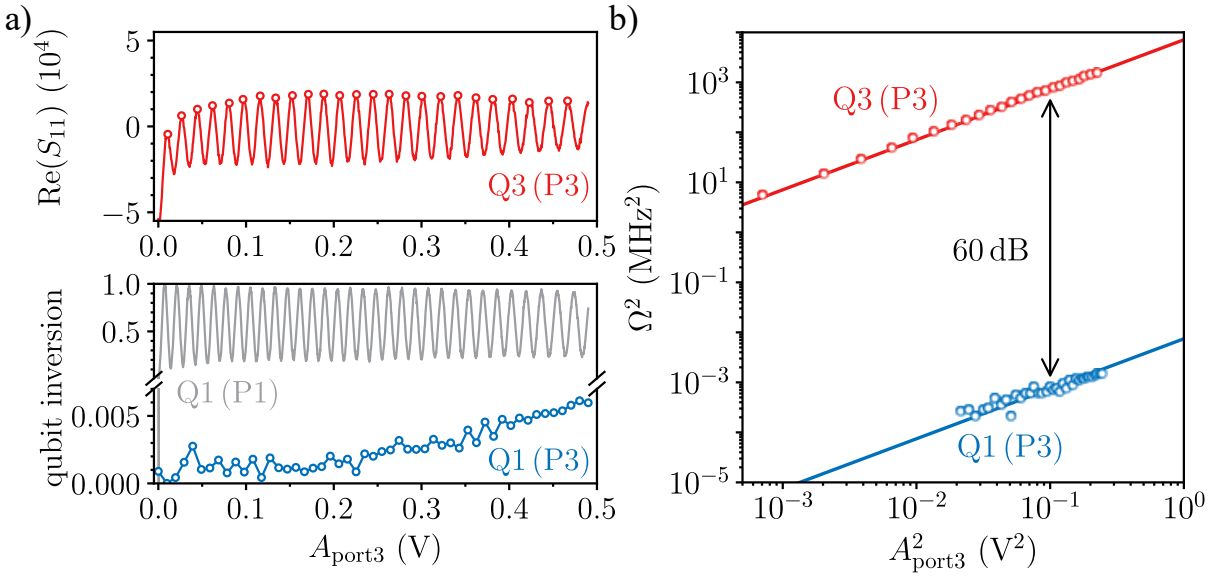

Figure 4.10.: **Port to qubit isolation**, figure and caption taken from [157]. **a)** Power Rabi oscillations of Q3 through port 3[vii] (P3, red) at the bp at the top and of Q1 through port 1 (P1, grey) or port 3 (P3, blue) at the bottom at the half flux point ($\Phi_{\mathrm{ext},1} = \Phi_0/2$) using a $t_{\mathrm{pulse}} = 640\,\mathrm{ns}$ pulse. Rabi frequency Ω_1 and Ω_3 are calculated for each circular marker. **b)** Rabi frequencies Ω_i of Q1 (blue) and Q3 (red) extracted from Rabi oscillations induced by driving at port 3. The lines are linear fits to the measured Rabi frequencies. The measured port-to-qubit isolation using Eq. 4.10 is 60 dB.

The Rabi frequencies Ω_i scale linearly with drive amplitude, as shown in Fig. 4.10b. From the ratio of slopes ($\Omega_1/A \approx 0.086\,\mathrm{MHz/V}$ and $\Omega_3/A \approx 84\,\mathrm{MHz/V}$), we extract the port-to-qubit crosstalk (or drive selectivity) [84, 58] as

$$10\log_{10}\left(\left(\frac{\Omega_1}{\Omega_3}\right)^2\right) \approx -60\ \mathrm{dB}, \tag{4.10}$$

enabling simultaneous on-resonance Rabi driving of Q1 and Q3 ($f_{\mathrm{Q1}} = f_{\mathrm{Q3}} = 3.465\,\mathrm{GHz}$) with a crosstalk error below 1‰.

To further highlight the isolation of our architecture, we perform simultaneous power Rabi oscillations on the resonant qubits Q1 and Q3, through their respective ports. No measurable crosstalk is observed, as evidenced by the orthogonal Rabi patterns in Fig. 4.11a.
We quantify the longitudinal (zz) interaction between Q1 and Q3 by measuring Ramsey fringes on Q1, with and without applying a π-pulse to Q3. We repeat this measurement 2000 times. The resulting frequency differences δf_{Q1} depending on the Q3 state are shown in Fig. 4.11b. The data follow a Gaussian distribution with mean of $\overline{\delta f_{\mathrm{Q1}}} = -690 \pm 60\,\mathrm{Hz}$.

[vii] The Rabi oscillations of Q3 are measured at the bp with $T_1 \approx 800\,\mathrm{ns}$ and $T_2 \approx 160\,\mathrm{ns}$[iv]. The Rabi drive pulse has a duration $t_{\mathrm{pulse}} = 640\,\mathrm{ns} > T_2$, which limits the visible contrast and prevents a full qubit inversion. Nevertheless, the number of Rabi cycles can be reliably extracted from Re(S_{11}).

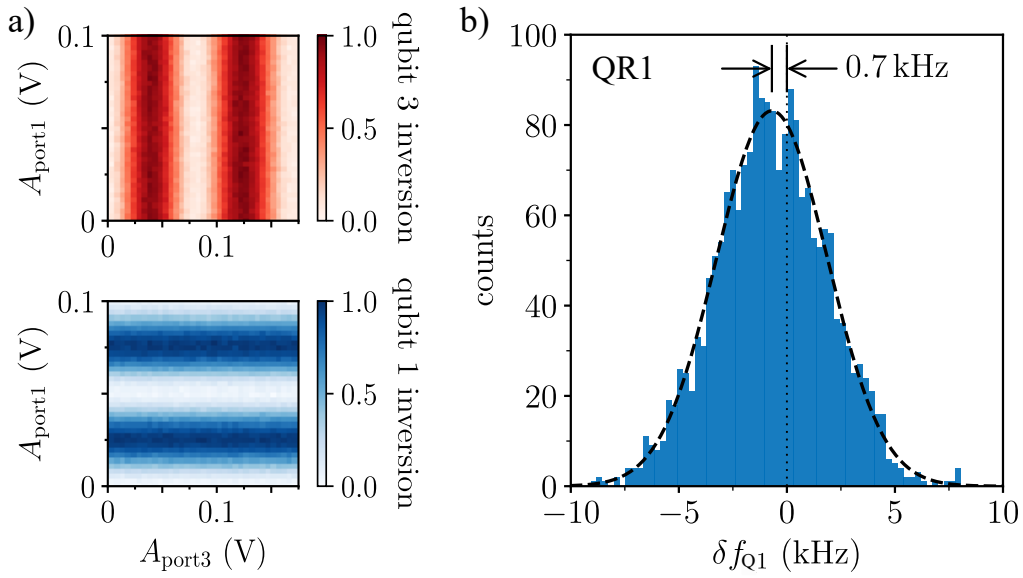

Figure 4.11.: **Simultaneous Rabi drive and zz-crosstalk**, figure and caption taken from [157]. **a)** Simultaneous Rabi drive of Q1 and Q3 on resonance taken in an earlier cooldown ($f_{\mathrm{Q1}} = f_{\mathrm{Q3}} = 3.689\,\mathrm{GHz}$) with the coupler switched off ($f_{\mathrm{Q2}} = 3.437\,\mathrm{GHz}$). The x- and y-axis depict the drive amplitudes at port 1 and port 3, respectively. The qubits can be manipulated independently while being on resonance. **b)** Measured zz-crosstalk between Q1 and Q3. We extract δf_{Q1} from the difference of Ramsey fringe frequency of Q1 when the Q3 population is inverted. From a Gaussian fit to the measured δf_{Q1} histogram we extract $\overline{\delta f_{\mathrm{Q1}}} = -690 \pm 60\,\mathrm{Hz}$.

Compared to conventional flip-chip architectures based on coplanar waveguides [58], our design achieves several orders of magnitude higher isolation. Relative to similar 3D-integrated floating chip architectures [84], the isolation is at least comparable and often an order of magnitude better. This demonstrates effective microwave shielding across enclosures, even with capacitive extenders present and qubits operated on resonance.

4.4. Coupling the qubits

The effective transverse coupling strength $g_{13}^{\mathrm{eff}}/2\pi$ between Q1 and Q3 can be tuned by varying the coupler detuning $\Delta f_{\mathrm{Q2}} = f_{\mathrm{Q2}} - f_{\mathrm{Q1}}$, which is controlled using the FBL. We extract $g_{13}^{\mathrm{eff}}/2\pi$ from avoided crossings between Q1 and Q3, which we measure using Ramsey interferometry or spectroscopy. Fig. 4.12 shows examples of avoided crossings measured at three different coupler detunings. At $\Delta f_{\mathrm{Q2}} = -127\,\mathrm{MHz}$, we extract a coupling of $g_{13}^{\mathrm{eff}}/2\pi = 23 \pm 23\,\mathrm{kHz}$ from Ramsey measurements, which could not be resolved more accurately due to the limited $T_2 \approx 1.9\,\mu\mathrm{s}$ of Q1. For $\Delta f_{\mathrm{Q2}} = 0\,\mathrm{MHz}$, spectroscopy yields $g_{13}^{\mathrm{eff}}/2\pi = 1.6 \pm 0.5\,\mathrm{MHz}$, while at $\Delta f_{\mathrm{Q2}} = 226\,\mathrm{MHz}$, Ramsey data gives $g_{13}^{\mathrm{eff}}/2\pi = 111 \pm 15\,\mathrm{kHz}$.

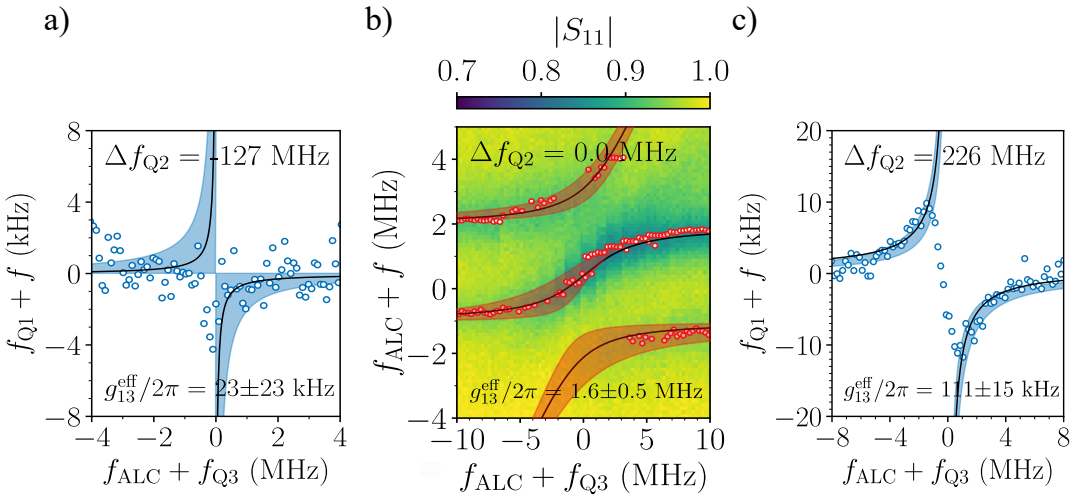

Figure 4.12.: **Avoided crossing between Q1 and Q3 for different coupler Q2 detuning, a)** $\Delta f_{Q2} = -127\,\mathrm{MHz}$, **b)** $\Delta f_{Q2} = 0\,\mathrm{MHz}$ and **c)** $\Delta f_{Q2} = 226\,\mathrm{MHz}$ measured by Ramsey fringes (blue) and spectroscopy (red) on Q1. The colormap in b) shows the amplitude of the reflected measurement signal on Q1, $|S_{11}|$. We fit the avoided crossings (black lines) and estimated fit errors, highlighted by the colored areas. During measurements Q1 is fixed at $f_{Q1} = 3.465\,\mathrm{GHz}$, while f_{Q3} is swept through this frequency. The horizontal axis is expressed as $f_{ALC}+f_{Q3}$, where f_{ALC} denotes the center frequency of the avoided level crossing.

Frequencies from Ramsey fringes are extracted by fitting a damped oscillation (see Eq. 2.29), and are shown as blue points in Fig. 4.12a,c. Spectroscopy data is analyzed by fitting Lorentzian line shapes to the I-quadrature signal to extract the center frequencies f_0, modeled as:

$$L(f) = \frac{a\,\gamma^2}{\gamma^2+(f-f_0)^2} + \text{offset}, \tag{4.11}$$

where γ is the half-width at half-maximum, and a the peak amplitude. The extracted spectroscopy points are shown in red in Fig. 4.12b.

To extract the coupling strength from the observed avoided crossings, we model the system using a two-level Hamiltonian:

$$\mathcal{H}_{2\mathrm{lv}}/h = \begin{pmatrix} f_{Q1} & g_{13}/2\pi \\ g_{13}/2\pi & f_{Q3} \end{pmatrix}, \tag{4.12}$$

which has eigenfrequencies

$$f_\pm = \frac{f_{Q1}+f_{Q3}}{2} \pm \sqrt{\left(\frac{f_{Q1}-f_{Q3}}{2}\right)^2 + (g_{13}/2\pi)^2}. \tag{4.13}$$

We fit these to the measured frequency splittings to extract $g_{13}/2\pi$ for each detuning. For detunings where the coupler is close to resonance with the qubits, the interaction becomes effectively three-body. In this regime, we use a three-level Hamiltonian:

$$\mathcal{H}_{3\mathrm{lv}}/h = \begin{pmatrix} f_{Q1} & g_{12}/2\pi & g_{13}/2\pi \\ g_{12}/2\pi & f_{Q2} & g_{23}/2\pi \\ g_{13}/2\pi & g_{23}/2\pi & f_{Q3} \end{pmatrix}, \tag{4.14}$$

which we diagonalize numerically. The extracted couplings $g_{ij}/2\pi$ are obtained by fitting the eigenvalues to the measured avoided crossings. Errors for the two- and three-level avoided crossings are estimated by adjusting $g_{13}/2\pi$ until the computed curves span the full range of observed data points near the crossings. The adjusted curves for error estimation correspond to the colored regions in Fig. 4.12.

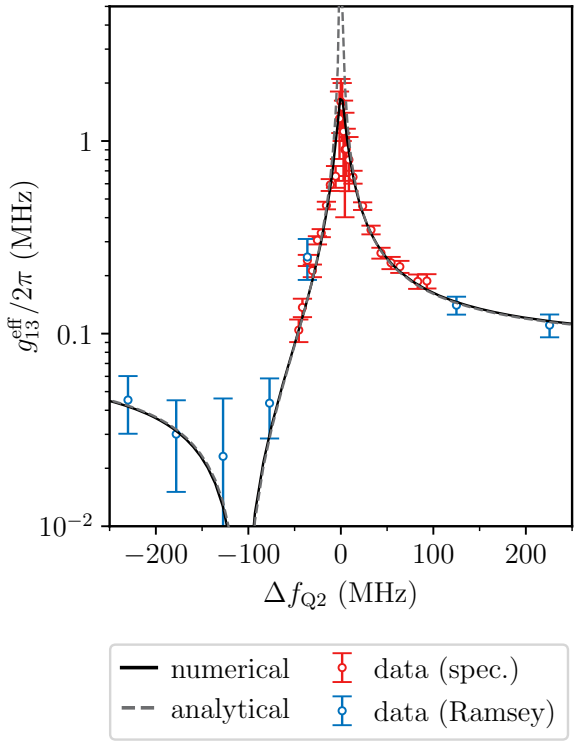

Figure 4.13.: **Effective qubit-qubit coupling strength $g_{13}^{\mathrm{eff}}/2\pi$ vs. coupler detuning Δf_{Q2}.** The data points show the measured coupling strength $g_{13}^{\mathrm{eff}}/2\pi$ between Q1 & Q3 that are operated on resonance ($f_{\mathrm{Q1}} = f_{\mathrm{Q3}} = 3.465\,\mathrm{GHz}$) for different coupler detunings Δf_{Q2} measured using spectroscopy (red) or Ramsey fringes (blue). The error-bars are estimated, see Fig. 4.12. The numerical (continuous) and analytical (dashed) theoretical curves correspond to an effective two-qubit model obtained using a Schrieffer-Wolff transformation[viii].

To quantitatively describe the dependence of the effective coupling g_{13}^{eff} on the coupler detuning, we employ the Schrieffer-Wolff transformation[viii] (SWT) [166, 167]. The SWT is a perturbative unitary transformation that block-diagonalizes the full three-qubit Hamiltonian, eliminating non-participating degrees of freedom. In our setting it reduces the Hilbert space of the three coupled qubits (Q1,Q2,Q3) to an effective two-qubit Hamiltonian where the coupler remains in its ground state,

$$\mathcal{H}_{\mathrm{eff}} = \frac{\omega_1}{2}\sigma_1^z + \frac{\omega_3}{2}\sigma_3^z + J_{xx}\,\sigma_1^x\sigma_3^x + J_{yy}\,\sigma_1^y\sigma_3^y + J_{zz}\,\sigma_1^z\sigma_3^z. \tag{4.15}$$

Here, J_{xx} and J_{yy} encode the transverse exchange, and J_{zz} is the residual longitudinal (zz) coupling. We evaluate g_{13}^{eff} using two complementary routes: a numerically exact SWT that retains the full circuit nonlinearity, and a second-order analytical SWT that provides a compact parametric dependence on the coupler detuning. Further information on both approaches is given in App. A.8.

The extracted $g_{13}^{\mathrm{eff}}/2\pi$ values are plotted in Fig. 4.13. The avoided crossings of each data point are shown in App. A.13. The solid (numerical) and dashed (analytical) lines in Fig. 4.13 represent fits of the SWT

[viii] This work was done in collaboration with the research group of Juan Jose Garcia-Ripoll (CSIC, Madrid). Gabriel Jauma and Manuel Pino performed the calculation for the SWT.

models to the measured effective coupling strength $g_{13}^{\text{eff}}/2\pi$. To fit the SWT we use two parameters: the effective qubit-coupler coupling capacitances $C_{12} = C_{23} \approx 44$ aF, and the direct qubit-qubit coupling $C_{13} \approx 1$ aF, which results from the combined effect of capacitive extenders and shunt paths to ground (see Fig. 4.1). The individual qubit and coupler parameters needed for the SWT are independently determined from fits to their respective flux-dependent spectra and listed in Tab. 4.2.

We identify two points of interest in Fig. 4.13. At $\Delta f_{\text{Q2}} = 0\,\text{MHz}$, the coupling reaches a maximum of $g_{13}^{\text{eff,max}}/2\pi \approx 1.6\,\text{MHz}$, while around $\Delta f_{\text{Q2}} \approx -100\,\text{MHz}$ destructive interference leads to a vanishing effective coupling, $g_{13}^{\text{eff}}/2\pi \approx 0\,\text{MHz}$. We achieve a measured on/off ratio of: $R_{\text{on/off}} = 1.6\,\text{MHz}/23\,\text{kHz} \approx 70$ in our architecture.

The observed dependence of g_{13}^{eff} on the coupler detuning is in qualitative agreement with our full-system simulations of two qubits and a coupler which are shown in App. A.9.

Population swapping

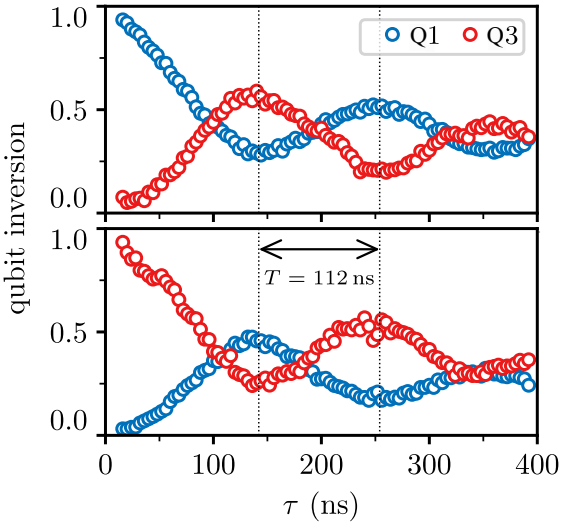

Figure 4.14.: **Qubit inversion between Q1 (blue circles) and Q3 (red circles) vs. pulse length** τ, figure and caption taken from [157]. We excite Q1 (top plot) / Q3 (bottom plot) with a π pulse and then use the FBL to tune the coupler with a rectangular flux pulse from the idle point to the bp. The qubit inversion is simultaneously measured for varying pulse lengths τ. We observe a population swapping in $T = 112\,\text{ns}$.

In a previous cooldown[iv] using the same setup, we characterized population transfer between Q1 and Q3. During that cooldown, we measured a maximal effective coupling of $g_{13}^{\text{eff,max}}/2\pi \approx 2.5\,\text{MHz}$ at the coupler bias point ($\Delta f_{\text{Q2}} = 0\,\text{MHz}$), see Ref. [157] and App. A.13.

To demonstrate coherent population exchange, we apply a rectangular flux pulse to tune the coupler from its idle point to the bias point. Both qubits are read out simultaneously following the pulse of length τ. Initializing either Q1 or Q3 in the excited state with a π-pulse leads to coherent oscillations in the qubit populations, as shown in Fig. 4.14. We extract a swap time of $T_{\text{swap}} \approx 112\,\text{ns}$, consistent with $g_{13}^{\text{eff}}/2\pi \approx 2.5\,\text{MHz} \approx \pi/T_{\text{swap}}$. We achieve a population transfer of approximately 59 % from Q1 to Q3

and of 47 % from Q3 to Q1.

To realize high-fidelity two-qubit gates in this architecture, coherence times must be improved. For example, Q3 has coherence times of $T_1 \approx 800\,\text{ns}$ and $T_2^* \approx 160\,\text{ns}$ at the bias point. Improving coherence at these operating points is therefore essential and remains the focus of ongoing research.

5. Conclusion and Outlook

Through the developments described in this thesis, modular and scalable hardware platforms for superconducting quantum processors have been demonstrated and validated. At the core of this work are two complementary advances: a dispersive readout scheme based on kinetic-inductive coupling and a modular flip-chip architecture for arrays of coupled qubits.

In Chapter 3, we demonstrated dispersive coupling between a harmonic readout mode and a GFQ consisting of a single JJ shunted by a grAl superinductor. By embedding the readout mode into the high kinetic inductance qubit-loop, we implemented an effective inductive coupling, where the loop asymmetry acts as a shared inductance. In this work we derived a full circuit model of the system and confirmed its validity by comparing the predicted spectra and dispersive shifts to measurements of nine devices. The effectiveness of the coupling mechanism for dispersive readout was demonstrated through quantum non-demolition measurements, which yielded more than 90 % active state preparation fidelity and less than 0.1 % leakage outside the computational subspace. The presented design enables a local qubit-resonator interaction without using any large on-chip capacitors, making it a compact and robust approach. It is therefore well suited for scaling superconducting quantum devices.

In Chapter 4, we demonstrated a linear array of three coupled GFQs. Each qubit was hosted on a dedicated chip inside an individual microwave enclosure. The „one qubit one enclosure“ design suppresses microwave crosstalk between the outermost qubits below $-60\,\mathrm{dB}$. This level of isolation enables their operation on resonance. The center qubit acts as a flux-tunable coupler, such that the architecture simultaneously provides strong isolation and tunable coupling. In addition, the system is fully modular and allows for the replacement of individual circuit parts without disturbing the remaining setup. These features distinguish our approach from planar coplanar waveguide architectures, where qubits are limited by spurious chip modes and residual capacitive coupling, and they demonstrate the combination of modularity and tunable coupling in a single scalable platform.

The inductively coupled QR-system was designed to operate within the modular flip-chip architecture. The kinetic-inductance-based GFQ enables dispersive readout, while the modular design provides strong isolation and tunable coupling. In combination, these elements form a hardware concept that enables modular and scalable superconducting quantum processors.

Outlook

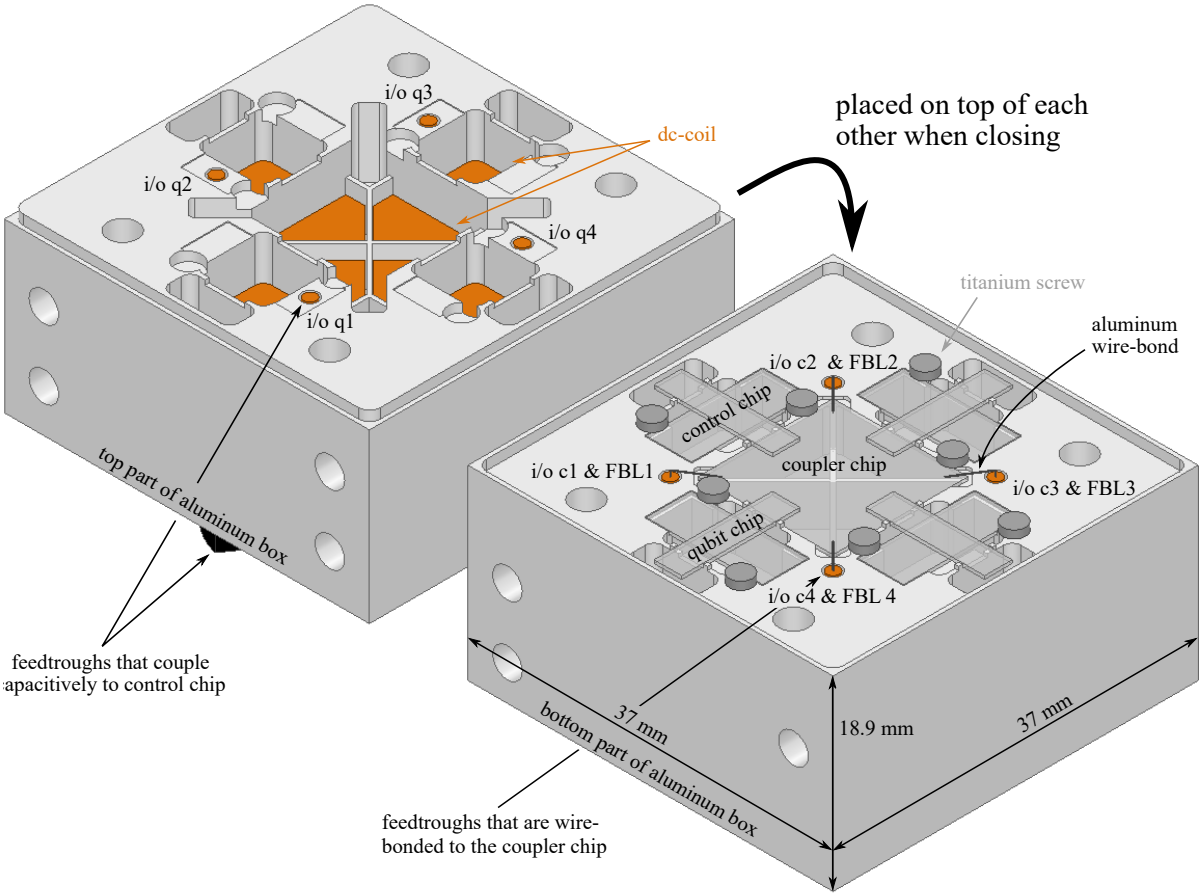

Figure 5.1.: **Concept for a scalable two-dimensional grid in a modular architecture,** adapted from [157]. The aluminum box hosts individual enclosures for four qubits on the sides and a single center enclosure containing the coupling elements. Each qubit enclosure contains one control and one qubit chip, is accessed via a feedthrough through the lid that couples capacitively to the control chip (i.e. the pad for bonding in Fig. 4.1.e), and has an individual dc-coil. The dc-coils are attached on the inside of the lid and their bottom plates must be in direct electrical contact with the enclosure walls. The middle enclosure holds the coupler chip that is wire-bonded to four feed-throughs embedded in the bottom part of the box. The coupler enclosure is divided into 4 subsections to increase the cavity's eigenfrequency.

Building on these results, the next steps focus on improving coherence and finding innovative two-qubit gates, while exploring extensions of the architecture towards larger processor modules. In the following, we summarize the ongoing efforts and near-term extensions of this work.

A priority is the improvement of qubit coherence times T_1 and T_2. We explored the replacement of grAl superinductances with arrays of JJs. However, as discussed in section 3.4, this approach introduced additional decoherence channels which need to be identified and suppressed. Another possibility is the use of transmon qubits, which do not require a superinductor and are therefore not limited by the inductive losses of grAl.

After demonstrating strong isolation and static tunable coupling, the next step is the implementation of two-qubit gates within this architecture using on-resonant qubits. Such gates can be realized by dynamic modulation of the coupler via the FBL. In this scheme, the data qubits remain fixed in frequency and require no FBL, while only the coupler chip is driven dynamically. Demonstrating such gates, however, remains challenging with the present coherence times and is therefore the subject of ongoing work.

The next step towards scalability is the extension of the three-qubit linear array to a four-qubit prototype arranged in a two-dimensional grid, as shown in Fig. 5.1. Access to the enclosures is provided by out-of-plane feedthroughs, which couple capacitively to the control chips and are wire-bonded to the coupler chip in the central enclosure. The coupler enclosure should be subdivided to suppress cavity modes to preserve the strong isolation observed in the linear array. An all-to-all reconfigurable router, similar to Ref. [168], could serve as the coupling element. Such a four-qubit module represents a first step towards scalable two-dimensional lattices. A systematic characterization of isolation, crosstalk, and gate fidelities in this geometry will provide a key benchmark on the path towards larger modular processors.

In summary, the developed modular flip-chip architecture with kinetic-inductance-based readout provides a scalable platform with strong qubit isolation, and its extension towards larger grids defines a clear path for the realization of multi-qubit superconducting processors.

6. Methods

6.1. Fabrication of QR-systems

The fabrication process described in this section is an improved and more reproducible version of the „old“ process described in Ref. [136], incorporating additional pre-cleaning steps (Piranha cleaning, isopropanol and ultrasonic bath), temperature control during spin-coating, and an oxygen plasma cleaning step.

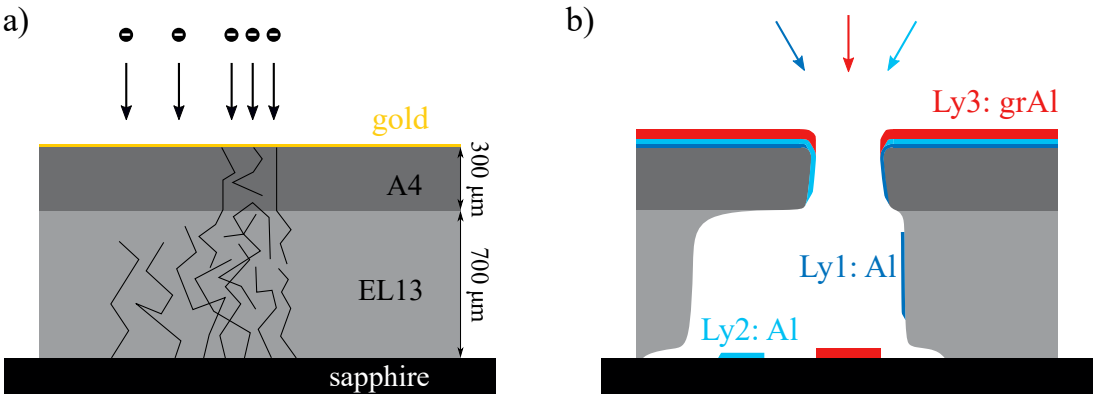

Figure 6.1.: **Fabrication with electron-beam and three angle evaporation process. a)** We use electron-beam lithography to write structures into our bi-layer (1. MMA(8.5)MAA EL13: 700 nm; 2. 950 PMMA A4: 300 nm) resist stack. A 5 nm gold layer is sputtered on top of the resist stack to mitigate charging effects arising from the insulating nature of the resist layers. Different sensitivity of the resists allows the formation of undercuts, as shown in panel b. **b)** After development of the resist stack for 90 s in a cold IPA:H_2O (3:1) solution maintained at 6°C, shadow evaporation is performed in three steps. The first two aluminum layers are deposited under a tilt angle of $\alpha \approx \pm 30°$, with an intermediate controlled oxidation to form the tunnel barrier. Subsequently, the granular aluminum (grAl) layer is deposited at 0 ° to complete the structure. In a subsequent lift-off process, the resist stack and all metal deposited on top of it are removed, leaving only the patterned structures in direct contact with the substrate.

The devices are fabricated on a double-side polished c-plane 2 inch sapphire wafer with a thickness of 330 µm. We choose sapphire wafers for their low microwave dielectric losses, high crystalline quality, and chemical stability [169]. The wafers are pre-cleaned using a Piranha solution (3:1 mixture of 96 % H_2SO_4 and 35 % H_2O_2) for 10 minutes. This aggressive oxidizer effectively removes organic residues, as well as metallic and carbon contaminants [170]. For additional pre-cleaning, we place the wafers for 5 min in an isopropanol bath at 60 °C, followed by 5 min in an ultrasonic cleaner operated at maximum

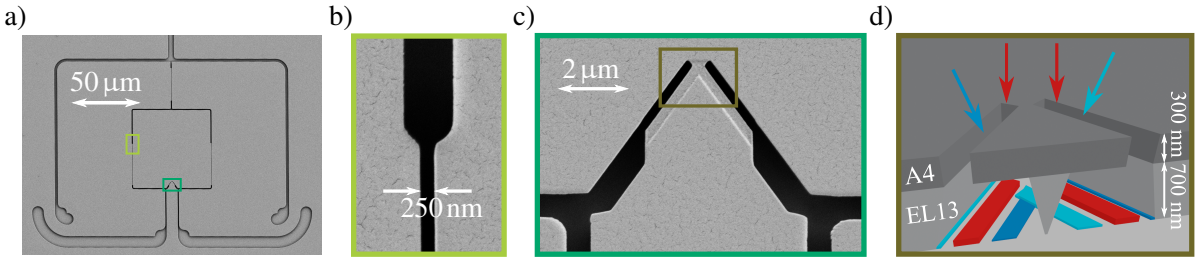

Figure 6.2.: **Fabrication using a three-angle evaporation process**, figure and caption taken from [136]. **a)** Scanning electron microscope image of the device during fabrication after e-beam patterning and development of the two-layer resist stack. The surface is covered by a gold film for imaging. **b)** Zoom-in on the pattern defining the connection of the thin grAl inductor to the Al-shunted islands. **c)** Zoom-in on the cross-junction pattern used to fabricate the JJ. In the brown-highlighted area, an undercut is used to separate the Al depositions from the zero-angle grAl deposition. **d)** Sketch of the Dolan-bridge and the depositions of the three different layers of Al (blue) and grAl (red). The undercut in the EL-13 (700 nm) + PMMA-A4 (300 nm) resist stack allows to create the entire device in a single three-angle evaporation step with subsequent evaporation angles $-\alpha, 0°, \alpha$, where $\alpha \in [26°, 32°]$, depending on the sample.

power. We then blow dry the wafers and place them on a 200 °C hotplate for 5 min to ensure complete evaporation of any isopropanol residues.

A bilayer resist stack consisting of MMA(8.5)MAA EL13 (700 nm) and 950 PMMA A4 (300 nm) is spin-coated onto the wafer. To ensure consistent resist viscosity during spin-coating, we store small quantities of resist for daily use at room-temperature. Each layer is spin-coated using the following recipe: a 2 s acceleration ramp at 1000 rot/s^2 to 2000 rot/s, followed by 100 s at constant speed, and a 2 s deceleration ramp with 1000 rot/s^2. After spin-coating, the wafer is baked for 5 min at 200°C on a hotplate. To ensure thermal equilibration before applying the resist layers, the wafers are placed for 30 s on a $10 \times 10 \times 5$ cm^3 stainless steel block. Prior to electron-beam lithography, an approximately 5 nm thick gold layer is sputtered onto the resist surface to suppress charging during exposure, as shown in Fig. 6.1a.

Electron-beam lithography is performed using a 50 keV system to define the mask pattern. At this relatively low acceleration voltage, forward scattering of electrons in the resist leads to a lateral broadening of the exposed region near the substrate. In addition, backscattered electrons generate a second undercut in the lower resist layer after development. Following exposure, the gold layer is removed by immersion in a 15 % Lugol-iodine solution and then rinsed in deionized water to remove Lugol residues. The resist is developed for 90 s in a cold IPA:H_2O (3:1) solution maintained at 6°C, stop-bathed in deionized water, and blow-dried using a nitrogen gun. Representative images of the resulting mask structures are shown in Fig. 6.2.

To remove any resist residues from the developed structures, the wafer is placed in an oxygen plasma cleaner. We use an oxygen flow of 20 % of 50 sccm at 50 % of the generator's maximum power (type: RFG 13.56 MHz / 300 W Generator). The plasma is applied for 1 min and 36 s. Using white-light

interferometry [171], we estimate an etch rate of 10 nm/min and 9 nm/min for the resists EL13 and A4, respectively. While the oxygen plasma cleaner removes organic residues through uniform chemical etching in an oxygen plasma, cleaning with a Kaufman ion source as it is used in our shadow evaporator relies on the directed bombardment of ions, resulting in a more aggressive cleaning process that combines physical sputtering and chemical activation [172].
The JJs are built using a Niemeyer-Dolan bridge [173] structure, visible in Fig. 6.2c.d, with an asymmetric undercut for the Al feedlines [174]. The full three-angle evaporation process is carried out in a commercial Plassys MEB 550S^{TM} system. A schematic of the evaporation steps is shown in Fig. 6.1b. After evaporation, liftoff is performed by immersing the wafer in a 60°C acetone bath for one hour. During this time, the bath is stirred briefly (2 minutes) every 20 minutes to promote removal of the resist. Following the acetone bath, the wafer is transferred to an ethanol bath and placed in an ultrasonic cleaner at the lowest power setting for 1 minute. Finally, the wafer is blow-dried using a nitrogen gun.
A comparison of the relaxation times obtained with the fabrication process detailed in Ref. [136] and with the process described here is shown in App. A.3. All qubits measured after 1 January 2025 were fabricated using the new process. No significant improvement of T_1 or T_2^* is observed.

Evaporation Procedure

Our shadow evaporator (Plassys MEB 550S^{TM}) has two chambers: a load-lock chamber used for sample loading and oxidation, and an ultra-high vacuum (UHV) main chamber for deposition. The detailed evaporation sequence is as follows:

- Pump the load-lock chamber for at least 2 hours until the base pressure is below 5×10^{-7} mbar.
- If the plasma cleaner is used, this step is omitted: Plasma clean the substrate at 0° angle using a Kaufman ion source (200 V beam voltage, 10 mA, 10 sccm O_2, 5 sccm Ar).
- Deposition of a thin titanium layer at 0° angle with the shutter closed (10 s at 0.2 nm/s) serves as a titanium gettering step to suppress outgassing and reduce contamination from the evaporator during the initial stage of the main deposition [175].
- Evaporate aluminum at $-\alpha$ (first angle) with open shutter using crucible 1 (22 nm at 1 nm/s).
- Oxidize the junction statically in pure O_2 at pressure p_{O_2} and for a time t_{O_2}. The pressure is increased linearly at a rate of 2.5 mbar/s until p_{O_2} is reached. After oxidation, depending on p_{O_2} an additional 10 s to 30 s are required to evacuate the O_2 from the load-lock chamber. This rise and pump time is not included in t_{O_2}.
- Evaporate aluminum at $+\alpha$ (second angle) using crucible 1 (33 nm at 1 nm/s).
- Perform a argon milling step at 0° (400 V beam voltage, 15 mA, 4 sccm Ar, no O_2).

- Regulate the aluminum evaporation rate at 0° to 2 nm/s using crucible 2.
- Introduce O_2 flow at 9.4 sccm and start planetary rotation at 5 rpm.
- Evaporate for approximately 40 s (corresponding to 80 nm of grAl) with open shutter.
- Terminate the process by closing the shutter, stopping oxygen flow, halting planetary rotation, and ramping down the deposition rate.

Tables of measured room-temperature resistances of the JJs and the grAl inductors can be found in App. A.6.

Static discharges

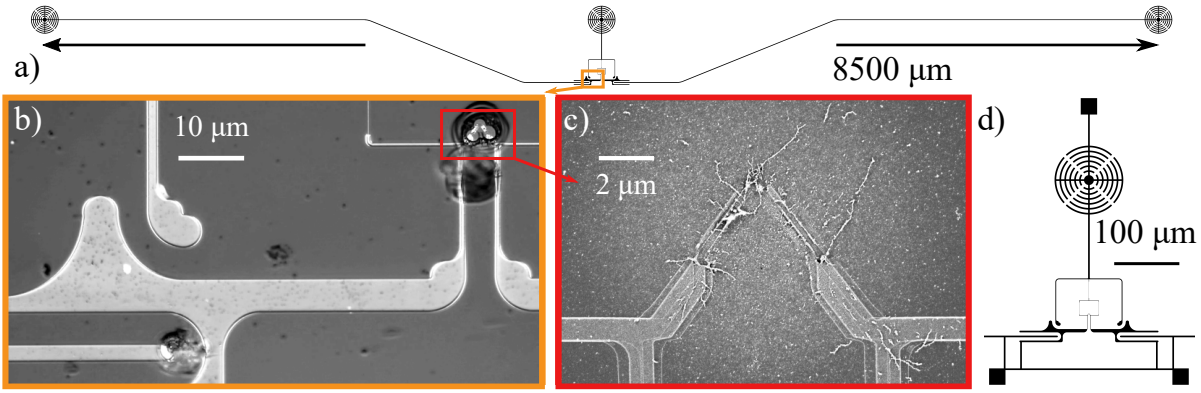

Figure 6.3.: **Static discharges**, figure and caption adapted from [157]. **a)** The layout of the qubit chip shows the capacitive extenders reaching close to the edges of the sapphire chip with dimensions of approx. 9 mm. The QR system in the middle of the chip couples capacitively to the extenders via the Josephson junction electrodes. **b)** The inset shows an optical image of the center part of the chip after the final dicing process of the 2" sapphire wafer into 2.85×10 mm^2 qubit chips. Residues from discharge events are visible in the protective resist (Microposit S1818) used during dicing, both at the position of the JJ and the coupling capacitor. **c)** A scanning-electron micrograph of an exploded junction reveals that the explosion happened exactly at the junction position, leaving intact the bigger capacitive pads, but destroying the junction and its connecting films. **d)** Layout of a GFQ with capacitive extenders shunted to the junction electrodes via a bridges. Three test pads are added for room-temperature probing. The bridges must be removed before mounting the sample.

The capacitive extenders that we added to the GFQs have a length of approx. 4 mm (Fig. 6.3a). They introduce additional fabrication challenges by increasing the risk of electric discharge during resist spinning and dicing. As shown in Fig. 6.3bc, electrostatic discharges can arc across the gap between the capacitive extenders and the junction electrodes, resulting in an explosion of the JJ. To prevent this, we shunt the junctions with a Al film during fabrication as shown in Fig. 6.3d. The Al shunts should be removed only directly before mounting the sample in the box, as electrostatic discharges can, for example, already occur from walking through the building. Removal can be done either mechanically by

scratching through the shunts at a probe station using a needle, or via optical lithography and wet etching. In the case of wet etching, the sample is first spin-coated with S1805 resist from Shipley. The resist is then exposed to UV light for 4 s at 13 mW/cm^2 through a mask that defines the etch pattern. Finally, the sample is developed in MF319, which removes the Al in the exposed regions after approx. 10 min.

Device evolution

The GFQ architecture has undergone several generations of design refinements. The first and newest generations are shown in Fig. 6.4 and Fig. 6.5. Each iteration improved layout symmetry, enhanced fabrication robustness, and added compatibility with extensions such as capacitive extenders and the optional replacement of grAl with JJ arrays.

Junction array from Dolan bridges

Two different JJs form in each Dolan bridge unit cell due to the double-angle evaporation process. One JJ with length l_{j1}, forms underneath the bridge and the other JJ of length l_{j2} forms between two adjacent bridges, as shown in Fig. 6.6. Due to the shadow geometry, these JJs generally differ in size. To achieve identical JJs ($l_{j1} = l_{j2}$), the bridge and gap geometry must be adjusted.

The outer JJ length is determined by the overlap of shadows from both edges of a single bridge:

$$l_{j1} = 2\tan(\alpha)h_{r1} - l_{bridge}. \tag{6.1}$$

The inner JJ length is set by the shadowing across the resist gap between two bridges:

$$l_{j2} = l_{gap} - \tan(\alpha)(h_{r2} + h_{ly1}). \tag{6.2}$$

Setting $l_{j1} = l_{j2}$ yields the condition:

$$l_{gap} = 2\tan(\alpha)h_{r1} - l_{bridge} - \tan(\alpha)(h_{r2} + h_{ly1}). \tag{6.3}$$

This expression defines the required bridge spacing to obtain equal junctions for a given resist stack and evaporation angle.

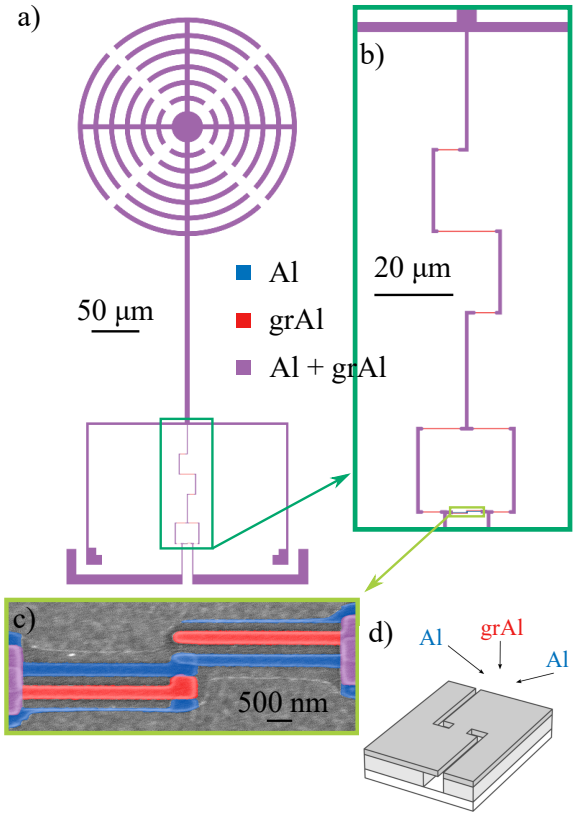

Figure 6.4.: **First-generation GFQ device. a)** Layout of the first-generation GFQ. All grAl segments are oriented perpendicular to the vertical symmetry axis of the device due to the JJ design, necessitating a meandered geometry for the readout inductance. During shadow evaporation the device is tilted along the axis perpendicular to the vertical symmetry axis. Al is shown in blue, pure grAl in red, and grAl shunted by Al in purple. **b)** Zoom-in on the grAl segments. **c)** SEM micrograph of the device JJ. In this design, slight angular misalignment during evaporation can alter the JJ size. **d)** Schematic of the resist stack for JJ fabrication (taken from [69]), combining a Niemeyer-Dolan bridge [173] at the center with an asymmetric undercut for the Al feedlines [174].

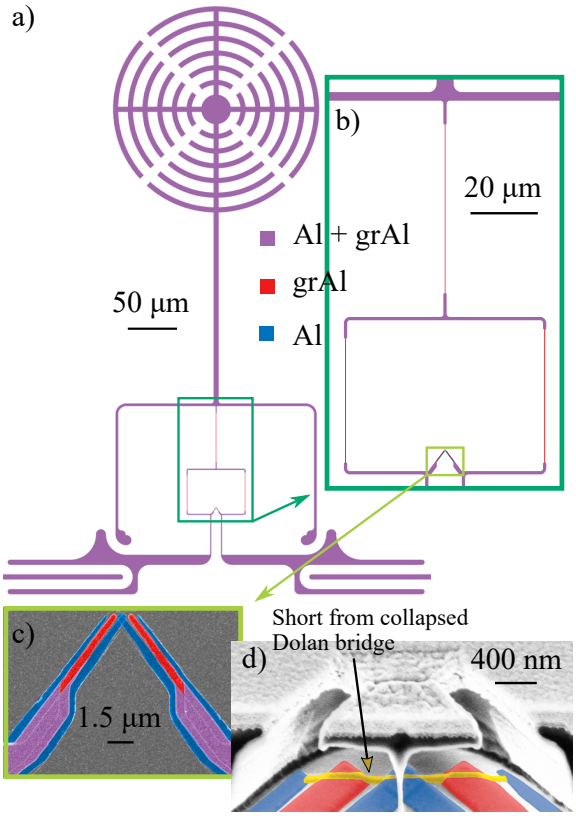

Figure 6.5.: **Current generation of GFQ devices. a)** Layout of the current GFQ design. Compared to the previous generation, all grAl segments are rotated by 90 °, allowing a more symmetric arrangement of circuit elements. As a result, the evaporation tilt axis is rotated by 90 ° compared to the previous designs. **b)** Zoom-in on the grAl segments. All corners are removed to suppress electric field localization. The new JJ design permits alignment of all grAl inductors along the vertical symmetry axis. **c)** SEM micrograph of the fabricated JJ. This design is less sensitive to slight angular misalignments during shadow evaporation, as the JJ size remains largely unaffected. **d)** SEM image of the resist stack and evaporated layers before liftoff, cut open with a focused ion beam (FIB). The image shows a faulty JJ where the Niemeyer-Dolan bridge [173] collapsed, forming a short (highlighted in yellow).

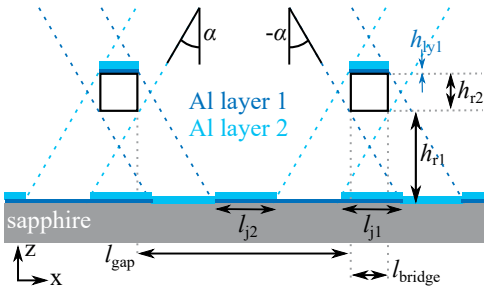

Figure 6.6.: **Schematic cross-section of a Dolan bridge JJ array.** The JJs have lengths l_{j1} and l_{j2}, with bridge widths l_{bridge} and gaps between bridges l_{gap} defined in x-direction. In z-direction, the height of the lower resist is h_{r1}, the height of the top resist (defining the Dolan bridge) is h_{r2}, and the thickness of the first evaporated Al layer is h_{ly1}. The first Al layer (dark blue) is evaporated under an angle of $-\alpha$, while the second aluminum layer (light blue) is evaporated under an angle of $+\alpha$. Due to the shadowing geometry, two different junction lengths l_{j1} and l_{j2} are formed. These can be made equal by appropriate choice of l_{gap} and l_{bridge} for a fixed resist stack and evaporation angle $\pm\alpha$.

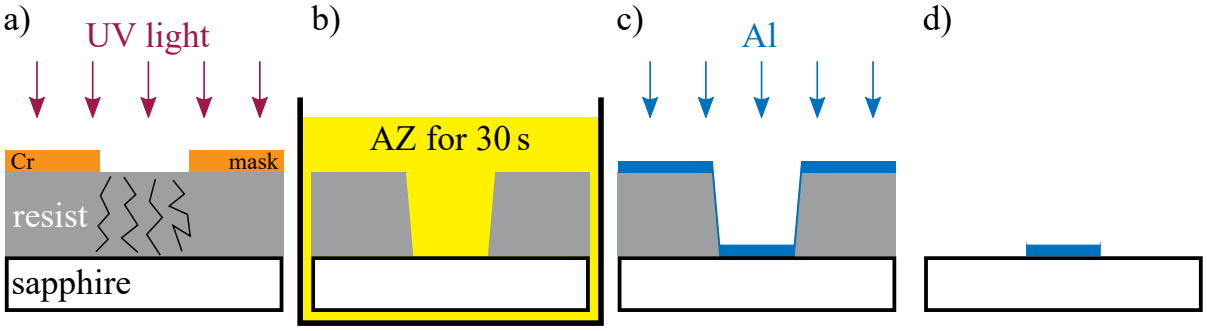

Figure 6.7.: **Fabrication with positive resist.** **a)** UV exposure in the mask aligner (500 W XeHg lamp, λ = 365 nm, hard contact with 13 mW/cm^2 for 4 s) through a Cr mask on a spin-coated S1805 resist layer (thickness approx. 500 nm). **b)** Development for 30 s in AZ developer (or MF319, which etches Al) removes the exposed resist, resulting in an overcut profile. **c)** Aluminum is deposited uniformly over the patterned resist. **d)** Liftoff for 1 h in acetone removes the resist and excess metal, leaving behind the defined Al features.

6.2. Fabrication of control chips

The control chips are fabricated using optical lithography in a SUSS MA6 mask aligner with a 500 W XeHg lamp (λ = 365 nm). We use the positive photoresist (exposed areas are dissolved by the developer) S1805 (DuPont™). The resist is spin-coated at room-temperature at 4500 rpm for 60 s, resulting in an approx. 500 nm thick layer. The wafer is baked at 115 °C for 60 s. UV exposure is performed in hard contact mode (13 mW/cm^2) for 4 s through a Cr mask. As shown in Fig. 6.7, exposed regions are developed in AZ developer or MF319 (which etches Al) for 30 s, stop-bathed in deionized water, and dried with a nitrogen gun. The developed resist exhibits an overcut profile due to UV absorption in the resist, which causes different dissolution rates at the top and bottom. After development, Al is evaporated at 0 ° angle. Liftoff was performed in acetone at 60 °C for 60 min, with brief stirring (2 min) every 20 min.

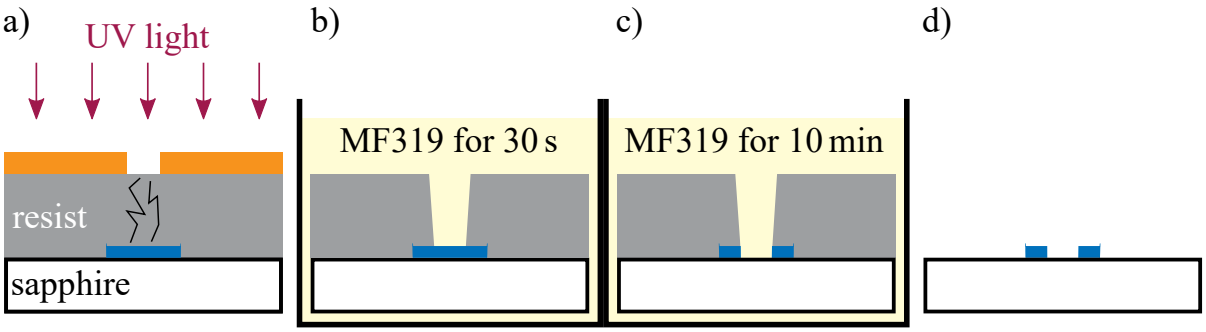

Figure 6.8.: **Wet etching of Al using MF319. a)** UV exposure through a Cr mask on a spin-coated S1805 resist layer (thickness approx. 500 nm), using the same mask aligner settings as in Fig. 6.7. **b)** Development for 30 s in MF319 removes the exposed resist. **c)** Prolonged exposure (10 min) to MF319 selectively etches away the exposed Al. **d)** Resist stripping is done for 5 min in 60 °C acetone, revealing selectively etched Al structures.

6.3. Wet etching with MF319

We use wet etching to selectively remove the Al shunts that are required during fabrication of the GFQs with capacitive extenders (see Fig. 6.3). Compared to mechanical removal at a probe station using needles, wet etching provides cleaner results, but requires significantly more effort. The initial steps follow the same procedure as in section 6.2: the wafer is spin-coated with S1805 resist, baked at 115 °C for 60 s, and exposed to UV light (13 mW/cm^2 for 4 s) through a Cr mask that defines the etch pattern. After development in MF319 for 30 s, the sample is immersed in MF319 for an additional 10 min to etch away the exposed Al. Finally, the resist is stripped in 60 °C acetone for 5 min. A schematic of the full process is shown in Fig. 6.8.

6.4. Measurement setup

The room-temperature and cryogenic setup is shown in Fig. 6.9. Qubit control and readout are performed using the commercial OPX+ and Octave platform by Quantum Machines [176]. The system provides synchronized RF signal generation and digitization via IQ mixing. The OPX+ generates low frequency I/Q waveforms, which are upconverted to RF in the Octave using IQ mixers driven by local oscillators. Q1, Q3, and R1 use the internal LO. To enable simultaneous readout of R1 and R3, we use a second, external LO [182], since the readout frequencies (f_{R1} = 6.508 GHz and f_{R3} = 5.226 GHz) cannot be accommodated within the Octave's ±350 MHz IF bandwidth using a single LO. The separate Octave channels of R1 and Q1, as well as R3 and Q3, are combined using power combiners before entering the fridge.

For single-tone and two-tone spectroscopy measurements, we do not use the time-domain setup but instead operate in continuous-wave mode using a vector network analyzer (VNA) [177] and RF signal generator [182], as shown for the middle coupler qubit. This approach is as of now sufficient for our three-qubit experiment, as we are only interested in extracting the coupling strength and isolation as a

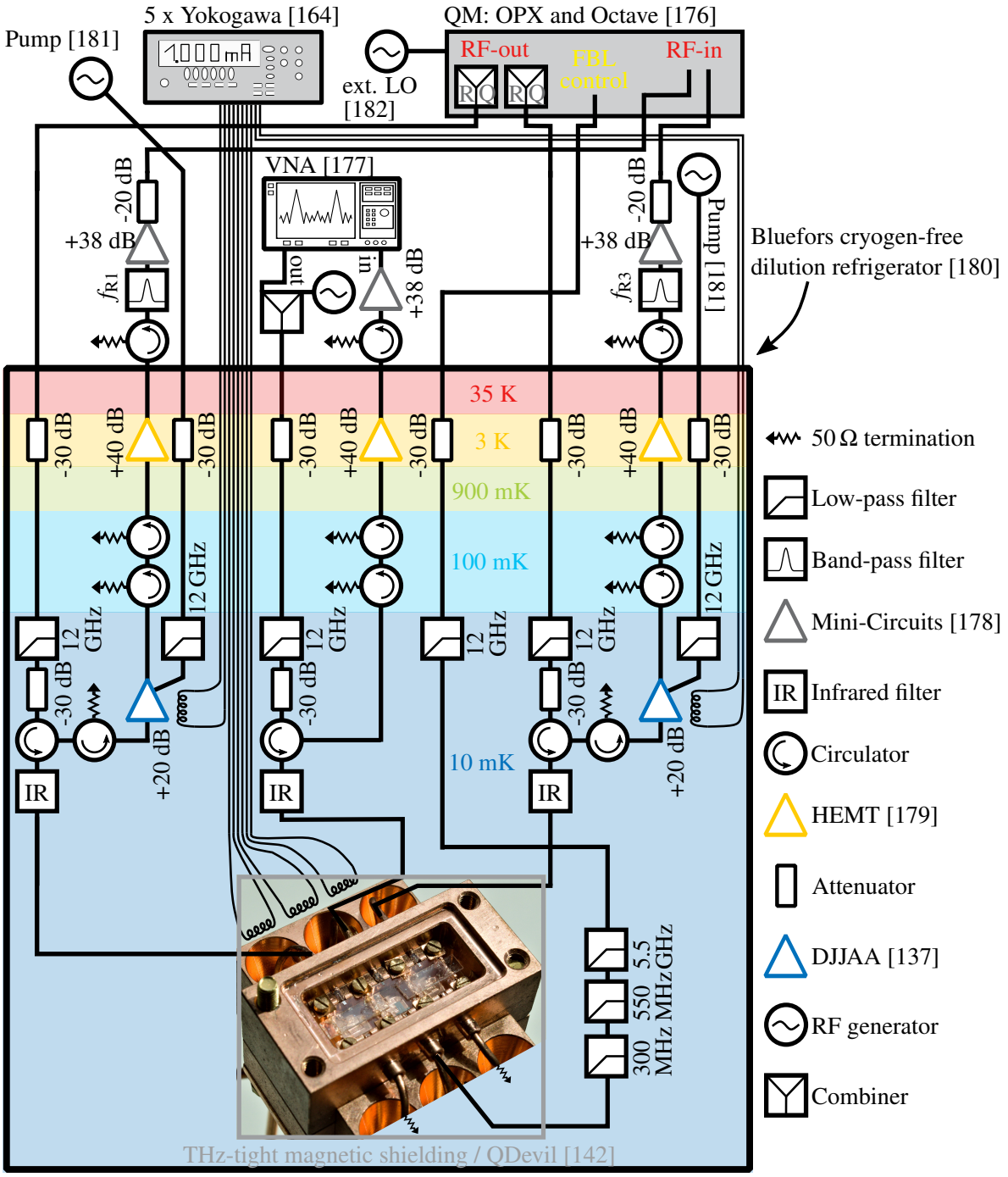

Figure 6.9.: **Cryogenic and room-temperature measurement setup.** RF setup used to control and read out our three-qubit architecture in a dilution refrigerator with a base temperature of 10 mK. The diagram shows the equipment used for measurement, temperature stages, DC lines and the attenuation/gain of individual components. The RF generator is required to pump the DJJAAs [137].

function of coupler detuning. Determining the coupler's quantum state is not required at this stage. This may change when implementing two-qubit gates involving the coupler.

We use coaxial cables with $Z_0 = 50\,\Omega$ for all RF lines in the cryostat to prevent reflections of the high-frequency signal. The input lines are constructed with identical components up to the qubits. Attenuators and low-pass filters are installed at different temperature stages to reduce the influence of thermal noise sources on the readout signal. Attenuators thermalize the center conductor, suppress noise from warmer stages and damp reflections from impedance mismatches [35]. Low-pass filters are used to suppress high-frequency and infrared radiation that can generate quasiparticles [35].

The signal reflected from the sample is directed by a circulator into the output line. The configuration differs between the outer qubit lines and the middle line used for the coupler qubit. For the outer qubits, the next element after the circulator is an isolator, which prevents the DJJAA pump from leaking into the qubit and suppresses reflected signals. This is followed by a DJJAA [121], operated as a quantum-limited parametric amplifier. When pumped, the DJJAA amplifies the signal, and when unpumped, it acts as a near-perfect reflector. On the middle line of the coupler qubit, there are no further elements on the 10 mK stage. At the 100 mK stage, all lines have isolators to suppress reflections, thermal noise, and back-propagating power from the HEMT amplifier at 3 K. Outside of the cryostat, additional isolators eliminate reflections from the room-temperature amplifiers and the band-pass filters. The filters, tuned to f_{R1} and f_{R3}, suppress the DJJAA pump tones and prevent saturation of the Mini-Circuits amplifiers. Since the noise of the first amplifier stage dominates the total system noise [133], quantum-limited amplification by the DJJAAs is essential for high-fidelity readout.

The signal requires approximately 240 ns to travel from the OPX+ to the sample and back. After down-conversion in the Octave, the I and Q components are digitized and integrated by the OPX+ to extract the qubit state.

For fast flux control, the coupler is equipped with a flux line driven by the OPX+. Since we only apply signals in the 100 MHz range, no LO is required. We install a -30 dB attenuator at the 3 K stage and several low-pass filters with cutoffs down to 300 MHz at the 10 mK stage. No attenuator is added to the 10 mK stage to prevent heating the fridge when applying voltages (in our case ± 1 V) to the FBL. The filters reflect high-frequency noise/signals, while the attenuators absorb and thermalize it. This prevents qubit decay and suppresses noise from higher-temperature stages.

DC biases are applied using Yokogawa [164] current sources, which allow stable and remote tuning. For the qubits, stable biasing is essential. Low-tech lab sources can be used for the DJJAAs, but they drift over time and require manual adjustment every 12 hours, which is impractical. To pump the DJJAAs we use RF generators from Windfreak Technologies [181], which are much cheaper than the RF generator required for the LO.

6.5. Resonator circle-fit

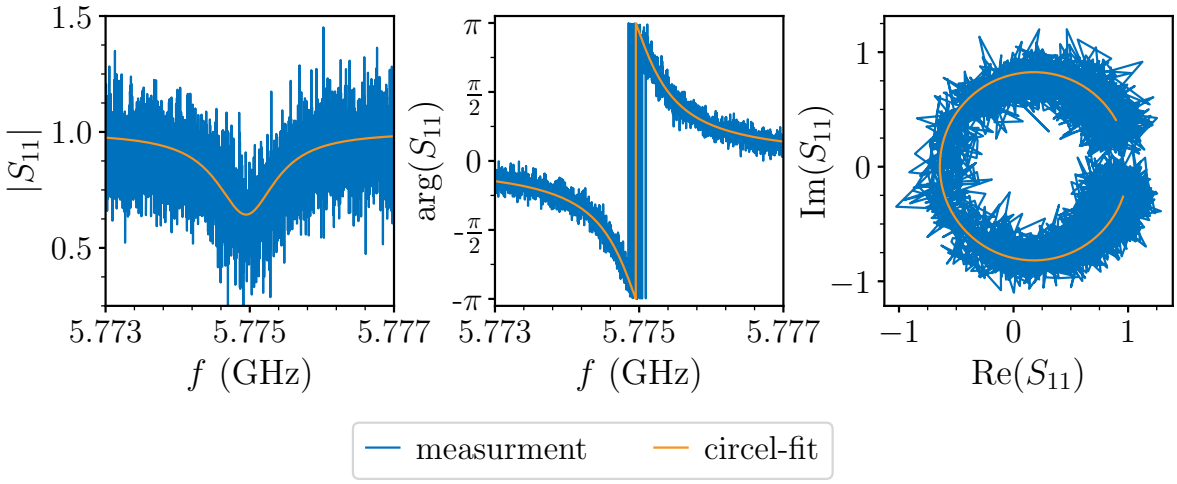

Figure 6.10.: **Measured reflection data with circle-fit for qubit q6.** The magnitude, phase, and complex plane (left to right) of the measured (blue) $S_{11}(f)$ are shown. Eq. 6.4 is fitted (orange) to the measured data. The resonance dip and circle shape are clearly visible despite noise in the raw data.

To determine f_r, Q_i, and Q_c from single-tone spectroscopy, we perform circle fits to the complex reflection coefficient $S_{11}(f)$. Following the circle fitting approach of Ref. [183] we rewrite Eq. 2.59 as

$$S_{11}(\omega) = \frac{\hat{b}\mathrm{out}(\omega)}{\hat{b}\mathrm{in}(\omega)} = 1 - \frac{\kappa_c}{-i(\omega_R-\omega)+(\kappa_c+\kappa_i)/2} = \frac{(\omega-\omega_R)^2+\frac{1}{4}(\kappa_i^2-\kappa_c^2)+i\kappa_c(\omega-\omega_R)}{(\omega-\omega_R)^2+\frac{1}{4}(\kappa_i+\kappa_c)^2}, \tag{6.4}$$

where κ_i accounts for internal dissipation, and κ_c describes coupling to the feedline. By fitting the measured complex $S_{11}(f)$ values to Eq. 6.4 as shown for q7 in Fig. 6.10 we can extract $f_R = \omega_R/2\pi = 5.7750\,\mathrm{GHz}$, $Q_i = \omega_R/\kappa_i = 5169$ and $Q_c = \omega_R/\kappa_c = 6291$.

A value of $Q_c \approx 6{\cdot}10^3$ is expected, as the resonator is strongly coupled to the measurement port. However, a $Q_i \approx 5{\cdot}10^3 \ll 10^5$ indicates additional loss channels of the readout mode on top of the inductive loss in the grAl (see section 3.4 and App. A.3) that contribute to internal dissipation. These include coupling to the opposite port and capacitive leakage through the extenders to neighboring devices (see App. A.10). Since these losses do not occur via the measurement port, they are included in Q_i.

A. Appendix

A.1. Electrostatic finite-element simulations

Tab. A.1 lists the capacitances of all simulated qubits using the ANSYS Maxwell electrostatic finite-element solver.

Qubit	C_{11} [fF]	C_{22} [fF]	C_{33} [fF]	C_{44} [fF]	$C_{12,21}$ [fF]	$C_{13,31}$ [fF]	$C_{23,32}$ [fF]	$C_{14,41}$ [fF]	$C_{24,42}$ [fF]	$C_{34,43}$ [fF]
q1	33.42	33.28	99.36	2.92	11.77	8.67	8.63	0.29	0.29	0.84
q2	32.45	32.39	76.93	3.03	3.22	6.34	6.30	0.32	0.36	0.72
q3	16.47	16.51	68.69	4.78	3.38	5.59	5.60	0.60	0.61	1.89
q4	16.44	16.48	68.89	4.75	3.40	5.61	5.62	0.48	0.49	2.12
q5	33.84	33.76	74.27	4.94	4.20	6.76	6.73	0.57	0.58	2.01
q6	33.59	33.58	76.00	5.41	4.29	6.79	6.77	0.48	0.48	2.56
q7	16.07	16.19	71.19	4.19	3.27	5.61	5.65	0.34	0.35	2.07
q8	53.37	53.39	126.97	14.17	5.67	28.44	28.42	2.13	2.15	4.86
q9	17.30	17.23	73.67	5.39	3.72	6.04	6.03	0.57	0.56	2.34
q10	19.51	19.52	116.36	8.95	7.35	5.34	5.35	0.57	0.56	4.03
q11	33.06	33.22	99.98	2.90	11.64	8.65	8.71	0.28	0.27	0.83
q12	33.06	33.10	92.67	2.75	11.51	7.88	7.90	0.30	0.29	0.77
q13	33.59	33.60	73.62	4.33	4.01	6.74	6.75	0.60	0.61	1.61
q14	17.30	17.23	73.67	5.39	3.72	6.04	6.03	0.57	0.56	2.34
q_{ex}	16.13	16.13	71.19	4.19	3.27	5.63	5.63	0.35	0.35	2.07

Table A.1.: **Simulated capacitance values**, taken from [136]. Capacitances depicted in Fig. 3.2a simulated with the 3D electrostatic finite element solver Ansys Maxwell for different qubits with a convergence accuracy of 10 aF. Differences in the qubit capacitances are due to different sizes of the circuit islands for different designs. Compared to Fig. 3.1a, the following applies: $C_{12,21} = C_s$, $C_{13,31} \approx C_r$ and $C_{23,32} \approx C_r$.

A.2. Measured and fitted spectra

In Tab. A.2 we list the fit parameters L_r, L_q, Δ_k, E_J and C_J that are obtained by fitting the extended circuit model described in section 3.1 to the measured spectra shown in Fig. A.1. The next column contains the calculated $L_\square$, obtained from the fitted L_q. Additionally, we use the extracted parameters from the fits to calculate the dispersive shift $\chi_{fit}/2\pi$ via Eq. 2.50 and compare it to the measured value χ_{meas} in the last two columns of Tab. A.2.

In Fig. A.2 we fit the flux qubit Hamiltonian (see Eq. 2.32) to the measured spectrum of q15, which uses a JJ array as inductance. We extract the following parameters: $L_q = 31.1\,\text{nH}$, $C_q = 33.9\,\text{fF}$ ($\Rightarrow E_c \approx 0.6\,\text{GHz}$), and $E_{J,\alpha} = 7.6\,\text{GHz}$.

In Fig. A.3 the full qubit spectra of Q1, Q2 and Q3 from Chapter 4 are shown. The qubit parameters were extracted using the flux qubit Hamiltonian (see Eq. 2.32) and are listed in Tab. 4.2.

device	L_r [nH]	L_q [nH]	Δ_k [nH]	E_J [GHz]	C_J [fF]	$L_\square$ [pH/□]	$\frac{\chi_{fit}}{2\pi}$ [MHz]	$\frac{\chi_{meas}}{2\pi}$ [MHz]
q1	15.03	13.61	−0.07	13.44	4.82	77.4	0.28	0.06
q2	6.53	16.34	−0.24	13.74	6.01	59.3	1.55	1.19
q3	29.36	40.35	0.69	13.72	3.78	100.9	−1.75	−1.80
q4	30.14	47.07	0.64	13.89	5.01	86.0	−0.56	−0.52
q5	11.90	33.38	0.39	9.88	4.02	70.6	2.05	2.00
q6	7.40	46.96	0.36	6.77	3.34	68.9	0.47	0.53
q7	11.73	39.06	0.28	4.83	1.85	67.1	0.98	0.91
q8	0.55	16.25	0.20	3.09	2.58	56.4	0.58	0.45
q9	18.89	26.91	0.17	1.28	1.86	54.8	0.11	0.07
q10	11.10	18.55	0.22	11.84	2.13	56.9	-	-
q11	9.82	12.91	−0.31	11.75	4.97	71.4	-	-
q12	6.54	24.68	−0.30	13.44	4.97	62.0	-	-
q13	7.60	28.28	0.86	5.14	4.37	81.2	-	-
q14	19.62	25.21	0.17	3.33	3.58	51.4	-	-

Table A.2.: **Device fit parameters L_r, L_q, Δ_k, E_J and C_J, calculated $L_\square$ and dispersive shift $\chi/2\pi$,** taken from [136]. The extended circuit model introduced in section 3.1 is used to calculate the fit parameters L_r, L_q, Δ_k, E_J and C_J, and $\chi_{fit}/2\pi$.

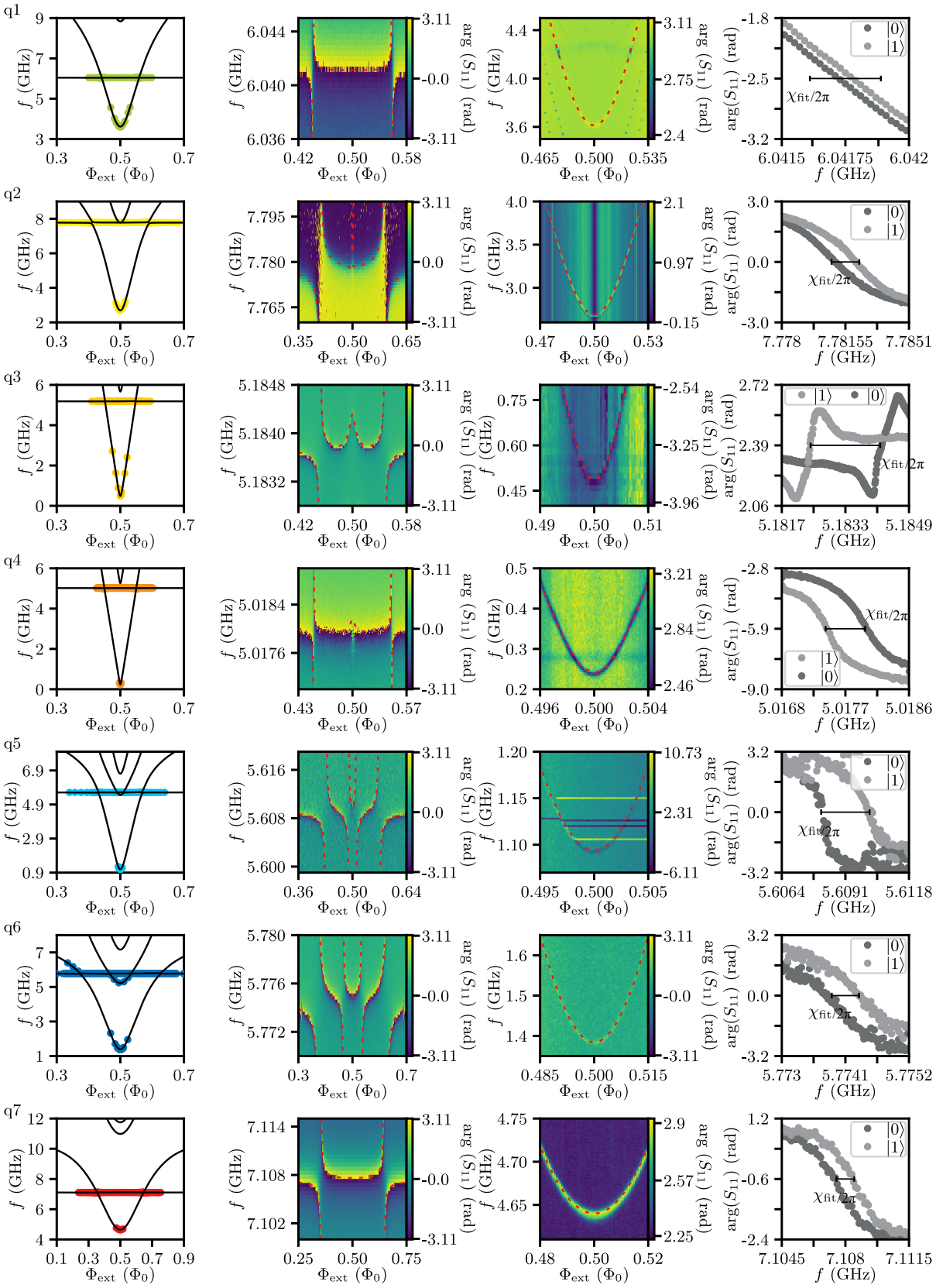
q1
q2
q3
q4
q5
q6
q7
f (GHz)
Φ_{ext} (Φ_0)
arg (S_{11}) (rad)
arg(S_{11}) (rad)
$|0\rangle$
$|1\rangle$
$\chi_{\text{fit}}/2\pi$

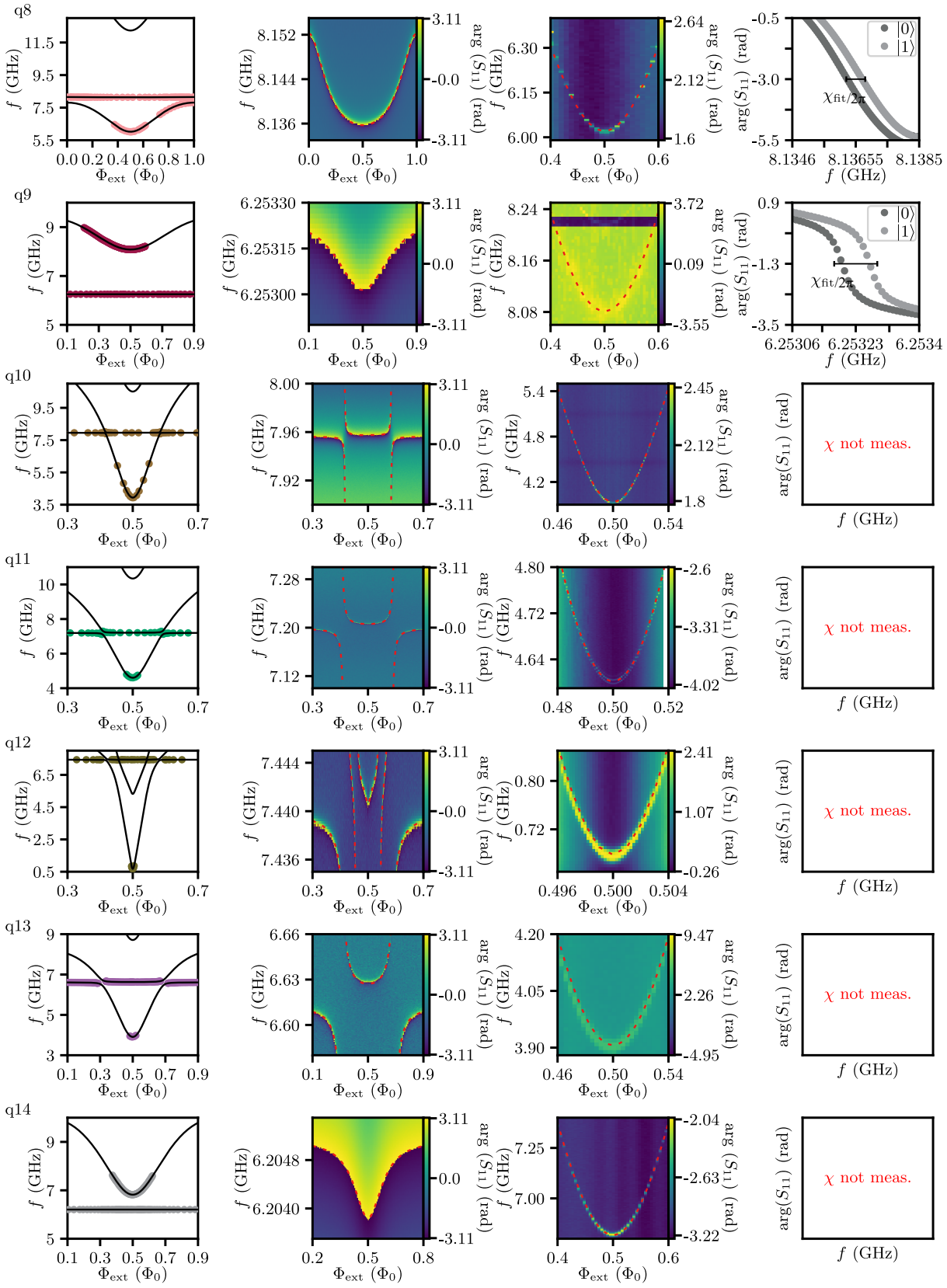
q8
q9
q10
q11
q12
q13
q14
f (GHz)
Φ_{ext} (Φ_0)
arg (S_{11}) (rad)
arg(S_{11}) (rad)
$|0\rangle$
$|1\rangle$
$\chi_{\text{fit}}/2\pi$
χ not meas.

Figure A.1.: **Qubit spectra and dispersive shifts $\chi/2\pi$ at $\Phi_{ext} = 0.5\Phi_0$,** figure and caption taken from [136]. In the first column plots the data points are extracted from single-tone and two-tone spectroscopy of the resonator and qubit, shown in column 2 and 3, respectively. The black lines (red dotted lines in column 2 and 3) show fits to the circuit model. The measured dispersive shifts plotted in the 4th column for devices q1 to q9 are extracted from pulsed single shot readout. The response of the resonator for the qubit in the ground (excited) state is shown in dark (light) grey markers. The $\chi/2\pi$ value calculated from the circuit model is shown as a horizontal black line. The measured and calculated $\chi/2\pi$ values are tabulated in Tab. A.2.

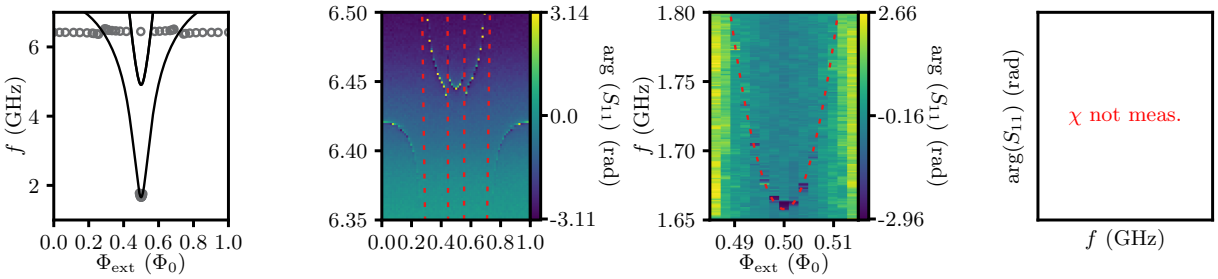

Figure A.2.: **Spectrum of q15 which uses a JJ array as inductance.** In the first column plot the data points (grey circles) are extracted from single-tone and two-tone spectroscopy of the resonator and qubit, shown in column 2 and 3, respectively. The black lines (red dotted lines in column 2 and 3) show fits to the flux qubit Hamiltonian (see Eq. 2.32). No dispersive shift was measured for this device.

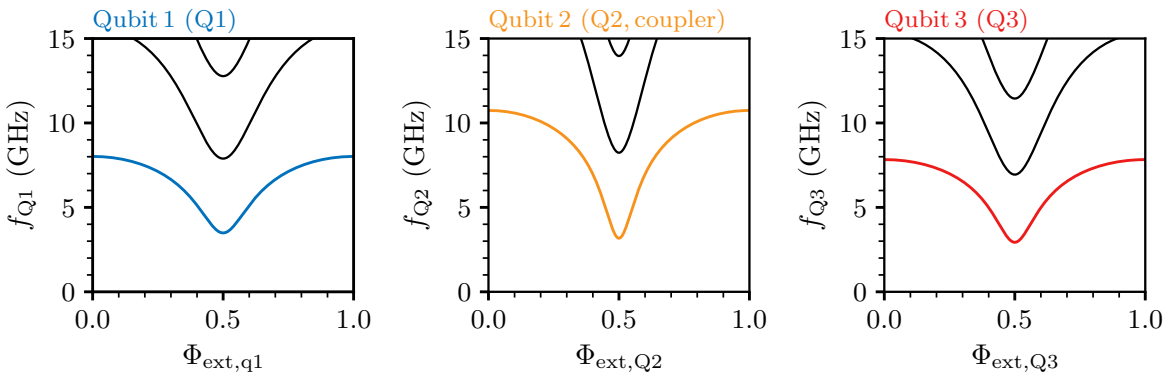

Figure A.3.: **Full qubit spectra for Q1, Q2 and Q3 from Chapter 4,** calculated using the flux qubit Hamiltonian (see Eq. 2.32) and the values listed in Tab. 4.2.

A.3. Coherence times

A summary of the measured free energy relaxation times T_1, Ramsey decoherence times T_2^*, and echo decoherence times T_2^{echo} at the half flux point ($\Phi_{\text{ext}} = 0.5\Phi_0$) for the GFQ devices in Chapter 3 is given in Tab. A.3. A summary of T_1 and T_2^* of most GFQ devices measured during this PhD is shown in Fig. A.4. As can be seen, the GFQ generation and the improved fabrication process (see section 6.1) have no significant effect on the relaxation times.

As described in section 3.4, the inductive loss of grAl can be estimated using Eq. 3.43. The quality factors Q_{ind} derived from the measured T_1 values are listed in the fifth column of Tab. A.3, yielding $10^5 < Q_{\text{ind}} \lessapprox 10^6$, consistent with the estimated inductive losses in grAl [120].

device	T_1 (µs)	T_2^* (µs)	T_2^{echo} (µs)	$Q_{\text{ind}}(\times 10^6)$
q1	7.6±1.7 / 9.8 / 3.2±0.3	5.7±1.0 / 2.1	10.8 / 12.6	0.9 / 1.1 / 0.4
q2	10.3	2.0	–	1.6
q3	2.6	–	–	2.1
q4	1.3	2.1	–	2.0
q5	4.3	2.4	–	1.0
q6	–	–	–	–
q7	11.2 / 8.0 / 5.0	6.0/ 3.3	7.7	0.7 / 0.7 / 0.4
q8	1.4	2.3	–	0.1
q9	3.7	–	–	0.2
q10	4.1	–	–	0.5
q11	10.5±1.0 / 9.9 / 6.2±0.4	5.7±0.2 / 2.6	– / 4.8	1.0 / 0.9 / 0.6
q12	–	–	–	–
q13	4.4	1.4	–	0.4
q14	4.6	–	–	0.3

Table A.3.: **Measured coherence times at the half-flux sweet spot for different samples**, figure and caption taken from [136]. For measurements with a statistically relevant amount of repetitions we show the mean value and standard deviation. Values separated by forward slashes are taken from different cooldowns, several months apart and measured in different sample holders. Between cooldowns the samples have been stored in ambient conditions.

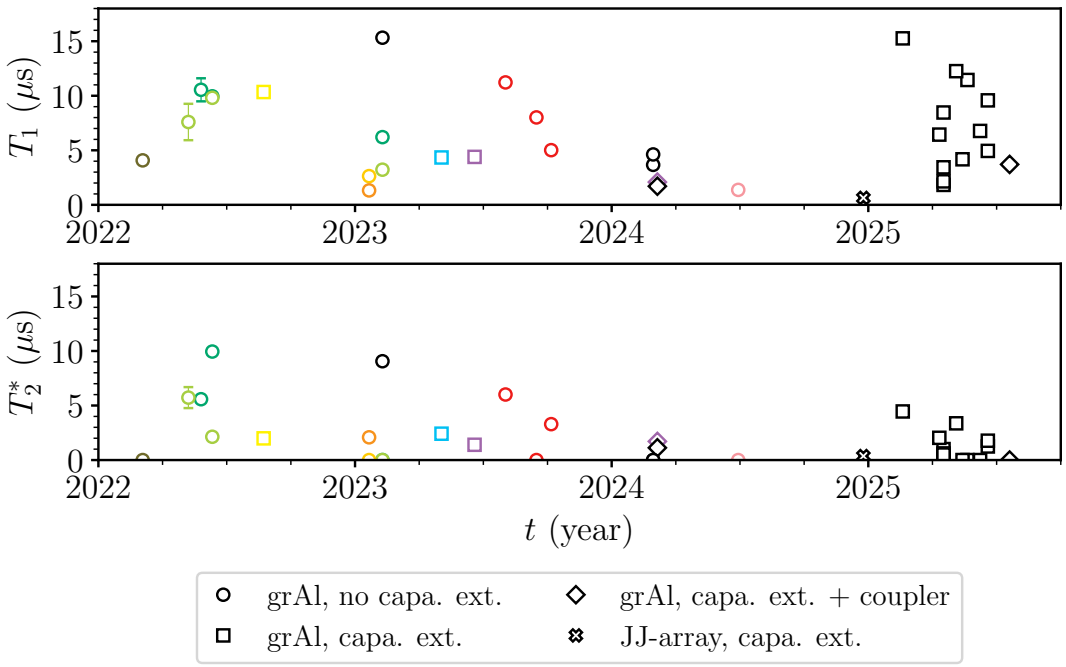

Figure A.4.: **Overview of the GFQs T_1 and T_2^* for most devices measured during this PhD thesis.** Marker shapes define the type of GFQ (grAl or JJ arrays, with or without capacitive extenders and with or without coupler chip in e2). Black markers are used for GFQs which are not shown in Fig. 3.8, all other colors are consistent with the colors used in Fig. 3.8. All qubits after 1 January 2025 were fabricated with the improved process as described in section 6.1.

A.4. Matrix elements for the GFQs

We use Eq. 3.43 to estimate the GFQs inductive losses through their environment [154]. The different terms of Eq. 3.43 capture different physical mechanisms:

$$\frac{1}{T_1} = \underbrace{\frac{8\pi^3 E_L}{hQ_{ind}}}_{\text{environment}} \quad \underbrace{\left|\langle 0|\hat{\varphi}|1\rangle\right|^2}_{\text{transition matrix element}} \quad \underbrace{\left(1+\coth\left(\frac{hf_q}{2k_B T}\right)\right)}_{\text{thermal factor}}.$$

The first term containing E_L and Q_{ind} quantifies the losses in the inductive environment. The transition matrix element $\langle 0|\hat{\varphi}|1\rangle$ governs both control and dissipation: its magnitude $|\langle 0|\hat{\varphi}|1\rangle|$ sets the Rabi rate for flux driving, while its magnitude squared $|\langle 0|\hat{\varphi}|1\rangle|^2$ sets the relaxation rate via the inductive environment. Larger values imply stronger coupling and thus shorter T_1 via this channel, while smaller values suppress relaxation but also reduce the efficiency of flux-based control (smaller Rabi rates)[i]. The thermal factor accounts for stimulated processes at finite temperature. Here, T corresponds to the effective qubit temperature, representing the temperature of the qubit's electromagnetic environment at the transition frequency f_q, approximated from the measured population ratio (we use $T \approx 45$ mK, see section 3.3). Following the method described in Ref. [107], we numerically diagonalize the fluxonium Hamiltonian (see Eq. 2.32) in a truncated harmonic-oscillator basis (normal-mode basis) to obtain eigenstates and eigenenergies, from which the transition matrix elements (flux and charge dipoles) are extracted.

The matrix elements for the GFQs in Chapter 3 and Chapter 4 are listed in Tab. A.4.

[i] The diagonal matrix elements $\langle n|\hat{\varphi}|n\rangle$ determine Z-type (pure) dephasing from low-frequency flux noise.

device	$\langle 0\|\hat{\varphi}\|1\rangle$ (rad)
q1	0.137
q2	0.169
q3	0.343
q4	0.368
q5	0.247
q6	0.236
q7	0.184
q8	0.093
q9	0.133
q10	0.173
q11	0.121
q12	0.251
q13	0.084
q14	0.143
Q1	0.152

Table A.4.: **Matrix elements.** Calculated values of the flux matrix element $\langle 0|\hat{\varphi}|1\rangle$ for the devices discussed in Chapter 3 obtained from numerical diagonalization of the fluxonium Hamiltonian. Additionally, we show the matrix element of Q1 from Chapter 4.

A.5. Photon number calibration using measurement-induced dephasing

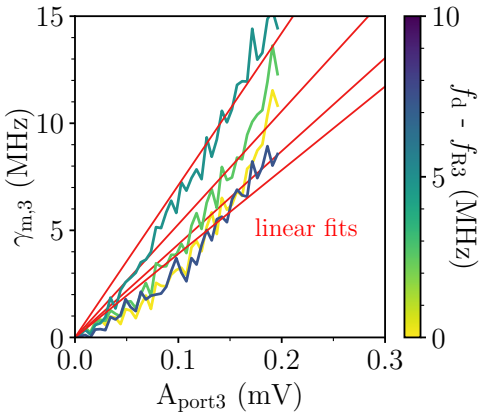

Figure A.5.: **Linear fitting of $\gamma_{m,3}$ vs. drive amplitude.** Readout-induced dephasing rate $\gamma_{m,3}$ vs. applied drive amplitude A_{port3} for several drive frequencies f_d near the resonator frequency f_{R3}. The color encodes the detuning $f_d - f_{R3}$. Red lines are linear fits at fixed f_d. Their slopes $m(f_d) = \partial\gamma/\partial P$ are used in Eq. A.2 to extract the conversion factor in Eq. A.3

We can use the measurement induced dephasing to perform a photon number calibration of a resonator. With known $f_r, \kappa/2\pi$ and $\chi/2\pi$ we rewrite Eq. 4.6 as

$$\gamma(f_d, P) = \underbrace{\alpha P}_{\epsilon^2(P)} \underbrace{4\pi^2\left[\frac{1}{\kappa^2/4+(2\pi f_d-2\pi f_r+\chi/2)^2}+\frac{1}{\kappa^2/4+(2\pi f_d-2\pi f_r-\chi/2)^2}\right]}_{=S(f_d)} \underbrace{\frac{\kappa\chi^2/8\pi}{\kappa^2/4+\chi^2/4+(2\pi f_d-2\pi f_r)^2}}_{=F(f_d)}, \tag{A.1}$$

where α converts the applied drive power P (in V) to the drive amplitude ϵ^2 at the resonator. At fixed f_d, γ is linear in P with slope

$$m(f_d) = \frac{\partial\gamma}{\partial P} = \alpha\, S(f_d)\, F(f_d), \tag{A.2}$$

as shown in Fig. A.5 for an arbitrary set of f_d in QR-system 3. We measure $\gamma(f_d, P)$ for several P values at multiple f_d, extract $m(f_d)$ from linear fits in P, and determine

$$\alpha = \underset{\alpha}{\text{argmin}} \sum_{f_d}\Big[m(f_d) - \alpha\, S(f_d)\, F(f_d)\Big]^2. \tag{A.3}$$

For $2\pi|f_d - f_r| \gg \chi/2$, the contributions to the sum become negligible since the Lorentzian factors $S(f_d)$ and $F(f_d)$ decay as $1/|f_d - f_r|^2$. Substituting $\epsilon^2(P) = \alpha P$, we get for the state-dependent photon number:

$$n_{|0\rangle}(f_d, P) = \frac{\epsilon^2(P)\,4\pi^2}{\kappa^2/4+(2\pi f_d-2\pi f_r+\chi/2)^2} \quad \text{and} \quad n_{|1\rangle}(f_d, P) = \frac{\epsilon^2(P)\,4\pi^2}{\kappa^2/4+(2\pi f_d-2\pi f_r-\chi/2)^2}. \tag{A.4}$$

For better comparison it makes sense to use the average photon number $\bar{n}$ at the midpoint $f_d = f_r$, where

$$\frac{\bar{n}}{P} = \frac{n_{|0\rangle}+n_{|1\rangle}}{2P}\bigg|_{f_d=f_r} = \frac{\alpha}{(\frac{\kappa}{2\pi})^2/4+(\frac{\chi}{2\pi}/2)^2}. \tag{A.5}$$

Compared to a photon-number calibration that uses only the AC-Stark shift, this method has the advan-

tage that it uses the full detuning dependence $S(f_\mathrm{d})F(f_\mathrm{d})$ and does not require resolving small qubit-frequency shifts, yielding a more robust global estimate of α. The trade-off is that it requires multiple time-domain dephasing measurements over power and detuning.

A.6. Room-temperature resistances

Room-temperature resistance measurements of the Al JJs and the grAl inductors are summarized in Tab. A.5. For the JJs, the Josephson energy E_J is calculated using the Ambegaokar-Baratoff (AB) relation (see Eq. 2.16) and compared to the E_J value extracted from cryogenic measurements.

Date	grAl: $R_\square$ (Ω)	grAl: ρ [μΩcm]	JJ: R (kΩ)	JJ(AB): E_J (GHz)	JJ(cryo): E_J (GHz)
Feb 2022	92±4	642±31	18.8±2.3	8.2±1.0	–
Mar 2022	91±5	638±33	14.3±0.5	10.7±0.4	–
Apr 2022	85±9	577±80	10.9±2.2	14.5±2.4	–
Apr 2022	99±6	694±44	11.2±1.2	13.8±1.4	$13.4_{\,q1} \wedge 11.75_{\,q11} \wedge 13.44_{\,q12}$
Jun 2022	87±18	608±127	8.9±2.3	18.3±4.5	$13.7_{\,q2}$
Aug 2022	88±2	615±14	–	–	–
Sep 2022	94±3	657±20	14.5±0.9	10.6±0.7	–
Nov 2022	120±6	842±41	11.5±1.1	13.5±1.4	–
Nov 2022	134±6	936±41	13.8±3.4	11.5±1.9	–
Nov 2022	92±3.9	646±28	9.6±2.8	17.0±3.3	–
Dec 2022	126	879	12.2	13.5	$13.7_{\,q3} \wedge 13.9_{\,q4}$
Dec 2022	143±8	1002±56	15.7±1.1	9.8±7.1	–
Feb 2023	98	685	24.6±1.5	6.2±0.4	$6.8_{\,q5} \wedge 9.9_{\,q6}$
Mar 2023	76±3	534±22	26.6±2.9	5.8±0.7	–
Sep 2023	74±0	516±1	8.6 / 12.7	17.9 / 12.1	–
Oct 2023	92	771	–	–	–
Dec 2023	67±4	466±27	19.4	7.9	–

Table A.5.: **Resistivity of different grAl films and JJs at room-temperature as a function of deposition date.** Measured E_J values at cryogenic temperatures are indexed with their corresponding qubit names. All devices were fabricated using the same evaporation procedure as outlined in Ref. [136] (referred to as the „*old*“ process in section 6.1). We assume a thickness of 70 nm for the grAl films. For the pure Al films we assume $T_{c,Al} \approx 1.3$ K (see section 2.2). Error bars represent the statistical uncertainty of the averaged values. Test structures with different sizes are separated by / . The variability of resistivities over timescales of months may be due to changes in the aluminum crucible, humidity, or other cleanroom conditions.

A.7. Dephasing Measurements for Q3

In Fig. A.6a we show the dephasing measurements for Q3, in b the corresponding fits using Eq. 4.6, and in c the calculated dephasing rate based on the average fit parameters listed in Tab. 4.4.

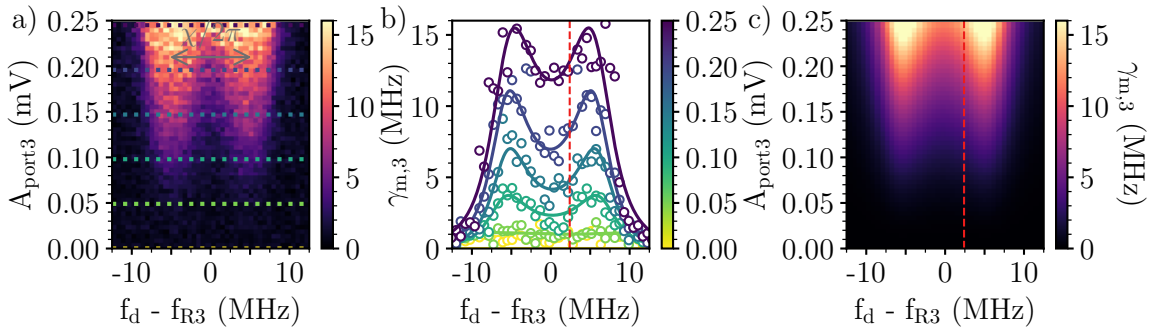

Figure A.6.: **Dephasing of Q3.** **a)** Measured dephasing $\gamma_{m,3}$ from Ramsey experiments as a function of drive frequency f_d and drive amplitude A_{port3}. **b)** Fits to Eq. 4.6 for selected drive amplitudes. **c)** Predicted dephasing using the average fit parameters from Tab. 4.4. The red line marks $f_d - f_{R3} = 2.4\,\text{MHz}$, where $\gamma_{m,3}$ values in Fig. 4.9 are extracted.

A.8. Schrieffer-Wolff transformation

In superconducting qubit systems with more than two interacting elements, it is often desirable to derive an effective model involving only the lowest energy levels of the devices. This model should capture the relevant dynamics while eliminating non-participating degrees of freedom. Such an approach is useful in our system, which consists of a linear array of three coupled flux qubits (Q1,Q2,Q3), where the middle qubit (Q2) acts as a tunable coupler. In our configuration, the coupling between the computational outer qubits is mediated by virtual excitations of the coupler. Therefore, a suitable effective model would eliminate the coupler degree of freedom by restricting the coupler to its ground state and the outer qubits to their computational subspaces. In our case, the corresponding uncoupled (before any perturbation is introduced) low-energy subspace is $\mathscr{H}_{\text{eff}} = \text{span}\left\{|i\rangle_{\text{Q1}}|0\rangle_{\text{Q2}}|j\rangle_{\text{Q3}} \,\middle|\, i,j \in \{0,1\}\right\} \subset \mathscr{H}$, where $\mathscr{H}$ is the full Hilbert space of the three-qubit system including all higher excited states.

A method for obtaining such effective models is the Schrieffer-Wolff transformation (SWT), first introduced in 1966 [166]. Following Bravyi et al. [167], the SWT can be understood as a version of degenerate perturbation theory. It applies to systems described by a Hamiltonian $\mathcal{H} = \mathcal{H}_0 + \epsilon V$, where $\mathcal{H}_0$ is the unperturbed part with a known spectrum, and V is a small perturbation that does not preserve the low-energy subspace $\mathscr{H}_{\text{eff}}$. $\mathscr{H}_{\text{eff}}$ is invariant under $\mathcal{H}_0$. The goal is to construct an effective Hamiltonian $\mathcal{H}_{\text{eff}}$ that acts only within $\mathscr{H}_{\text{eff}}$ and reproduces the low energy eigenvalues of the full Hamiltonian $\mathcal{H}$. The SWT constructs a unitary transformation U, such that the transformed Hamiltonian $\tilde{\mathcal{H}} = U\mathcal{H}U^\dagger$ approximately preserves $\mathscr{H}_{\text{eff}}$. The effective Hamiltonian is then defined as the restriction of the transformed Hamiltonian to $\mathscr{H}_{\text{eff}}$:

$$\mathcal{H}_{\text{eff}} = P_0\tilde{\mathcal{H}}P_0 = P_0U\mathcal{H}U^\dagger P_0, \tag{A.6}$$

where P_0 is the projector onto $\mathscr{H}_{\text{eff}}$. The challenge of the SWT is to find a suitable unitary transformation U that block-diagonalizes $\mathcal{H}$ up to a desired order in ϵ, thereby decoupling $\mathscr{H}_{\text{eff}}$ from the rest of the Hilbert space to that order.

In some numerical applications, it is useful to express the SWT in terms of projectors onto the relevant subspaces. As stated in [167], section 2.2, the unitary transformation can be written as

$$\tilde{U} = \sqrt{(P_0 - Q_0)(P - Q)}, \tag{A.7}$$

where P is the projector onto the interacting low-energy subspace of $\mathcal{H}$ which adiabatically evolves from $\mathscr{H}_{\text{eff}}$ as the perturbation V is turned on. $Q = \mathbb{I} - P$ projects onto its orthogonal complement. Similarly, $Q_0 = \mathbb{I} - P_0$ is the projector onto $\mathscr{H}_{\text{eff}}^{\perp}$. In contrast to U from Eq. A.6, the projector-based unitary transformation $\tilde{U}$ is constructed to map the interacting low-energy subspace onto the unperturbed subspace $\mathscr{H}_{\text{eff}}$. The effective Hamiltonian is then obtained by projecting the transformed Hamiltonian onto $\mathscr{H}_{\text{eff}}$:

$$\mathcal{H}_{\text{eff}} = P_0\tilde{U}P\mathcal{H}P\tilde{U}^\dagger P_0. \tag{A.8}$$

This expression encodes the low energy dynamics of the interacting system within the reference subspace $\mathscr{H}_{\text{eff}}$.

Deriving g_{13} for a capacitively coupled three qubit array

We aim to derive the effective coupling g_{13}^{eff} between the outer qubits Q1 and Q3 in an array of three capacitively coupled qubits. The system is described by the Hamiltonian

$$\mathcal{H} = \underbrace{\sum_{i=1}^{3} \mathcal{H}_{\text{FQ},i}}_{\substack{\text{uncoupled} \\ \text{qubit Hamiltonians}}} + \underbrace{\frac{1}{2}\sum_{i,j=1}^{3} C_{ij}^{-1} Q_i Q_j}_{\substack{\text{capacitive coupling} \\ \text{between all qubits}}}, \tag{A.9}$$

with the single flux qubit (FQ) terms defined as in Eq. 2.33:

$$\mathcal{H}_{\text{FQ},i} = \frac{C_{ii}^{-1}}{2} Q_i^2 + \frac{1}{2L_i}\Phi_i^2 - E_{\text{J},i}\cos\left(\frac{2\pi}{\Phi_0}(\Phi_i + \Phi_i^{\text{ext}})\right). \tag{A.10}$$

Here, Q_i and Φ_i are the charge and flux operators of qubit i, and L_i and $E_{\text{J},i}$ are its inductance and Josephson energy. The matrix $\mathbf{C}_{ij}^{-1}$ is the inverse of the capacitance matrix $\mathbf{C}$, which describes all capacitive couplings in the circuit. Diagonal elements contain self-capacitances, while off-diagonal elements account for mutual coupling.

To evaluate g_{13}, we apply the Schrieffer-Wolff transformation to the full system using two complementary approaches: a numerically exact method that captures the full circuit nonlinearities, and a semi-analytical perturbative treatment that provides physical insight into the coupling mechanism.

Numerical (n) approach. The first method follows the numerically exact SWT introduced in Ref. [184], which works directly with the full circuit Hamiltonian in Eq. A.9. We define

$$\mathcal{H} = \mathcal{H}_0 + \epsilon V \quad \text{with} \quad \mathcal{H}_0 = \sum_{i=1}^{3} \mathcal{H}_{\text{FQ},i} \quad \text{and} \quad V = \frac{1}{2}\sum_{i \neq j} C_{ij}^{-1} Q_i Q_j .$$

Using Eq. A.8, where P_0 projects onto the unperturbed low energy subspace $\mathscr{H}_{\text{eff}}$, and P onto the corresponding interacting subspace, constructed from the numerically obtained eigenstates of $\mathcal{H}$, we compute the effective Hamiltonian

$$\mathcal{H}_{\text{eff}}^{\text{n}} = \frac{\omega_1}{2}\sigma_1^z + \frac{\omega_3}{2}\sigma_3^z + J_{xx}\sigma_1^x\sigma_3^x + J_{yy}\sigma_1^y\sigma_3^y + J_{zz}\sigma_1^z\sigma_3^z. \tag{A.11}$$

The effective coupling $g_{13}^{\text{n,eff}}$ is obtained from the splitting between the one-excitation eigenstates of $\mathcal{H}_{\text{eff}}^{\text{n}}$, expressed in the basis $\{|00\rangle, |01\rangle, |10\rangle, |11\rangle\}$ of Q1 and Q3 as:

$$\mathcal{H}_{\text{eff}}^{\text{n}} = \begin{pmatrix} \frac{\omega_1+\omega_3}{2} + J_{zz} & 0 & 0 & J_{xx} - J_{yy} \\ 0 & \frac{\omega_1-\omega_3}{2} - J_{zz} & J_{xx} + J_{yy} & 0 \\ 0 & J_{xx} + J_{yy} & \frac{-\omega_1+\omega_3}{2} - J_{zz} & 0 \\ J_{xx} - J_{yy} & 0 & 0 & \frac{-\omega_1-\omega_3}{2} + J_{zz} \end{pmatrix}. \tag{A.12}$$

On resonance $\omega_1 = \omega_3$, the energy gap between the eigenstates $|10\rangle$ and $|01\rangle$ is $2g_{13}^{\mathrm{n,eff}} = 2|J_{xx}+J_{yy}|$, which we compare directly to experimental data in Fig. 4.13. Numerical simulations show $J_{zz} < 10^{-2}\times |J_{xx}+J_{yy}|$, which is below our experimental resolution.

Analytical (a) approach. The second method uses an analytical SWT based on second-order perturbation theory. Following Ref. [185], we start from a simplified model in which all qubits are truncated to their lowest two levels, and the coupler Q2 is assumed to be far detuned ($|\omega_2-\omega_{1,3}| \gg g_{12}, g_{23}$). By projecting the full Hamiltonian in Eq. A.9 onto the non-interacting subspace of the three qubits $\mathscr{H}_0 = \mathrm{span}\left\{|i\rangle_{\mathrm{Q1}}|j\rangle_{\mathrm{Q2}}|k\rangle_{\mathrm{Q3}} \,\middle|\, i,j,k \in \{0,1\}\right\}$, we obtain the reduced Hamiltonian

$$\mathcal{H}_{\mathrm{2lv}}^{\mathrm{a}} = \frac{\tilde{\omega}_1}{2}\sigma_1^z+\frac{\tilde{\omega}_2}{2}\sigma_2^z+\frac{\tilde{\omega}_3}{2}\sigma_3^z+g_{12}\sigma_1^y\sigma_2^y+g_{23}\sigma_2^y\sigma_3^y, \tag{A.13}$$

with the bare qubit frequencies $\tilde{\omega}_i$. The direct couplings are obtained by projecting the capacitive interaction onto $\mathscr{H}_0$:

$$g_{ij} = C_{ij}^{-1}\,\langle 0_i|Q_i|1_i\rangle\,\langle 0_j|Q_j|1_j\rangle, \tag{A.14}$$

where we neglect the direct coupling $g_{13} \ll g_{12}, g_{23}$ in the analytical treatment.

We now apply the SWT to the Hamiltonian in Eq. A.13 using a perturbative expansion up to second order, following the approach of Ref. [186]. We decompose the system into

$$\mathcal{H}_{\mathrm{2lv}}^{\mathrm{a}} = \mathcal{H}_0+\epsilon V \quad \text{with} \quad \mathcal{H}_0 = \sum_{i=1}^{3}\frac{\tilde{\omega}_i}{2}\sigma_i^z \quad \text{and} \quad V = g_{12}\sigma_1^y\sigma_2^y+g_{23}\sigma_2^y\sigma_3^y.$$

The second-order effective Hamiltonian consists of the projected term $\mathcal{H}_{\mathrm{eff},1}^{\mathrm{a}} = P_0\mathcal{H}_{\mathrm{2lv}}^{\mathrm{a}}P_0$, and corrections due to virtual transitions through the excited states $k \in \{|010\rangle, |110\rangle, |011\rangle, |111\rangle\} = \mathscr{H}_{\mathrm{ce}}$:

$$\mathcal{H}_{\mathrm{eff},2}^{\mathrm{a}} = \mathcal{H}_{\mathrm{eff},1}^{\mathrm{a}}+\frac{1}{2}\sum_{\substack{i,j\in\mathscr{H}_0,\\ k\in\mathscr{H}_{\mathrm{ce}}}}\left(\frac{1}{E_i-E_k}+\frac{1}{E_j-E_k}\right)\langle i|V|k\rangle\,\langle k|V|j\rangle\,|i\rangle\,\langle j|. \tag{A.15}$$

Here, E_n denotes the energy of state $|n\rangle$ under $\mathcal{H}_0$. Assuming Q1 and Q3 are on resonance ($\tilde{\omega}_1 = \tilde{\omega}_3 = \omega$), the resulting second-order effective Hamiltonian reads:

$$\mathcal{H}_{\mathrm{eff},2}^{\mathrm{a}} = \frac{\tilde{\omega}_1}{2}\sigma_1^z+\frac{\tilde{\omega}_3}{2}\sigma_3^z+g_{13}^{\mathrm{a,eff}}\sigma_1^y\sigma_3^y, \tag{A.16}$$

with renormalized qubit frequencies

$$\tilde{\omega}_1 = \omega+g_{12}^2\left(\frac{1}{\Delta}-\frac{1}{\Sigma}\right), \quad \tilde{\omega}_3 = \omega+g_{23}^2\left(\frac{1}{\Delta}-\frac{1}{\Sigma}\right), \tag{A.17}$$

and effective coupling

$$g_{13}^{\mathrm{a,eff}} = g_{12}g_{23}\left(\frac{1}{\Delta}-\frac{1}{\Sigma}\right), \tag{A.18}$$

where the detunings are defined as $\Delta = \omega-\omega_2$ and $\Sigma = \omega+\omega_2$.

Since no $\sigma^x\sigma^x$ or $\sigma^z\sigma^z$ terms appear in Eq. A.16, the effective coupling $g_{13}^{\mathrm{a,eff}}$ corresponds directly to

the energy splitting between the one-excitation states $|10\rangle$ and $|01\rangle$. Its dependence on ω_2 is shown as a dashed line in Fig. 4.13. Note that this second-order expansion diverges near resonance ($\omega_2 \approx \omega$), an artifact of perturbation theory that is absent in the numerically exact SWT [167].

The analytical approach provides a simple closed-form expression and physical intuition for the coupling mechanism, but neglects higher-order corrections and circuit nonlinearities. In contrast, the numerical SWT captures the full three-qubit interaction, including $\sigma^z\sigma^z$ terms and excitation-mediated effects, at the cost of requiring numerical diagonalization.

A.9. Simulations

In this section we present both single-enclosure and full-box simulations. The single-enclosure simulations demonstrate the necessity of coupling capacitive extenders symmetrically to islands **1** and **2** of the QR-systems, and are further used to extract the mutual inductance and losses of Q2 with the FBL. The full-box simulations, performed with the simplified coupler chip, include a comparison of single-line and double-line capacitive extenders, a simulation of the effective coupling g_{13}^{eff} between Q1 and Q3, and an analysis of different band-pass filter designs combined with varying numbers of enclosure walls to minimize crosstalk between the outer enclosures.

Single enclosure simulations

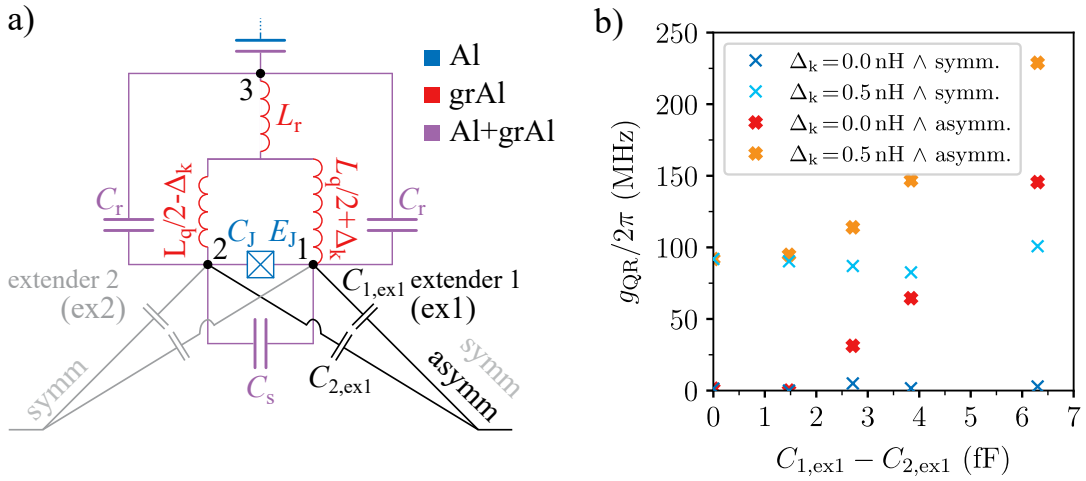

Figure A.7.: **Coupling capacitive extenders to the QR-system. a)** Circuit diagram illustrating the coupling of capacitive extenders to the QR-system. In the symmetric configuration (grey+black), one capacitive extender couples to each of islands **1** and **2**, while in the asymmetric configuration (black) only a single extender couples to island 1. The capacitances $C_{1,ex1}$ and $C_{2,ex1}$ denote the coupling capacitances between islands 1 or 2 and the extender ex1, respectively. **b)** Dependence of the qubit-readout coupling strength g_{QR} on the difference $C_{1,ex1}-C_{2,ex1}$. Results are shown for symmetric and asymmetric configurations, and for $\Delta_k = 0$ and $\Delta_k = 0.5$ nH. In the symmetric case, g_{QR} remains independent of $C_{1,ex1}-C_{2,ex1}$, whereas in the asymmetric case a strong dependence is observed.

To maintain the concept of inductive coupling when adding capacitive extenders to the QR-system, the extenders must be connected symmetrically to both GFQ islands **1** and **2**. As can be seen in Fig. A.7, if capacitive extenders are connected only to a single island, the qubit-readout coupling g_{QR} strongly depends on the capacitance $C_{i,ex1}$ between extender ex1 and island i. When extenders are added symmetrically to islands **1** and **2**, the coupling remains independent of $C_{i,ex1}$.

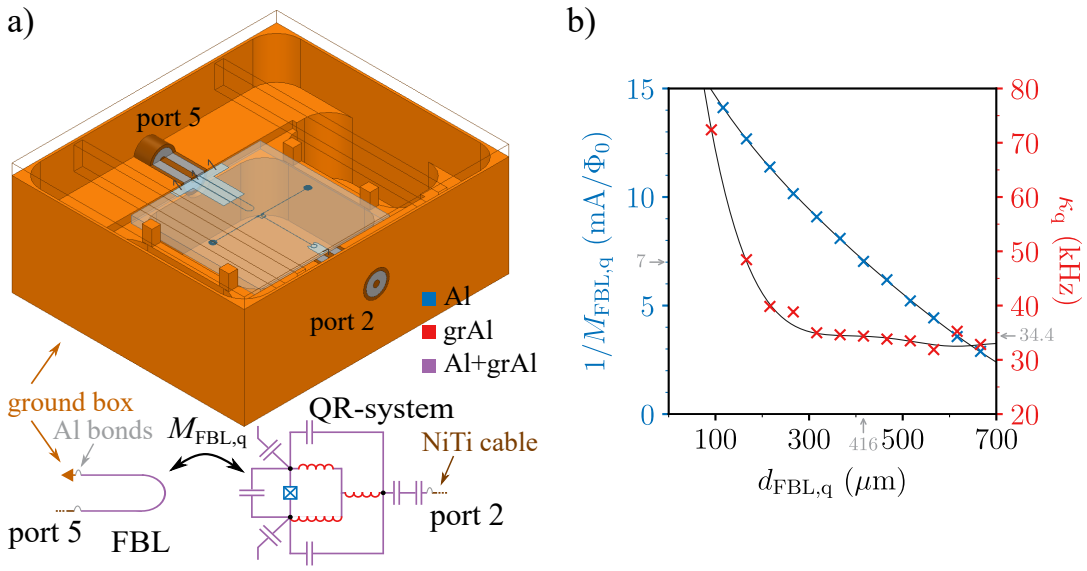

Figure A.8.: **Simulations for FBL. a)** 3D model of the coupler-chip enclosure used to simulate the coupler qubits (Q2) bandwidth κ_{q} and the mutual inductance $M_{\mathrm{FBL,q}}$ between the FBL and the qubit loop. κ_{q} is obtained from ANSYS eigenmode simulations, while $M_{\mathrm{FBL,q}}$ is calculated with ANSYS Maxwell3D magnetostatics using a simplified model containing only the FBL and qubit loop. A schematic of the simulation setup is shown below the box. **b)** Simulated dependence of the mutual inductance $1/M_{\mathrm{FBL,q}}$ (blue) and coupler qubit bandwidth κ_{q} (red) on the distance $d_{\mathrm{FBL,q}}$ between the FBL and the qubit loop. The grey arrows indicate the values for the device used in this thesis: for Q2 $d_{\mathrm{FBL,q}} \approx 416\,\mu\mathrm{m}$, resulting in $M_{\mathrm{FBL,q}} \approx 7\,\mathrm{mA}/\Phi_0$ and $\kappa_{\mathrm{q}} \approx 34.4\,\mathrm{kHz}$. The black lines are guides to the eye.

The FBL must be placed at a distance from the qubit loop that is small enough to induce sufficient magnetic flux to activate the coupler, yet large enough to avoid the FBL becoming the dominant decay channel. In Fig. A.8 we show simulation results for the coupler qubit Q2 from Chapter 4. As shown in the figure, we choose a distance of $d_{\mathrm{FBL,q}} \approx 416\,\mu\mathrm{m}$ between the FBL and the qubit loop. At this distance the mutual inductance is $M_{\mathrm{FBL,q}} \approx 7\,\mathrm{mA}/\Phi_0$, which allows activation of the coupling via the FBL while keeping its impact on the qubit lifetime moderate.

Full box simulations

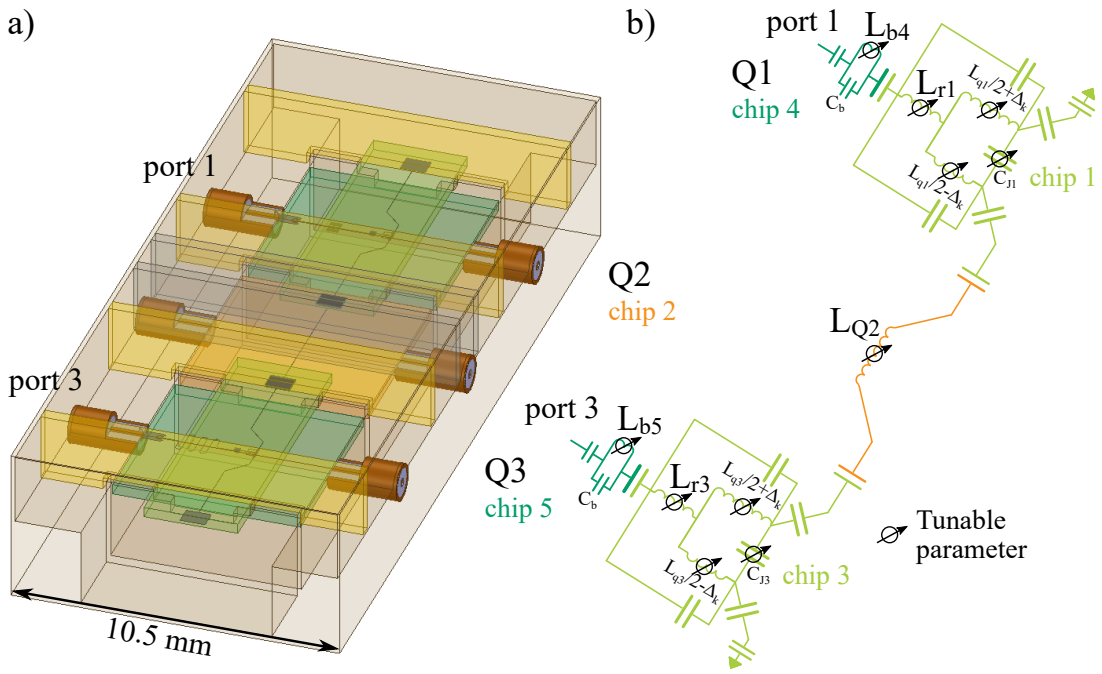

Figure A.9.: **Full box simulations.** **a)** Simplified sample box to reduce meshing complexity used for full-box simulations. All components are made partially transparent for better visibility. Qubit chips are shown in light green, control chips in dark green, the coupler chip in orange, the walls attached to the lid between the enclosures in gold, and the wall above the coupler chip in silver. **b)** Equivalent circuit model used in the simulations, including all tunable lumped elements. The color of each circuit element corresponds to the chip coloring in panel a). The coupler chip is simplified and contains only a tunable inductance, which allows control of the chip's resonance frequency.

All simulations in this subsection are performed in the sample box shown in Fig. A.9. The outer enclosures with the control and qubit chips include detailed models of the band-pass filters and QR-systems equipped with capacitive extenders. The coupler chip is simplified compared to the chips shown in Fig. 4.1 and modeled as a $\lambda/2$ resonator with two coupling pads at the ends and a tunable inductance L_{Q2} in the middle. Depending on the simulation goal, slight adaptations to the box are made, such as using different band-pass filter designs, varying the type of capacitive extenders, or changing the number of shielding walls between the enclosures.

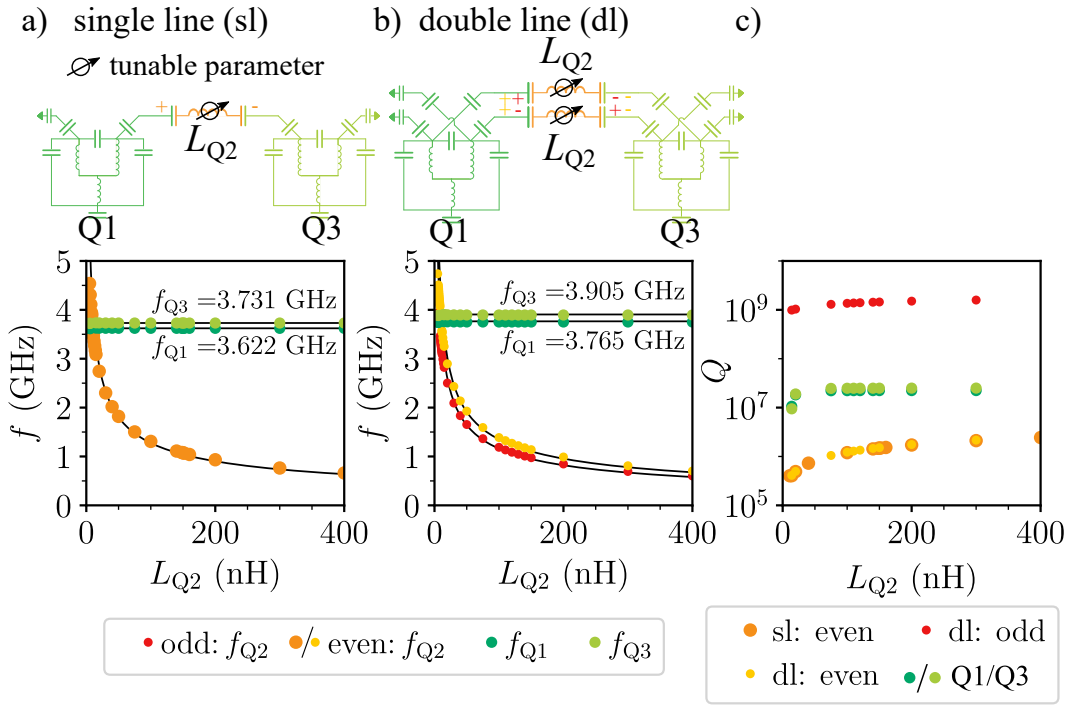

Figure A.10.: **Simulations with single-line (sl) and double-line (dl) capacitive extenders.** All simulations are performed in the sample box shown in Fig. A.9 with the ANSYS eigenmode solver. **a)** Frequencies of the qubit modes (green) and the coupler mode (orange) as a function of the coupler inductance L_{Q2} using a single-line capacitive extender, as indicated in the sketch above the plot. **b)** Same simulation as in a), but using a double-line capacitive extender. In this case, two coupler modes appear: an even mode (gold) where both capacitive extenders charge symmetrically (++ to −−) and an odd mode (red) where the two extenders charge anti-symmetric (+− to −+). Note, that the two tunable inductances L_{Q2} on the coupler chip can not be varied independently. **c)** Simulated quality factors Q of the coupler modes for single-line and double-line configurations. The odd mode of the double-line coupler exhibits a significantly higher Q factor than the even modes. The green Q-factors of the qubits are a lower bound.

When designing the sample box we simulated different extender types as shown in Fig. A.10, comparing single-line and double-line capacitive extenders. The idea of the double-line extender is to use a differential mode between the two parallel strips that charge with opposite polarity, thereby concentrating the electric field between them.

For the single-line extender, a single coupler mode is obtained which can be tuned in frequency via a tunable inductance L_{Q2}. In contrast, the double-line configuration supports two modes: an even mode, where both extenders charge symmetrically (identical to the single-line mode), and an odd mode, where the extenders charge antisymmetrically and the electric field is concentrated between them. The odd mode has a quality factor three orders of magnitude higher than the even mode, making it an attractive candidate for the coupler mode. However, the double-line design inevitably retains the even mode, and suppressing it would require at least a second independently tunable inductance. Since this would add considerable complexity to the system, we chose to use the simpler single-line capacitive extender design

for the proof-of-principle demonstration of our architecture.

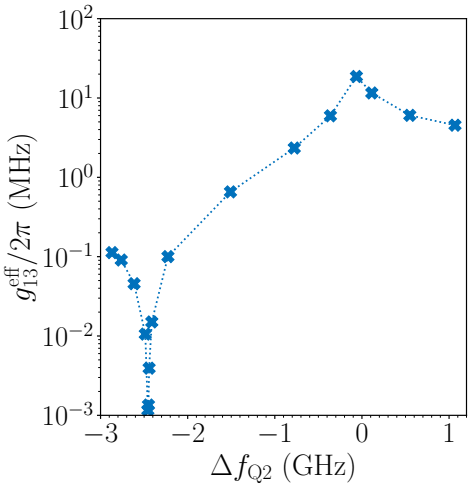

Figure A.11.: **Simulated effective coupling $\mathbf{g_{13}^{eff}/2\pi}$ between Q1 and Q3** as a function of the coupler detuning Δf_{Q2}, extracted from avoided crossings in ANSYS eigenmode simulations. The simulations are performed in the box shown in Fig. A.9 without control chips. We simulate a maximum coupling of $g_{13}^{\mathrm{eff,\,max}}/2\pi \approx 19\,\mathrm{MHz}$ and a point of destructive interference of $\Delta f_{\mathrm{Q2}} \approx -2.5\,\mathrm{GHz}$.

Using the single-line capacitive extenders ($f_{\mathrm{Q1,sim}} = 3.662\,\mathrm{GHz}$ and $f_{\mathrm{Q3,sim}} = 3.731\,\mathrm{GHz}$) and the sample box shown in Fig. A.9, we simulate g_{13}^{eff} by analyzing avoided level crossings when driving Q3 through Q1 for different coupler detunings Δf_{Q2} (set by sweeping L_{Q2}). In Fig. A.11 the simulated values of g_{13}^{eff} are plotted as a function of Δf_{Q2}. The simulation yields a maximum coupling of $g_{13}^{\mathrm{eff,max}}/2\pi \approx 19\,\mathrm{MHz}$ and a point of destructive interference at $\Delta f_{\mathrm{Q2}} \approx -2.5\,\mathrm{GHz}$.

Encouraged by these results, we implemented the architecture experimentally as described in Chapter 4. If we compare the simulated data in Fig. A.11 to the measured data in Fig. 4.13, we obtain good qualitative agreement. The quantitative differences can be attributed to the simplifications made in the simulation, such as modeling the coupler chip with a tunable inductance rather than a GFQ and using larger coupling pads.

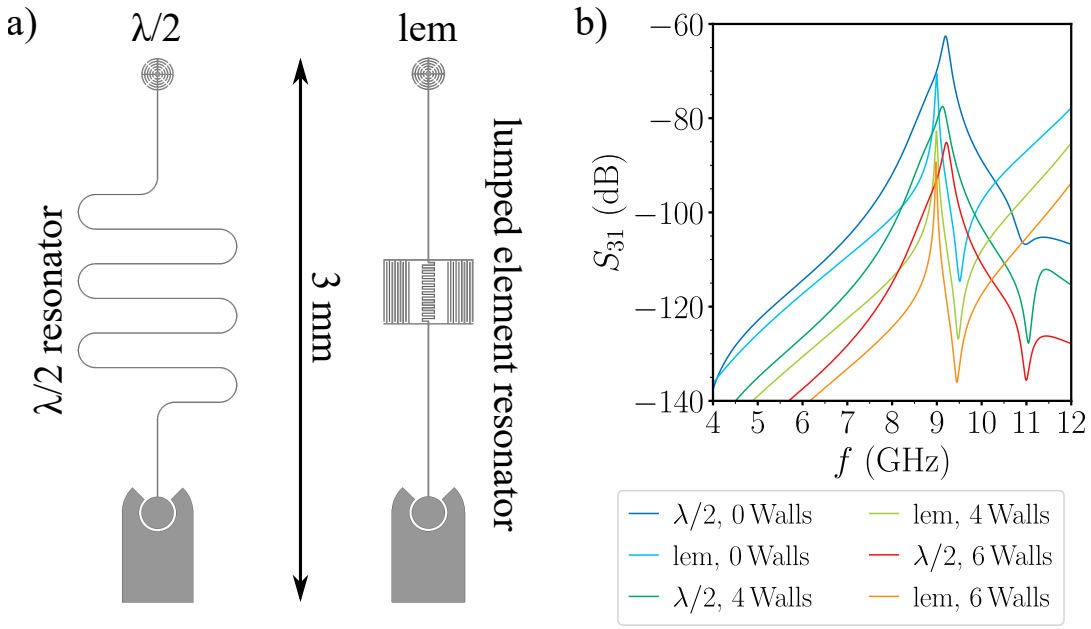

Figure A.12.: **Simulated crosstalk of band-pass filters on the control chips using $\lambda/2$ or lumped element (lem) resonators.** All simulations are performed in the box shown in Fig. A.9 without qubit or coupler chips and with different numbers of shielding walls, obtained with ANSYS driven modal simulations. **a)** Geometry of the two resonator types used as band-pass filters on the control chip. **b)** Simulated crosstalk S_{31} between port 1 and port 3 for both resonator types. The band-pass filters have a resonance frequency of $f_b \approx 9\,\text{GHz}$. Curves correspond to a different number of shielding walls: reddish = six walls (full shielding), green = the four golden walls, and blue = no walls.

To minimize crosstalk between the outer enclosures in our architecture, we simulated different types of band-pass filters with resonance frequencies around $f_b \approx 9\,\text{GHz}$ in combination with varying numbers of shielding walls between the enclosures (see Fig. A.9). The results are shown in Fig. A.12. The simulations indicate that the highest isolation is achieved using a lumped-element band-pass filter together with six shielding walls, which we use in our architecture.

A.10. Low-pass filters for the FBLs

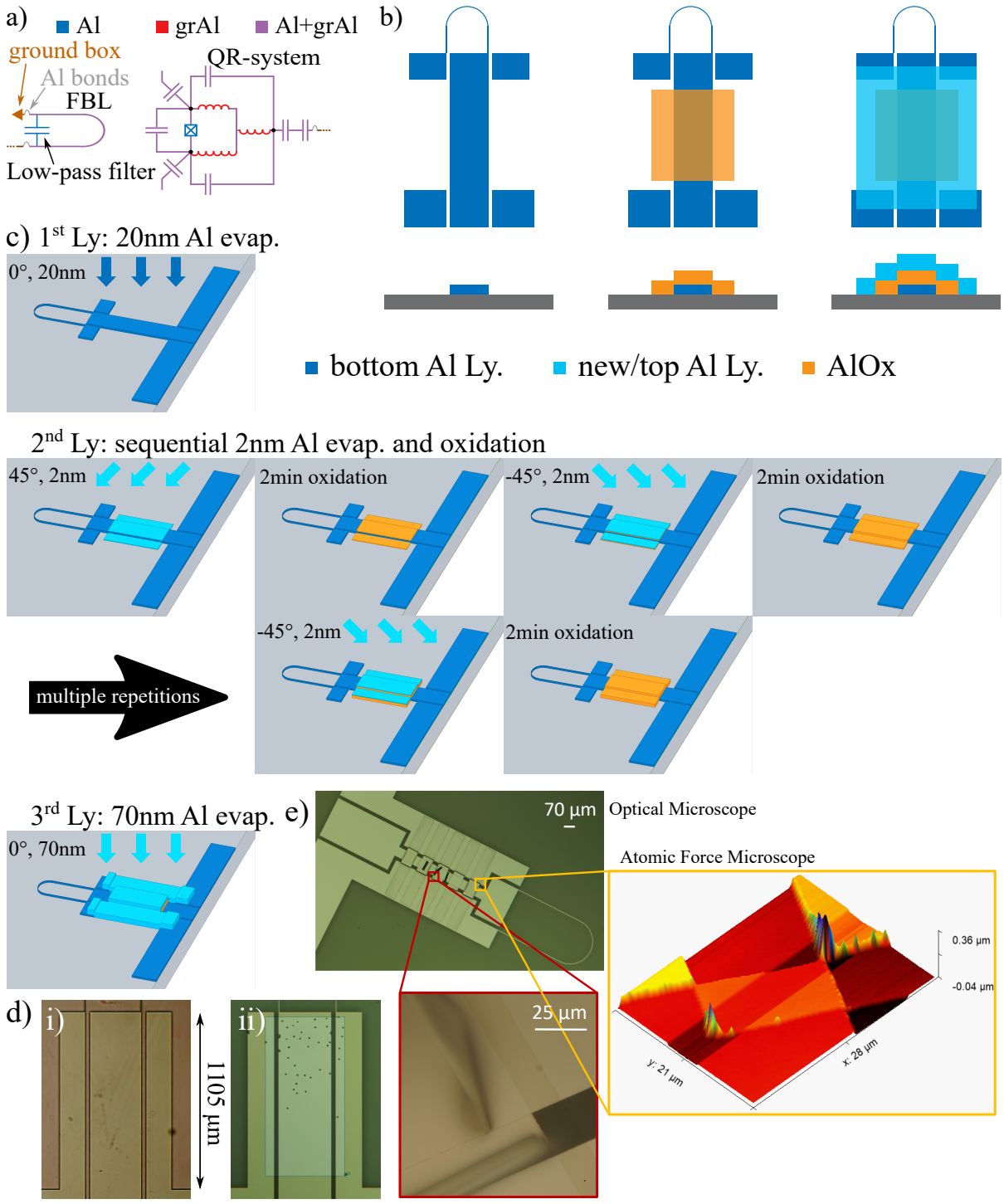

Figure A.13.: **Attempts to implement a low-pass filter for the FBL. a)** Schematic of the FBL inductively coupled to the QR-system. A capacitance is introduced between the FBL input and the ground connection. A sufficiently large capacitance prevents qubit photons from leaking out of the (lossless) sample box into the coaxial cable. **b)** Concept of realizing this capacitance as a parallel-plate capacitor formed by two Al films separated by an AlO_x dielectric ($\varepsilon_r \approx 10$). **c)** Working fabrication process: first a 20 nm bottom Al layer (dark blue) is deposited. A second optical mask is then used to define the capacitor barrier by sequential angled evaporations of 2 nm Al at ±45°, each followed by 2 min oxidation. This sequence is repeated until an oxide barrier thickness of ≈ 40 nm is obtained. Finally, a third optical lithography step defines a 70 nm Al top layer to connect both sides of the FBL. **d)** Problems encountered with this approach: when performing e-beam lithography for the second and third layers, the bottom Al film often ruptures. In (i) the bottom layer before e-beam lithography is shown, while in (ii) the same region after e-beam lithography displays black spots indicating the ruptures. **e)** As an alternative, atomic layer deposition (ALD) was used to form the AlO_x barrier. However, atomic force microscopy revealed sharp tips at the film edges, which may cause peeling or rolling-off of the top Al layer.

In the initial design of the architecture, we aimed to equip not only the coupler qubit but also the outer qubits with FBLs. To suppress qubit decay through the FBLs, we planned to integrate low-pass filters directly into the lines. The concept is to insert a capacitor into the FBL input as shown in Fig. A.13a, which acts as a potential barrier by providing a low impedance at qubit frequencies and thereby preventing photons from leaking into the coaxial cable. As discussed in Ref. [187], planar two-dimensional designs do not yield sufficient capacitance, which motivated us to use a full three-dimensional plate-capacitor geometry with a dielectric barrier, requiring three separate evaporation steps. The developed process is illustrated in Fig. A.13b,c and consists of three optical lithography steps, each using a dedicated mask. In the first step, a 20 nm Al base layer is evaporated. In the second step, the capacitor barrier is formed by sequentially evaporating 2 nm thick Al layers at ±45°, each followed by oxidation, ensuring complete coverage of the base layer and preventing shunts through the AlO_x barrier. Repeating this sequence produces an AlO_x barrier of about 40 nm thickness. In the final step, a 70 nm Al top layer is evaporated, connecting both sides of the FBL and completing the plate capacitor.

During the development of this procedure we tested several alternative approaches that were not successful. Here we summarize the most important insights from these failures. For the second and third evaporation steps, optical lithography proved essential: when e-beam lithography was used instead, the bottom Al layer frequently ruptured („exploded“), as shown in Fig. A.13d. It is well established that e-beam exposure can induce structural damage and plastic deformation in thin Al and AlO_x films, which provides a likely explanation for our observations [188, 189, 190]. As an alternative, we also explored atomic layer deposition (ALD) for the oxide barrier. However, the third Al layer often peeled off after lift-off, as shown in Fig. A.13e. Atomic force microscopy revealed sharp spikes at the barrier edges, which likely caused the instability of the top Al film.

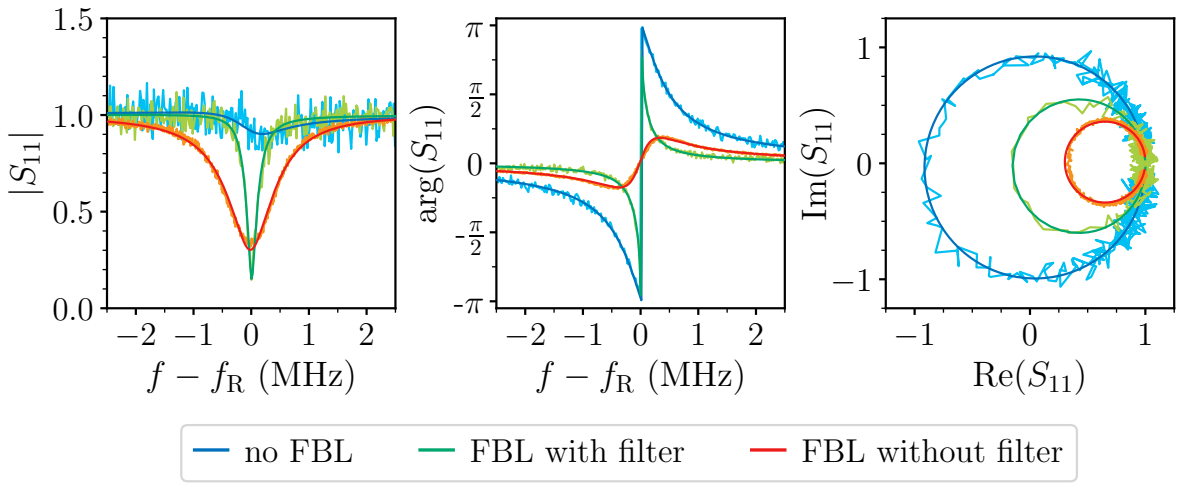

Figure A.14.: **Measured reflection response of the readout resonator with and without FBLs.** The blue curve shows the case without an FBL, where the resonance is sharp and nearly all power is reflected, indicating minimal loss. Adding an unfiltered FBL (red curve) introduces a strong additional loss channel. When a low-pass filter is added to the FBL (green curve), this loss is substantially reduced, and the resonator remains closer to the no-FBL case. Measurements were performed over the span of two years on different devices. The blue and red dataset were taken on devices without capacitive extenders, while the green dataset was measured on a device with capacitive extenders. No coupler chip was mounted in e2.

To verify the effect of the FBL on the readout resonator, we compared three different control chips with no FBL, an unfiltered FBL, and an FBL equipped with an on-chip low-pass filter. The corresponding measurements are shown in Fig. A.14. Without an FBL, the resonator has a nearly lossless response in which almost all incident power is reflected. The phase response shows a clear 2π roll, which is essential for dispersive qubit readout, as the qubit state is inferred from shifts in the resonator frequency. Adding an unfiltered FBL drastically modifies the response: the resonance dip deepens significantly, indicating strong coupling of the resonator to the FBL and additional dissipation through this channel. The corresponding phase roll is suppressed. The low-pass filter improves the phase response towards a 2π roll. Note that the measurements were taken over a year apart with different band-pass filters on the chips, and only single datasets are available for the FBL cases. The results therefore illustrate qualitative trends only.

In the final design of our architecture, we chose not to implement the FBL with low-pass filter for the outer qubits in order to maintain simplicity (implementing the low-pass filter entails multiple additional cleanroom steps) and ensure a clean microwave environment. Since the FBL would be located on the control chip rather than on the qubit chip, its implementation would also demand more precise chip alignment. Finally, because our architecture provides excellent qubit-qubit isolation, it is not necessary to tune the qubits in and out of resonance during operation, making FBLs unnecessary for the outer qubits.

A.11. Aluminum sample box

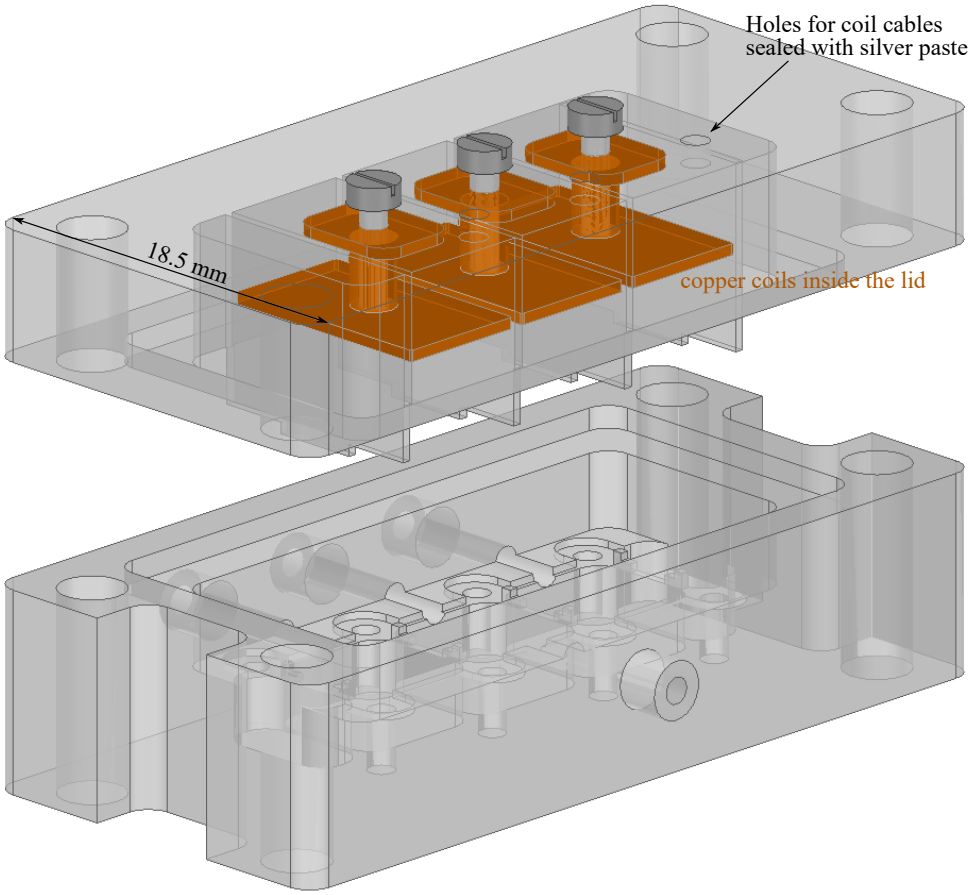

Figure A.15.: **Aluminum sample box.** The bottom part of the box is identical to the copper version, while the lid differs. Copper coils for static flux biasing are integrated inside the lid as no magnetic field can penetrate from the outside into the box. The coils are mounted to the lid using M1.2 titanium screws with a length of 3 mm. Holes for the coil cables are made into the lid and sealed with silver paste.

To reduce magnetic crosstalk between neighboring enclosures, we designed an Al sample box (see Fig. A.15). Superconducting Al screens magnetic fields in length scales of the London penetration depth λ_L ($\lambda_L \approx 45\,\text{nm}$ for Al [103]). As shown in Tab. A.6, the crosstalk between neighboring enclosures is not significantly reduced compared to the copper box. The bottom plate of the copper coils must be in electrical contact with the enclosure walls to push parasitic modes above 20 GHz. We make this contact with solder containing lead, which becomes superconducting. A superconducting box also reduces losses from currents in the box ground. In our setup, this mechanism does not limit coherence, as discussed in section 4.1.

$1/M_{ij}$	j=1 (mA/Φ_0)	j=2 (mA/Φ_0)	j=3 (mA/Φ_0)
i=1	3.17 (100 %)	49.8 (6.4 %)	148 (2.1 %)
	29.0 (100 %)	508 (5.7 %)	< 3600 (< 0.8 %)
i=2	52.7 (8.8 %)	4.68 (100 %)	58.7 (8.0 %)
	–	–	–
i=3	106 (2.3 %)	33.4 (7.2 %)	2.4 (100 %)
	< 4000 (< 0.5 %)	469 (4.6 %)	21.8 (100 %)

Table A.6.: **Comparison of flux crosstalk in a copper and Al box.** Mutual inductances $1/M_{ij}$ in mA/Φ_0 between the coils mounted on top of each enclosure and the corresponding QR systems. The index i labels the QR systems and j the coils. Values in orange correspond to the copper box, while values in grey correspond to the aluminum box. For each row, the relative crosstalk between coil j and QR system i is given in brackets, normalized to the on-diagonal value $1/M_{ii}$ (defined as 100 % crosstalk).

A.12. Magnetic flux hose

Thanks to a collaboration with the research group of Gerhard Kirchmair in Innsbruck, Austria, we received a magnetic flux hose to test with our modular architecture. For completeness, we summarize Ref. [191] and insights from discussions with Philipp Straub (Kirchmair group) in the following paragraph.

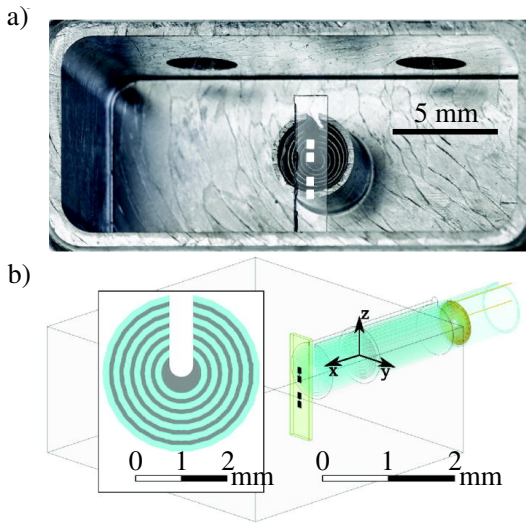

Figure A.16.: **Magnetic flux hose in waveguide**, figure and caption taken from [191]. **a)** Photograph of one half of a rectangular waveguide cavity with two transmon qubits fabricated on sapphire pieces separated by a distance of about 3 mm. The cavity has a hole in the middle of the back wall to attach a magnetic hose. **b)** Schematic of the setup highlighting the hose, with a coil (yellow) on the external side and a qubit (black structures on the two pieces of sapphire (green)) on the other. Inset: Cross section of the hose, showing the shell structure (grey = ferromagnetic layers, light blue = superconducting layers) with a vertical cut.

A magnetic hose is a metamaterial structure designed to transport magnetic flux through a superconducting enclosure without compromising coherence times. It allows fast magnetic flux control within timescales < 100 ns for qubits embedded in 3D structures [191]. A hose as described in [191] consists of concentric cylindrical layers alternating between ferromagnetic ($\mu_r \gg 1$) and superconducting ($\mu_r \to 0$) materials, as shown in Fig. A.16[ii]. The ferromagnetic layers provide high axial magnetic permeability ($\mu_\parallel \to \infty$), while the superconducting layers suppress radial magnetic field components ($\mu_\perp \to 0$), effectively guiding the magnetic field along the hose axis. This allows the magnetic field to be focused on a target qubit. To prevent the formation of screening currents that would otherwise enforce flux quantization, all layers are longitudinally cut. This enables the transport of fast time-varying fields on the order of 100 MHz (limited by the coil). In addition to flux transport, the hose also acts as an effective microwave filter. The outer superconducting layer acts as a $\lambda/4$ resonator that reflects electromagnetic waves below a threshold frequency, while the longitudinal cut acts as a waveguide with a cutoff frequency. For the example hose shown in Fig. A.16 the resonator reflects all frequencies $\leq$10 GHz, while the waveguide has a cutoff frequency > 60 GHz. This minimizes microwave leakage and protects the qubit from decoherence.

[ii]The devices used in this work employ a newer version of the flux hose design described in Ref. [191]. Details of the updated design are not disclosed.

Intuitively, a hose through a superconducting enclosure seems to contradict flux quantization. However, since the magnetic field is guided in and out through the same opening, the net flux remains zero.

Integration of the magnetic flux hoses into the architecture

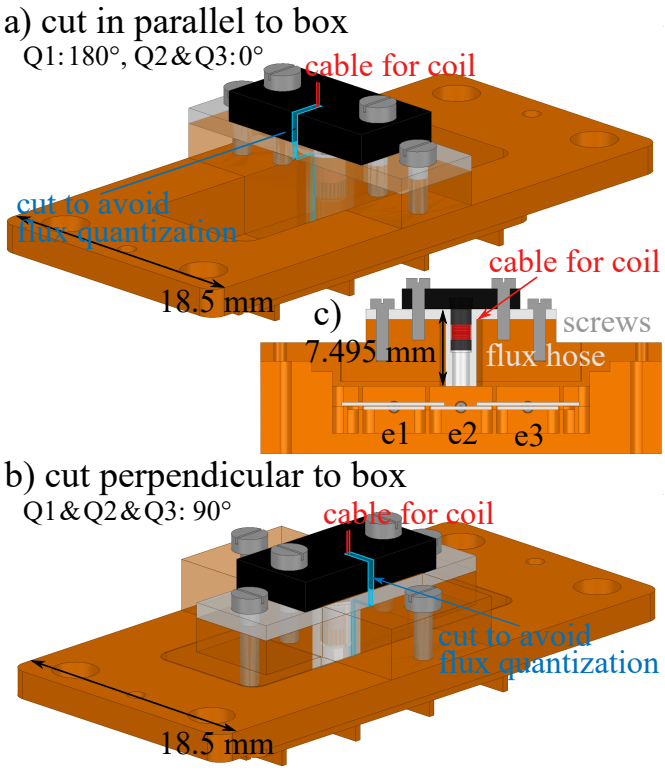

Figure A.17.: **Integrating flux hoses into the architecture. a,b)** Adapter structures in the lid allow the integration of flux hoses into the box. The panels show two possible orientations of the cut in the hose (a: parallel, b: perpendicular to the box). The orientation of this cut strongly affects magnetic crosstalk, see Tab. A.7 **c)** Cross-section of the box with adapter and flux hose mounted in the middle enclosure. This flux hose has a length of 7.495 mm.

device	1/M(0°) [mA/Φ_0]	1/M(90°) [mA/Φ_0]	1/M(180°) [mA/Φ_0]
Q2	9.2	8.6	–
Q1	–	123.4	3400
Q3	70.8	82.1	–

Table A.7.: **Crosstalk measurements between the flux hose above Q2 (the coupler)**, equipped with a coil that has 35 windings. The mutual inductance $1/M$ between the flux hoses and the qubits depends strongly on the orientation of the cut in the hose. The number in brackets indicates the rotation angle of the cut relative to the qubit (black for 0° and 180° measured during cooldown 1, and grey for 90° measured during cooldown 2). The hose is positioned in the center above Q2.

We integrate flux hoses to reduce magnetic crosstalk between neighboring enclosures and to possibly replace on-chip FBLs (the latter still needs to be tested). We use a flux hose with a length of 7.495 mm that we can equip with two different coils that have 5 or 35 windings. Fig. A.17 shows the integration of flux hoses in the lid and illustrates how the orientation of the cut in the hose affects magnetic crosstalk. The corresponding crosstalk measurements between neighboring enclosures with the coil that has 35

windings are summarized in Tab. A.7. Depending on the orientation of the cut, magnetic crosstalk varies by approx. two orders of magnitude. Minimal crosstalk is achieved when the cut is rotated by 180° away from the qubit, resulting in a crosstalk of $9.2/3400 \approx 0.3\,\%$. This is a reduction of magnetic crosstalk by more than an order of magnitude compared to the individual coils in the copper or Al box (see Tab. 4.1 and App. A.11).

A.13. Avoided level crossings

Avoided level crossings for Fig. 4.13

In Fig. A.18, Fig. A.19, Fig. A.20 and Fig. A.21 we show the measured avoided level crossings between Q1 and Q3 for different coupler detunings Δf_{Q2}, which are used in Fig. 4.13. The avoided level crossings are obtained by sweeping f_{Q3} through f_{Q1}, which is kept constant during measurements. Data points and curves in red are obtained from two-tone spectroscopy on Q1, while those in blue are measured using Ramsey fringes on Q1. For each subplot, the corresponding coupler detuning Δf_{Q2} and extracted coupling strength g_{13}^{eff} are indicated. Black lines show fits using the extracted g_{13}^{eff}, and the shaded regions around the fits represent the fit uncertainties.

Avoided level crossings for population swaps

In Fig. A.22a we show the effective coupling strength g_{13}^{eff} vs. the coupler detuning Δf_{Q2} during a pervious cooldown using the same setup[iv]. Here we extract a maximum coupling strength of $g_{13}^{\mathrm{eff,max}} \approx 2.5\,\mathrm{MHz}$, which is in good agreement with the time needed to swap excitations between Q1 and Q3 ($T_{\mathrm{swap}} \approx 112\,\mathrm{ns}$). In Fig. A.22b,c and Fig. A.23 we show the measured avoided level crossings between Q1 and Q3 for different coupler detunings $\Delta f_{\mathrm{Q2}} \equiv \Delta f_{\mathrm{c}}$, which are used in Fig. A.22a. The avoided level crossings are obtained by sweeping f_{Q3} through f_{Q1}, which is kept constant during measurements.

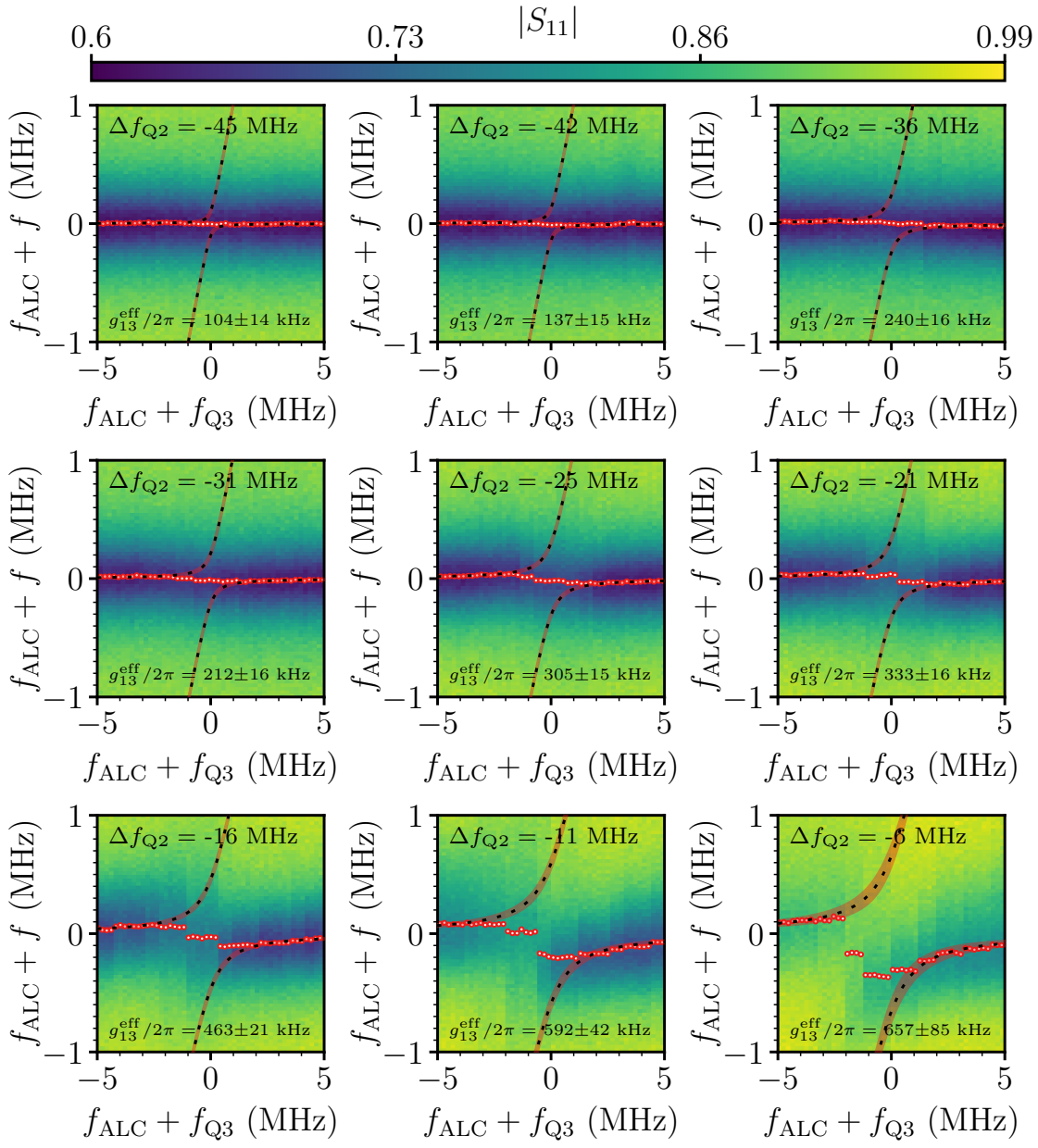

Figure A.18.: **Avoided level crossings** measured using two-tone spectroscopy on Q1 for coupler detunings in the range of $-45\,\mathrm{MHz} \leq \Delta f_{Q2} \leq -6\,\mathrm{MHz}$. The colormap displays the magnitude of the reflection coefficient $|S_{11}|$. The horizontal axis is expressed as f_{ALC}+f_{Q3}, where f_{ALC} denotes the center frequency of the avoided level crossing.

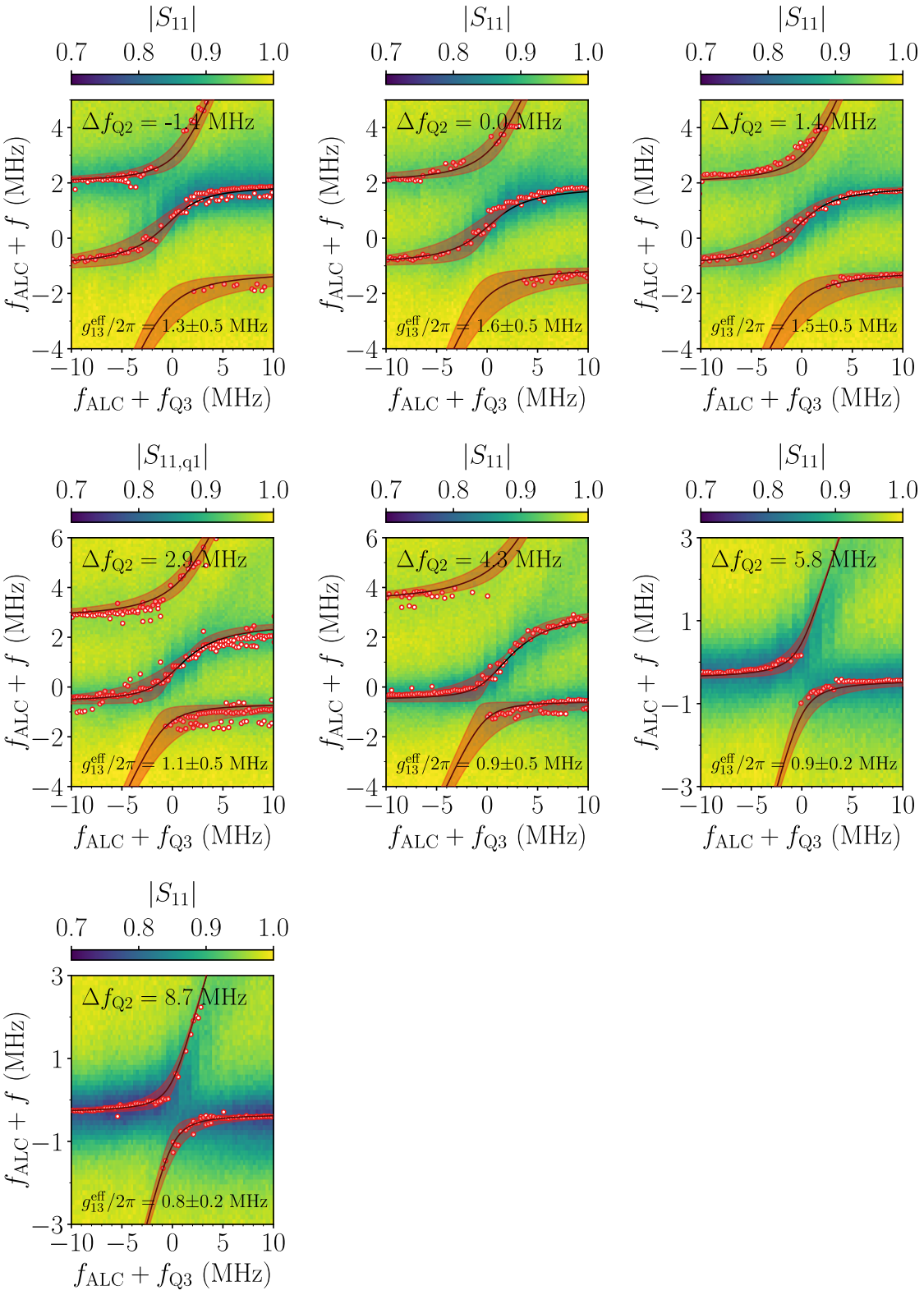

Figure A.19.: **Avoided level crossings** measured using two-tone spectroscopy on Q1 for coupler detunings in the range of $-1.4\,\mathrm{MHz} \leq \Delta f_{Q2} \leq 8.7\,\mathrm{MHz}$. The colormaps displays the magnitude of the reflection coefficient $|S_{11}|$. The horizontal axis is expressed as f_{ALC}+f_{Q3}, where f_{ALC} denotes the center frequency of the avoided level crossing.

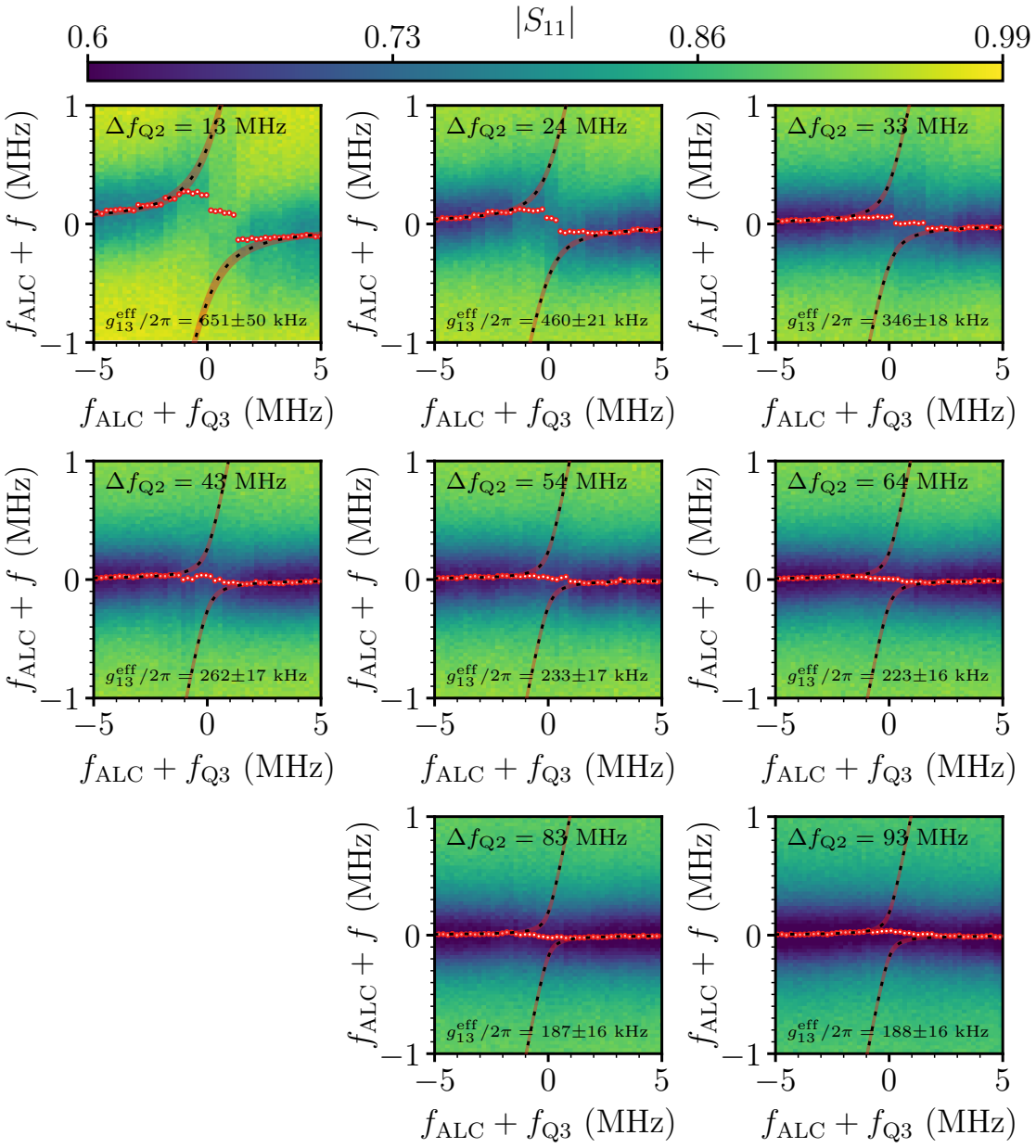

Figure A.20.: **Avoided level crossings** measured using two-tone spectroscopy on Q1 for coupler detunings in the range of 13 MHz $\leq \Delta f_{Q2} \leq$ 92 MHz. The colormap displays the magnitude of the reflection coefficient $|S_{11}|$. The horizontal axis is expressed as f_{ALC}+f_{Q3}, where f_{ALC} denotes the center frequency of the avoided level crossing.

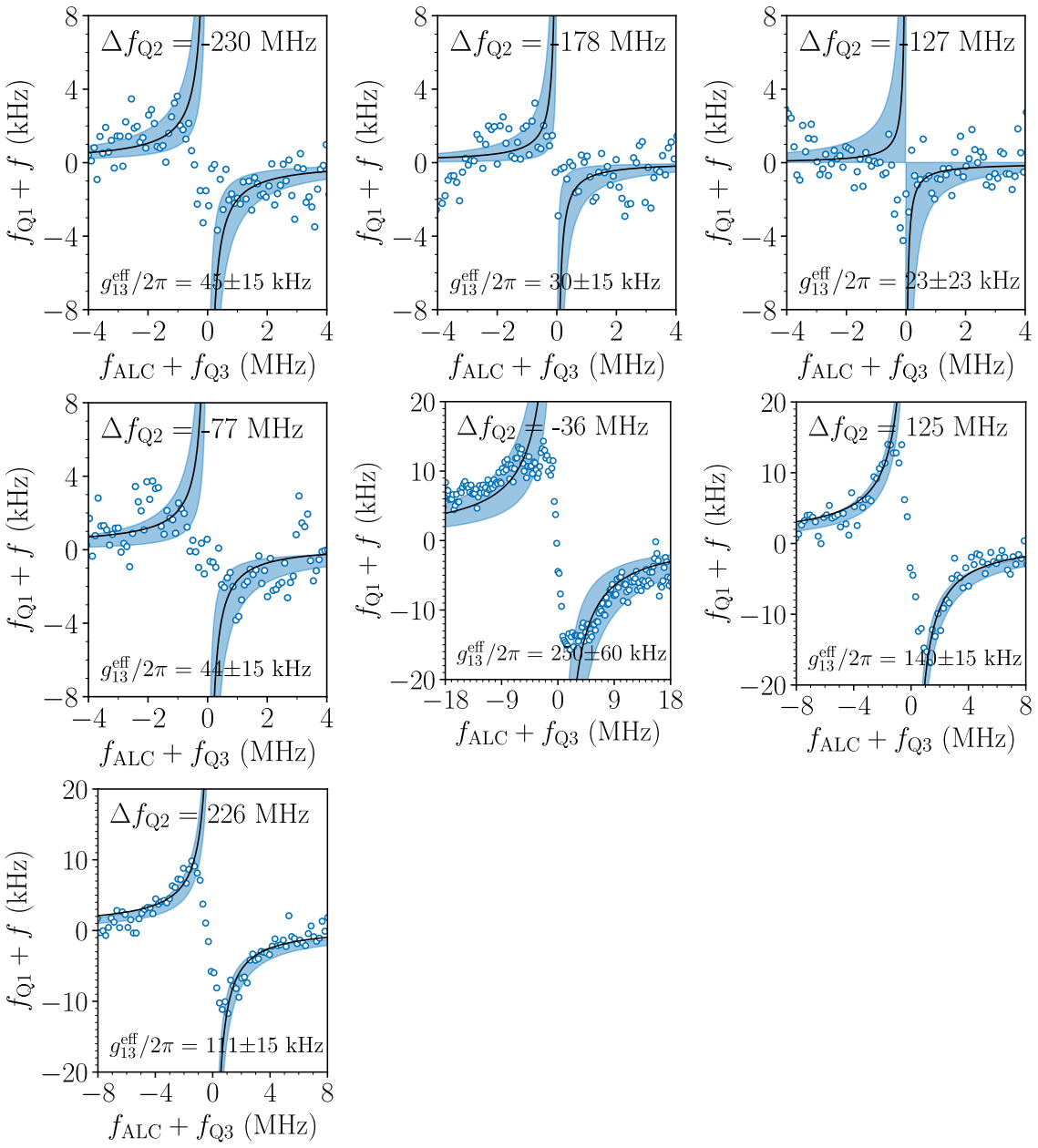

Figure A.21.: **Avoided level crossings** measured using Ramsey fringes on Q1 for different coupler detunings Δf_{Q2}. The horizontal axis is expressed as f_{ALC}+f_{Q3}, where f_{ALC} denotes the center frequency of the avoided level crossing. f_{Q1} = 3.465 GHz is constant during measurements.

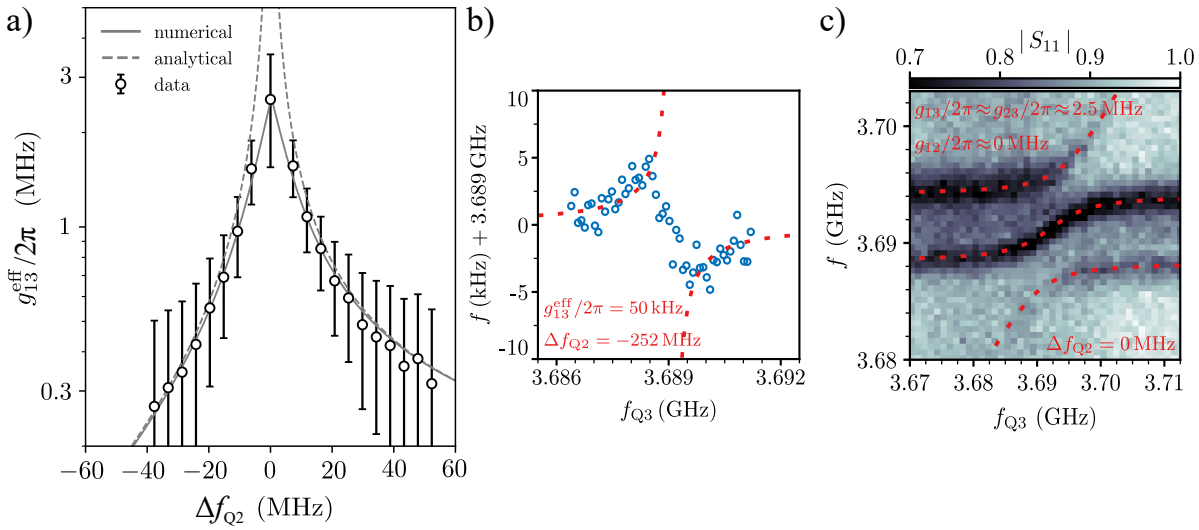

Figure A.22.: **Effective qubit-qubit coupling strength and avoided level crossings**, figure and caption taken from [157]. **a)** Measured effective coupling strength $g_{13}^{\text{eff}}/2\pi$ between Q1 and Q3 operated on resonance ($f_{Q1} = f_{Q3} = 3.689\,\text{GHz}$) as a function of the coupler detuning Δf_{Q2}. The error bars represent the spectroscopic linewidth of the f_{Q1} transition used to extract the level splittings. The solid and dashed curves show numerical and analytical results obtained from an effective two-qubit model using a Schrieffer-Wolff transformation (see App. A.8). **b,c)** Avoided level crossings between Q1 and Q3 measured for $\Delta f_{Q2} = -252\,\text{MHz}$ (bp off) and $\Delta f_c = 0\,\text{MHz}$ (bp on). For $\Delta f_c = -252\,\text{MHz}$ we use Ramsey fringes to determine f_{q1}, while for $\Delta f_c = 0\,\text{MHz}$ spectroscopy on Q1 is performed. The colormaps show the magnitude of the reflected measurement signal $|S_{11}|$, with the extracted g_{13} values indicated in red and the dashed red lines corresponding to fits.

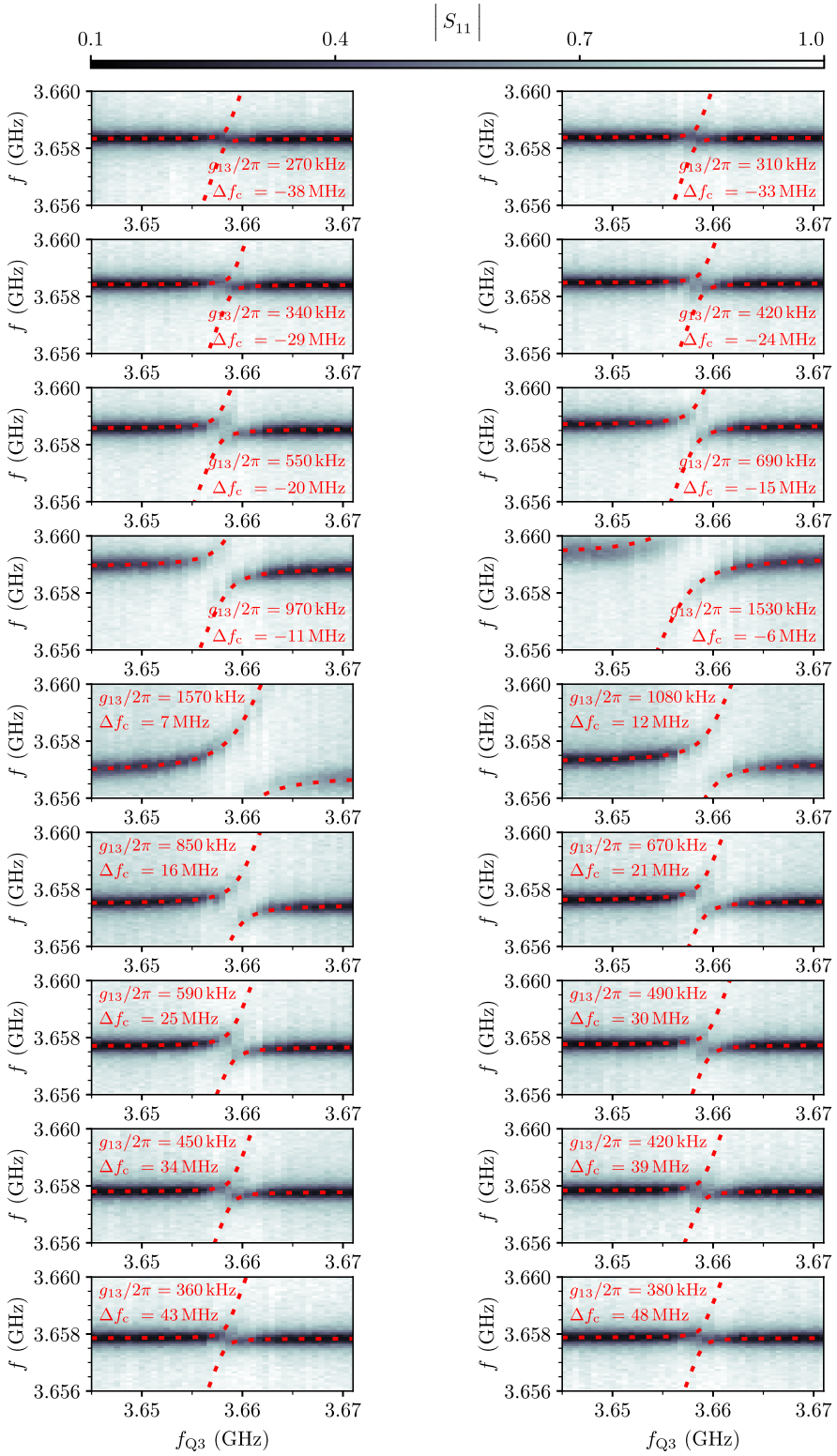

Figure A.23.: **Avoided Level Crossings between Q1 and Q3 for different coupler detunings $\Delta f_{Q2} \equiv \Delta f_c$**, figure and caption taken from [157]. Measurements are performed by using spectroscopy on Q1. The colormap shows the amplitude of the reflected measurement signal on Q1, $|S_{11}|$. The extracted g_{13} values from the fits (dashed red lines) are listed in red.

B. Acknowledgments

First of all, I would like to thank Prof. Ioan M. Pop for his guidance and advice, and for setting an inspiring example of scientific intuition that has made my PhD an exciting journey. I greatly appreciated our discussions about science and life and numerous excursions and hikes. I am deeply grateful to Prof. Wolfgang Wernsdorfer for his help with the BlueFors cryostat and for the countless late-night shifts he spent to ensure that our system was always running reliably. Finally, I would like to thank Prof. Sebastian Kempf for introducing me to the field of superconducting electronics during my Master thesis and for establishing the contact to the Black Forest Quantum (BFQ) group.

I thank all members of the BFQ group for creating a great working environment and company throughout these years. I thank Roudy, Zhongyi, and Gabriel for their dedicated efforts and valuable contributions to our shared projects. Many thanks to the second-floor workshop, in particular to Maik, for going to their limits in order to build the many complicated sample boxes.

Thanks go to Martin, Patrick W., and Mathieu for the many inspiring discussions about the project, as well as for their practical advice on measurements and cleanroom work. I also thank Lucas, Silvia, and Bettina for their valuable assistance during wafer and chip fabrication. I am grateful to the amplifier team, NicoZ and Mitchell, for providing quantum-limited amplifiers, to NicoG for always helping whenever problems arose with the Quantum Machines hardware, and for Patrick P. for his help with the cryostat. Thanks also to Denis for good times in the CFN office, and to Ameya for the collegial atmosphere, engaging discussions, and her great cooking.

Very special thanks go to my colleague Simon Geisert, with whom I shared this PhD project. Thank you for your help with measurements, brainstorming, and shared suffering during fabrication and bonding, as well as for all the late-night shifts mounting samples into the fridge. I also thank Paul and Philipp for their contributions and support with the project, and Thomas Reisinger for handling so many purchases for the group.

I am grateful to my best friend Franz for his encouragement and for all the great (bicycle) tours we made together. Finally, I want to thank my girlfriend Ronja for enduring many busy nights, always finding motivating words, and for all the wonderful excursions and shared experiences that provided much-needed breaks from work. Above all, I thank my parents and my sister for their unwavering support throughout this journey.

C. Bibliography

[1] C.L. Degen, F. Reinhard, and P. Cappellaro. Quantum sensing. *Reviews of Modern Physics*, 89(3):035002, July 2017.

[2] Nabeel Aslam, Hengyun Zhou, Elana K. Urbach, Matthew J. Turner, Ronald L. Walsworth, Mikhail D. Lukin, and Hongkun Park. Quantum sensors for biomedical applications. *Nature Reviews Physics*, 5(3):157–169, February 2023.

[3] David P. DiVincenzo. Quantum computation. *Science*, 270(5234):255–261, October 1995.

[4] Artur Ekert and Richard Jozsa. Quantum computation and shor's factoring algorithm. *Reviews of Modern Physics*, 68(3):733–753, July 1996.

[5] Michael A. Nielsen and Isaac L. Chuang. *Quantum computation and quantum information*. Cambridge University Press, Cambridge [u.a.], 10th anniversary ed., repr. edition, 2012.

[6] Frank Arute, Kunal Arya, Ryan Babbush, Dave Bacon, Joseph C. Bardin, Rami Barends, Rupak Biswas, Sergio Boixo, Fernando G. S. L. Brandao, David A. Buell, Brian Burkett, Yu Chen, Zijun Chen, Ben Chiaro, Roberto Collins, William Courtney, Andrew Dunsworth, Edward Farhi, Brooks Foxen, Austin Fowler, Craig Gidney, Marissa Giustina, Rob Graff, Keith Guerin, Steve Habegger, Matthew P. Harrigan, Michael J. Hartmann, Alan Ho, Markus Hoffmann, Trent Huang, Travis S. Humble, Sergei V. Isakov, Evan Jeffrey, Zhang Jiang, Dvir Kafri, Kostyantyn Kechedzhi, Julian Kelly, Paul V. Klimov, Sergey Knysh, Alexander Korotkov, Fedor Kostritsa, David Landhuis, Mike Lindmark, Erik Lucero, Dmitry Lyakh, Salvatore Mandrà, Jarrod R. McClean, Matthew McEwen, Anthony Megrant, Xiao Mi, Kristel Michielsen, Masoud Mohseni, Josh Mutus, Ofer Naaman, Matthew Neeley, Charles Neill, Murphy Yuezhen Niu, Eric Ostby, Andre Petukhov, John C. Platt, Chris Quintana, Eleanor G. Rieffel, Pedram Roushan, Nicholas C. Rubin, Daniel Sank, Kevin J. Satzinger, Vadim Smelyanskiy, Kevin J. Sung, Matthew D. Trevithick, Amit Vainsencher, Benjamin Villalonga, Theodore White, Z. Jamie Yao, Ping Yeh, Adam Zalcman, Hartmut Neven, and John M. Martinis. Quantum supremacy using a programmable superconducting processor. *Nature*, 574(7779):505–510, October 2019.

[7] Iulia Buluta and Franco Nori. Quantum simulators. *Science*, 326(5949):108–111, 2009.

[8] I.M. Georgescu, S. Ashhab, and Franco Nori. Quantum simulation. *Reviews of Modern Physics*, 86(1):153–185, March 2014.

[9] Francesco Tacchino, Alessandro Chiesa, Stefano Carretta, and Dario Gerace. Quantum computers as universal quantum simulators: State-of-the-art and perspectives. *Advanced Quantum Technologies*, 3(3), December 2019.

[10] L.-M. Duan, M. D. Lukin, J. I. Cirac, and P. Zoller. Long-distance quantum communication with atomic ensembles and linear optics. *Nature*, 414(6862):413–418, November 2001.

[11] Nicolas Gisin and Rob Thew. Quantum communication. *Nature Photonics*, 1(3):165–171, March 2007.

[12] L. Steffen, Y. Salathe, M. Oppliger, P. Kurpiers, M. Baur, C. Lang, C. Eichler, G. Puebla-Hellmann, A. Fedorov, and A. Wallraff. Deterministic quantum teleportation with feed-forward in a solid state system. *Nature*, 500(7462):319–322, August 2013.

[13] John Singleton. *Band Theory and Electronic Properties of Solids*. Oxford University PressOxford, August 2001.

[14] Alexander M. Gabovich, Volodymyr I. Kuznetsov, and Alexander I. Voitenko. Tunneling as a marker of quantum mechanics (review article). *Low Temperature Physics*, 50(11):925–947, November 2024.

[15] Jack D. Hidary. *Superposition, Entanglement and Reversibility*, pages 3–9. Springer International Publishing, 2019.

[16] Peter W. Shor. Polynomial-time algorithms for prime factorization and discrete logarithms on a quantum computer. *SIAM Journal on Computing*, 26(5):1484–1509, October 1997.

[17] Lov K. Grover. A fast quantum mechanical algorithm for database search. In *Proceedings of the twenty-eighth annual ACM symposium on Theory of computing - STOC '96*, STOC '96, pages 212–219. ACM Press, 1996.

[18] Richard P. Feynman. Simulating physics with computers. *International Journal of Theoretical Physics*, 21(6–7):467–488, June 1982.

[19] Alán Aspuru-Guzik and Philip Walther. Photonic quantum simulators. *Nature Physics*, 8(4):285–291, April 2012.

[20] Pengfei Wang, Chun-Yang Luan, Mu Qiao, Mark Um, Junhua Zhang, Ye Wang, Xiao Yuan, Mile Gu, Jingning Zhang, and Kihwan Kim. Single ion qubit with estimated coherence time exceeding one hour. *Nature Communications*, 12(1), January 2021.

[21] T.P. Harty, D.T.C. Allcock, C.J. Ballance, L. Guidoni, H.A. Janacek, N.M. Linke, D.N. Stacey, and D.M. Lucas. High-fidelity preparation, gates, memory, and readout of a trapped-ion quantum bit. *Physical Review Letters*, 113(22):220501, November 2014.

[22] C.J. Ballance, T.P. Harty, N.M. Linke, M.A. Sepiol, and D.M. Lucas. High-fidelity quantum logic gates using trapped-ion hyperfine qubits. *Physical Review Letters*, 117(6):060504, August 2016.

[23] Colin D. Bruzewicz, John Chiaverini, Robert McConnell, and Jeremy M. Sage. Trapped-ion quantum computing: Progress and challenges. *Applied Physics Reviews*, 6(2), May 2019.

[24] Karen Wintersperger, Florian Dommert, Thomas Ehmer, Andrey Hoursanov, Johannes Klepsch, Wolfgang Mauerer, Georg Reuber, Thomas Strohm, Ming Yin, and Sebastian Luber. Neutral atom quantum computing hardware: performance and end-user perspective. *EPJ Quantum Technology*, 10(1), August 2023.

[25] Simon J. Evered, Dolev Bluvstein, Marcin Kalinowski, Sepehr Ebadi, Tom Manovitz, Hengyun Zhou, Sophie H. Li, Alexandra A. Geim, Tout T. Wang, Nishad Maskara, Harry Levine, Giulia Semeghini, Markus Greiner, Vladan Vuletić, and Mikhail D. Lukin. High-fidelity parallel entangling gates on a neutral-atom quantum computer. *Nature*, 622(7982):268–272, October 2023.

[26] Joanna W. Lis, Aruku Senoo, William F. McGrew, Felix Rönchen, Alec Jenkins, and Adam M. Kaufman. Midcircuit operations using the omg architecture in neutral atom arrays. *Physical Review X*, 13(4):041035, November 2023.

[27] Sergei Slussarenko and Geoff J. Pryde. Photonic quantum information processing: A concise review. *Applied Physics Reviews*, 6(4), October 2019.

[28] Guido Burkard, Thaddeus D. Ladd, Andrew Pan, John M. Nichol, and Jason R. Petta. Semiconductor spin qubits. *Reviews of Modern Physics*, 95(2):025003, June 2023.

[29] Nard Dumoulin Stuyck, Andre Saraiva, Will Gilbert, Jesus Cifuentes Pardo, Ruoyu Li, Christopher C. Escott, Kristiaan De Greve, Sorin Voinigescu, David J. Reilly, and Andrew S. Dzurak. Cmos compatibility of semiconductor spin qubits, 2024.

[30] The Royal Swedish Academy of Sciences. Press release: The nobel prize in physics 2025. `https://www.nobelprize.org/prizes/physics/2025/press-release/`, 2025. Accessed 2025-10-19.

[31] C. Dickel, J. J. Wesdorp, N. K. Langford, S. Peiter, R. Sagastizabal, A. Bruno, B. Criger, F. Motzoi, and L. DiCarlo. Chip-to-chip entanglement of transmon qubits using engineered measurement fields. *Physical Review B*, 97(6):064508, February 2018.

[32] N. Leung, Y. Lu, S. Chakram, R. K. Naik, N. Earnest, R. Ma, K. Jacobs, A. N. Cleland, and D. I. Schuster. Deterministic bidirectional communication and remote entanglement generation between superconducting qubits. *npj Quantum Information*, 5(1), February 2019.

[33] P. Magnard, S. Storz, P. Kurpiers, J. Schär, F. Marxer, J. Lütolf, T. Walter, J.-C. Besse, M. Gabureac, K. Reuer, A. Akin, B. Royer, A. Blais, and A. Wallraff. Microwave quantum link between superconducting circuits housed in spatially separated cryogenic systems. *Physical Review Letters*, 125(26):260502, December 2020.

[34] Simon Storz, Josua Schär, Anatoly Kulikov, Paul Magnard, Philipp Kurpiers, Janis Lütolf, Theo Walter, Adrian Copetudo, Kevin Reuer, Abdulkadir Akin, Jean-Claude Besse, Mihai Gabureac, Graham J. Norris, Andrés Rosario, Ferran Martin, José Martinez, Waldimar Amaya, Morgan W. Mitchell, Carlos Abellan, Jean-Daniel Bancal, Nicolas Sangouard, Baptiste Royer, Alexandre Blais, and Andreas Wallraff. Loophole-free bell inequality violation with superconducting circuits. *Nature*, 617(7960):265–270, May 2023.

[35] S. Krinner, S. Storz, P. Kurpiers, P. Magnard, J. Heinsoo, R. Keller, J. Lütolf, C. Eichler, and A. Wallraff. Engineering cryogenic setups for 100-qubit scale superconducting circuit systems. *EPJ Quantum Technology*, 6(1), May 2019.

[36] Xiu Gu, Anton Frisk Kockum, Adam Miranowicz, Yu-xi Liu, and Franco Nori. Microwave photonics with superconducting quantum circuits. *Physics Reports*, 718–719:1–102, November 2017.

[37] P. Krantz, M. Kjaergaard, F. Yan, T. P. Orlando, S. Gustavsson, and W. D. Oliver. A quantum engineer's guide to superconducting qubits. *Applied Physics Reviews*, 6(2), June 2019.

[38] A. Wallraff, D. I. Schuster, A. Blais, L. Frunzio, R.-S. Huang, J. Majer, S. Kumar, S. M. Girvin, and R. J. Schoelkopf. Strong coupling of a single photon to a superconducting qubit using circuit quantum electrodynamics. *Nature*, 431(7005):162–167, September 2004.

[39] Alexandre Blais, Arne L. Grimsmo, S.M. Girvin, and Andreas Wallraff. Circuit quantum electrodynamics. *Reviews of Modern Physics*, 93(2):025005, May 2021.

[40] Andreas Reiserer and Gerhard Rempe. Cavity-based quantum networks with single atoms and optical photons. *Reviews of Modern Physics*, 87(4):1379–1418, December 2015.

[41] R. Vijay, D. H. Slichter, and I. Siddiqi. Observation of quantum jumps in a superconducting artificial atom. *Physical Review Letters*, 106(11):110502, March 2011.

[42] Johannes Heinsoo, Christian Kraglund Andersen, Ants Remm, Sebastian Krinner, Theodore Walter, Yves Salathé, Simone Gasparinetti, Jean-Claude Besse, Anton Potočnik, Andreas Wallraff, and Christopher Eichler. Rapid high-fidelity multiplexed readout of superconducting qubits. *Physical Review Applied*, 10(3):034040, September 2018.

[43] François Swiadek, Ross Shillito, Paul Magnard, Ants Remm, Christoph Hellings, Nathan Lacroix, Quentin Ficheux, Dante Colao Zanuz, Graham J. Norris, Alexandre Blais, Sebastian Krinner,

and Andreas Wallraff. Enhancing dispersive readout of superconducting qubits through dynamic control of the dispersive shift: Experiment and theory. *PRX Quantum*, 5(4):040326, November 2024.

[44] I. Takmakov, P. Winkel, F. Foroughi, L. Planat, D. Gusenkova, M. Spiecker, D. Rieger, L. Grünhaupt, A.V. Ustinov, W. Wernsdorfer, I.M. Pop, and N. Roch. Minimizing the discrimination time for quantum states of an artificial atom. *Physical Review Applied*, 15(6):064029, June 2021.

[45] Max Hofheinz, E. M. Weig, M. Ansmann, Radoslaw C. Bialczak, Erik Lucero, M. Neeley, A. D. O'Connell, H. Wang, John M. Martinis, and A. N. Cleland. Generation of fock states in a superconducting quantum circuit. *Nature*, 454(7202):310–314, July 2008.

[46] Max Hofheinz, H. Wang, M. Ansmann, Radoslaw C. Bialczak, Erik Lucero, M. Neeley, A. D. O'Connell, D. Sank, J. Wenner, John M. Martinis, and A. N. Cleland. Synthesizing arbitrary quantum states in a superconducting resonator. *Nature*, 459(7246):546–549, May 2009.

[47] C. Eichler, D. Bozyigit, C. Lang, L. Steffen, J. Fink, and A. Wallraff. Experimental state tomography of itinerant single microwave photons. *Physical Review Letters*, 106(22):220503, June 2011.

[48] C. Eichler, C. Lang, J. M. Fink, J. Govenius, S. Filipp, and A. Wallraff. Observation of entanglement between itinerant microwave photons and a superconducting qubit. *Physical Review Letters*, 109(24):240501, December 2012.

[49] Gerhard Kirchmair, Brian Vlastakis, Zaki Leghtas, Simon E. Nigg, Hanhee Paik, Eran Ginossar, Mazyar Mirrahimi, Luigi Frunzio, S. M. Girvin, and R. J. Schoelkopf. Observation of quantum state collapse and revival due to the single-photon kerr effect. *Nature*, 495(7440):205–209, March 2013.

[50] Brian Vlastakis, Gerhard Kirchmair, Zaki Leghtas, Simon E. Nigg, Luigi Frunzio, S. M. Girvin, Mazyar Mirrahimi, M. H. Devoret, and R. J. Schoelkopf. Deterministically encoding quantum information using 100-photon schrödinger cat states. *Science*, 342(6158):607–610, November 2013.

[51] K. Geerlings, Z. Leghtas, I. M. Pop, S. Shankar, L. Frunzio, R. J. Schoelkopf, M. Mirrahimi, and M. H. Devoret. Demonstrating a driven reset protocol for a superconducting qubit. *Physical Review Letters*, 110(12):120501, March 2013.

[52] K. W. Murch, U. Vool, D. Zhou, S. J. Weber, S. M. Girvin, and I. Siddiqi. Cavity-assisted quantum bath engineering. *Physical Review Letters*, 109(18):183602, October 2012.

[53] S. Shankar, M. Hatridge, Z. Leghtas, K. M. Sliwa, A. Narla, U. Vool, S. M. Girvin, L. Frunzio, M. Mirrahimi, and M. H. Devoret. Autonomously stabilized entanglement between two superconducting quantum bits. *Nature*, 504(7480):419–422, November 2013.

[54] Christian Kraglund Andersen, Ants Remm, Stefania Lazar, Sebastian Krinner, Johannes Heinsoo, Jean-Claude Besse, Mihai Gabureac, Andreas Wallraff, and Christopher Eichler. Entanglement stabilization using ancilla-based parity detection and real-time feedback in superconducting circuits. *npj Quantum Information*, 5(1), August 2019.

[55] Rajeev Acharya, Igor Aleiner, Richard Allen, Trond I. Andersen, Markus Ansmann, Frank Arute, Kunal Arya, Abraham Asfaw, Juan Atalaya, Ryan Babbush, Dave Bacon, Joseph C. Bardin, Joao Basso, Andreas Bengtsson, Sergio Boixo, Gina Bortoli, Alexandre Bourassa, Jenna Bovaird, Leon Brill, Michael Broughton, Bob B. Buckley, David A. Buell, Tim Burger, Brian Burkett, Nicholas Bushnell, Yu Chen, Zijun Chen, Ben Chiaro, Josh Cogan, Roberto Collins, Paul Conner, William Courtney, Alexander L. Crook, Ben Curtin, Dripto M. Debroy, Alexander Del Toro Barba, Sean Demura, Andrew Dunsworth, Daniel Eppens, Catherine Erickson, Lara Faoro, Edward Farhi, Reza Fatemi, Leslie Flores Burgos, Ebrahim Forati, Austin G. Fowler, Brooks Foxen, William Giang, Craig Gidney, Dar Gilboa, Marissa Giustina, Alejandro Grajales Dau, Jonathan A. Gross, Steve Habegger, Michael C. Hamilton, Matthew P. Harrigan, Sean D. Harrington, Oscar Higgott, Jeremy Hilton, Markus Hoffmann, Sabrina Hong, Trent Huang, Ashley Huff, William J. Huggins, Lev B. Ioffe, Sergei V. Isakov, Justin Iveland, Evan Jeffrey, Zhang Jiang, Cody Jones, Pavol Juhas, Dvir Kafri, Kostyantyn Kechedzhi, Julian Kelly, Tanuj Khattar, Mostafa Khezri, Mária Kieferová, Seon Kim, Alexei Kitaev, Paul V. Klimov, Andrey R. Klots, Alexander N. Korotkov, Fedor Kostritsa, John Mark Kreikebaum, David Landhuis, Pavel Laptev, Kim-Ming Lau, Lily Laws, Joonho Lee, Kenny Lee, Brian J. Lester, Alexander Lill, Wayne Liu, Aditya Locharla, Erik Lucero, Fionn D. Malone, Jeffrey Marshall, Orion Martin, Jarrod R. McClean, Trevor McCourt, Matt McEwen, Anthony Megrant, Bernardo Meurer Costa, Xiao Mi, Kevin C. Miao, Masoud Mohseni, Shirin Montazeri, Alexis Morvan, Emily Mount, Wojciech Mruczkiewicz, Ofer Naaman, Matthew Neeley, Charles Neill, Ani Nersisyan, Hartmut Neven, Michael Newman, Jiun How Ng, Anthony Nguyen, Murray Nguyen, Murphy Yuezhen Niu, Thomas E. O'Brien, Alex Opremcak, John Platt, Andre Petukhov, Rebecca Potter, Leonid P. Pryadko, Chris Quintana, Pedram Roushan, Nicholas C. Rubin, Negar Saei, Daniel Sank, Kannan Sankaragomathi, Kevin J. Satzinger, Henry F. Schurkus, Christopher Schuster, Michael J. Shearn, Aaron Shorter, Vladimir Shvarts, Jindra Skruzny, Vadim Smelyanskiy, W. Clarke Smith, George Sterling, Doug Strain, Marco Szalay, Alfredo Torres, Guifre Vidal, Benjamin Villalonga, Catherine Vollgraff Heidweiller, Theodore White, Cheng Xing, Z. Jamie Yao, Ping Yeh, Juhwan Yoo, Grayson Young, Adam Zalcman, Yaxing Zhang, and Ningfeng Zhu. Suppressing quantum errors by scaling a surface code logical qubit. *Nature*, 614(7949):676–681, February 2023.

[56] Rajeev Acharya, Dmitry A. Abanin, Laleh Aghababaie-Beni, Igor Aleiner, Trond I. Andersen, Markus Ansmann, Frank Arute, Kunal Arya, Abraham Asfaw, Nikita Astrakhantsev, Juan Atalaya, Ryan Babbush, Dave Bacon, Brian Ballard, Joseph C. Bardin, Johannes Bausch, Andreas Bengtsson, Alexander Bilmes, Sam Blackwell, Sergio Boixo, Gina Bortoli, Alexandre Bourassa, Jenna Bovaird, Leon Brill, Michael Broughton, David A. Browne, Brett Buchea, Bob B. Buckley, David A. Buell, Tim Burger, Brian Burkett, Nicholas Bushnell, Anthony Cabrera, Juan Campero, Hung-Shen Chang, Yu Chen, Zijun Chen, Ben Chiaro, Desmond Chik, Charina Chou, Jahan Claes, Agnetta Y. Cleland, Josh Cogan, Roberto Collins, Paul Conner, William Courtney, Alexander L. Crook, Ben Curtin, Sayan Das, Alex Davies, Laura De Lorenzo, Dripto M. Debroy, Sean Demura, Michel Devoret, Agustin Di Paolo, Paul Donohoe, Ilya Drozdov, Andrew Dunsworth, Clint Earle, Thomas Edlich, Alec Eickbusch, Aviv Moshe Elbag, Mahmoud Elzouka, Catherine Erickson, Lara Faoro, Edward Farhi, Vinicius S. Ferreira, Leslie Flores Burgos, Ebrahim Forati, Austin G. Fowler, Brooks Foxen, Suhas Ganjam, Gonzalo Garcia, Robert Gasca, Élie Genois, William Giang, Craig Gidney, Dar Gilboa, Raja Gosula, Alejandro Grajales Dau, Dietrich Graumann, Alex Greene, Jonathan A. Gross, Steve Habegger, John Hall, Michael C. Hamilton, Monica Hansen, Matthew P. Harrigan, Sean D. Harrington, Francisco J. H. Heras, Stephen Heslin, Paula Heu, Oscar Higgott, Gordon Hill, Jeremy Hilton, George Holland, Sabrina Hong, Hsin-Yuan Huang, Ashley Huff, William J. Huggins, Lev B. Ioffe, Sergei V. Isakov, Justin Iveland, Evan Jeffrey, Zhang Jiang, Cody Jones, Stephen Jordan, Chaitali Joshi, Pavol Juhas, Dvir Kafri, Hui Kang, Amir H. Karamlou, Kostyantyn Kechedzhi, Julian Kelly, Trupti Khaire, Tanuj Khattar, Mostafa Khezri, Seon Kim, Paul V. Klimov, Andrey R. Klots, Bryce Kobrin, Pushmeet Kohli, Alexander N. Korotkov, Fedor Kostritsa, Robin Kothari, Borislav Kozlovskii, John Mark Kreikebaum, Vladislav D. Kurilovich, Nathan Lacroix, David Landhuis, Tiano Lange-Dei, Brandon W. Langley, Pavel Laptev, Kim-Ming Lau, Loïck Le Guevel, Justin Ledford, Joonho Lee, Kenny Lee, Yuri D. Lensky, Shannon Leon, Brian J. Lester, Wing Yan Li, Yin Li, Alexander T. Lill, Wayne Liu, William P. Livingston, Aditya Locharla, Erik Lucero, Daniel Lundahl, Aaron Lunt, Sid Madhuk, Fionn D. Malone, Ashley Maloney, Salvatore Mandrà, James Manyika, Leigh S. Martin, Orion Martin, Steven Martin, Cameron Maxfield, Jarrod R. McClean, Matt McEwen, Seneca Meeks, Anthony Megrant, Xiao Mi, Kevin C. Miao, Amanda Mieszala, Reza Molavi, Sebastian Molina, Shirin Montazeri, Alexis Morvan, Ramis Movassagh, Wojciech Mruczkiewicz, Ofer Naaman, Matthew Neeley, Charles Neill, Ani Nersisyan, Hartmut Neven, Michael Newman, Jiun How Ng, Anthony Nguyen, Murray Nguyen, Chia-Hung Ni, Murphy Yuezhen Niu, Thomas E. O'Brien, William D. Oliver, Alex Opremcak, Kristoffer Ottosson, Andre Petukhov, Alex Pizzuto, John Platt, Rebecca Potter, Orion Pritchard, Leonid P. Pryadko, Chris Quintana, Ganesh Ramachandran, Matthew J. Reagor, John Redding, David M. Rhodes, Gabrielle Roberts, Eliott Rosenberg, Emma Rosenfeld, Pedram Roushan, Nicholas C. Rubin, Negar Saei, Daniel Sank, Kannan Sankaragomathi, Kevin J. Satzinger, Henry F. Schurkus, Christopher Schuster, An-

drew W. Senior, Michael J. Shearn, Aaron Shorter, Noah Shutty, Vladimir Shvarts, Shraddha Singh, Volodymyr Sivak, Jindra Skruzny, Spencer Small, Vadim Smelyanskiy, W. Clarke Smith, Rolando D. Somma, Sofia Springer, George Sterling, Doug Strain, Jordan Suchard, Aaron Szasz, Alex Sztein, Douglas Thor, Alfredo Torres, M. Mert Torunbalci, Abeer Vaishnav, Justin Vargas, Sergey Vdovichev, Guifre Vidal, Benjamin Villalonga, Catherine Vollgraff Heidweiller, Steven Waltman, Shannon X. Wang, Brayden Ware, Kate Weber, Travis Weidel, Theodore White, Kristi Wong, Bryan W. K. Woo, Cheng Xing, Z. Jamie Yao, Ping Yeh, Bicheng Ying, Juhwan Yoo, Noureldin Yosri, Grayson Young, Adam Zalcman, Yaxing Zhang, Ningfeng Zhu, and Nicholas Zobrist. Quantum error correction below the surface code threshold. *Nature*, 638(8052):920–926, December 2024.

[57] Sandoko Kosen, Hang-Xi Li, Marcus Rommel, Daryoush Shiri, Christopher Warren, Leif Grönberg, Jaakko Salonen, Tahereh Abad, Janka Biznárová, Marco Caputo, Liangyu Chen, Kestutis Grigoras, Göran Johansson, Anton Frisk Kockum, Christian Križan, Daniel Pérez Lozano, Graham J Norris, Amr Osman, Jorge Fernández-Pendás, Alberto Ronzani, Anita Fadavi Roudsari, Slawomir Simbierowicz, Giovanna Tancredi, Andreas Wallraff, Christopher Eichler, Joonas Govenius, and Jonas Bylander. Building blocks of a flip-chip integrated superconducting quantum processor. *Quantum Science and Technology*, 7(3):035018, June 2022.

[58] Sandoko Kosen, Hang-Xi Li, Marcus Rommel, Robert Rehammar, Marco Caputo, Leif Grönberg, Jorge Fernández-Pendás, Anton Frisk Kockum, Janka Biznárová, Liangyu Chen, Christian Križan, Andreas Nylander, Amr Osman, Anita Fadavi Roudsari, Daryoush Shiri, Giovanna Tancredi, Joonas Govenius, and Jonas Bylander. Signal crosstalk in a flip-chip quantum processor. *PRX Quantum*, 5(3):030350, September 2024.

[59] Yao Lu, Aniket Maiti, John W. O. Garmon, Suhas Ganjam, Yaxing Zhang, Jahan Claes, Luigi Frunzio, Steven M. Girvin, and Robert J. Schoelkopf. High-fidelity parametric beamsplitting with a parity-protected converter. *Nature Communications*, 14(1), September 2023.

[60] N. Janzen, M. Kononenko, S. Ren, and A. Lupascu. Aluminum air bridges for superconducting quantum devices realized using a single-step electron-beam lithography process. *Applied Physics Letters*, 121(9), August 2022.

[61] Jeffrey P. Gambino, Shawn A. Adderly, and John U. Knickerbocker. An overview of through-silicon-via technology and manufacturing challenges. *Microelectronic Engineering*, 135:73–106, March 2015.

[62] D. R. W. Yost, M. E. Schwartz, J. Mallek, D. Rosenberg, C. Stull, J. L. Yoder, G. Calusine, M. Cook, R. Das, A. L. Day, E. B. Golden, D. K. Kim, A. Melville, B. M. Niedzielski, W. Woods, A. J. Kerman, and W. D. Oliver. Solid-state qubits integrated with superconducting through-silicon vias. *npj Quantum Information*, 6(1), July 2020.

[63] J. A. Alfaro-Barrantes, M. Mastrangeli, D. J. Thoen, S. Visser, J. Bueno, J. J. A. Baselmans, and P. M. Sarro. Highly-conformal sputtered through-silicon vias with sharp superconducting transition. *Journal of Microelectromechanical Systems*, 30(2):253–261, April 2021.

[64] Jiexun Yu, Yao Zheng, Shengjuan Zhou, Qian Wang, Sishi Wu, Haihua Wu, Tiefu Li, and Jian Cai. Indium-based flip-chip interconnection for superconducting quantum computing application. In *2022 23rd International Conference on Electronic Packaging Technology (ICEPT)*, pages 1–6. IEEE, August 2022.

[65] Kaitlin N. Smith, Gokul Subramanian Ravi, Jonathan M. Baker, and Frederic T. Chong. Scaling superconducting quantum computers with chiplet architectures. In *2022 55th IEEE/ACM International Symposium on Microarchitecture (MICRO)*, pages 1092–1109. IEEE, October 2022.

[66] Mark Field, Angela Q. Chen, Ben Scharmann, Eyob A. Sete, Feyza Oruc, Kim Vu, Valentin Kosenko, Joshua Y. Mutus, Stefano Poletto, and Andrew Bestwick. Modular superconducting-qubit architecture with a multichip tunable coupler. *Physical Review Applied*, 21(5):054063, May 2024.

[67] Fei Yan, Simon Gustavsson, Archana Kamal, Jeffrey Birenbaum, Adam P Sears, David Hover, Ted J. Gudmundsen, Danna Rosenberg, Gabriel Samach, S Weber, Jonilyn L. Yoder, Terry P. Orlando, John Clarke, Andrew J. Kerman, and William D. Oliver. The flux qubit revisited to enhance coherence and reproducibility. *Nature Communications*, 7(1), November 2016.

[68] Long B. Nguyen, Yen-Hsiang Lin, Aaron Somoroff, Raymond Mencia, Nicholas Grabon, and Vladimir E. Manucharyan. High-coherence fluxonium qubit. *Physical Review X*, 9(4):041041, November 2019.

[69] Lukas Grünhaupt, Martin Spiecker, Daria Gusenkova, Nataliya Maleeva, Sebastian T. Skacel, Ivan Takmakov, Francesco Valenti, Patrick Winkel, Hannes Rotzinger, Wolfgang Wernsdorfer, Alexey V. Ustinov, and Ioan M. Pop. Granular aluminium as a superconducting material for high-impedance quantum circuits. *Nature Materials*, 18(8):816–819, April 2019.

[70] D. Rieger, S. Günzler, M. Spiecker, P. Paluch, P. Winkel, L. Hahn, J. K. Hohmann, A. Bacher, W. Wernsdorfer, and I. M. Pop. Granular aluminium nanojunction fluxonium qubit. *Nature Materials*, 22(2):194–199, December 2022.

[71] Yulin Wu, Wan-Su Bao, Sirui Cao, Fusheng Chen, Ming-Cheng Chen, Xiawei Chen, Tung-Hsun Chung, Hui Deng, Yajie Du, Daojin Fan, Ming Gong, Cheng Guo, Chu Guo, Shaojun Guo, Lianchen Han, Linyin Hong, He-Liang Huang, Yong-Heng Huo, Liping Li, Na Li, Shaowei Li, Yuan Li, Futian Liang, Chun Lin, Jin Lin, Haoran Qian, Dan Qiao, Hao Rong, Hong Su, Lihua Sun, Liangyuan Wang, Shiyu Wang, Dachao Wu, Yu Xu, Kai Yan, Weifeng Yang, Yang Yang,

Yangsen Ye, Jianghan Yin, Chong Ying, Jiale Yu, Chen Zha, Cha Zhang, Haibin Zhang, Kaili Zhang, Yiming Zhang, Han Zhao, Youwei Zhao, Liang Zhou, Qingling Zhu, Chao-Yang Lu, Cheng-Zhi Peng, Xiaobo Zhu, and Jian-Wei Pan. Strong quantum computational advantage using a superconducting quantum processor. *Physical Review Letters*, 127(18):180501, October 2021.

[72] J. F. Marques, B. M. Varbanov, M. S. Moreira, H. Ali, N. Muthusubramanian, C. Zachariadis, F. Battistel, M. Beekman, N. Haider, W. Vlothuizen, A. Bruno, B. M. Terhal, and L. DiCarlo. Logical-qubit operations in an error-detecting surface code. *Nature Physics*, 18(1):80–86, December 2021.

[73] Sebastian Krinner, Nathan Lacroix, Ants Remm, Agustin Di Paolo, Elie Genois, Catherine Leroux, Christoph Hellings, Stefania Lazar, Francois Swiadek, Johannes Herrmann, Graham J. Norris, Christian Kraglund Andersen, Markus Müller, Alexandre Blais, Christopher Eichler, and Andreas Wallraff. Realizing repeated quantum error correction in a distance-three surface code. *Nature*, 605(7911):669–674, May 2022.

[74] Youngseok Kim, Christopher J. Wood, Theodore J. Yoder, Seth T. Merkel, Jay M. Gambetta, Kristan Temme, and Abhinav Kandala. Scalable error mitigation for noisy quantum circuits produces competitive expectation values. *Nature Physics*, 19(5):752–759, February 2023.

[75] L. Cardani, F. Valenti, N. Casali, G. Catelani, T. Charpentier, M. Clemenza, I. Colantoni, A. Cruciani, G. D'Imperio, L. Gironi, L. Grünhaupt, D. Gusenkova, F. Henriques, M. Lagoin, M. Martinez, G. Pettinari, C. Rusconi, O. Sander, C. Tomei, A. V. Ustinov, M. Weber, W. Wernsdorfer, M. Vignati, S. Pirro, and I. M. Pop. Reducing the impact of radioactivity on quantum circuits in a deep-underground facility. *Nature Communications*, 12(1), May 2021.

[76] Matt McEwen, Lara Faoro, Kunal Arya, Andrew Dunsworth, Trent Huang, Seon Kim, Brian Burkett, Austin Fowler, Frank Arute, Joseph C. Bardin, Andreas Bengtsson, Alexander Bilmes, Bob B. Buckley, Nicholas Bushnell, Zijun Chen, Roberto Collins, Sean Demura, Alan R. Derk, Catherine Erickson, Marissa Giustina, Sean D. Harrington, Sabrina Hong, Evan Jeffrey, Julian Kelly, Paul V. Klimov, Fedor Kostritsa, Pavel Laptev, Aditya Locharla, Xiao Mi, Kevin C. Miao, Shirin Montazeri, Josh Mutus, Ofer Naaman, Matthew Neeley, Charles Neill, Alex Opremcak, Chris Quintana, Nicholas Redd, Pedram Roushan, Daniel Sank, Kevin J. Satzinger, Vladimir Shvarts, Theodore White, Z. Jamie Yao, Ping Yeh, Juhwan Yoo, Yu Chen, Vadim Smelyanskiy, John M. Martinis, Hartmut Neven, Anthony Megrant, Lev Ioffe, and Rami Barends. Resolving catastrophic error bursts from cosmic rays in large arrays of superconducting qubits. *Nature Physics*, 18(1):107–111, December 2021.

[77] C. D. Wilen, S. Abdullah, N. A. Kurinsky, C. Stanford, L. Cardani, G. D'Imperio, C. Tomei, L. Faoro, L. B. Ioffe, C. H. Liu, A. Opremcak, B. G. Christensen, J. L. DuBois, and R. McDermott.

Correlated charge noise and relaxation errors in superconducting qubits. *Nature*, 594(7863):369–373, June 2021.

[78] Ted Thorbeck, Andrew Eddins, Isaac Lauer, Douglas T. McClure, and Malcolm Carroll. Two-level-system dynamics in a superconducting qubit due to background ionizing radiation. *PRX Quantum*, 4(2):020356, June 2023.

[79] E. Yelton, C. P. Larson, V. Iaia, K. Dodge, G. La Magna, P. G. Baity, I. V. Pechenezhskiy, R. McDermott, N. A. Kurinsky, G. Catelani, and B. L. T. Plourde. Modeling phonon-mediated quasiparticle poisoning in superconducting qubit arrays. *Physical Review B*, 110(2):024519, July 2024.

[80] Hanhee Paik, D. I. Schuster, Lev S. Bishop, G. Kirchmair, G. Catelani, A. P. Sears, B. R. Johnson, M. J. Reagor, L. Frunzio, L. I. Glazman, S. M. Girvin, M. H. Devoret, and R. J. Schoelkopf. Observation of high coherence in josephson junction qubits measured in a three-dimensional circuit qed architecture. *Physical Review Letters*, 107(24):240501, December 2011.

[81] Alexander P. M. Place, Lila V. H. Rodgers, Pranav Mundada, Basil M. Smitham, Mattias Fitzpatrick, Zhaoqi Leng, Anjali Premkumar, Jacob Bryon, Andrei Vrajitoarea, Sara Sussman, Guangming Cheng, Trisha Madhavan, Harshvardhan K. Babla, Xuan Hoang Le, Youqi Gang, Berthold Jäck, András Gyenis, Nan Yao, Robert J. Cava, Nathalie P. de Leon, and Andrew A. Houck. New material platform for superconducting transmon qubits with coherence times exceeding 0.3 milliseconds. *Nature Communications*, 12(1), March 2021.

[82] Aaron Somoroff, Quentin Ficheux, Raymond A. Mencia, Haonan Xiong, Roman Kuzmin, and Vladimir E. Manucharyan. Millisecond coherence in a superconducting qubit. *Physical Review Letters*, 130(26):267001, June 2023.

[83] Qiang Liu, Mengmeng Li, Kunzhe Dai, Ke Zhang, Guangming Xue, Xinsheng Tan, Haifeng Yu, and Yang Yu. Extensible 3d architecture for superconducting quantum computing. *Applied Physics Letters*, 110(23), June 2017.

[84] Peter A. Spring, Shuxiang Cao, Takahiro Tsunoda, Giulio Campanaro, Simone Fasciati, James Wills, Mustafa Bakr, Vivek Chidambaram, Boris Shteynas, Lewis Carpenter, Paul Gow, James Gates, Brian Vlastakis, and Peter J. Leek. High coherence and low cross-talk in a tileable 3d integrated superconducting circuit architecture. *Science Advances*, 8(16), April 2022.

[85] Michael Mollenhauer, Abdullah Irfan, Xi Cao, Supriya Mandal, and Wolfgang Pfaff. A high-efficiency elementary network of interchangeable superconducting qubit devices. *Nature Electronics*, 8(7):610–619, June 2025.

[86] D. Rosenberg, D. Kim, R. Das, D. Yost, S. Gustavsson, D. Hover, P. Krantz, A. Melville, L. Racz, G. O. Samach, S. J. Weber, F. Yan, J. L. Yoder, A. J. Kerman, and W. D. Oliver. 3d integrated superconducting qubits. *npj Quantum Information*, 3(1), October 2017.

[87] Nicholas T Bronn, Vivekananda P Adiga, Salvatore B Olivadese, Xian Wu, Jerry M Chow, and David P Pappas. High coherence plane breaking packaging for superconducting qubits. *Quantum Science and Technology*, 3(2):024007, February 2018.

[88] W. Meissner and R. Ochsenfeld. Ein neuer effekt bei eintritt der supraleitfähigkeit. *Die Naturwissenschaften*, 21(44):787–788, November 1933.

[89] Christian Enss and Siegfried Hunklinger. *Low-temperature physics*. Springer Berlin, Heidelberg, 2005.

[90] Michael Tinkham. *Introduction to superconductivity*. McGraw-Hill international editions. McGraw-Hill, 1996.

[91] J. Bardeen, L. N. Cooper, and J. R. Schrieffer. Theory of superconductivity. *Physical Review*, 108(5):1175–1204, December 1957.

[92] Fritz London and Heinz London. *Proceedings of the Royal Society of London. Series A - Mathematical and Physical Sciences*, 149(866):71–88, March 1935.

[93] Mikko Tuokkola, Yoshiki Sunada, Heidi Kivijärvi, Jonatan Albanese, Leif Grönberg, Jukka-Pekka Kaikkonen, Visa Vesterinen, Joonas Govenius, and Mikko Möttönen. Methods to achieve near-millisecond energy relaxation and dephasing times for a superconducting transmon qubit. *Nature Communications*, 16(1), July 2025.

[94] Iqm quantum computers achieves new technology milestones with 99.9 % 2-qubit gate fidelity and 1 millisecond coherence time. `https://meetiqm.com/press-releases/iqm-quantum-computers-achieves-new-technology-milestones-with-99-9-2-qubit-gate-fidelity-a?utm_source=chatgpt.com`. Accessed: 2025-07-14.

[95] Uri Vool and Michel Devoret. Introduction to quantum electromagnetic circuits. *International Journal of Circuit Theory and Applications*, 45(7):897–934, June 2017.

[96] A. A. Golubov, M. Yu. Kupriyanov, and E. Il'ichev. The current-phase relation in josephson junctions. *Reviews of Modern Physics*, 76(2):411–469, April 2004.

[97] B.D. Josephson. Possible new effects in superconductive tunnelling. *Physics Letters*, 1(7):251–253, July 1962.

[98] L. Kuzmin and D. Haviland. Observation of the bloch oscillations in an ultrasmall josephson junction. *Physical Review Letters*, 67(20):2890–2893, November 1991.

[99] Frank Deppe, Shiro Saito, Hirotaka Tanaka, and Hideaki Takayanagi. Determination of the capacitance of nm scale josephson junctions. *Journal of Applied Physics*, 95(5):2607–2613, March 2004.

[100] M. A. Sillanpää, T. Lehtinen, A. Paila, Yu. Makhlin, L. Roschier, and P. J. Hakonen. Direct observation of josephson capacitance. *Physical Review Letters*, 95(20):206806, November 2005.

[101] Yu-Lin Wu, Hui Deng, Hai-Feng Yu, Guang-Ming Xue, Ye Tian, Jie Li, Ying-Fei Chen, Shi-Ping Zhao, and Dong-Ning Zheng. Fabrication of al/alox/al josephson junctions and superconducting quantum circuits by shadow evaporation and a dynamic oxidation process. *Chinese Physics B*, 22(6):060309, June 2013.

[102] Vinay Ambegaokar and Alexis Baratoff. Tunneling between superconductors. *Physical Review Letters*, 10(11):486–489, June 1963.

[103] Siegfried Hunklinger. *Festkörperphysik*. De Gruyter, November 2017.

[104] R. Meservey and P. M. Tedrow. Measurements of the kinetic inductance of superconducting linear structures. *Journal of Applied Physics*, 40(5):2028–2034, April 1969.

[105] Y. Nakamura, Yu. A. Pashkin, and J. S. Tsai. Coherent control of macroscopic quantum states in a single-cooper-pair box. *Nature*, 398(6730):786–788, April 1999.

[106] Jens Koch, Terri M. Yu, Jay Gambetta, A. A. Houck, D. I. Schuster, J. Majer, Alexandre Blais, M. H. Devoret, S. M. Girvin, and R. J. Schoelkopf. Charge-insensitive qubit design derived from the cooper pair box. *Physical Review A*, 76(4):042319, October 2007.

[107] W. C. Smith, A. Kou, U. Vool, I. M. Pop, L. Frunzio, R. J. Schoelkopf, and M. H. Devoret. Quantization of inductively shunted superconducting circuits. *Physical Review B*, 94(14):144507, October 2016.

[108] Fei Yan, Youngkyu Sung, Philip Krantz, Archana Kamal, David K. Kim, Jonilyn L. Yoder, Terry P. Orlando, Simon Gustavsson, and William D. Oliver. Engineering framework for optimizing superconducting qubit designs. June 2020.

[109] M. Peruzzo, A. Trioni, F. Hassani, M. Zemlicka, and J. M. Fink. Surpassing the resistance quantum with a geometric superinductor. *Physical Review Applied*, 14(4):044055, October 2020.

[110] N. Maleeva, L. Grünhaupt, T. Klein, F. Levy-Bertrand, O. Dupre, M. Calvo, F. Valenti, P. Winkel, F. Friedrich, W. Wernsdorfer, A. V. Ustinov, H. Rotzinger, A. Monfardini, M. V. Fistul, and I. M. Pop. Circuit quantum electrodynamics of granular aluminum resonators. *Nature Communications*, 9(1), September 2018.

[111] Vladimir E. Manucharyan, Jens Koch, Leonid I. Glazman, and Michel H. Devoret. Fluxonium: Single cooper-pair circuit free of charge offsets. *Science*, 326(5949):113–116, October 2009.

[112] Yu. Krupko, V. D. Nguyen, T. Weißl, É. Dumur, J. Puertas, R. Dassonneville, C. Naud, F. W. J. Hekking, D. M. Basko, O. Buisson, N. Roch, and W. Hasch-Guichard. Kerr nonlinearity in a superconducting josephson metamaterial. *Physical Review B*, 98(9):094516, September 2018.

[113] Nicholas A. Masluk, Ioan M. Pop, Archana Kamal, Zlatko K. Minev, and Michel H. Devoret. Microwave characterization of josephson junction arrays: Implementing a low loss superinductance. *Physical Review Letters*, 109(13):137002, September 2012.

[114] I. M. Pop, I. Protopopov, F. Lecocq, Z. Peng, B. Pannetier, O. Buisson, and W. Guichard. Measurement of the effect of quantum phase slips in a josephson junction chain. *Nature Physics*, 6(8):589–592, June 2010.

[115] B. Abeles, Roger W. Cohen, and G. W. Cullen. Enhancement of superconductivity in metal films. *Physical Review Letters*, 17(12):632–634, September 1966.

[116] Roger W. Cohen and B. Abeles. Superconductivity in granular aluminum films. *Physical Review*, 168(2):444–450, April 1968.

[117] D. C. Mattis and J. Bardeen. Theory of the anomalous skin effect in normal and superconducting metals. *Physical Review*, 111(2):412–417, July 1958.

[118] H Rotzinger, S T Skacel, M Pfirrmann, J N Voss, J Münzberg, S Probst, P Bushev, M P Weides, A V Ustinov, and J E Mooij. Aluminium-oxide wires for superconducting high kinetic inductance circuits. *Superconductor Science and Technology*, 30(2):025002, November 2016.

[119] Uwe S. Pracht, Nimrod Bachar, Lara Benfatto, Guy Deutscher, Eli Farber, Martin Dressel, and Marc Scheffler. Enhanced cooper pairing versus suppressed phase coherence shaping the superconducting dome in coupled aluminum nanograins. *Physical Review B*, 93(10):100503, March 2016.

[120] Lukas Grünhaupt, Nataliya Maleeva, Sebastian T. Skacel, Martino Calvo, Florence Levy-Bertrand, Alexey V. Ustinov, Hannes Rotzinger, Alessandro Monfardini, Gianluigi Catelani, and Ioan M. Pop. Loss mechanisms and quasiparticle dynamics in superconducting microwave resonators made of thin-film granular aluminum. *Physical Review Letters*, 121(11):117001, September 2018.

[121] Patrick Winkel, Kiril Borisov, Lukas Grünhaupt, Dennis Rieger, Martin Spiecker, Francesco Valenti, Alexey V. Ustinov, Wolfgang Wernsdorfer, and Ioan M. Pop. Implementation of a transmon qubit using superconducting granular aluminum. *Physical Review X*, 10(3):031032, August 2020.

[122] Nicolas Zapata, Ivan Takmakov, Simon Günzler, Simon Geisert, Soeren Ihssen, Mitchell Field, Ameya Nambisan, Dennis Rieger, Thomas Reisinger, Wolfgang Wernsdorfer, and Ioan M. Pop. Granular aluminum parametric amplifier for low-noise measurements in tesla fields. *Physical Review Letters*, 133(26):260604, December 2024.

[123] K. Borisov, D. Rieger, P. Winkel, F. Henriques, F. Valenti, A. Ionita, M. Wessbecher, M. Spiecker, D. Gusenkova, I. M. Pop, and W. Wernsdorfer. Superconducting granular aluminum resonators resilient to magnetic fields up to 1 tesla. *Applied Physics Letters*, 117(12), September 2020.

[124] Fabio Henriques, Francesco Valenti, Thibault Charpentier, Marc Lagoin, Clement Gouriou, Maria Martínez, Laura Cardani, Marco Vignati, Lukas Grünhaupt, Daria Gusenkova, Julian Ferrero, Sebastian T. Skacel, Wolfgang Wernsdorfer, Alexey V. Ustinov, Gianluigi Catelani, Oliver Sander, and Ioan M. Pop. Phonon traps reduce the quasiparticle density in superconducting circuits. *Applied Physics Letters*, 115(21), November 2019.

[125] John M. Martinis. Saving superconducting quantum processors from qubit decay and correlated errors generated by gamma and cosmic rays. December 2020.

[126] H. J. Kimble. Strong interactions of single atoms and photons in cavity qed. *Physica Scripta*, T76(1):127, 1998.

[127] Serge Haroche and Jean-Michel Raimond. *Exploring the Quantum*. Oxford University Press, August 2006.

[128] Alexandre Blais, Ren-Shou Huang, Andreas Wallraff, S. M. Girvin, and R. J. Schoelkopf. Cavity quantum electrodynamics for superconducting electrical circuits: An architecture for quantum computation. *Physical Review A*, 69(6):062320, June 2004.

[129] E.T. Jaynes and F.W. Cummings. Comparison of quantum and semiclassical radiation theories with application to the beam maser. *Proceedings of the IEEE*, 51(1):89–109, 1963.

[130] Bernard Yurke and John S. Denker. Quantum network theory. *Physical Review A*, 29(3):1419–1437, March 1984.

[131] David M. Pozar. *Microwave engineering*. John Wiley & Sons, Inc., Hoboken, NJ, fourth edition edition, 2012. Enthält Übungsaufgaben.

[132] Carlton M. Caves. Quantum limits on noise in linear amplifiers. *Physical Review D*, 26(8):1817–1839, October 1982.

[133] A. A. Clerk, M. H. Devoret, S. M. Girvin, Florian Marquardt, and R. J. Schoelkopf. Introduction to quantum noise, measurement, and amplification. *Reviews of Modern Physics*, 82(2):1155–1208, April 2010.

[134] M. Hatridge, S. Shankar, M. Mirrahimi, F. Schackert, K. Geerlings, T. Brecht, K. M. Sliwa, B. Abdo, L. Frunzio, S. M. Girvin, R. J. Schoelkopf, and M. H. Devoret. Quantum back-action of an individual variable-strength measurement. *Science*, 339(6116):178–181, January 2013.

[135] U. Vool, I.M. Pop, K. Sliwa, B. Abdo, C. Wang, T. Brecht, Y.Y. Gao, S. Shankar, M. Hatridge, G. Catelani, M. Mirrahimi, L. Frunzio, R.J. Schoelkopf, L.I. Glazman, and M.H. Devoret. Non-poissonian quantum jumps of a fluxonium qubit due to quasiparticle excitations. *Physical Review Letters*, 113(24):247001, December 2014.

[136] Simon Geisert, Soeren Ihssen, Patrick Winkel, Martin Spiecker, Mathieu Fechant, Patrick Paluch, Nicolas Gosling, Nicolas Zapata, Simon Günzler, Dennis Rieger, Denis Bénâtre, Thomas Reisinger, Wolfgang Wernsdorfer, and Ioan M. Pop. Pure kinetic inductance coupling for cqed with flux qubits. *Applied Physics Letters*, 125(6), August 2024.

[137] Patrick Winkel, Ivan Takmakov, Dennis Rieger, Luca Planat, Wiebke Hasch-Guichard, Lukas Grünhaupt, Nataliya Maleeva, Farshad Foroughi, Fabio Henriques, Kiril Borisov, Julian Ferrero, Alexey V. Ustinov, Wolfgang Wernsdorfer, Nicolas Roch, and Ioan M. Pop. Nondegenerate parametric amplifiers based on dispersion-engineered josephson-junction arrays. *Physical Review Applied*, 13(2):024015, February 2020.

[138] Feng Bao, Hao Deng, Dawei Ding, Ran Gao, Xun Gao, Cupjin Huang, Xun Jiang, Hsiang-Sheng Ku, Zhisheng Li, Xizheng Ma, Xiaotong Ni, Jin Qin, Zhijun Song, Hantao Sun, Chengchun Tang, Tenghui Wang, Feng Wu, Tian Xia, Wenlong Yu, Fang Zhang, Gengyan Zhang, Xiaohang Zhang, Jingwei Zhou, Xing Zhu, Yaoyun Shi, Jianxin Chen, Hui-Hai Zhao, and Chunqing Deng. Fluxonium: An alternative qubit platform for high-fidelity operations. *Physical Review Letters*, 129(1):010502, June 2022.

[139] Herbert Goldstein, Charles Poole, John Safko, and Stephen R. Addison. Classical mechanics, 3rd ed. *American Journal of Physics*, 70(7):782–783, June 2002.

[140] Martin Rymarz and David P. DiVincenzo. Consistent quantization of nearly singular superconducting circuits. *Physical Review X*, 13(2):021017, May 2023.

[141] F. Yoshihara, S. Ashhab, T. Fuse, M. Bamba, and K. Semba. Hamiltonian of a flux qubit-lc oscillator circuit in the deep–strong-coupling regime. *Scientific Reports*, 12(1), April 2022.

[142] Quantum Machines. Accessed: 2025-05-23.

[143] G. Rastelli, I. M. Pop, and F. W. J. Hekking. Quantum phase slips in josephson junction rings. *Physical Review B*, 87(17):174513, May 2013.

[144] Daria Gusenkova, Martin Spiecker, Richard Gebauer, Madita Willsch, Dennis Willsch, Francesco Valenti, Nick Karcher, Lukas Grünhaupt, Ivan Takmakov, Patrick Winkel, Dennis Rieger,

Alexey V. Ustinov, Nicolas Roch, Wolfgang Wernsdorfer, Kristel Michielsen, Oliver Sander, and Ioan M. Pop. Quantum nondemolition dispersive readout of a superconducting artificial atom using large photon numbers. *Physical Review Applied*, 15(6):064030, June 2021.

[145] Marie Frédérique Dumas, Benjamin Groleau-Paré, Alexander McDonald, Manuel H. Muñoz-Arias, Cristóbal Lledó, Benjamin D'Anjou, and Alexandre Blais. Measurement-induced transmon ionization. *Physical Review X*, 14(4):041023, October 2024.

[146] Ross Shillito, Alexandru Petrescu, Joachim Cohen, Jackson Beall, Markus Hauru, Martin Ganahl, Adam G.M. Lewis, Guifre Vidal, and Alexandre Blais. Dynamics of transmon ionization. *Physical Review Applied*, 18(3):034031, September 2022.

[147] Joachim Cohen, Alexandru Petrescu, Ross Shillito, and Alexandre Blais. Reminiscence of classical chaos in driven transmons. *PRX Quantum*, 4(2):020312, April 2023.

[148] Ted Thorbeck, Zhihao Xiao, Archana Kamal, and Luke C.G. Govia. Readout-induced suppression and enhancement of superconducting qubit lifetimes. *Physical Review Letters*, 132(9):090602, February 2024.

[149] T. Walter, P. Kurpiers, S. Gasparinetti, P. Magnard, A. Potočnik, Y. Salathé, M. Pechal, M. Mondal, M. Oppliger, C. Eichler, and A. Wallraff. Rapid high-fidelity single-shot dispersive readout of superconducting qubits. *Physical Review Applied*, 7(5):054020, May 2017.

[150] Mats O. Tholén, Riccardo Borgani, Giuseppe Ruggero Di Carlo, Andreas Bengtsson, Christian Križan, Marina Kudra, Giovanna Tancredi, Jonas Bylander, Per Delsing, Simone Gasparinetti, and David B. Haviland. Measurement and control of a superconducting quantum processor with a fully integrated radio-frequency system on a chip. *Review of Scientific Instruments*, 93(10), October 2022.

[151] D. Ristè, C. C. Bultink, K. W. Lehnert, and L. DiCarlo. Feedback control of a solid-state qubit using high-fidelity projective measurement. *Physical Review Letters*, 109(24):240502, December 2012.

[152] Y. Sunada, S. Kono, J. Ilves, S. Tamate, T. Sugiyama, Y. Tabuchi, and Y. Nakamura. Fast readout and reset of a superconducting qubit coupled to a resonator with an intrinsic purcell filter. *Physical Review Applied*, 17(4):044016, April 2022.

[153] Irfan Siddiqi. Engineering high-coherence superconducting qubits. *Nature Reviews Materials*, 6(10):875–891, September 2021.

[154] T.M. Hazard, A. Gyenis, A. Di Paolo, A.T. Asfaw, S.A. Lyon, A. Blais, and A.A. Houck. Nanowire superinductance fluxonium qubit. *Physical Review Letters*, 122(1):010504, January 2019.

[155] Leon Ding, Max Hays, Youngkyu Sung, Bharath Kannan, Junyoung An, Agustin Di Paolo, Amir H. Karamlou, Thomas M. Hazard, Kate Azar, David K. Kim, Bethany M. Niedzielski, Alexander Melville, Mollie E. Schwartz, Jonilyn L. Yoder, Terry P. Orlando, Simon Gustavsson, Jeffrey A. Grover, Kyle Serniak, and William D. Oliver. High-fidelity, frequency-flexible two-qubit fluxonium gates with a transmon coupler. *Physical Review X*, 13(3):031035, September 2023.

[156] Raymond A. Mencia, Wei-Ju Lin, Hyunheung Cho, Maxim G. Vavilov, and Vladimir E. Manucharyan. Integer fluxonium qubit. *PRX Quantum*, 5(4):040318, November 2024.

[157] Soeren Ihssen, Simon Geisert, Gabriel Jauma, Patrick Winkel, Martin Spiecker, Nicolas Zapata, Nicolas Gosling, Patrick Paluch, Manuel Pino, Thomas Reisinger, Wolfgang Wernsdorfer, Juan Jose Garcia-Ripoll, and Ioan M. Pop. Low crosstalk modular flip-chip architecture for coupled superconducting qubits. *Applied Physics Letters*, 126(13), March 2025.

[158] M. D. Reed, B. R. Johnson, A. A. Houck, L. DiCarlo, J. M. Chow, D. I. Schuster, L. Frunzio, and R. J. Schoelkopf. Fast reset and suppressing spontaneous emission of a superconducting qubit. *Applied Physics Letters*, 96(20), May 2010.

[159] Eyob A. Sete, John M. Martinis, and Alexander N. Korotkov. Quantum theory of a bandpass purcell filter for qubit readout. *Physical Review A*, 92(1):012325, July 2015.

[160] John R. Clem and V. G. Kogan. Kinetic impedance and depairing in thin and narrow superconducting films. *Physical Review B*, 86(17):174521, November 2012.

[161] E. P. Harris and D. E. Mapother. Critical field of superconducting aluminum as a function of pressure and temperature above 0.3°k. *Physical Review*, 165(2):522–532, January 1968.

[162] David López-Núñez, Alba Torras-Coloma, Queralt Portell Montserrat, Elia Bertoldo, Luca Cozzolino, Gemma Rius, M. Martínez, and P. Forn-Díaz. Magnetic penetration depth of aluminum thin films, 2023.

[163] Edward M. Purcell. *Electricity and Magnetism*. Cambridge University Press, Cambridge, third edition. edition, 2013. Title from publisher's bibliographic system (viewed on 05 Feb 2019).

[164] Yokogawa. Gs200 dc voltage / current source pulse generator. `https://tmi.yokogawa.com/de/solutions/products/generators-sources/source-measure-units/gs200/`. Accessed: 2025-08-07.

[165] Jay Gambetta, Alexandre Blais, D. I. Schuster, A. Wallraff, L. Frunzio, J. Majer, M. H. Devoret, S. M. Girvin, and R. J. Schoelkopf. Qubit-photon interactions in a cavity: Measurement-induced dephasing and number splitting. *Physical Review A*, 74(4):042318, October 2006.

[166] J. R. Schrieffer and P. A. Wolff. Relation between the anderson and kondo hamiltonians. *Physical Review*, 149(2):491–492, September 1966.

[167] Sergey Bravyi, David P. DiVincenzo, and Daniel Loss. Schrieffer–wolff transformation for quantum many-body systems. *Annals of Physics*, 326(10):2793–2826, October 2011.

[168] Xuntao Wu, Haoxiong Yan, Gustav Andersson, Alexander Anferov, Ming-Han Chou, Christopher R. Conner, Joel Grebel, Yash J. Joshi, Shiheng Li, Jacob M. Miller, Rhys G. Povey, Hong Qiao, and Andrew N. Cleland. Modular quantum processor with an all-to-all reconfigurable router. *Physical Review X*, 14(4):041030, November 2024.

[169] Conal E. Murray. Material matters in superconducting qubits. *Materials Science and Engineering: R: Reports*, 146:100646, October 2021.

[170] Kevin W. Kirby, Karthik Shanmugasundaram, V Bojan, and J. Ruzyllo. Interactions of sapphire surfaces with standard cleaning solutions. *ECS Transactions*, 11(2):343–349, September 2007.

[171] Jungjae Park, Yong Jai Cho, Won Chegal, Joonyoung Lee, Yoon-Soo Jang, and Jonghan Jin. A review of thin-film thickness measurements using optical methods. *International Journal of Precision Engineering and Manufacturing*, 25(8):1725–1737, June 2024.

[172] Stephen Sammut. A comprehensive review of plasma cleaning processes used in semiconductor packaging. *Applied Sciences*, 15(13):7361, June 2025.

[173] G. J. Dolan. Offset masks for lift-off photoprocessing. *Applied Physics Letters*, 31(5):337–339, September 1977.

[174] Florent Lecocq, Ioan M Pop, Zhihui Peng, Iulian Matei, Thierry Crozes, Thierry Fournier, Cécile Naud, Wiebke Guichard, and Olivier Buisson. Junction fabrication by shadow evaporation without a suspended bridge. *Nanotechnology*, 22(31):315302, July 2011.

[175] R.E. Clausing. *A LARGE-SCALE GETTER PUMPING EXPERIMENT USING VAPOR DEPOSITED TITANIUM FILMS*. November 1961.

[176] Quantum-Machines. Octave: Up/down conversion up to 18 ghz with auto calibration. `https://docs.quantum-machines.co/latest/docs/Hardware/octave/`. Accessed: 2025-08-07.

[177] Keysight. E5071c ena vector network analyzer. `https://www.keysight.com/nl/en/product/E5071C/e5071c-ena-vector-network-analyzer.html`. Accessed: 2025-08-07.

[178] Mini-Circuits. Wideband amplifier zva-183g-s+. `https://www.minicircuits.com/pdfs/ZVA-183G-S+.pdf`. Accessed: 2025-08-06.

[179] Low Noise Factory. 4-8 ghz cryogenic low noise amplifier: Lnf-lnc4_8g. https://quantummicrowave.com/product/4-8-ghz-cryogenic-low-noise-amplifier-lnf-lnc4_8g/. Accessed: 2025-08-06.

[180] Bluefors. Bluefors cryogen-free dilution refrigerators. https://bluefors.com/products/dilution-refrigerator-measurement-systems/. Accessed: 2025-08-06.

[181] Windfreak Technologies. Synthhd (v2): 10mhz – 15ghz dual channel microwave rf signal generator. https://windfreaktech.com/product/microwave-signal-generator-synthhd/. Accessed: 2025-08-07.

[182] Keysight. N5173b exg x-series microwave analog signal generator, 9 khz to 40 ghz. https://www.keysight.com/nl/en/product/N5173B/exg-x-series-microwave-analog-signal-generator-9-khz-40-ghz.html. Accessed: 2025-08-07.

[183] D. Kajfez. Linear fractional curve fitting for measurement of high q factors. *IEEE Transactions on Microwave Theory and Techniques*, 42(7):1149–1153, July 1994.

[184] María Hita-Pérez, Gabriel Jaumà, Manuel Pino, and Juan José García-Ripoll. Three-josephson junctions flux qubit couplings. *Applied Physics Letters*, 119(22), November 2021.

[185] María Hita-Pérez, Gabriel Jaumà, Manuel Pino, and Juan José García-Ripoll. Ultrastrong capacitive coupling of flux qubits. *Physical Review Applied*, 17(1):014028, January 2022.

[186] Fei Yan, Philip Krantz, Youngkyu Sung, Morten Kjaergaard, Daniel L. Campbell, Terry P. Orlando, Simon Gustavsson, and William D. Oliver. Tunable coupling scheme for implementing high-fidelity two-qubit gates. *Physical Review Applied*, 10(5):054062, November 2018.

[187] Matthew D. Reed. *Entanglement and Quantum Error Correction with Superconducting Qubits*. PhD thesis, Yale University, 2013.

[188] Krishna Kanth Neelisetty, Xiaoke Mu, Sebastian Gutsch, Alexander Vahl, Alan Molinari, Falk von Seggern, Mirko Hansen, Torsten Scherer, Margit Zacharias, Lorenz Kienle, VS Kiran Chakravadhanula, and Christian Kübel. Electron beam effects on oxide thin films—structure and electrical property correlations. *Microscopy and Microanalysis*, 25(3):592–600, March 2019.

[189] Ahmed M. Jasim, Xiaoqing He, Yangchuan Xing, Tommi A. White, and Matthias J. Young. Cryo-epdf: Overcoming electron beam damage to study the local atomic structure of amorphous ald aluminum oxide thin films within a tem. *ACS Omega*, 6(13):8986–9000, March 2021.

[190] Sandra Stangebye, Yin Zhang, Saurabh Gupta, Ting Zhu, Olivier Pierron, and Josh Kacher. Understanding and quantifying electron beam effects during in situ tem nanomechanical tensile testing on metal thin films. *Acta Materialia*, 222:117441, January 2022.

[191] O. Gargiulo, S. Oleschko, J. Prat-Camps, M. Zanner, and G. Kirchmair. Fast flux control of 3d transmon qubits using a magnetic hose. *Applied Physics Letters*, 118(1), January 2021.

D. List of Figures

E. List of Tables

Declaration of Authorship

I hereby declare that I have developed and written the enclosed thesis independently and have not used sources or means other than those indicated in the text and references.
Language assistance tools, including AI-based applications (i.e. ChatGPT and Microsoft Copilot), were used for text editing and phrasing. All scientific content, data analysis, and interpretations are my own work.

PLACE, DATE Signature